Constrained marker-based VMAT plan optimization towards real-time tumour tracking

by

Azeez Adeyemi Omotayo

A Thesis submitted to the Faculty of Graduate Studies of the

University of Manitoba

in partial fulfillment of the requirements for the degree of

DOCTOR OF PHILOSOPHY (PhD)

Department of Physics & Astronomy

University of Manitoba

Winnipeg, MB Canada

Abstract

This work investigates the incorporation of visibility parameters and constraints into the optimization of volumetric modulated arc therapy (VMAT) plans using fiducial markers. We propose that by incorporating fiducial marker constraints into the optimization, one may produce treatment plans that ensure a higher visibility of fiducials throughout the irradiation (a requirement for real-time tumour tracking techniques), in addition to simultaneously satisfying dosimetric requirements. We investigated this approach on a dynamic thorax phantom and multiple patient disease sites (prostate, liver and lung) using a radiotherapy optimization development software (*MonArc*).

For all the investigated datasets, three fiducial markers were implanted inside or around the planning target volume (PTV) and a VMAT plan was created for each patient. We modified *MonArc* to analyze beam's-eye-views (BEV) of the gantry arc control points to include marker-based visibility constraints of type 'hard' (i.e. requiring 100% visibility of all markers, HC) and 'soft' (i.e. penalizes visibility for one marker [SC_I] or two markers [SC_{II}] only) in the optimization process. Dose distributions from the constrained plans (i.e. HC, SC_I, and SC_{II}) were compared to the non-constrained plan (NC) using several metrics including the conformity index, homogeneity index, PTV average index and doses to organs-at-risk (OAR).

Across all the disease sites, one marker is always fully visible at all BEV apertures (i.e. 100% of the gantry arc control points) for the constrained plans. All three markers were fully visible in at least 33% of BEV apertures for the constrained plans, while also satisfying the required dosimetric objectives. Although dose metrics showed some deterioration for constrained plans (-6% for SC_I up to -15% for HC, when compared to NC using the PTV average index), the required dosimetric objectives were still satisfied in at least 90% of patients. In conclusion, we

demonstrated that marker-based constraints can be incorporated into VMAT, to produce treatment plans satisfying both the visibility and dosimetric objectives. This approach should ensure greater clinical success when applying real-time tracking algorithms for VMAT delivery.

Acknowledgements

I would like to gratefully acknowledge financial support for this project provided by CancerCare Manitoba and Research Manitoba. Much thanks!

My utmost gratitude goes to a few people who have supported and contributed throughout this project. First, I would like to thank my co-supervisors, Dr. Boyd McCurdy and Dr. Sankar Venkataraman for taking a chance on me as a PhD student. I am very grateful for their support as well as patience during my research at CancerCare Manitoba. Dr. McCurdy's insights and thorough feedback had saved me years when I may have been frustrated with slow progress, while the SBRT expertise of Dr. Venkataraman helped in understanding the clinical challenges. It was a pleasure working with both and I look forward to continued collaboration in the future where I hope to continue to benefit from their in-depth knowledge and clinical skills.

I would like to thank valued members of my Advisory committee: Dr. Jorge Alpuche, Dr. Francis Lin, and Dr. Sherif Sherif for their assistance, patience and advice throughout my project. I would also like to thank my external examiner Dr. Andrew Jirasek from University of British Columbia for his suggestions on improving this thesis write-up. This thesis would never have been completed without contributions from a host of people, namely Dr. Karl Otto for providing the optimization development software (*MonArc*) for my work and the avenue to active guidance and support for its use via Dr. Erika Chin and Dr. Byron Wilson. I am also grateful to Dr. Stephen Pistorius, the academic director of the Medical Physics graduate program at University of Manitoba, for his valuable advice and suggestions on improving my research work.

I would like to thank the following people for their invaluable contribution, especially Timothy van Beek for assistance with code/software organization for *MonArc* implementation. Thankful for the valuable company and help from colleagues, current and past – Dr Suliman

Barhoum, Dr Troy Teo, Dr Martin Heusen, Sajjad Aftabi, Parandoush Abbasian, Pawel Siciarz, Dr Reza Teimoorischiani, Dr Kaiming Guo, Princess Anusionwu, Dr Robert Bergen, Ivan Kutuzov, as well as staff at CancerCare Manitoba: Dr Niranjan Venugopal, Dr Eric van Uytven, Dr David Sasaki, Dr Idris Elbakri, Dr Harry Ingleby, Samantha Eustace, Deanne Dombrosky, Bryan Mcintosh and Dr Daniel Rickey.

Finally, I am truly indebted to my lovely mother Al-Hajja Basirat Omotayo, my father Al-Hajj Musbau (Olufowora) Omotayo, the Ajisebutu family, my siblings and their respective family too numerous to be mentioned here for their endearing support, encouragement, source of motivation and continuous prayers. And to my beautiful fiancée, Dr. Shakirat Oyetunji, thank you for your incredible support, patience and understanding throughout this journey.

Dedication

To my loving parents, and my creator Almighty Allah

Table of Contents

List of Tables

List of Figures and Illustrations

List of Abbreviations

AAPM	American Association of Physicist in Medicine
AP	Anterior-posterior
BEV	Beam's eye view
CI	Conformity index
CP	Control points
CRT	Conformal radiation therapy
CT	Computed tomography
DAO	Direct aperture optimization
DMLC	Dynamic multi-leaf collimator
EPID	Electronic portal imaging device
GM	Gradient measure
HC	Hard constraints/hard-constrained
HI	Homogeneity index
IGRT	Image-guided radiotherapy
IGART	Image-guided adaptive radiotherapy
IM	Internal margin
IMRT	Intensity-modulated radiotherapy
ITV	Internal target volume
kV	kilovoltage
LINAC/Linacs	Linear accelerator(s)
LQ	Linear quadratic
LR	Left-right

MLC	Multi-leaf collimator
MRI	Magnetic resonance imaging
MSE	Mean squared error
MU	Monitor units
MV	Megavoltage
NTCP	Normal tissue control probability
OBI	On-board imager
OAR	Organ-at-risk
PRV	Planning organ at risk volume
PTV	Planning target volume
RMSE	Root-mean squared error
RPM	Real-time position management™ (Varian)
RT	Radiation therapy/radiotherapy
SC	Soft constraints/soft-constrained
SI	Superior-inferior
SBRT	Stereotactic body radiation therapy
SRS	Stereotactic radiosurgery
SVR	Support vector regression
TCP	Tumour control probability
TR	Therapeutic ratio
VMAT	Volumetric modulated arc therapy

Chapter 1 Overview and Rationale of Thesis

1.1 Introduction

Cancer is the leading cause of mortality in Canada and is responsible for 30% of all deaths[1]. In Canada, it is estimated that 225,800 new cancer diagnoses and 83,300 deaths will occur in 2020[1]. Lung, liver and prostate cancer accounts for 32% of all cancer mortalities, with lung cancer alone accounting for 25.5%[1]. For cancer, oncological treatment options include surgical removal, radiation therapy and chemotherapy.

Radiation therapy primarily involves treatment of diseased tissue, primarily cancerous tumour cells, using high-energy radiation. The clinical application of radiation therapy or radiotherapy (RT) is based on the integration of detailed knowledge of both the physics of radiation transport and the radiobiology of cells. RT may be delivered internally via radioactive nuclides or externally via medical linear accelerators (linacs). The focus of this work specifically relates only to high-energy photon beams produced by linacs.

In the clinic, RT treatments are planned with three-dimensional, contoured anatomical volumes that are obtained usually via computed tomography (CT) imaging about two weeks before first day of treatment. Due to the relatively poor soft tissue contrast of CT imaging, often it is difficult or impossible to visualize the tumour in projection images before and during treatment. Furthermore, some tumours (especially those in the thorax) exhibit characteristics such as regular or irregular respiratory motion that may make safe delivery of the therapeutic treatment beam even more challenging. However, small, radio-opaque fiducial 'markers' can be inserted at or near the tumour tissue, before treatment simulation or delivery occurs. For example, this can be done via implantation of gold-seed (fiducial) markers, which are very dense (and more easily visible in x-ray images) and easily sterilized. As a result, tumour motion management techniques are necessary

to account for and safely deliver the optimal RT beam and dose to the tumour, as well as reducing the corresponding exposure of normal tissues that may be at risk to the treatment dose. Our work involves formally incorporating the visibility of fiducial markers into the optimization of RT plans, to aid with tumour tracking.

1.2 Thesis description and overview

Chapter 2 provides a brief introduction to the important concepts of tumour motion management and motion compensation techniques. Recently proposed tumour motion compensation methods can be divided mainly into five categories, namely: 1) motion-encompassing; 2) forced-shallow breathing; 3) breath control; 4) respiratory gating, and 5) dynamic tumour tracking[2]. Motion encompassing is the oldest and simplest approach where a 3D margin is added around the tumour tissue to encompass the largest motion extent of the target, thus ensuring the intended prescription dose is delivered to the entire target volume but is also known to over-irradiate surrounding tissue. Reducing over-irradiation, forced-shallow breathing, breath control, and gating techniques require the therapeutic beam application only during a breath hold or specific phases of the breathing cycle[3], but are not comfortable for the patient or efficient to deliver. Dynamic tumour tracking is the most promising approach as it allows the most aggressive shrinking of target margins and can be delivered much more efficiently (although it is more complex than the aforementioned methods) while maintaining comfort of the patient. It mainly involves two processes: (i) localizing the target position in real-time and (ii) collimating or simultaneously steering the therapeutic beam or patient to adapt to the target motion. The decision to apply any of these methods in the clinic is dependent on factors such as treatment time, patient

comfort, tumour characteristics and clinical capacity. The basic physics and processes of these motion management techniques are explained in 0.

Properly designing RT treatment delivery plans and estimating dose deposition within the patient are central pillars of the treatment. RT treatment plans typically require treatment margins to account for several uncertainties including patient setup errors and patient motion[4,5]. The patient motion margin, also called the internal margin (IM), may account for factors such as respiratory motion, variation in the filling of the bladder and rectum, swallowing, heartbeat and movement of the bowels. However, the increased margin also exposes a larger volume of the surrounding healthy normal tissues to the treatment dose, making it more difficult to deliver sufficient dose to the tumour without damaging the neighbouring healthy tissues. It is critically important to minimize these margins during treatment planning and delivery since any margin will directly impact the quality of the achievable plan. For example in lung tumour plans, the mean dose to the lung (recall, the remaining healthy lung is an OAR) and V_{20} (i.e. percentage of total lung volume receiving $\geq$ 20Gy dose) have been shown to correlate with lung complications such as pulmonary fibrosis and radiation pneumonitis[6–9].

Chapter 3 provides an introduction and summary of treatment planning and optimization techniques. A standard optimization approach called 'direct aperture optimization' (DAO) is introduced, and the main inverse planning approaches including some more recent refinements to DAO are described. The chapter then describes a special RT treatment delivery technique called volumetric modulated adaptive therapy (VMAT), which offers advantages over previous standard clinical delivery technologies such as three-dimensional conformal radiation therapy (3D-CRT), and intensity modulated radiation therapy (IMRT). VMAT delivers the treatment dose to the target tumour during one or more continuous rotational arcs of a linac gantry[10–12] , as opposed to static-

gantry IMRT. VMAT has also been shown to require shorter treatment times compared to IMRT[10,12–15]. More so, the use of DAO in VMAT systems results in fewer treatment beam-output monitor units (MU) required to deliver the treatment plan when compared to IMRT optimized using fluence based methods[16,17]. For this thesis, DAO was the primary optimization method employed for all investigated treatment plans, using an optimization development software called *MonArc*. DAO was chosen because it provides better efficiency in the optimization due to its distribution of the radiation beam treatment delivery restrictions in VMAT, as opposed to when used for the static-gantry delivery in IMRT.

In clinical practice, radio-opaque gold seeds (called fiducial markers) implanted in, or in close proximity to the tumour, have been used for image-guided radiation therapy (IGRT). They are used for target localization for several tumour sites since they act as surrogates to overcome inherent poor soft tissue contrast of the projection x-ray imaging available on linacs. Fiducial markers have also been used to aid tumour tracking as they can be seen via 2D projections on portal images produced by electronic portal imaging devices (EPIDs) that are readily available with current linacs. With the visibility of the markers in the beam's-eye-view (BEV) during treatment, the tumour can be 'seen' and tracked in real-time such that the most optimal delivery of the prescribed dose could be achieved in order to improve clinical performance.

Chapter 4 introduces the process of using fiducial markers for BEV image guidance and tumour localization for improved tracking in RT delivery. This process was developed by incorporating visibility parameters associated with the fiducial markers in the BEV of the therapy beam into the optimization of VMAT plans. We added separate fiducial marker-based visibility constraints to the standard dosimetric constraints in the *MonArc* development software and investigated the feasibility of this approach for a dynamic thorax phantom, a sample lung patient

and a sample prostate patient. The treatment planning performance is analyzed relative to standard non-constrained VMAT plans.

Chapter 5 presents a comprehensive retrospective clinical investigation of three motion-dependent disease sites, exhibiting different motion characteristics: prostate, lung and liver. The treatment planning performance of the marker-visibility constrained VMAT plans are also analyzed relative to non-constrained VMAT plans.

Finally, Chapter 6 summarizes the main findings of this thesis and describes future work required to implement a robust treatment technique that can synchronize the patient breathing into the marker-based plan optimization process for real-time tumour tracking.

1.3 Thesis rationale and objective

Currently, clinical implementations of real-time tumour monitoring and tracking are limited to two specialized commercial systems: (i) robotic CyberKnife® system[18] (Accuray Inc. CA, USA), and (ii) Vero® gimbaled linac system[19] (Mitsubishi, Japan and BrainLAB AG, Germany). Estimated installation base for CyberKnife® and Vero® systems are 150 and 4 respectively in the USA[20], compared to over 4000 standard C-arm linac systems. Recently, the Vero® linac has been discontinued from production. Approaches for the most common C-arm linacs that follow tumour motion with respect to the treatment beam in real-time are limited to research prototypes[21–25]. A dynamic multi-leaf collimator (DMLC)-based system, via an electromagnetically-guided transponder (Calypso®) has been investigated for prostate and lung tumour tracking[26]. Another method uses the patient couch (couch tracking), which moves such that the tumour is stationary with respect to the treatment beam[24,27]. However, the transponder system is only commercially available for gating applications (not real-time tumour tracking), and

the couch system is not currently commercially available. Hence, real-time tumour tracking via DMLC-based fiducial markers is the most likely future commercial option for C-arm linacs.

Preliminary results of using DMLC show a reduction of the gamma failure rate (dose difference at 3%/3mm) from 22.5% to 0.2% with tracking and prediction incorporated[28]. In a multi-institutional study involving four real-time tracking systems (i.e. CyberKnife®, DMLC, Vero® and couch tracking), dose accuracy improved with the mean gamma failure rate (at 2%/2mm) decreasing from 15.2% (without compensation) to 1.6% (with compensation)[29] for all lung traces from a database of stereotactic patients treated based on RTOG 1021 protocol. Similar results were obtained for prostate motion traces. The differences between all four tracking systems were small[29] (with an average 2%/2mm gamma failure rate of < 3%). Thus, uncompensated tumour motion can be a significant error when put in the context of the other contributing dosimetric errors in RT. For example, MLC tracking performed on a simulated motion phantom led to a 33.9% reduction in the mean PTV volume of ten lung stereotactic RT patients over the standard Internal Treatment Volume (ITV)-based approach recommended by ICRU 83, whereby the treatment fields are enlarged to account for motion and uncertainty[26]. MLC tracking also led to reduction in OAR dose spillage over the ITV-based approach.

It is known that VMAT treatments lead to reduced monitor units (MU) and thus reduced beam-on time and treatment duration[30]. Intrafraction tumour motion management is critically important for stereotactic body RT (SBRT), where ablative doses are delivered to the tumour in fewer fractions than conformal RT, and tighter margins are needed to adequately spare the healthy tissues. The VMAT technique is able to deliver highly conformal treatment plans in a very time efficient manner making it attractive for SBRT[31,32]. This will be especially important as SBRT is being expanded to more clinical indications including larger target sizes. More information on

VMAT and SBRT is presented in Section 3.4 and Chapter 4. Due to the high doses per fraction in SBRT, treatment times are also increased with two main consequences. First, breathing pattern changes and significant positional drifts of the tumour are more likely to occur within a (longer) fraction. Second, set-up and drift-related errors may no longer be considered random in recipes based on margins[5,33], and are likely to have a greater impact on dosimetric errors[34]. Adding in a requirement of fiducial marker visibility to the optimization process of VMAT should allow real-time tumour tracking algorithms to be applied more successfully in the clinical setting. This has not been done before, so we developed and validated the technique on some simple cases (i.e. feasibility study on a thorax phantom as well as an example patient case), then studied the method in more detail with several realistic clinical examples (i.e. prostate, lung and liver SBRT patient datasets).

The objective of this thesis is to investigate the incorporation of fiducial marker visibility into the optimization of VMAT treatment plans. Thus, we aim to develop a 3D treatment planning optimization approach for VMAT that facilitates real-time tumour tracking using fiducial marker-based constraints. Hence, this work aims to provide a tool that improves the clinical performance of dynamic tumour tracking techniques. However, our approach can be equally applied to all the motion management strategies listed in Section 2.5.5. Thus, two particular aspects will be addressed.

Firstly, the potential of including implanted fiducial markers into the RT plan optimization process is investigated. Due to the implementation of marker implantation in order to robustly follow tumour motions successfully, an efficient integration of a visibility metric for different markers into the plan optimization might result in improved performance of real-time tumour tracking algorithms.

Secondly, treatment plan quality varies depending on the spatial tumour locations and characteristics of patient geometry, in general, for a particular disease site. Hence, we investigate the potential of our modified marker-based optimization method on three different disease sites where there has been strong interest in tumour motion tracking, including lung, liver and prostate. The validation of this marker-based optimization method at multiple disease sites provides some confidence that the method can be successfully applied at a variety of sites and geometries, and provides quantitative information characterizing the trade-offs between various degrees of enforced marker visibility and the dosimetry quality of the optimized plan.

Note that an inherent assumption is that this approach will improve the performance of real-time tumour tracking algorithms during VMAT delivery. This assumption is reasonable based on real-time tracking algorithms described in the literature using MLC-based BEV tracking for lung and prostate patients[35–37], and a more detailed discussion is provided in Section 3.4.5. The excerpt below clearly describes the identified need for better marker visibility for real-time tracking algorithms as early as 2009 from Mao *et al*[36] (**emphasis mine**):

> *"A more general problem is that there will always be segments where fiducials are blocked partially or completely by the MLC in many IMRT* **(or VMAT)** *plan…We propose to take the fiducial information into consideration during the IMRT inverse planning process. With the development of segment-based dose optimization methods* **(e.g. DAO as used in *MonArc*)**, *it should be feasible to ensure the visibility of at least one fiducial during the inverse planning process."*

1.4 Thesis hypothesis

Following the very few studies that have examined marker-based tracking[37–39] for IMRT or VMAT delivery, we recognize that 'seeing' the markers in the exiting therapy beam (i.e. the markers are visible/observable within the BEV of the treatment aperture) is a critical feature of successful implementation of those tumour tracking methods. We hypothesize that fiducial marker visibility in the BEV of the therapy beam can be included during the dosimetric optimization of VMAT treatment plans, and furthermore that this approach will exhibit a trade-off between marker visibility throughout the treatment arcs versus dosimetric quality in produced treatment plans.

1.5 Novelty and scientific contribution

The novelty and scientific contributions generated from the work done in fulfilling the two specific problems identified in Section 1.3 include:

- **Novelty/Contribution 1 – incorporation of fiducial marker visibility into planning optimization.** In RT inverse planning, contoured targets and surrounding structures, together with the calculation of doses to these structures, are used during treatment plan optimization to create a series of MLC apertures and beam intensities that can achieve the prescribed doses. To date, fiducial markers are not considered in this method. However, we have included fiducial markers as structures, like the targets and OARs, in the optimization process. Instead of dose to the fiducials, we calculate their visibility within the MLC defined aperture, and incorporate that term into the plan optimization. Using the markers as structures simplifies the inclusion of their visibility into the optimization process. This is to our knowledge, the first study to incorporate visibility of markers as VMAT optimization parameters.

(*Part of this work was presented at the 2018 AAPM Annual Scientific Meeting in Nashville, TN USA*).

- **Novelty/Contribution 2 – investigation of fiducial marker-based constrained optimization in VMAT.** We utilized an RT optimization and development software (*MonArc*), by modifying it to include marker visibility into the objective function calculation. *MonArc* is the pre-cursor research software to the current version of VMAT planning software in the Eclipse® (Varian Medical Systems, USA) treatment planning system (TPS) used in our clinic. With the inclusion of the fiducial markers, we can create treatment plans with different constrained requirements on specific markers, which aids tumour tracking while satisfying dosimetric objectives. This work presents the preliminary investigation of marker-based optimization in a dynamic thorax motion phantom as well as an example prostate patient.

  (*This work was published in the Journal of Applied Clinical Medical Physics,* https://doi.org/10.1002/acm2.12892. *The formulation and implementation of the algorithms and the analysis of the results were performed by the author of this dissertation. The creation and delineation of the markers in a CT dataset for one example lung patient was performed by Dr. N. Venugopal of CancerCare Manitoba*).

- **Novelty/Contribution 3 – investigation of fiducial marker-based constrained optimization in SBRT plans.** To the best of our knowledge, this work presents the first robust investigation of marker-based constrained optimization in VMAT plans at multiple tumour sites with different motion characteristics and geometries including

liver, lung, and prostate. The significance of this work is that it demonstrates and quantifies the effects of trade-offs between marker-visibility objectives and dosimetric objectives in treatment plan quality. In this work, we discovered that constrained plans based on one specific marker (SC_I) were able to produce plans that are not significantly different from the reference non-constrained clinical plans (NC) for all the investigated diseased sites. Thus, dosimetric and marker visibility requirements were both satisfied, thus suggesting real-time monitoring on implanted markers are feasible during SBRT VMAT delivery.

(*An abstract on this implementation was submitted and accepted for presentation at the 2020 AAPM-COMP Joint Scientific Meeting in Vancouver, BC. This work was published in the Biomedical Physics and Engineering Express journal, https://dx.doi.org/10.1088/2057-1976/abce0c. The implementation of the algorithms and the analysis of the results were performed by the author of this dissertation)*.

Chapter 2 Motion Management in Radiation Therapy

2.1 Characterization of respiratory motion

Respiration is an involuntary physiological process of regulating gas exchange (intake of oxygen and output of carbon dioxide) between the human body and surrounding environment[2]. Respiratory motion is caused by the respiratory muscles. The primary respiratory muscle is the diaphragm which lies mainly in the transverse plane, separating the chest and the abdomen[40,41]. Respiratory movements can be divided into inspiration and expiration. During inspiration, the diaphragm contracts thus resulting in a displacement towards the abdomen. Therefore, organs and structures within the abdomen will be displaced anteriorly and inferiorly[41]. The secondary respiratory muscles are the intercostal muscles (lying along the rib cage). During inspiration, the external intercostal muscles contract thus the ribs displaces superiorly and anteriorly. This leads to an increment in the diameter of the thoracic cavity[40,41].

Respiration causes organ movement in the thoracic and abdominal regions, affecting for example lungs, liver, pancreas, esophagus, and breast. In addition, the prostate and kidneys are also known to move due to respiration. Thoracic, abdominal, and pelvic tumours undergo translational as well as rotational motion. During 'quiet breathing', exhalation occurs passively without muscles interacting[41]. In the case of 'deep breathing', exhalation occurs actively as additional respiratory muscles are used (e.g. internal intercostal muscles). Multiple studies have investigated the characteristics of internal respiratory motion, some of which will be presented here as an overview.

Diaphragm: Wade *et al*[42] investigated the relationship between diaphragm motion, torso diameter and tidal volume of 10 healthy subjects. For normal breathing, they reported a diaphragm

movement of 15 mm and an increased torso circumference of 7 mm in supine position. For deep breathing, the diaphragm motion range was 70–130 mm and the chest circumference increase by 50–110 mm. In another study of thoracic displacements in 20 lung cancer patients during deep inspiration and deep exhalation[43], mean values between inspiration and expiration displacement of 34.3 ± 20.4 mm and maximum displacement of 67.8 mm were reported in the superior-inferior direction. Organ motion in the superior-inferior plane was 8.0 ± 4.5 mm, with a much reduced left-right motion at 5.8 ± 5.0 mm[43].

Lung: Many studies have investigated the motion range of the lung[44–47]. Shirato *et al*[45] investigated the movement of fiducial markers in the lungs of 21 patients. They reported an average motion of 8.2 mm in left-right (LR), 10.7 mm in superior-inferior (SI), and 8.8 mm in anterior-posterior (AP) direction. In extreme cases, the motion was ≥ 28 mm for SI and AP. Dietrich and Suh[47,48] investigated 26 motion traces and differentiated between markers in the upper, middle and lower lungs. They reported the highest variance in the lower lung with amplitude ranging between 1.5 – 14.0 mm for SI, 0.6 – 7.0 mm for AP, and 0.1 – 12.6 mm for LR dimensions[48]. They also reported an overall mean respiratory period of 3.7±0.8 s in another study. Hysteresis (i.e. target trajectory difference between inspiration and expiration) has also been reported for lung tumours to range between 1 – 5 mm[46,49].

Liver: Liver motion due to respiration has been reported by many studies[40,50–52]. Kitamura *et al*[50] investigated the motion of 20 liver tumours via fluoroscopy. They reported mean amplitude of 4 mm (range, 1 – 12 mm) in LR direction, 9 mm (range, 2 – 19 mm) in SI direction, and 5 mm (range, 2 – 12 mm) in AP direction. They also reported a hysteresis effect for four tumours. Brix

et al[52] used two-dimensional MRI images for respiration-induced liver motion in five healthy volunteers. They reported mean breathing amplitude was 1.6 mm (LR), 11.0mm (SI), and 2.5mm (AP). Park *et al*[51] also reported on liver motion characteristics using x-ray projection images, with the aid of fiducial markers in 20 liver patients. They reported a liver motion range of 2.8 ± 1.6 mm, 5.3 ± 3.1 mm, and 16.5 ± 5.7 mm for LR, AP, and SI directions, respectively. That is, liver motion is most dominant in the SI direction, followed by the AP and the LR directions, respectively. They also reported that motion in the AP and SI directions were highly correlated, whereas motion in the LR direction had a more variable relationship with the AP/SI motions.

Prostate: Padhani *et al*[53] reported using cine magnetic resonance imaging (MRI) to measure prostate motion over a single 7 minute period in 55 patients. Prostate movements in the AP direction were seen in 16 patients, and in 12 patients the movement was less than 5 mm. The median prostate AP displacement range was −5 to +14 mm[53]. Hewson *et al*[54] recently reported on a multi-institutional tracking method for prostate tumours in 44 patients. The translational motion ranged between [−5.7 and 9.8 mm], [−3.6 and 4.3 mm], and [−9.5 and 8.2 mm] in the AP, LR and SI directions respectively. They also reported prostate rotation of between −9.5° and 6.6°, −17.6° and 30.3°, and −11.4° and 14.4° about the AP, LR and SI axes[54], respectively.

Pancreas: Dietrich and Suh[48(pp3-13)] investigated the motion of pancreatic tumours for nine patients. They reported a motion range from 0.2 – 9.4 mm in SI, 0.3 – 4.8 mm in RL, and 0.9 – 4.8 mm in AP directions, respectively. Gierga *et al*[55] investigated seven patients, where a motion range varying from 4.4 – 9.9 mm was reported. Goldstein *et al*[56] reported that the mean gross tumour volume (GTV) excursion was 5.2 ± 2.3 mm (SI), 3.0 ± 1.7 mm (AP) and 3.0 ± 1.8 mm (LR),

respectively. They also reported mean respiratory-induced SI motion of the right and left kidney was 7.2 ± 3.0 mm (range, 1.7 – 13.8) and 6.4 ± 2.3 mm (range, 2.2 – 11.1), respectively. The authors also reported that neither the left nor the right kidney SI movement correlated with the GTV SI motion. This shows different characteristics than the pancreatic tumours as the kidney OARs showed significantly greater motion compared to the target, meaning larger tumour margins will be required to compensate for the dose to the tumour.

Kidney: The characteristics of kidney motion reveal a complex pattern and were observed to be strongly associated with respiration. The right kidney tends to move more than the left kidney due to its location being proximal to the liver. In a review summary of fifteen publications[57], the author reported mean kidney motion of up to 13 mm and 11 mm for the right and left kidneys, respectively. Kidney movement of up to 8.1 mm in the AP direction and 6.2 mm in the LR direction were reported with no indications that breathing technique can influence the extent of this motion. Abhilash *et al*[58] reported on respiration-induced kidney motion in 48 normal and 62 diseased subjects. The average movements of the right and left kidneys were 24.5 ± 6.4 mm and 17.0 ± 3.6 mm in the SI-direction; 13.6 ± 3.7 mm and 9.8 ± 3.3 mm in the LR-direction, respectively. No motion was reported in the AP-direction.

In conclusion, there are many different tumour motion characteristics with motion correlation in different directions, location, motion patterns, and relative displacement of the OAR; this suggests that careful attention is needed in characterizing tumour motion during the planning and treatment of cancer patients. If not accounted for, tumour movement can cause the tumour to become misaligned with the radiation beam, thereby compromising cancerous tumour control and increasing normal tissue toxicity[59].

2.2 Observation and imaging of respiratory motion

The extent of respiration-induced tumour motion is mainly measured using imaging methods such as fluoroscopy[40,46], computed tomography (CT)[60], and magnetic resonance imaging (MRI)[61].

Fluoroscopy: The most direct imaging tool to observe respiratory motion is fluoroscopy. However, the acquisition of fluoroscopy is time-limited in order to prevent excess exposure to ionizing radiation. Furthermore, some tumours cannot be directly observed by fluoroscopy, hence may require surrogate markers to visualize the tumour, such as implanted fiducial markers.

4D-CT: In recent years, 4D-CT imaging has moved into common clinical use. In contrast to breath-hold CT acquisition, 4D-CT image acquisition occurs during free breathing and projection data are sorted into phase bins due to position within the respiratory cycle, based on direct anatomical information (e.g. position of diaphragm) or surrogate data (e.g. optical skin markers or spirometry). Thus a series of 3D-CT datasets are acquired, with each analogous to a different part of the respiratory cycle[48]. 4D-CT imaging is valuable in observing the motion amplitude of lung tumours and to determine customized treatment volumes. A disadvantage of 4D-CT is that it only shows tumour motion averaged over a few respiratory cycles and is not necessarily exactly representative of the tumour motion of the patient at a future appointment.

MRI: MRI can also be acquired and binned into respiratory phases to generate a 4D-MR[62,63]. Advantages are that there is no need to use ionizing radiation for image acquisition compared to fluoroscopy and CT, and better image contrast is achieved for soft tissue. However, current pulse

sequences are not yet fast enough to obtain data in real-time. In addition, most RT departments usually do not have MR scanners in their establishments, due to high cost.

PET: PET scans can be obtained in synchronization such that respiratory motion is monitored, while counts in each detector are associated with a time point in the respiration signal. The counts can then be binned into separate scans representing individual phases in the breathing cycle (i.e. a 4D-PET)[64–66]. However, 4D-PET scans are also not widely used in RT departments, also due to high cost.

2.3 Challenges of imaging respiratory motion

In general, CT scans takes place on roughly the same time scale as that of respiration. The acquisition of a single CT slice (or Section in a multi-slice scanner) typically takes 0.5–1 s, while a respiratory cycle typically takes 3–6 s. As such, target tumours and organs at risk (OARs) move, both during slice acquisition and in-between sequential slice acquisitions, which creates image artifacts[66]. The problem becomes more challenging when changing from standard CT scanners (for diagnostic uses) to mobile C-arm scanners often used in image guided-interventions[41,67]. The acquisition time for an entire thorax volume can be up to several minutes. Depending on the acquisition time, all modalities mentioned in Section 2.2 are affected by respiratory motion to some extent. The resulting artifacts can be broadly divided into those being caused by: a) motion during image acquisition (e.g. blurring or streaks) and b) between images (e.g. registration)[68].

The nature of the artifacts also depends on the CT scanner settings and on the characteristics of the patient breathing cycle. An example artifact is image blurring. Blurring will occur when the slice acquisition time is long compared to the respiration cycle time. Another

artifact is the partial projection effect, which occurs when both the target tumour motion and the patient movement through the CT scanner interfere with each other, causing the structure to not appear in its actual shape[66]. With these artifacts, the target tumour shape, volume (and associated contours) are not accurately represented in the corresponding images. It is therefore highly desirable to reduce or eliminate these artifacts. For example, the use of breath-hold CT and active breathing control has also been reported to reduce artifacts[69] related to tumour motion. This later led to the development of respiratory-synchronized CT scans, or '4D-CT' scans, where CT slice acquisitions are synchronized with the patient's respiratory cycle during the imaging. Nonetheless, some artifacts – such as partial-volume and distortion artifacts – are still noticeable even in 4D-CT images, due to irregularity of the breathing pattern over the duration of entire scan acquisition or mismatches of respiratory phases or abdominal displacements[70].

In the case of MRI, the MRI acquisition time (typically 20 min – 2 h) is longer compared to CT images. As a result, MRI's are generally more prone to motion artifacts. Furthermore, MR techniques such as contrast-enhanced MRI have acquisition times that invalidates breath-hold techniques[68]. MRI motion artefacts are expressed as blurring effects or as ghost images of the moving structure[71].

In the case of PET, respiratory motion leads to two main artifact effects[64,65]. First, the volume of the structure which is highlighted by a radioactive marker such as 18F-fluorodioxydoglucose (FDG) is overestimated. Second, it affects the accuracy of quantitation of FDG accumulation, leading to a reduction of the measured standard uptake value (SUV). These may lead to reduced visibility and increase in PTV volume[65]. Nehmeh *et al*[65] investigated a respiratory gating approach for PET based on an external surrogate in both phantoms and one patient. The authors reported a 28% decreased lesion volume and a 56.5% increase of the SUV[65],

using respiratory gating for motion artifact correction. With the more recent availability of clinical 4D PET-CT scanners, motion artifacts are reduced but still share some of the same remaining issues of 4D-CT described above.

2.4 Radiation therapy and imaging equipment

The most common method for radiation therapy delivery is the use of high energy photons generated externally to a patient. The research focus of this work was tailored specifically to high energy photon beams produced by linear accelerators.

2.4.1 Linear Accelerators

A high energy radiation beam of photons is produced by a medical linear accelerator (linac) (Figure 2-1). Electrons are initially accelerated from rest via an electron gun, and then transmitted through an accelerating waveguide where the electrons reach high velocity (i.e. high energy). These high energy electrons are directed to strike a metal target (often tungsten). The collisions with target atomic nuclei result in emission of bremsstrahlung photons, which are used as the treatment beam. Electron collisions with target orbital electrons can also create atomic shell vacancies that produce low energy characteristic x-ray emission, but their contribution to the resultant photon beam is negligible for electron energies in the megavoltage (MV) range required for RT.

Several components in the linac treatment head help shape and control the radiation beam that is delivered to the patient (Figure 2-1). The primary collimator defines the maximum diameter circular field. The flattening filter is a cone-shaped piece of metal designed to preferentially attenuate photons at the center of the forward peaked incident photon beam, such that the dose

deposition profile is uniform at a certain depth in water. The dual ionization chamber (or 'monitor' chamber) is a safety feature and monitors the radiation beam output (measured in monitor units, MU) as well as the beam flatness. Linacs are typically calibrated such that 1 MU corresponds to a dose of 1 cGy measured at the depth of maximum dose and under a set of standard or reference conditions. The maximum dose rate in most linacs is 600 MU/min. Recently, manufacturers have developed linacs with higher dose rates (1400–2400 MU/min) by removing the flattening filter[72,73]. Below the monitor chamber, the linac also has a secondary collimator system composed of moveable upper and lower jaws that further collimate the radiation beam into rectangular fields. Below this lies a final, more complex collimation component, the multi-leaf collimator (MLC). The MLC is composed of multiple opposing leaf pairs that are individually controlled to move in and out of the beam in order to create irregular fields that conform to the tumour shape, and also allow for complex intensity modulated beams (Section 0). Once beyond the MLC collimator, the radiation beam enters the body towards the target tissue.

When the tumour is targeted from multiple angles, a high dose region can be created that encompasses the tumour, while substantially sparing the surrounding healthy tissue. Due to radiobiological reasons, the total prescribed dose is usually divided into daily fractions to which the patient is exposed over many days or weeks. The total dose and fractionation (number of daily fractions) depends on the cancer type and tumour size, but commonly 2 Gy fractions are used over several weeks (for example 5000 cGy in 25 fractions, delivered over 5 weeks). However, recently there has been a trend within the radiation oncology community to explore higher doses per fraction, delivered in fewer fractions. Due to the reduced number of fractions in this approach, the required accuracy per fraction is increased (compared to conventional fractionation) and is termed stereotactic radiosurgery (SRS) if applied to tumours in the spine and brain, and stereotactic body

radiation therapy (SBRT) for tumours in the rest of the body. An associated risk is that the larger dose per fraction in SBRT can increase the probability and severity of toxicity in adjacent OARs.

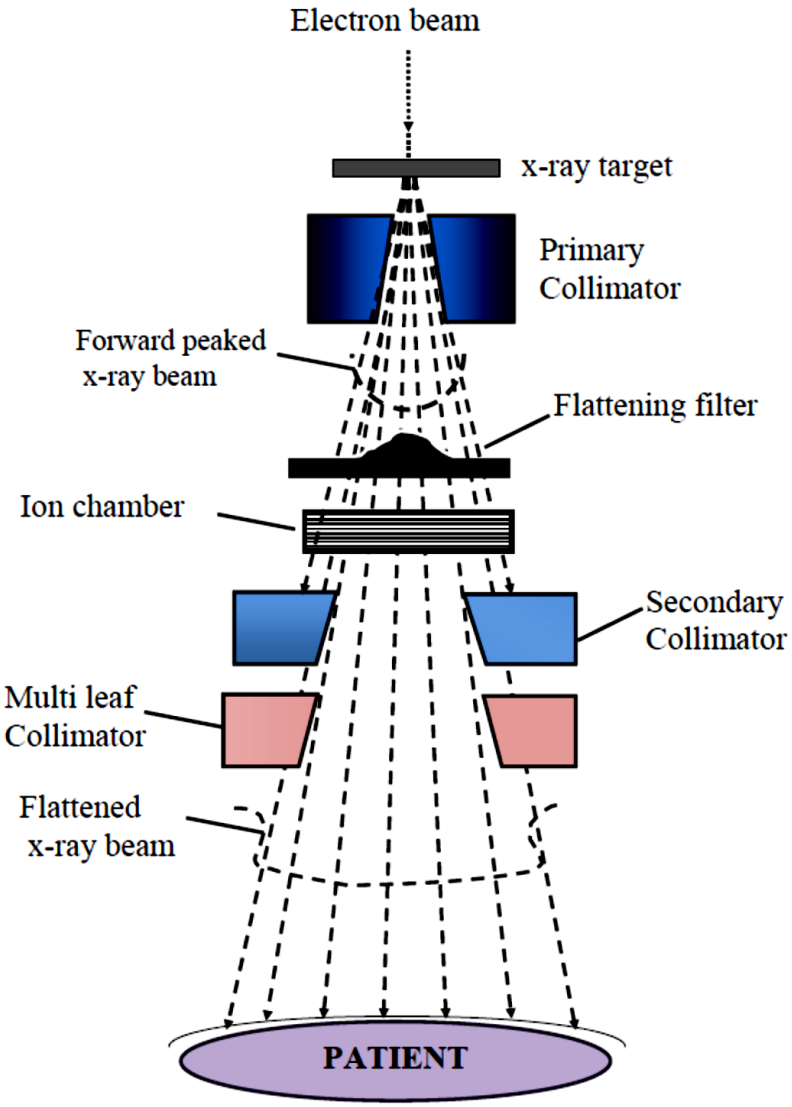

Figure 2-1: Schematic diagram of the various components in a linear accelerator used for creating photon and electron beams. Reproduced from Asuni[74] with permission.

2.4.2 Imaging Systems

The integration of imaging systems with the linac is another essential component of modern radiation therapy. In-room imaging systems are used for pre-treatment verification of patient setup, incorporated into motion management strategies during treatment and also utilized in post-treatment checks of radiation delivery accuracy[75]. Figure 2-2(a) displays a flat panel electronic portal imaging device (EPID) which consists of a matrix of amorphous silicon detectors mounted on the opposite end to the linac head, allowing it to detect the MV treatment radiation resulting in 2D images of both the beam portals and patient anatomy. A linac is also equipped with an on-board imager (OBI) that provides diagnostic (kV) quality imaging (Figure 2-2(b)). The kV energy imaging gives better image quality than the MV imaging of the EPID due to better contrast. The OBI can provide 2D radiographs, fluoroscopic images, or 3D cone-beam computed tomography (CBCT) images. Although not as common, non-linac mounted imaging options are also available and include stereoscopic X-ray imaging (Figure 2-2(c)) and tracking of reflective body surface markers using an infrared tracking camera (Figure 2-2(d)).

(a)

(b)

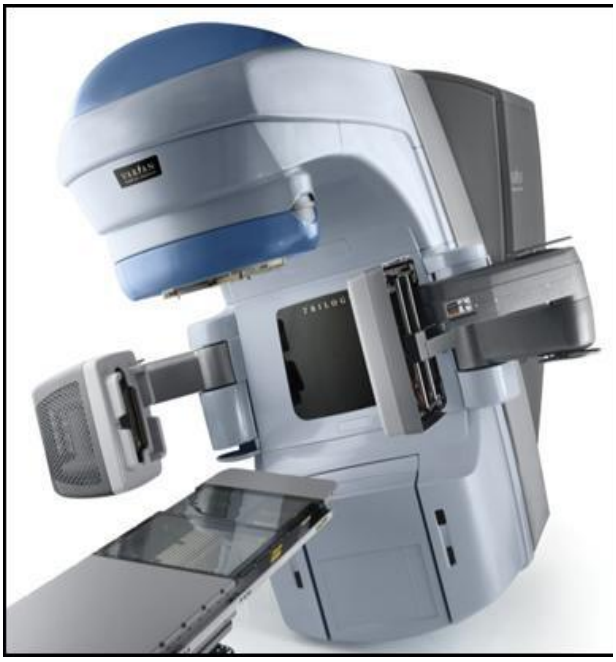

(c)

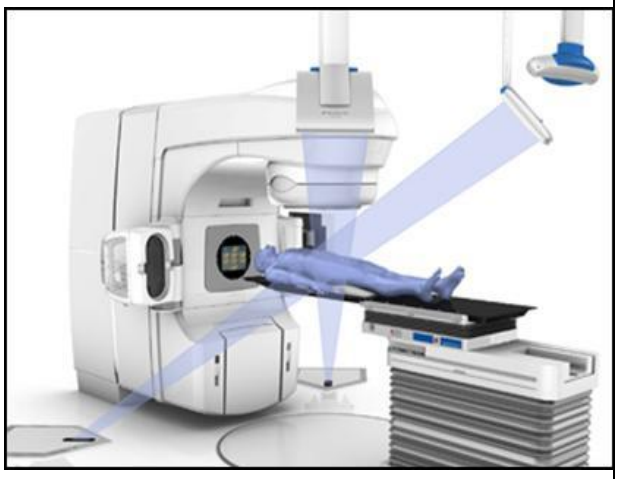

(d)

Figure 2-2: (a) Linac equipped with an EPID (b) Linac equipped with an OBI (Images courtesy of Varian Medical Systems Inc., All rights reserved) (c) Illustration of in-room stereoscopic X-ray imaging (d) Illustration of in-room infrared tracking of reflective markers on a patient surface. (Images courtesy of BrainLab AG. All rights reserved)

2.5 Motion compensation techniques

As mentioned in Section 2.1-2.3, the tumour can often move due to patient physiology, thus motivating techniques to modify radiation therapy delivery to compensate for this motion. Motion compensation techniques can be broadly divided into five categories[41]: motion-encompassing; forced-shallow breathing; breath-hold; respiration gating; dynamic tracking. The major drawbacks of the first four techniques are: potential healthy tissue irradiation, increased treatment time, patient discomfort, or a mixture of all three. More details regarding the techniques are briefly discussed below.

2.5.1 Motion-encompassing method

This is the simplest and most commonly used method to account for tumour motion. First, the range of the tumour's displacement is estimated from CT imaging (preferably 4DCT), and then treatment margins (Section 3.2.1) – up to 10 mm in superior-inferior direction – are added accordingly to accommodate the motion range (as illustrated in Figure 2-3). An advantage is that no special hardware is required and enables the patient to breathe freely. The disadvantage is that significant healthy tissue will be irradiated depending on motion range. Thus, there is increased chance of side effects including higher toxicity and an increased risk of a secondary cancer in the future[76–78]. This method also conflicts with SBRT's need to minimize healthy tissue exposure by conforming dose to as small a treatment volume as possible.

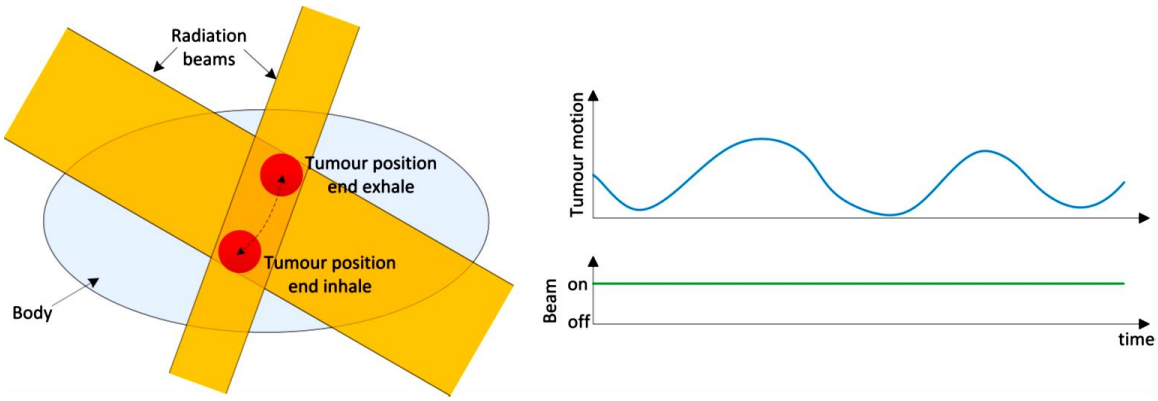

Figure 2-3: Illustration of the motion-encompassing method whereby target area is increased to cover the entire range of tumour motion. Reprinted from Durichen[41].

2.5.2 Forced-shallow breathing

An option to minimize intrafraction motion due to respiration is to limit the diaphragm's range of motion. For example, a pressure plate is applied to the patient's abdomen with enough force such that the motion of the diaphragm is constrained. Patient breathing becomes shallower which leads to a reduction in tumour motion range (see Figure 2-4). Negoro *et al*[79] demonstrated in 18 patients that abdominal compression can be used to efficiently reduce the range of lung tumour motion from 8–20 mm to 2–11 mm. The disadvantage of such systems is patient discomfort and residual tumour motion (i.e. tumour motion is not completely suppressed).

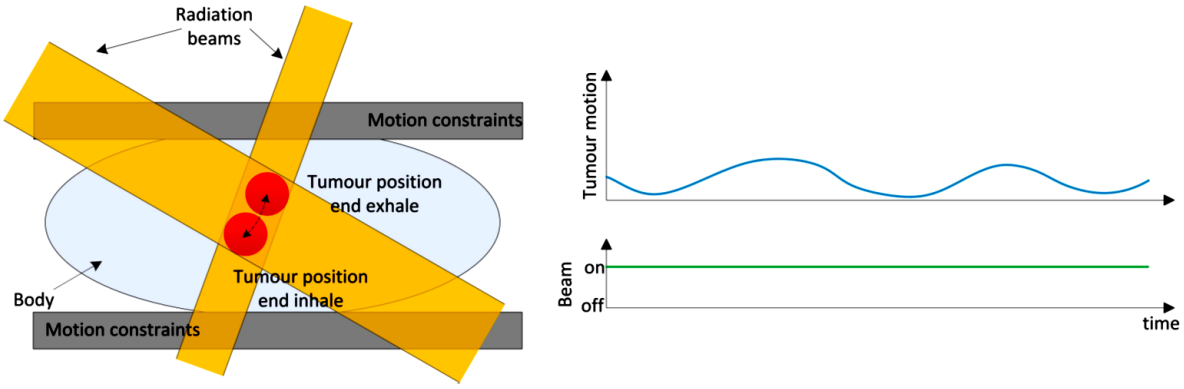

Figure 2-4: Forced-shallow breathing illustration; potential range of target motion is restricted due to constraints such as a pressure plate/abdominal press. Reprinted from Durichen[41].

2.5.3 Breath-hold techniques

This technique is established on the observation that tumour position is almost constant when constrained to a specific breath-holding period. However, the tumour motion then has to be analyzed in tandem with an external surrogate such as a spirometer[80] (a device used to measure the volume of air entering and exiting the lungs) or an external optical marker[81,82], before treatment. In practice, the patient receives a visual or acoustic signal which indicates that they hold their breath at a certain position[83] while the treatment beam is turned ON at the designated breath-hold positions (called patient coaching), which ideally lasts for at least 10s.

Implementation of breath-hold techniques has been approached in multiple ways. In deep-inspiration breath-hold (DIBH), the patient's breathing is monitored using a spirometer and the therapist is responsible for turning the beam ON during breath-hold and turning the beam OFF when the patient resumes respiration[43,84]. In active-breathing control (ABC), a balloon valve attached to the spirometer is inflated with an air compressor during breath-hold to help suspend the patient's respiration[46,69]. The main drawback of breath-hold techniques is that the treatment outcome relies on the patient's active cooperation during coaching. Ideally, patient coaching is performed before treatment to produce better on-treatment results.

The use of a spirometer can cause patient discomfort. An alternative to the spirometer is to use optical infrared external sensors, for example in Varian Medical System's real-time position management (RPM) system. In the RPM system, a box with reflective markers is placed on the patient's abdomen. An in-room infrared tracking camera detects motion of the reflective markers which is primarily in the AP direction during respiration. The patient's respiratory pattern is constantly monitored and beam-on and beam-offs can be triggered based on pre-defined thresholds[85]. The respiratory phase is indirectly inferred from the external measurement of the

patient's abdominal motion and its correspondence must be properly verified prior to treatment using some form of x-ray imaging.

2.5.4 Respiration gating techniques

'Respiration gating' and 'respiratory gated' refer to the synchronization of imaging and radiation delivery with respiration, such that image acquisition/radiation delivery only occurs during a certain part of the respiratory cycle[2]. This technique is based on the observation that the tumour position is almost constant within a specific window ("gate") during the respiratory cycle[41,44]. Respiratory gated techniques allow the patient to breathe freely while the treatment volume is minimized by irradiating the tumour only when present at a given location known as the gating window[44,86–88] as shown in Figure 2-5. However, the total treatment time increases. Thus for every patient, the gating window size and the resultant residual tumour motion has to be optimized to balance between treatment time and treatment volume accuracy[41,89].

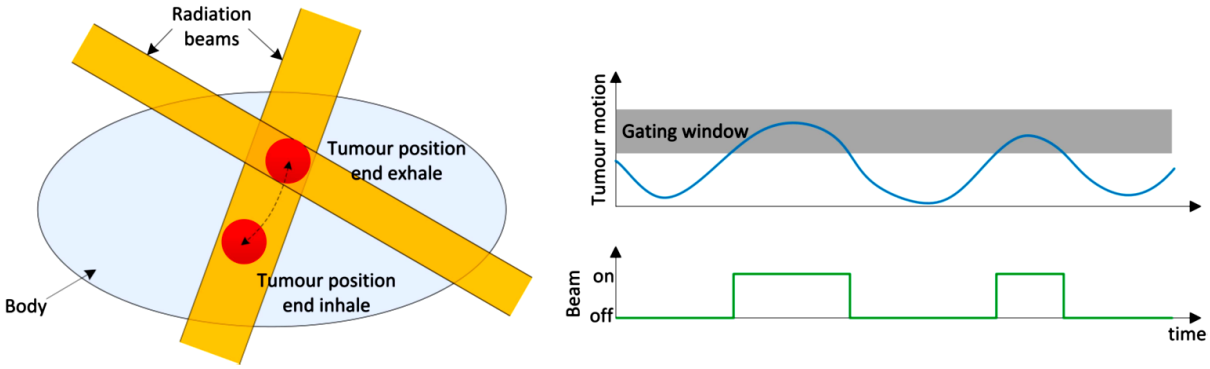

Figure 2-5: Respiratory gating illustration whereby beam is ON only if tumour position is within a preset respiratory phase (called gating window). Reprinted from Durichen[41].

Treating the tumour near maximum exhale allows the radiation beam to be active for a greater fraction of the respiratory cycle, hence benefitting treatment times. The exhale portion of

the respiratory cycle usually lasts longer and has more stable tumour positions than the inhale portion. In contrast, it can be more dosimetrically advantageous to treat the tumour near maximum-inhale when the lung volume has expanded (thus potentially moving OARs further away from the tumour).

In order to gate the radiation beam, continuous monitoring of the patient's breathing motion is required via either an external respiratory signal or an internal fiducial marker. Radiation delivery will automatically be triggered ON or OFF when the patient's breathing enters or exits the gating window. Options for an external respiratory signal include patient surface markers tracked with an infrared camera (e.g. RPM® system), a strain gauge within a belt wrapped about the patient's mid-section, or a 3D video camera that monitors the patient's ventral surface. Internal signals can be provided by implanting radiopaque fiducial markers in or near the tumour. These fiducial markers can then be detected via stereoscopic x-ray imaging system, or by the linac EPID or OBI systems.

The benefit of using external surrogate signals are that data acquisition and processing times are relatively fast and the patient receives no extra radiation exposure. However, the external surrogate motion may not accurately represent the internal tumour motion; such as a phase shift between external surrogate and the internal tumour motion which needs to be corrected by a correlation model during treatment simulation[2]. The disadvantage is that the correlation between the surrogate signal and the tumour position is not as robust as an internal signal and can drift over time[90]. It has been reported that if a phase shift exists between internal tumour motion and external surrogate motion during the simulation process, which changes over the course of radiotherapy treatment, then there may be a phase offset up to ± 0.65 s and amplitude mismatch of up to 5 mm[90,91]. For the internal fiducial marker approach, aside from the added radiation dose to the

patient, implantation of fiducial markers is invasive and (for lung tumours) carries the risk of pneumothorax[92]. Another drawback of gated approaches in general is that the discontinuous delivery of radiation results in longer treatment times.

The fraction of the respiratory cycle where the beam is enabled is referred to as the 'duty cycle' and its value depends on the patient's breathing pattern and gating window set. Generally, duty cycles can range from 30–50%[2], which translates to treatment times that are at least 2–3 times longer than plans delivered using a motion-encompassing method. Considering SBRT treatments are already longer than conventionally fractionated treatments due to the higher dose per fraction, gating of SBRT will further extend treatment times. Patients may experience greater discomfort leading to an increased risk of patient movement and associated dose delivery errors. Patient throughput will also decrease.

In principle, gating can be delivered based on either the phase or amplitude of respiratory motion. For regular and periodic respiratory motion, both the amplitude and phase gating would result in similar duty cycle and residual target motion. For irregular breathing, the amplitude gating may result in less residual error than phase gating, but the duty cycle would be higher. The breath-hold is also another form of gating in which the radiation beam is administrated during breath-hold. The main advantage of breath-hold is that the duty cycle is increased with minimal/no residual target motion, and the main disadvantage is that it may not be applicable to all lung cancer patients due to patient discomfort or inability to hold breath.

2.5.5 Dynamic tracking techniques

In dynamic tracking, the radiation beam dynamically tracks the tumour motion as the patient breathes freely. This allows treatment margins to remain small while simultaneously

maintaining continuous radiation delivery (i.e. 100% duty cycle). Dynamic tracking techniques are the most complex to implement and are not yet commercially available on standard linacs. They require three distinct steps: (i) knowledge of tumour location or position (i.e. real-time target determination), (ii) the ability to predict future tumour positions (via a prediction model) which is required to compensate for delays in processing and communication due to the treatment delivery system's response (i.e. time latency), and (iii) a method to reposition and modulate the treatment beam to the tumour (i.e. real-time beam adaptation). All the previously discussed motion compensation techniques in Sections 2.5.1–2.5.4 have disadvantages with respect to treatment time, patient comfort and accuracy. Dynamic tumour tracking offers the possibility to overcome these drawbacks.

2.5.5.1 Real-time target determination

The options for real-time target determination are the same as discussed in the previous section on respiratory gating techniques: either via MV imaging[93], KV imaging[94], stereoscopic imaging[95], hybrid systems[18,96] and alternatively via electromagnetic sensors[21,22,25,26,97,98]. There are indirect or direct methods to obtain the tumour position. An example of an indirect method is using an external surrogate (spirometer, optical block, pressure belt etc.) as discussed in Section 2.5.4. A more direct method of measuring tumour position is using fiducial markers inserted inside or near the target that follow the tumour motion, which can be imaged in real-time. Thus, a method or algorithm to segment and reliably determine the internal fiducial markers in complex anatomical image backgrounds is required.

Due to contrast differences between the marker and most tumours, it is an ideal visibility tracker for tumours in images. However, some marker segmentation algorithms based on pixel

intensity suffer when markers are in the vicinity of high contrast structures such as bones and very dense tissues. Approaches to resolve this include using **template matching** algorithms, whereby a region of interest (ROI) around the marker is defined, and a normalized cross-correlation is applied to select the highest cross correlation between a template and correlate pixels, to yield the marker location. However, such methods have high detection failure rates when applied to track internal fiducial markers that rely on MV imaging due to low contrast inherent between different materials in MV based images.

A refined and accurate template method for fiducial marker-based target determination is using a **pattern matching** algorithm as proposed by Mao *et al*[99] (2008), which can combine both MV and KV imaging to locate the tumor position in real-time. They tested their approach using gold (Au) cylindrical markers of 1.2 mm diameter and 5 mm length, on a Varian Trilogy linac with a-Si detectors for EPID MV-based and on-board kV-based images. Essentially, the workflow (as shown in Figure 2-6) involves an intensity-based search for the markers on the planning CT, which is easily segmented due to contrast differences from the image background. Then, this is followed by transformation of the marker's CT co-ordinates to the treatment isocenter co-ordinates in order to obtain the 3D positions (x, y, z) for the markers relative to the isocenter[100]. The 3D position is thus used to predict the expected projection location (u, v) of each marker on either the KV or MV detector, based on the rotational and geometric relationships between the gantry angle (ϕ) and distances from the image source to the isocenter (SAD) and imaging detector (SID). More details are available in Equations (1) and (2) of Mao *et al*[99].

The marker orientation is then determined using eight equally split bins to account for all possible orientations due to the unsymmetrical shape of marker projection length from different gantry rotations from 0°-180° (see Figure 2-6)[99]. Then finally, a trapezoidal pattern match was

used for the cylindrical marker shape to search and identify the unique cross-sectional patterns of every pixel in the ROI around the markers, because the signal intensity distribution along the cross section of the cylinder projection remains constant even when the marker projection changes. To identify the marker and differentiate overlapping markers, the pattern and the surrounding pixels was compared to determine the squared-correlation coefficient (R^2) and scaling factor (H) at each pixel location within a ROI group. These two criteria were used in combination as scoring index to achieve 100% detection of multiple markers (up to five) in a head phantom and a prostate patient[99].

Keall *et al*[93] developed a method based on MV-based EPID using a dynamic thorax phantom, with three gold fiducial markers, to track the tumour motion in real-time. The authors concluded that although EPID-based tumour tracking is feasible, there exists a system time latency which must be managed via a prediction model. Poulsen *et al*[94] described a method to localize the moving target position in real-time using a single kV imager via fluoroscopic imaging during the arc delivery. They reported a geometrical accuracy within 2 mm. Recently, a first clinical implementation of a KV-based intrafraction monitoring (KIM) system was reported[54,101,102]. This method has been implemented at four different centers in Australia.

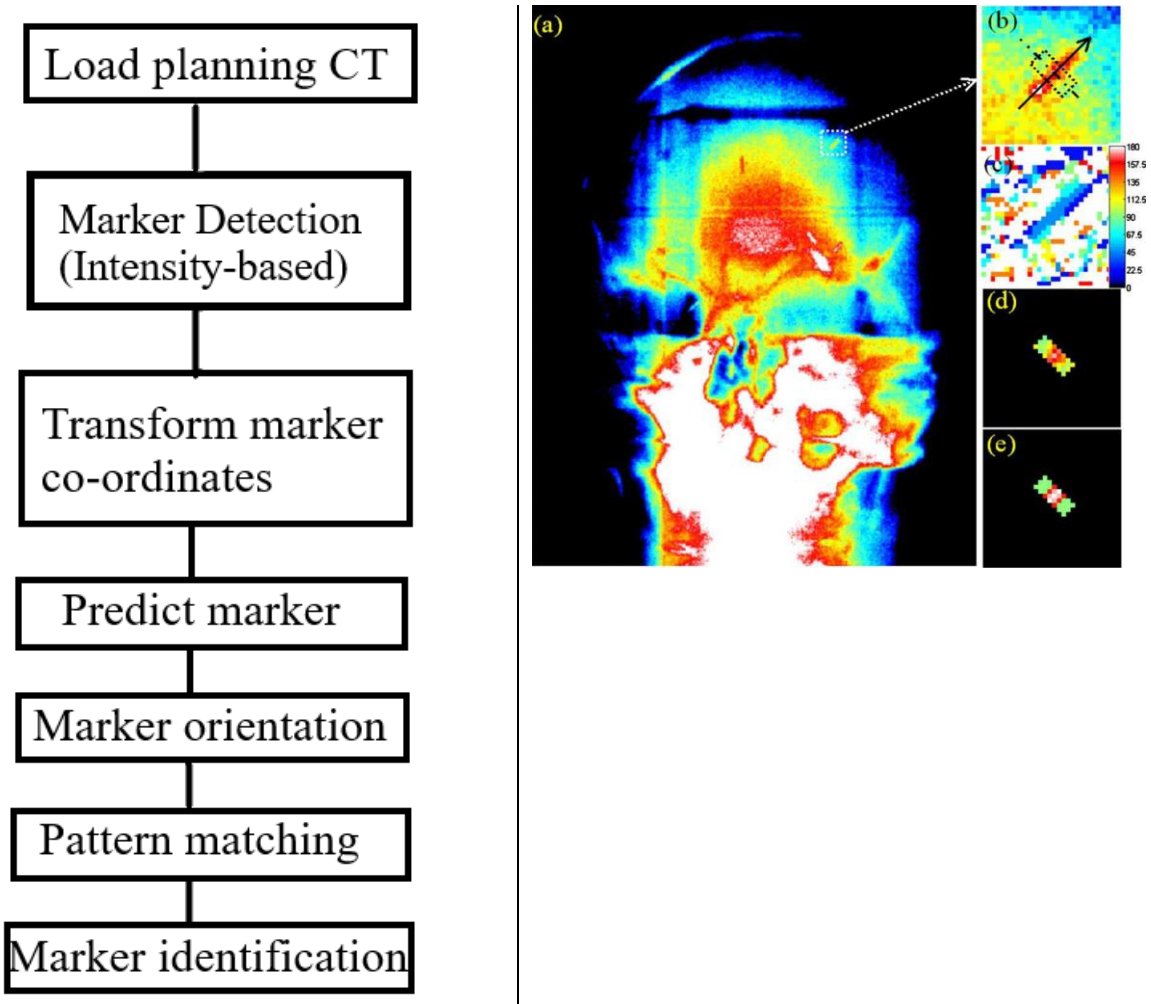

Figure 2-6: [Left]: Fiducial marker tracker algorithm flow-chart and computational path. [Right]: (a) MV image of a head phantom with embedded cylindrical fiducial (b) Magnified image of the selected marker displaying orientation and cross-section dotted line (c) Orientation map with pixel intensity corresponding to adjacent intensity orientation for the selected marker (d) and (e) Pattern matching to segmented cross-section. Figure adapted from Mao *et al*[99] used with permission from Wiley Inc.

For efficiency and improved accuracy, both MV and kV imagers may be used to acquire the moving target position. Cho *et al*[28] developed a method for real-time target position using hybrid kV/MV imaging, and reported a dosimetric and geometric accuracy < 1 mm. However, the latency of the integrated system was significant (~450 ms), thus requiring a prediction of the target

position in advance. Frequently, other forms of hybrid imaging systems that combine both internal and external respiratory acquisition methods are used. For example, continuous tracking of the respiratory cycle can be provided through external optical markers on the patient while periodic x-rays are taken to verify or update a correlation model between the external surrogate and the internal tumour motion[103].

However, a concern is that there is a high chance of a relatively significant radiation dose being imparted to the patient due to use of ionizing radiation during kV and MV imaging of patient for real-time target positioning. Thus, techniques have evolved to reduce or eliminate the ionizing radiation dose. One way of reducing dose is using such method as the 'Synchrony System' available with CyberKnife® robotic tracking system which uses both an external surrogate marker (via infrared camera) and internal tumour surrogate (via kV stereoscopic imaging) for tumour localization[48,104,105]. Prior to treatment delivery, the internal-external correlation is determined, and the treatment is continued with external surrogate tracking alone. The validity of this correlation is updated with frequent (but not continuous) x-ray imaging. One direct way of eliminating imaging-related dose is to use non-ionizing radiation, an approach taken with the electromagnetic (EM) transponder-based Calypso® target tracking system. Using implanted beacon transponders and an external EM array, it monitors target motion in real-time. The Calypso® system is a commercially available EM tracking system and has been successfully used for gated treatments[98], and recently extended for other tracking techniques[26,106].

2.5.5.2 Prediction and Correlation models

All beam adaptation systems have a common issue of time latency, due to delays caused by data acquisition, processing, and kinematic limitations of the specific system. These delays

result in a time lag or latency between when the tumour moves, and when the treatment system can react to that movement[41]. These time latencies vary from 50ms for VERO®[107], 115ms for CyberKnife®[105] up to 450ms for robotic patient couches[24,27,108] and MLCs[109]. Poulsen *et al*[109] developed a method to analyze the latency period of a prototype image-based DMLC tracking system. They reported a latency period of 380 ± 9 ms and 420 ± 12 ms for MV and kV image-based tracking, respectively. Time latency can be compensated by predicting either the external marker or the internal tumour position. Therefore, a model is required (prediction model or prediction algorithm). Many different approaches for respiratory motion prediction algorithms have been presented in the literature and are briefly discussed here.

Most of the mathematical models used for prediction include spline extrapolation techniques, sinusoidal models, adaptive filters such as autoregressive (AR) filters, least mean squares (LMS), recursive least squares (RLS), and kernel adaptive filters. Artificial neural networks (ANN), either with linear or non-linear activation functions, have also recently been used for respiratory motion compensation as first proposed by Murphy *et al*[110,111]. Kalman Filters (KF), a recursive and linear dynamic state estimation technique, have also been used for prediction[112]. To model non-linear target motion, the extended Kalman filter (EKF)[113–115] has been used. Support vector regression (SVR), using support vectors has also been combined with kernels to model non-linear tumour motion via different kernel functions[103,116,117]. Probabilistic approaches using kernel density estimation (KDE)[118] and Gaussian process (GP) regression[114,119] have also been implemented. Probabilistic approaches offers advantages by utilizing the second-order statistics of the conditional distribution, i.e. the variance, such that the "uncertainty" of the prediction model can be expressed[41]. Hence, this information could be used to detect potential large prediction errors[41,120].

Ever since image guidance was proposed for dynamic tumour tracking, increased interest in the correlation between external and internal motion has followed. Many investigations have explored the correlation of external optical markers and internal motion[91,121–124]. Few have reported a temporal shift between the internal and external motion. These temporal shifts led to a hysteresis effect as described by several researchers[18,96,125–127]. Hoisak *et al*[91] observed phase differences between tumour motion and respiratory volume between −0.3s to +0.5s and described tumour to abdominal motion phase shifts between −0.65s and +0.5s. Hysteresis is influenced by the patient's breathing pattern. Due to the tumour location, this can result in different trajectories. Interfractional variations were also investigated by Hoisak *et al*[91]. The correlation of abdominal displacement and respiratory volume (via spirometer) to an internal tumour motion (via fluoroscopy) was studied for five patients, via pre-treatment, pre-fraction and intra-fractional imaging. The correlation was consistent for one patient only over multiple days, and worked only when pre-treatment imaging was obtained[91].

In summary, tumour motion prediction and correlation algorithms have been implemented mainly using linear and quadratic regression models. In principle, more complex correlation algorithms such as the SVR method of Ernst *et al*[125] or the kernel method of Li *et al*[128] require larger training data compared to simpler models. Moreover, since fluoroscopy or CT is used to image the target to obtain position internally, such correlation models lead to increased radiation dose to patients[41].

2.5.5.3 Real-time beam adaptation

For linacs, the most common option for realigning the treatment field to the tumour trajectory is via continuous motion of the beam-shaping multi-leaf collimators (MLCs) consisting

of multiple leaves (i.e. dynamic MLC or DMLC tracking). As at the time of this writing, there are no widely accepted standards for using DMLC-based tracking for standard linacs and the concept has only been investigated in research-based or in-house applications. Other methods for beam realignment are either: moving the gantry in line with the tumour trajectory (i.e. dynamic tracking) which is available commercially on CyberKnife® (Accuray Inc., Sunnyvale, CA, USA)[48,105] and VERO® (BrainLab AG, Feldkirchen, Germany, and Mitsubishi Heavy Industries, Tokyo, Japan)[19,107] systems; or moving the patient via the treatment couch (i.e. couch tracking). Although couches capable of complex motion including up to six degrees-of-freedom (i.e. 6-DOF including *x*, *y*, *z*, pitch, roll and yaw) are commercially available including the Perfect Pitch™ (Varian Medical Systems, Palo Alto, CA, USA), the HexaPOD™ (Elekta Ltd., Montreal, Canada) and the RoboCouch™ (Accuray Inc., Sunnyvale, CA, USA), the ability of these couches to track tumour motion in real-time is not yet commercially available.

For DMLC-based tracking (Figure 2-7(a)), the individual leaves can be repositioned in real-time to shift the beam as well as to modify its field shape (aperture shape). For couch-based tracking, the patient is moved with the robotic couch to keep the tumour stationary with respect to the treatment beam. The HexaPOD is a parallel robotic manipulator that consists of a rigid body top plate, connected to a fixed base plate and defined by at least three stationary points on the grounded base connected to six independent kinematic legs[24] (Figure 2-7(b)). It was reported in a simulation study that the maximum tracking error of 1 mm from irregular breathing is achieved with HexaPOD. For Perfect Pitch, it is specified to reach a positioning accuracy of 0.5 mm. Its mechanics are based on serial kinematics with scissor kinematics for the vertical direction and with belts in the lateral and longitudinal directions[129]. The RoboCouch by Accuray Inc. is offered in combination with the manufacturer's CyberKnife system. Its repeatability is stated to be 0.1 mm,

and its mechanics are based on serial kinematics with revolute joints[129]. Again, it should be emphasized that none of these patient couch-based offerings have been available as a stand-alone commercial couch-based tracking solution at the moment.

For the CyberKnife® system, a miniature lightweight linac is mounted via an effector of an industrial robotic manipulator that can move freely in aim the treatment beam in six degrees-of-freedom (Figure 2-7(c)). Using the current tumour position, the robot can be programmed to reposition the linac thus moving spherically around the patient thereby increasing the possible angles to irradiate a tumour, compared to conventional gantry-based systems. For the VERO® system, the linac can be repositioned using a combination of an MLC attached to an O-ring which is fitted to two orthogonal gimbals allowing the linac and MLC to pan and tilt (Figure 2-7(d)) in order to follow the tumour target trajectory. This system showed an excellent geometric accuracy (< 1 mm) and system latency (< 50 ms with infrared camera tracking)[107]. However, the VERO® systems are no longer commercially available, and they have been in only very limited use across North America.

(a)

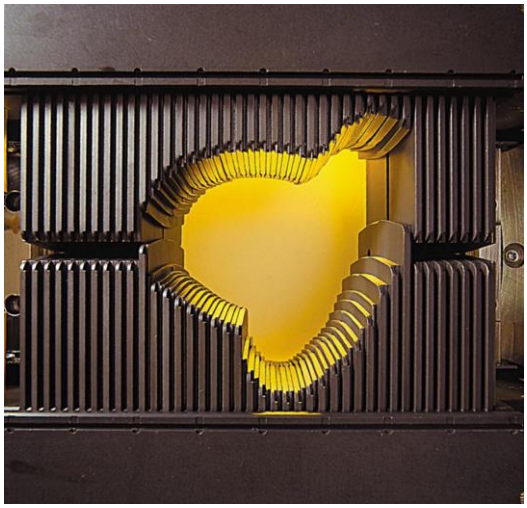

(b)

(c)*

(d)†

Figure 2-7: Clinically used dynamic tumour motion compensation systems. (a) Millennium 120-leaf MLC on a Varian Linac (b) 6-DOF robotic couch, HexaPOD‡ (c) CyberKnife system (d) VERO system

* Image courtesy of Accuray Inc. CA USA. All rights reserved
† Image courtesy of BrainLab AG, Munich Germany. All rights reserved
‡ Image courtesy © 2012 Medical Intelligence Medizintechnik GmbH (now Elekta). All rights reserved

In dynamic tracking, a 3D-CT representing one respiratory phase is chosen from the 4D-CT planning dataset. Plan optimization is performed on the selected 3D-CT image as if the patient was immobile (i.e. no motion encompassing margins) creating a 3D plan. Tumour trajectory information is only used to alter the treatment plan post-optimization. Essentially, the MLC apertures sequenced from the static plan are translated according to the displacement of the tumour centroid. The goal is to reproduce the planned dose distribution as closely as possible. This method is otherwise referred to as dynamic MLC (DMLC) tracking.

The modification of planned MLC apertures can be done either prior to treatment delivery using the 4D-CT planning dataset [Figure 2-8(a)] or during the delivery using data acquired from the real-time imaging system [Figure 2-8(b) using the static plan as the start plan]. In the first option, by adapting the MLC leaves to motion before plan delivery, it can be verified that MLC mechanical constraints, such as leaf speed, will not compromise the motion tracking capabilities. Also, a post-optimization 4D dose calculation (Section 0) can be performed to check that changing the 3D plan into a tracking plan did not create any unintended radiation hot spots in the OARs. However, this is not a real-time tumour tracking method, and the disadvantage of pre-treatment tracking is that the patient must then reproduce the same respiratory pattern seen in the planning 4D-CTs during treatment delivery.

The second option of translating MLC leaf positions based on real-time free-breathing patterns during delivery completely removes the burden of treatment compliance from the patient. However, this presents a challenging task of designing a system that can image and process tumour location, calculate new MLC leaf positions, and reposition MLCs in real-time without sacrificing treatment accuracy. The entire system's response and latency period must be minimized to reduce errors in the motion prediction algorithm. The drawback of real-time DMLC tracking is that

periods where the mechanical limits of the MLC leaves prevent accurate tracking cannot be anticipated and accidental creation of hot spots may not be discovered until a post-delivery 4D dose calculation.

Sawant *et al*[21,22] developed a robust DMLC tracking algorithm that obtains real-time information of target location from an independent tumour target monitoring system (e.g. RPM® or Calypso®), while dynamically repositioning the beam via MLCs to account for 3D target motion (Figure 2-8). The process for the DMLC-tracking algorithm is described as follows:

a) **Initialize MLC leaf positions:** The leaf sequence file from the treatment plan contains the MLC leaf positions defined as a function of MU and 2D spatial co-ordinates of each leaf projection onto treatment plane. At each "control point" defined in the file, the algorithm extracts the shape defined by the MLC leaves (Figure 2-8, Step 1) to form beam apertures so as to deliver a desired fluence[21].

b) **Estimate target motion from internal/external monitor**: Instantaneous 3D target position was obtained from an RPM[21] or Calypso[22] system. Note that the information from these systems represents a best estimate of the actual tumour position based on the correlation established between the external marker (IR block in the case of RPM), or the internal marker (EM transponders in the case of calypso) and the target centroid from the planning CT images.

c) **Prediction of target motion**: Using the estimated motion, the future target positions are predicted to account for the time delay (temporal latency) in system response from calculating new positions by the tracking algorithm and the MLC leaves.

d) **Transform MLC shape to account for target motion:** Using the tumour centroid positions obtained from (b), information about target motion in the BEV is used to remap each point of the original MLC shape to new location on the treatment plane[21].

e) **Calculate new leaf positions:** The relocated points are sequentially joined to form line segments. Leaf fitting is performed by determining the points of intersection of each leaf-pair trajectory with the segments constituting the aperture(s).

f) **Minimize radiation leakage through leaf tips:** Radiation leakage has been reported through the tips of closed MLC leaves. Minimize such leakage by moving the MLC leaf pairs that do not participate in the tracking process under the nearest jaws (Figure 2-8, Step 5).

The authors reported < 1mm and < 2mm geometric tracking accuracies for IMRT plans on prostate and respiratory lung motion trajectories respectively, which was simulated by a dynamic motion platform on a Varian 120-leaf MLC[21,22]. They also investigated dosimetric performance on VMAT for lung and prostate cases[23]. On average, 1.6% and 1.2% of dose points (i.e. 2Gy dose fractions to 95% PTV) failed the 3%/3mm gamma-test with DMLC tracking for lung and prostate plans, respectively; while 34% and 14% of dose points failed the gamma-test without DMLC tracking[23].

1	Read initial leaf positions from MLC file.	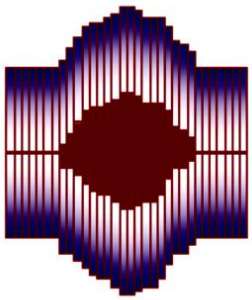
2	Extract the "shape" defined by the points corresponding to MLC leaf tips.	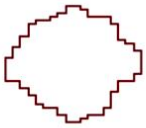
3	Transform this shape to match real-time target position/shape (estimated from a real-time position monitoring system).	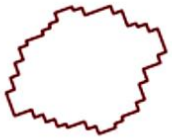
4	Determine the intersection points of MLC leaf trajectories with the transformed shape.	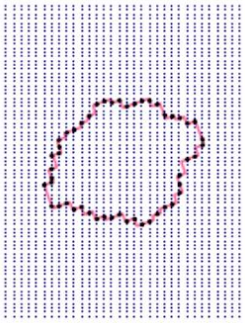
5	Send MLC leaves to the points of intersection. Closed leaf pairs adjacent to open aperture(s) are positioned at the midpoint of nearest open leaf pair. Peripheral closed leaf pairs are sent beneath the nearest jaw.	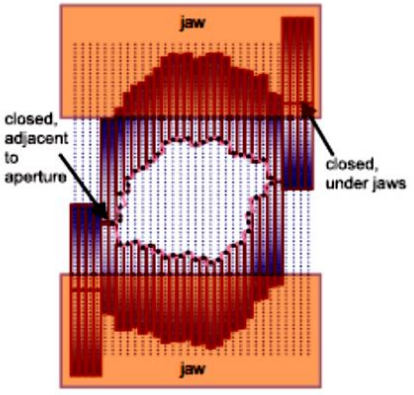

Figure 2-8: Diagram of the workflow when tumour tracking is performed using the dynamic MLC (DMLC) tracking. Figure reprinted from Sawant *et al*[21] used with permission from Wiley.

Chapter 3 Optimization in Radiation Therapy

In this chapter, an overview is provided of the use of optimization in radiation therapy (RT) as well as several related topics. The accuracy and therapeutic effects of RT, RT treatment planning, the process of creating treatment margins to account for target/tumor motion, as well as the benefits of dose fractionation are discussed in Sections 3.1 and 3.2. An introduction into intensity modulated radiation therapy (IMRT) as a treatment technique (Section 3.3) and specifically the 'direct aperture optimization' (DAO) method for IMRT (see 3.3.4.2) is discussed. Finally in Section 3.4, a more recent optimization technique (i.e. progressive resolution optimization, PRO) based on DAO is introduced for volumetric arc radiation therapy (VMAT) delivery whereby the gantry is able to rotate about the patient with multi-leaf collimators (MLCs) in motion while the therapeutic beam is being delivered. This technique was first developed as a research treatment planning optimization software ('*MonArc*') in 2007-2008 before being commercialized by Varian Medical Systems in 2009 as RapidArc©. The *MonArc* development software was modified and used extensively in this thesis, and in Section 3.4.5 we also describe the modifications required to add the constrained marker-based optimization via marker visibility in the BEV of every aperture, which is investigated throughout the remainder of this Thesis.

3.1 Accuracy and therapeutic ratio of radiation therapy

Ionizing radiation is capable of damaging both cancerous and healthy normal tissue cells. The goal of radiation therapy is to maximize tumour control while simultaneously reducing normal tissue complications to an acceptable level. A method to compare the tumour control rates against the normal tissue complication rates as a function of radiation doses is the Therapeutic Ratio (TR). TR determines the required accuracy in absolute dose delivery, and it strongly depends on two

important dose relationships: (i) the dose versus tumour control and (ii) the dose versus normal tissue complications[74].

Tumour control probability (TCP) is the probability of controlling tumour growth after receiving a radiation dose, while normal tissue complication probability (NTCP) is the probability of normal tissue complications after receiving radiation dose. The ratio of the TCP to the NTCP is known as the Therapeutic Ratio (TR). As shown in Figure 3-1(a)-(c), increasing the dose delivered to the tumour increases the tumour control probability (red curve), but at the cost of increased normal tissue complications (green curve). This is a major concern in patient treatment because it could lead to detrimental effects in normal tissues and organs (potentially causing serious functional issues or even patient death). Another concern that motivates optimizing the TR is that radiation-induced secondary cancers may occur in patients after high dose radiation treatments[74,76].

Brahme[130] has shown that for a typical tumour control probability, under-dosing the tumour by 5% will reduce the tumour control by 15%, and an increase in dose to surrounding healthy tissue by 5% may lead to negative side effects in certain organs at risk (OAR)[130]. Figure 3-1(a) displays the optimal therapeutic ratio where the TCP curve is far to the left of the NTCP curve such that tumour control is easily achieved without inducing unacceptable tissue injury. Conversely, Figure 3-1(b) illustrates a disadvantageous situation where the NTCP curve is to the left of the TCP curve and irradiation of the tumour will very likely cause treatment complications. If the tumour is radio-resistant (curve shifts further right) or if normal tissue is radiosensitive and complications arise after exposure to lower doses of radiation therapy (curve shifts further left) then the TR is lowered. Examples of the latter include high radio-sensitivity of normal organs, such as the liver, lung, intestine, and kidney. This is of particular benefit in dose fractionation and complex treatment techniques such as SBRT whereby high doses are delivered to the tumour over

fewer fractions. In general, radiation delivery techniques that can deposit highly conformal doses to targets have a better chance of achieving a high TR by sculpting the radiation dose to the tumour and limiting the dose to surrounding critical structures.

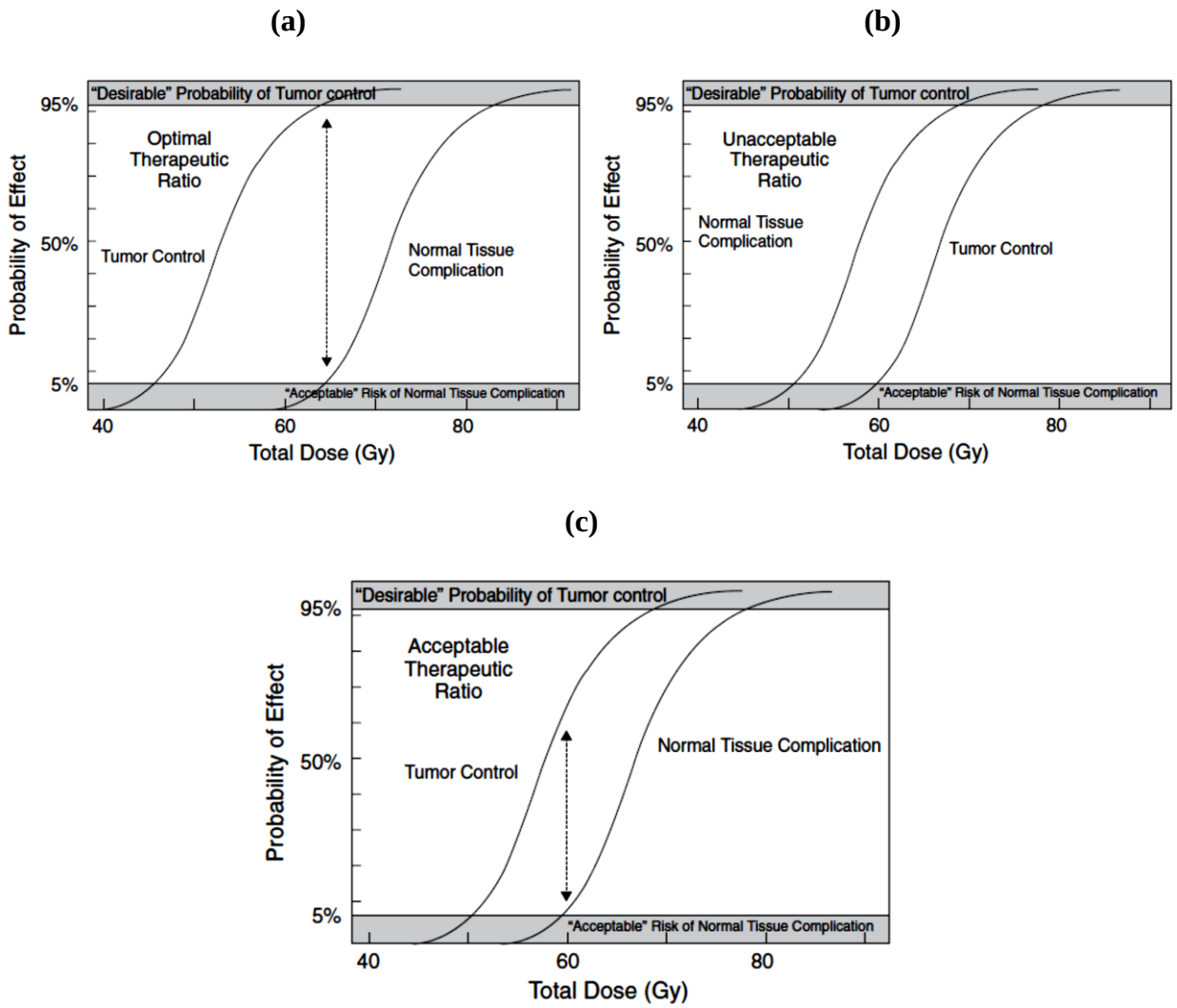

Figure 3-1: Examples of dose-response curves for tumour control probability (TCP) and normal tissue complication probability (NTCP) showing relationship between the tumour control and normal tissue tolerance. Treatments are either: (a) optimal, (b) unacceptable or (c) acceptable. Figure reprinted from Kinsella[131], used with permission from Springer.

3.2 Radiation Therapy Treatment Planning

Due to the likelihood of complications or damage to normal tissues, usage of external beam RT entails careful and precise planning to achieve the goal of maximizing dose to the target volumes (cancerous cells) while minimizing the dose to surrounding structures and organs at risk (OAR)[74]. Advanced RT treatment techniques (further discussed in Section 3.3–3.4) such as Intensity Modulated Radiation Therapy (IMRT) and Volumetric Modulated Arc Therapy (VMAT) have been developed to reach this goal by delivering highly conformal doses to the tumour with a high dose gradient (i.e. rapid dose fall-off) around critical normal tissue structures[10].

Radiation therapy treatment planning consists of the following steps: (a) identifying the planning volumes, (b) determining the dose objectives (i.e. required dose and coverage for the targets, dose limits for the OARs), (c) optimizing the required beam fluence to create a treatment plan and (d) evaluating the plan. Steps (a), (b), and (d) will be described in the following three subsections. The step of creating the optimal treatment plan however is dependent on the treatment technique and for the purposes of this thesis requires a more detailed description.

3.2.1 Planning Volumes

3D planning structures (volumes) are required for both the tumour target and surrounding critical structures, otherwise called organs-at-risk (OAR). Visibility of patient anatomy is most commonly provided by three-dimensional computed tomography (3D-CT). For the target volumes, a radiation oncologist typically contours the gross tumour volume (GTV) and clinical target volume (CTV) (Figure 3-2). GTV refers to the visible extent of the tumour growth. The CTV contains the GTV as well as surrounding tissues adjacent to the tumour that may contain subclinical microscopic malignant disease. An internal margin (IM) is then added to the CTV to

create the internal target volume (ITV). The IM is required to accommodate and compensate for variation in tumour position caused by physiologic movements, such as respiration, swallowing, coughing, filling of the bladder and rectum, heartbeat and bowel movements. Additionally, the IM accounts for tumour deformation that may occur over the course of treatment. Another margin, known as the setup margin (SM), is added to the ITV to produce the planning target volume (PTV). The SM accounts for uncertainties in both the positioning of the patient and alignment of the treatment fields. The PTV dose coverage is often used as one of the primary objectives in treatment planning. For example, dose within the PTV should be within +7% and -5% of the prescribed dose[75].

OAR structures are also contoured by a radiation oncologist or treatment planner. Occasionally, due to the motion of an OAR (e.g. bladder or rectum), it may be in the proximity of the PTV thus bringing it to within dangerous unexpected over-exposure. In such cases, an additional motion margin maybe added around the OAR, creating a planning organ at risk volume (PRV). Once a treatment plan has been generated, the volume enclosed by an isodose surface capable of achieving tumour control is defined as the treated volume. Ideally, the treated volume coincides precisely to the PTV, but this is not possible due to practical limitations in the available treatment techniques. The volume of tissue receiving doses that are relatively large in comparison to their radiation tolerance levels are defined as the irradiated volume.

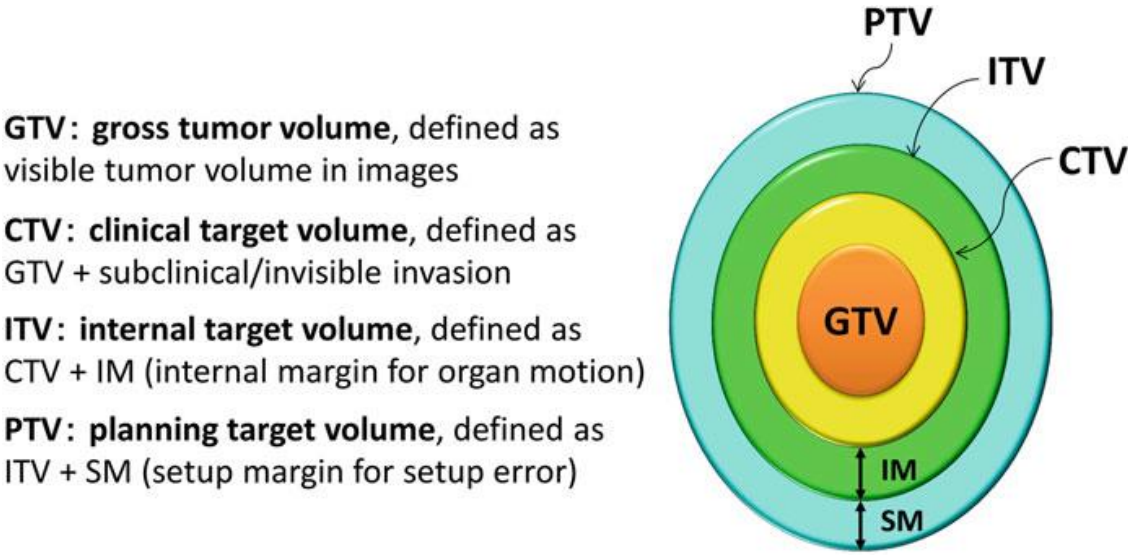

Figure 3-2: Target volumes used in radiation therapy. Reprinted from Fig 5.1 in Arimura[132] used with permission from Springer Nature.

3.2.2 Plan delivery schedule: Fractionation

In conventional RT, a radiation oncologist prescribes dose to the tumour based on published clinical evidence demonstrating patient outcomes and related toxicities associated with the prescription used. Often the dose is delivered in multiple fractions delivered once per day over several weeks rather than in a single large dose. The reason for this fractionation is based on radiobiological factors whereby the normal tissue cells can repair themselves more effectively than tumour cells. Therefore, irradiating a patient in smaller fractions separated by enough time for repair (typically considered 6 h), further improves the therapeutic ratio. Decades of empirical clinical experience supports this over many disease sites. In conventional RT fractionation, the number of daily fractions ranges from 20 – 40 with approximately 1.5 – 2.2 Gy dose delivered per fraction. However, more recently, higher doses per fraction over fewer fractions (termed hypo-fractionation) have been introduced for tumour treatments in RT for some clinical indications. The tumour control effects of fractionated deliveries will be further discussed below.

The Linear-Quadratic (LQ) model, defined by the relationship between the surviving fraction (SF) and dose (D), is represented as $\mathbf{SF(D) = \exp(-\alpha \cdot D - \beta \cdot D^2)}$; whereby α and β are the model parameters that characterize the intrinsic radio-sensitivity of the irradiated cells[131]. The ratio of both parameters, α/β, gives the measure of the sensitivity of the cells from the fractionation: cells with a higher α/β are less sensitive to the sparing effect of fractionation. It has been widely adopted in radiation oncology to calculate changes in dose per fraction (or number of fractions) required to achieve the same radiation effects on target or normal tissues as a standard fractionation.

In general, clinical results have validated the LQ model over a modest dose range of 1–5Gy per fraction. Implicit in LQ modeling of tumour response is that full reoxygenation occurs between each dose fraction. Therefore, it seems difficult to justify large single doses of radiation, because the LQ model and the detrimental effect of the lack of reoxygenation between fractions would predict that such doses would produce less tumour cell death for the same level of normal tissue damage[133]. To the contrary, clinical results with SBRT and hypo-fractionation[134,135], particularly for early-stage non-small cell lung cancer (NSCLC), have shown at least equivalent local control.

This unexpected result has been understood to arise due to several underlying reasons. While the LQ model predictions begin to deviate above ~5Gy for high dose rates[133,136], at lower dose rates it has been shown to fit experimental survival data well up to ~10Gy[136]. The observed responses for the large dose hypo-fractionation regimens of SBRT may be because of cell repair saturates at high doses. Also, Park *et al*[137] suggested that radiation doses >10Gy cause vascular damage that leads to indirect tumour cell death which would not be observed in the *in vitro* cell based experiments typically used to establish these dose relationships. Furthermore, an anti-tumour

immunity response has been reported in few mice-based studies as well due to high dose local irradiation. This immunity is attributed to a massive release of tumour-specific antigens as well as various pro-inflammatory and pro-oxidant cytokines from injury and death of tumour cells due to high dose irradiation. In summary, this led to a conclusion by Song *et al*[138] that additional cell death through an indirect mechanism may play an important role in the response of tumour to high-dose SBRT and that fraction size is important in exploiting the radiation-induced vascular damage. However, little clinical evidence on human tumours is available to support this hypothesis.

Finally, hypoxia has been observed in many cancers. Approximately 90% of all solid tumours have median oxygen concentrations less than the typical values of 40–60 mm Hg found in normal tissues, with many cancers having median oxygen levels below 10 mm Hg[133,139]. It is well known that hypoxic cells are radio resistant. Several investigators have now demonstrated that the extent of tumour hypoxia has a negative impact on the ability of RT to locally control certain tumours[140]. For hypo-fractionated RT, as the number of fractions decreases, the expected tumour cell survival increases (i.e. less tumour response) for the same BED or the same normal tissue damage[133]. Thus, reoxygenation of surviving hypoxic cells may occur to a certain extent owing to extensive cell death and thus decline in oxygen consumption for hypo-fractionated SBRT[138]. Also, repair of sub-lethal radiation damage in tumour cells may take place during protracted radiation exposure when tumours are irradiated with high doses per fraction[138].

3.2.3 Plan evaluation: Dose-Volume Histogram (DVH)

A dose-volume histogram (DVH) is a plot of the dose-volume frequency distribution and one of the main tools used to evaluate RT treatment plans. DVHs summarize the radiation dose distribution within patient volumes from proposed RT plans. A distinct DVH curve will

characterize each structure's radiation exposure and uniformity of dose in the structures. Two types of DVHs exist: differential (or direct) DVHs and cumulative (or integral) DVHs.

A cumulative DVH quantifies the volume of a structure that receives at least a given dose. For example, if the prescribed target dose is 72Gy, in an ideal situation 100% of the target will receive at least 72Gy while 100% of the critical structure at risk will receive 0Gy (Figure 3-3(a)). However, in a realistic DVH (Figure 3-3(b)), structures at risk that are near the target will be unavoidably irradiated such that the dose in the target will not be perfectly homogeneous. In this work, cumulative DVH will be used exclusively as it is the most common for clinical plan evaluation.

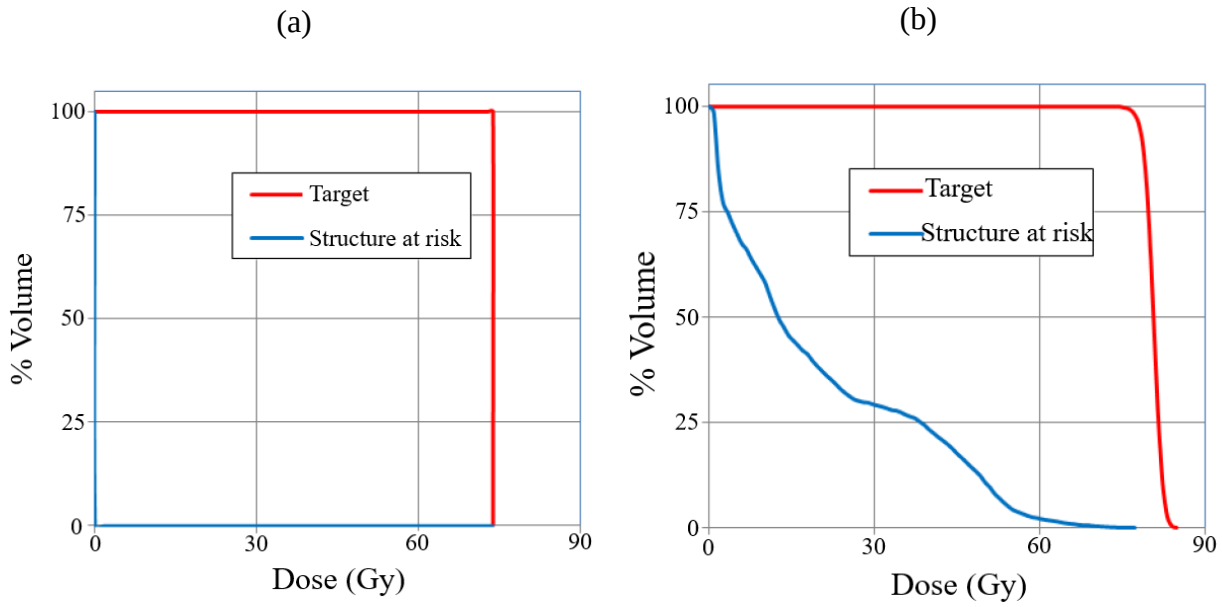

Figure 3-3: Representation of an (a) ideal, and (b) realistic cumulative DVHs. Figure adapted from Chin[75].

3.2.4 Dose calculation: via pencil-beam algorithm

During treatment plan optimization, dose deposited in the patient must be recomputed each time a treatment parameter is altered to calculate the new value of the objective function. This

process is a major limiting factor affecting the overall optimization time and generally a balance must be found between dose calculation efficiency and dose calculation accuracy.

Pencil-beam (PB) algorithms are the most commonly used algorithms in IMRT optimization due to their fast computation time. The fluence map for each beam is subdivided into small beamlets, usually of dimensions 0.25×0.25 cm^2. The beamlets are small enough that the intensity within each beamlet is uniform. The radiation passing through a beamlet is referred to as a 'pencil-beam'. At a given depth *d* in water, the spatial dose distribution in a plane perpendicular to the beam axis from a single pencil-beam can be modeled as a 2D dose kernel. The shape of the kernel changes with depth as it is influenced by depth dependent variables such as the photon energy spectrum and the distribution of secondary electrons. The kernel can be derived from measured beam data which is fitted to a double exponential function[141]:

$$K(r,d) = \frac{A(d)e^{-a(d)r} + B(d)e^{-b(d)r}}{r^2} \tag{3-1}$$

where *r* is radial distance from the interaction point of the radiation, with constants *A* and *B*.

To compute the dose to a voxel within the patient at coordinates *x*, *y* and depth *d*, the dose contributions from all the pencil-beams must be summed using the equation (Storchi *et al*[142]):

$$D(x,y,d) = \frac{\left(SSD + d_{ref}\right)^2}{(SSD+d)^2} \iint_{-\infty}^{+\infty} F(u,v)P(u,v,d)K(x-u,y-v,d)\mathrm{d}u\mathrm{d}v \tag{3-2}$$

where $d_{ref} =$ reference depth (defined by user for normalization); $SSD =$ source-to-surface distance; $F(u,v) =$ photon fluence map; $P(u,v,d) =$ primary beam off-axis intensity profile as a function of depth d (i.e. to include beam hardening); $K(x,y,d) =$ the pencil beam kernel.

The major disadvantage of pencil-beam algorithms is their limited ability to account for patient heterogeneity. Corrections for the presence of non-water equivalent materials can be made using 1-D radiological path length scaling in the axis parallel to the beam, but changes in electron

lateral scatter are ignored. This is known to result in treatment plan dosimetry errors, such as under-dosage in lung tumours, but are considered accurate enough (typically within 5%) for many modern dose calculation applications.

3.3 Introduction to IMRT

RT treatment plans must be carefully designed to minimize damage to healthy organs, while delivering sufficient dose to ablate the targeted tumour. In 3D-conformal radiation therapy (3DCRT), the aperture of each radiation field conforms to the target's projection in its BEV, and the intensity is uniform across the field. In 3DCRT, the human operator manually optimized the treatment plan, although this approach was clearly not a rigorous mathematical one and the quality of the produced plan depended on the skill and experience of the individual human operator. However for Intensity-modulated radiation therapy (IMRT), the intensity is modulated during beam delivery so that the radiation to an OAR within an individual field can be blocked or partially blocked, and any underdosing to the associated target volume can be compensated for by other fields[143]. This modulation of the incident energy fluence ('intensity') of the therapeutic radiation beams is accomplished via the use of computer-controlled multi-leaf collimators (MLCs). IMRT is especially powerful to treat targets with arbitrarily complex shapes, especially those that are concave[143] (e.g. some prostate and spinal cord patients). Due to the complexity of the required fluence patterns, manual 'optimization' is not possible and inverse planning algorithms have been required for the application of IMRT, whereby the optimum intensity modulated pattern for each field is found in order to achieve the overall dosimetric goal for the individual patient plan, through the mathematical process of minimizing cost functions associated with the clinical dose objectives.

Figure 3-4 shows an illustration of a complex fluence map derived through an inverse planning method. Each square represents a small discrete sub-beam of radiation or 'beamlet' within the larger delivered field. Darker shades correspond to beamlets with greater intensities. The ability to modulate the beam intensity across the radiation field allows IMRT to achieve a higher degree of dose conformality around the target and thus a lower dose to nearby structures or organs at risk (OARs) than would be possible with broad beams of more uniform intensity (as in 3D conformal radiation therapy). Multiple (e.g. 5–9) modulated beams from different directions are designed simultaneously during the inverse planning process, such that the superimposition of their delivered dose in the patient will result in a fairly homogeneous and conformal dose distribution covering the target[144] while avoiding the OARs.

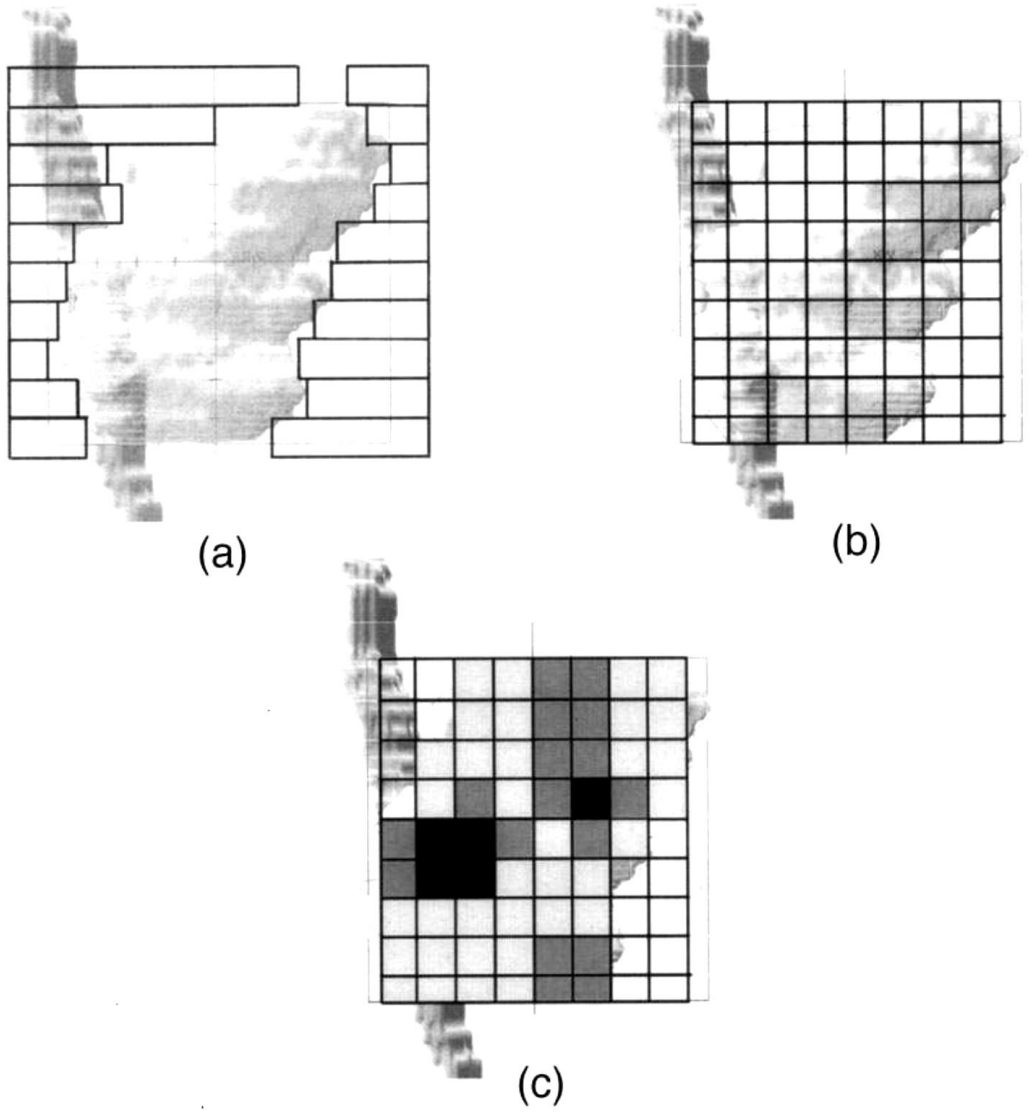

Figure 3-4: Illustration of the conventional inverse planning approach. (a) The leaves of the MLC are shaped to match the beam's eye view (BEV) of the tumour volume. (b) The BEV of the tumour is divided into a series of finite size pencil beams, and the corresponding pencil beam dose distributions are computed. (c) The pencil beam intensities are optimized, resulting in an optimized fluence map. The three shades in the fluence map represent three different energy levels. Figure printed from Shepard *et al*[17] used with permission from Wiley.

The derivation of the IMRT treatment plan with complex beam fluence maps to achieve the plan is referred to as an *inverse planning* problem. The desired dose outcomes, for example delivering the prescription dose uniformly to the entire target, are first specified. Afterwards, the

inverse planning method is applied to find beam fluence that will combine to achieve (or come as close as possible) the desired outcome. The inverse planning problem of IMRT has no exact solution as it is impossible to deliver the full prescription dose to the target without also irradiating nearby surrounding tissue. Also, beams with negative intensity are not feasible[145] since one cannot remove dose to the patient once it has been delivered. Thus, the IMRT inverse planning problem is formulated as an optimization problem that iteratively searches for treatment parameters (e.g. beam intensity/fluence maps) that minimize the dose differences between a realistic, deliverable plan and the desired plan (as shown in Figure 3-3).

The reliance on a computerized optimization algorithm to select treatment parameters contrasts with the method known as *forward planning*. In forward planning, it is the human operator ('treatment planner' or 'dosimetrist') who manually and iteratively adjusts the treatment beam parameters to obtain the desired dose distribution. Plans created in this manner are unable to match the level of dose conformity around the target or match the sparing of healthy tissues achievable in IMRT plans because the complex fluence patterns required are impossible to derive intuitively through manual adjustments.

Traditionally, intensity-modulated radiation therapy (IMRT) treatment plans are developed using a two-stage process. The first stage is finding an optimal intensity profile or fluence map for each beam, otherwise called the **fluence map optimization** (FMO) problem. This is followed by a **leaf-sequencing** stage in which the fluence maps are decomposed into a manageable number of beam aperture shapes that are deliverable by the multi-leaf collimators (MLCs), after accounting for the mechanical limits of the MLCs in creating fluence maps. The objective of this second stage is to create a series of beam apertures that reproduce the idealized fluence map as accurately as

possible. For clinical practicality, the second stage is also used to limit the total time that the radiation is delivered, i.e., the total beam-on time, and/or the total number of apertures used[146].

3.3.1 IMRT optimization, constraints and treatment goals

IMRT optimization starts with the planner specifying a set of treatment goals that will be used to define the objective function (Section 3.3.2). The desired patient dose is calculated (Section 3.2.4) from some initial treatment parameter settings (e.g. beam intensity profiles, beam orientations, dose rate etc.), denoted by x, and is used to compute the objective function at each iteration. For every iteration, the optimization algorithm (Section 3.3.3) selects a new set of treatment parameters (Section 3.3.4) to try to reduce the value of the objective function. If the value of the objective function converges to a minimum (either a 'local' or 'global' minimum), optimization may be stopped, and the new set of parameters are saved as optimization parameters (as x_{opt}). Note that in this context, convergence means that the iterative improvement to the calculated magnitude of the objective function has not exceeded a pre-set threshold. The most-optimal plan is produced if it converges to the global minimum (lowest value of objective function). If it hasn't converged, the process is repeated. Depending on the complexity of the problem and the choice of optimization algorithm, the number of iterations to achieve convergence for radiotherapy optimization problems can range between hundreds to hundreds of thousands[145].

To perform the optimization, the treatment planning goals must be quantified into clinically meaningful optimization objectives and constraints before the IMRT inverse planning problem can be solved. The treatment goals are often defined using desired points on a cumulative DVH (Section 3.2.3). These points are the dose-volume constraints[145] and can be defined for both OARs and target/tumour volumes. For a target structure, the user specifies a minimum and a maximum

allowable dose. For each OAR structure, the user only specifies the maximum allowed dose as well as additional dose volume constraints to define the desired shape of the corresponding DVH.

A maximal dose volume constraint is a point on the DVH that indicates a dose limit (D_{max}) and a percentage of the sensitive OAR structure ($V_{max}\%$) that is required to not exceed that dose limit. A minimal dose constraint is similar except the dose limit is a minimum (D_{min}) and the percentage of the structure ($V_{min}\%$) is required to exceed that dose limit (typically only used for target structures). The relative importance of each goal is controlled by the user applying a numerical weight, called a 'weighting' or 'penalty' factor. Figure 3-5(a) represents this constraint for an OAR, as a shaded region in the DVH plot. Applying several maximal constraints on an OAR can provide some control over the dose distribution in its volume. For target volumes (shown in Figure 3-5(b)), a maximal and a minimal dose-volume constraint can be defined to control target coverage and target dose inhomogeneity.

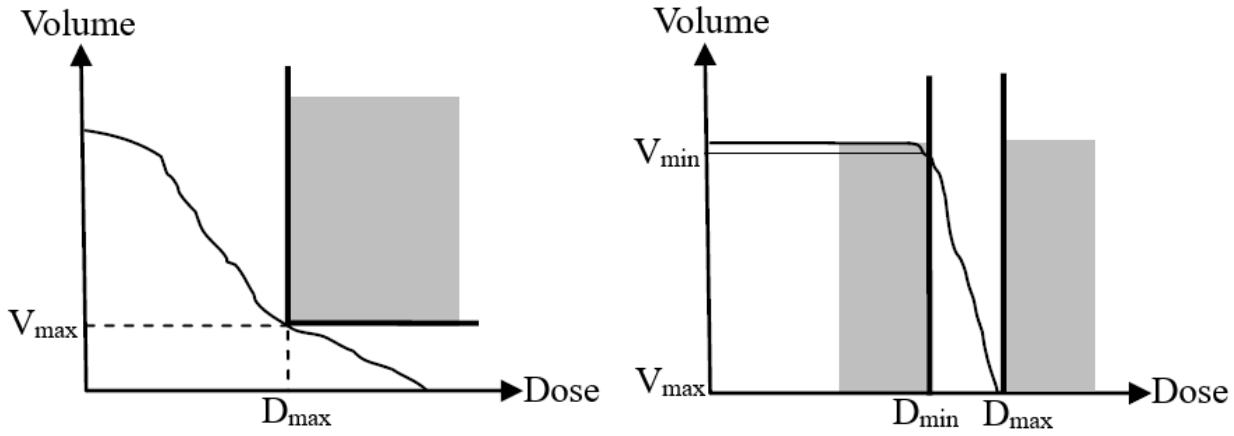

Figure 3-5: (a) Example of a maximum dose-volume constraint on an OAR. (b) Example of a minimum and maximum dose-volume constraint on the target. Adapted from Bortfeld[145] used with permission from Elsevier.

3.3.2 Objective Function

The objective function, sometimes called the cost function, guides the IMRT optimization. The objective function measures the treatment plan quality, by reducing the entire plan into a single numerical value that is to be minimized. The total objective function f, is defined as the sum of the objective functions for the OARs (f_{OAR}) and the target (f_{Target}). That is,

$$f = \sum_i \left(f_{OAR_i} + f_{Target}\right). \tag{3-3}$$

Each OAR can have more than one maximal dose-volume constraint, f^{max}. Thus, for a given OAR, f_{OAR} is

$$f_{OAR} = \sum_k f_k^{max}. \tag{3-4}$$

A common approach to cost functions in IMRT treatment planning is to minimize the mean square of the deviation (and thus minimize the variance) between the actual dose distribution and the treatment planning goals represented by the individual dose-volume constraints. Using this approach, each maximal dose-volume constraint f^{max}, is calculated as follows:

$$f^{max} = \frac{w_{max}}{N} \cdot \sum_j \left(D_j - D_{max}\right)^2 \cdot H\left(D_j - D_{max}\right) \cdot H\left(D_{max}^* - D_j\right) \tag{3-5}$$

whereby

$$H\left(D_j - D_{max}\right) = \begin{cases} 0, & when\ D_j \le D_{max} \\ 1, & when\ D_j > D_{max} \end{cases}. \tag{3-6}$$

and w_{max} represents the penalty/weight factor of the maximal constraint, D_{max} is the maximum dose in the constraint, D_j is the dose in the *j*th voxel and *N* is the total number of voxels in the structure. D_{max}^* is the dose that corresponds to the point of intersection between V_{max} and the DVH curve (Figure 3-6). The Heaviside operators act to enforce the maximal dose-volume constraint.

Both functions have non-zero values only for voxels where the constraint is exceeded. These voxels are represented by the shaded green areas in Figure 3-6. The maximal dose-volume constraints are denoted by red arrows.

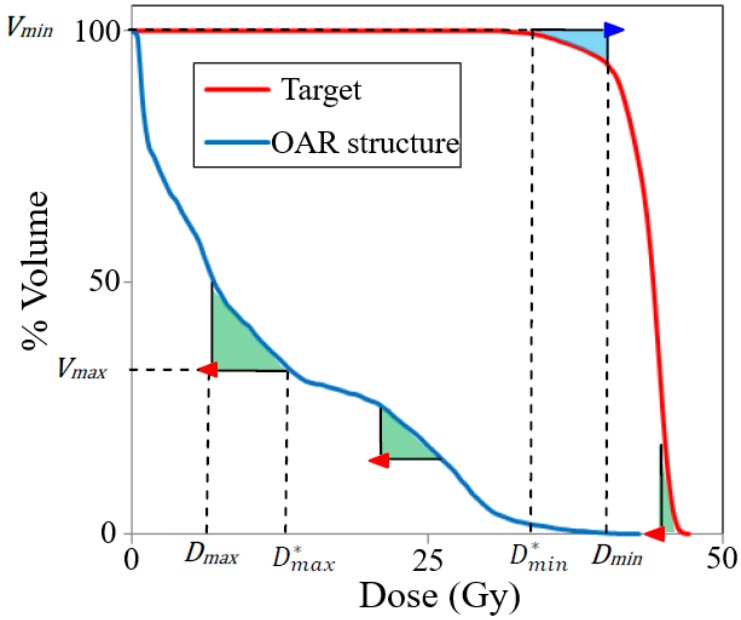

Figure 3-6: An example DVH plot/curve where the OAR structure has two maximal dose-volume constraints (red triangles) while the target has one maximal and one minimal (blue triangle) dose-volume constraint. Shaded green and blue areas indicate portions of the structures that do not meet the desired constraints. Figure adapted from Chin[75].

For the target, its objective function is composed of both maximal and minimal dose-volume constraints, although frequently only one of each is employed.

$$f_{Target} = f^{max} + f^{min} \tag{3-7}$$

$$f^{max} = \frac{w_{max}}{N} \cdot \sum_j \left(D_j - D_{max}\right)^2 \cdot H\left(D_j - D_{max}\right) \cdot H\left(D^*_{max} - D_j\right) \tag{3-8}$$

$$f^{min} = \frac{w_{min}}{N} \cdot \sum_j \left(D_{min} - D_j\right)^2 \cdot H\left(D_{min} - D_j\right) \cdot H\left(D_j - D^*_{min}\right) \tag{3-9}$$

where w_{min} is the weight of the minimal constraint, D_{min} is the minimal dose in the constraint and D^*_{min} is the dose that corresponds to the point of intersection between V_{min} and the DVH curve (Figure 3-6). Similar to Equation (3-6), the two Heaviside operators in Equations (3-8) and (3-9) penalize the objective function only for voxels that violate the minimal dose-volume constraint (Figure 3-6, shaded blue area). All constraint weights are manually chosen, and the weights of any particular constraint are determined by its value relative to other weights. For example, if a weight is low, then the solution to the optimization may exceed the dose-volume constraints (Figure 3-7(a)). In contrast, if it is critical that the constraint be met (Figure 3-7(b)), then the weight must be set higher. All constraints are normalized by their respective number of voxels, *N*, to prevent structures of large volumes from dominating the optimization.

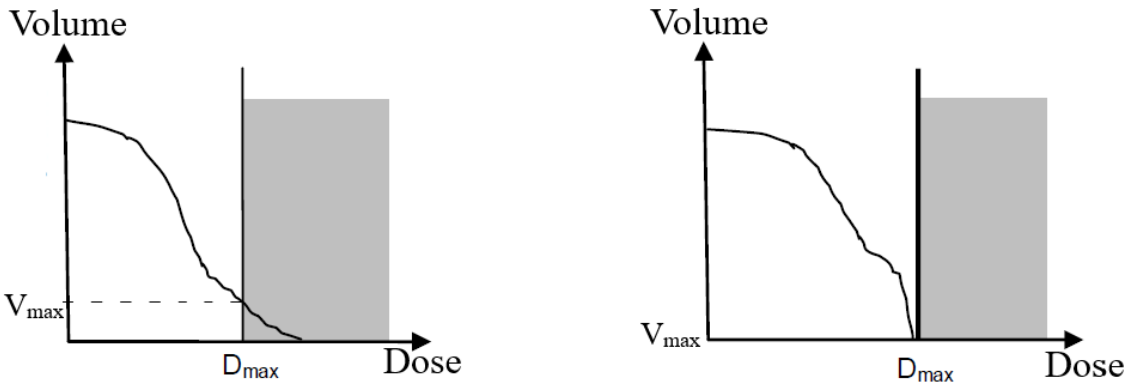

Figure 3-7: DVHs of an OAR where the shaded area represents the dose constraint. The likelihood of optimization achieving the desired constraint depends on the magnitude of the relative constraint weight. (a) Constraint was not met (b) Constraint was met. Adapted from Bortfeld[145] with permission from Elsevier.

3.3.3 Optimization algorithms

The optimization algorithm provides a strategy to search the solution space of the objective function. The solution space can be thought of as a multi-dimensional surface whose coordinates are given in terms of the treatment parameters, *x*, which control the dose deposition in the patient.

Optimization algorithms are categorized as either *deterministic* or *stochastic*. Deterministic algorithms are usually applied when the objective function is 'convex' (i.e. a single minimum exists) (Figure 3-8(a)); otherwise, they may become trapped in a local minimum. An example of a convex objective function solution space is that of static-gantry IMRT (where beam angles are fixed) with terms based only on dose constraints. Stochastic algorithms (e.g. simulated annealing and genetic algorithms) are iterative algorithms that are commonly applied to find the global minimum when the objective function is non-convex (i.e. multiple local minima) (Figure 3-8(b)). An example of a non-convex objective function solution space is that of static-gantry IMRT where the beam angles are also included in the optimization. Although stochastic algorithms have the advantage of avoiding getting trapped in local minima, in general, they are typically slower than deterministic approaches. They may also get trapped in local minima if, for example, the thermal cooling process is too fast (in the case of simulated annealing), or if the population evolution is not realistic (in the case of genetic algorithms).

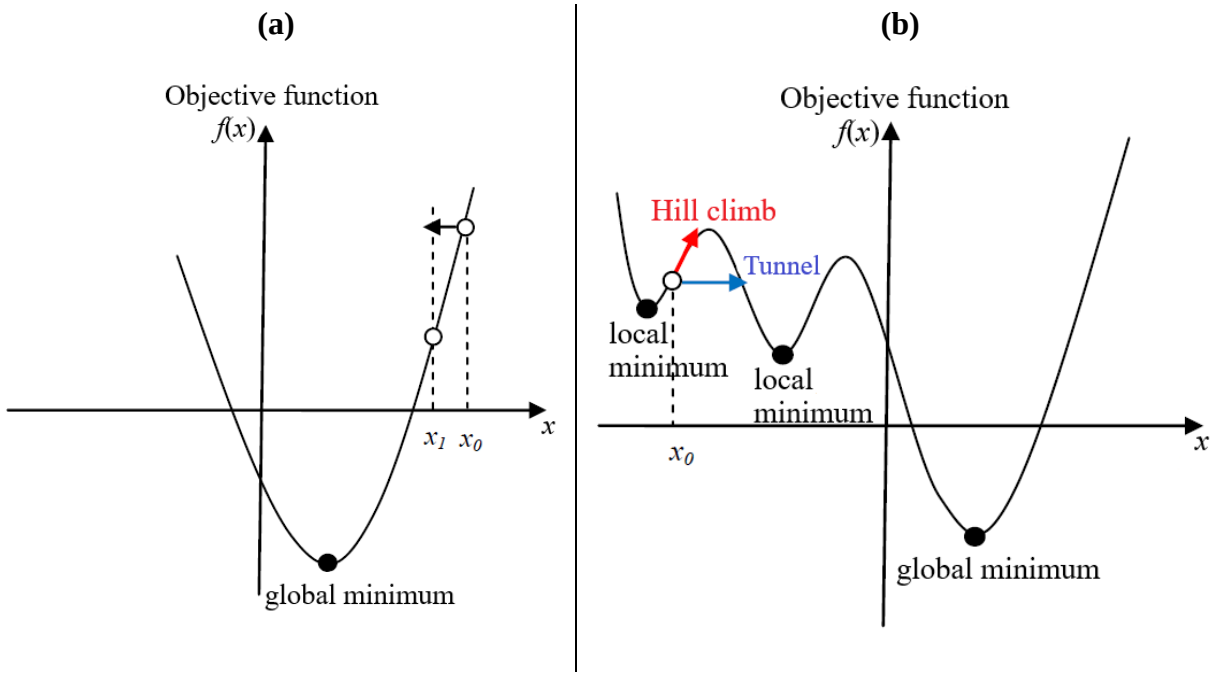

Figure 3-8: Illustrations of a 1-D (a) convex (deterministic) and (b) non-convex (stochastic) objective function.

Figure adapted from Bortfeld[145] used with permission from Elsevier.

3.3.3.1 Deterministic: Gradient-based methods

Examples of deterministic algorithms are those using gradient-based methods such as gradient descent and conjugated gradient methods[145,147,148]. Optimization is generally carried out via a series of partial optimizations along different directions in the multidimensional space. The process entails two components: choice of direction, and step-size along that direction[148]. The set of variable treatment parameters, *x*, are adjusted in iterative steps towards an optimal solution according to the following equation:

$$x_{k+1} = x_k + \alpha \cdot d_k \tag{3-10}$$

whereby k is the index of the step, α is the step size, and d_k is the change in direction. The simplest form of gradient descent is represented as

$$x_{k+1} = x_k - \alpha \cdot \partial f(x_k) \tag{3-11}$$

The drawback of gradient descent is that convergence of the objective function to a minimal optimal value is slow due to the gain of moving closer to the solution in one step being partially lost in the next step. This downside can be avoided by using the conjugated gradient approach which calculates the new direction using both the current gradient and the previous direction, as shown below in Equation (3-12):

$$d_{k+1} = -\partial f(x_{k+1}) + \frac{[\partial f(x_{k+1}) - \partial f(x_k)] \cdot \partial f(x_{k+1})}{\partial f(x_k) \cdot \partial f(x_k)} \cdot -\partial f(x_k) \tag{3-12}$$

3.3.3.2 Stochastic: Simulated Annealing

An example of a commonly used stochastic algorithm is *simulated annealing*[149]. Simulated annealing comes from the thermodynamic process of heating a material and then lowering the temperature at a slow rate to decrease its defects. It is useful in optimization to find global optima in the presence of many local optima (as expressed by a non-convex objective function). It is

essentially a "hill-climbing" approach whereby a move (i.e. small step in the solution space search) may be chosen whether it is the actual best downhill (i.e. more optimal solution) move or not. The decision logic is as follows: if the chosen move leads downhill, it is always accepted, otherwise, the move is accepted but with a probability less than 1. Thus, it is a probabilistic and an iterative search approach whereby the extent of the search is guided by a probability distribution (p) with a scale proportional to the temperature (T). The temperature decreases gradually (and the probability of taking an uphill step in a given iteration decreases with it) as the algorithm proceeds. The slower the rate of temperature decrease, the better the chances are of finding an optimal solution, but the longer the computation time.

Simulated annealing involves two parts. The first part is the determination of an iterative step size Δx_k, from a displacement distribution $D(\Delta x_k)$, where k represents the iteration number. As optimization progresses, the width of the displacement distribution will decrease such that smaller steps are taken when it approaches the objective function's global minimum. The second part involves determining whether the change to the treatment parameters moves the optimization closer to the optimal solution. If the objective function's value f decreases, the change is always accepted. On the other hand, if the difference in the objective function's value ∂f, is positive (i.e. f increases), the change may still be accepted but with an acceptance probability of p_k, where

$$p_k = \exp\left(-\partial f(x_k) \Big/ k_B T_k\right) \tag{3-13}$$

whereby T_k is the 'cooling' temperature, which decreases over the course of the optimization. By occasionally allowing the value of the objective/cost function to increase, the optimization is able to 'climb' out of a local minimum (Figure 3-8b). On the other hand, escape by 'tunneling' can also occur if the step size is sufficiently large (Figure 3-8b).

For the determination of the step size and to speed up the algorithm, two common annealing approaches are: Boltzmann annealing and fast simulated annealing. These two approaches accelerate the optimization using different representations of the step size which incorporates the 'cooling' temperature. The step size typically starts at a higher value and shortens after each iteration. In Boltzmann annealing, the displacement step size is sampled from a Gaussian distribution given by:

$$D_{Boltz}(\Delta x_k) = (2\pi T_k)^{-\frac{N}{2}} \cdot \exp\left(-\Delta x_k{}^2 \Big/ \mathrm{K_B} \cdot T_k\right) \tag{3-14}$$

$$T_k \geq T_0 \frac{1}{log(k)} \tag{3-15}$$

where *N* is the number of treatment parameters and K_B is the Boltzmann constant. In fast simulated annealing, the displacement step size is sampled from a Cauchy distribution given by:

$$D_{Fast-Boltz}(\Delta x_k) = \frac{T_k}{\left(\Delta x_k{}^2 + T_k{}^2\right)^{(N+1)/2}} \tag{3-16}$$

where $T_k = \frac{T_0}{k}$.

3.3.4 Optimization techniques and parameters for radiation therapy

The choice of treatment parameters is highly dependent on the method of RT delivery. Typically, IMRT is delivered on a linac with beam modulation defined by the movements of the MLC leaves. Therefore, example treatment parameters for IMRT would be beam angles, MLC leaf motion settings and beam monitor units. Some treatment parameters are typically chosen prior to optimization and include radiation type, beam energy and beam angles. Two common methods for IMRT optimization for the remaining parameters are: fluence map optimization and direct aperture optimization.

3.3.4.1 Fluence map optimization (FMO)

In fluence map optimization (FMO), the beam portals are discretized into uniform rectangular *beamlets* (or bixels) with dimensions ranging from 0.2×0.2 cm^2 to 1.0×1.0 cm^2. The fluence through each beamlet is the only type of treatment parameter used in the optimization and is described by a set of fluence amplitudes $x = \{x_j\}$, where j is the index of a beamlet. The dose distribution to each voxel in the patient from a beamlet can be pre-calculated as a discrete kernel and is nearly linear to the beamlets' energy fluence.

The use of a single set of treatment parameters, *x*, with a direct relationship to dose is advantageous to IMRT optimization as it simplifies its mathematical formulation. A gradient search method can be used for FMO regardless if the objective function based on dose-volume constraints creates a non-convex problem. While local minima may exist in the solution space, the likelihood of being trapped in a poor solution distant from the global minimum is low[150–152].

The disadvantage of FMO is that the output fluence maps are 'idealized'. That is, the fluence maps must be converted into deliverable MLC leaf motion sequences after optimization is completed. Figure 3-9 shows the two-step process for a fluence map that is easily decomposed into three MLC apertures of different intensities. However, realistic maps are often far more complex and can only be approximately recreated by the MLC. The actual MLC delivered treatment will be degraded from the planned treatment due to multiple factors not accounted for during FMO such as: conversion of continuous fluence into a discrete number of intensity levels, linac radiation head scatter, leakage via MLC leaves, MLC transmission, MLC mechanical constraints (leaf widths, leaf speed, inter-digitation), and dosimetry inaccuracies with small off-axis fields or low MU.

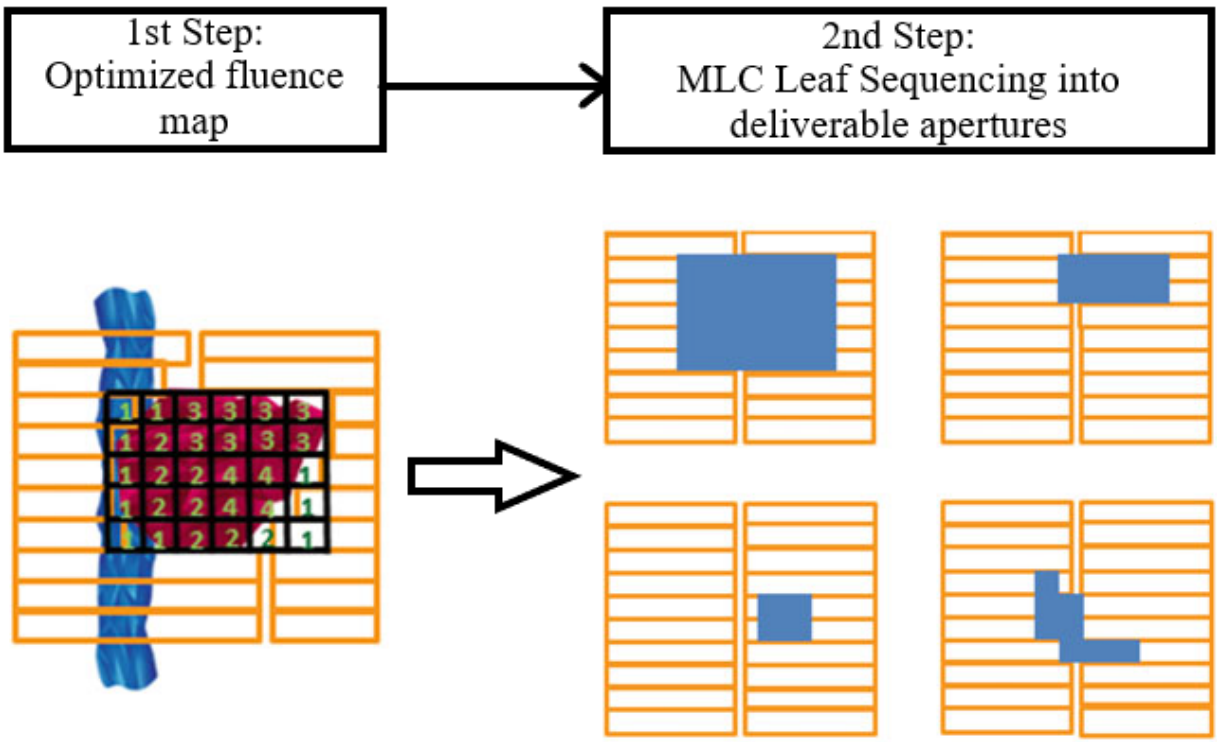

Figure 3-9: Illustration of fluence map intensity, decomposed into three sequenced MLC apertures. Adapted from Fig. 8.6 in Arimura[132]; used with permission from Springer Nature.

3.3.4.2 Direct aperture optimization (DAO)

In direct aperture optimization (DAO), the MLC aperture shapes and weights are directly included as optimization parameters in the planning process, thus avoiding the complex MLC leaf sequencing step necessary after FMO. A general DAO implementation will be described here, but other forms also exist[153–155]. Prior to DAO, each beam angle is assigned a set number of apertures. The number of apertures, *n*, determines the number of intensity levels[17] available (i.e. $2^n - 1$). Unlike in FMO, the aperture shape can vary continuously as there is no need to divide the final fluence map into a fixed number of discrete intensity levels. For most cases, five apertures per beam is enough flexibility for intensity modulation. All aperture shapes are initialized to conform to the beam's eye view (BEV) of the target. BEV is defined as the two-dimensional projection of

a specific structure onto a virtual plane at the treatment isocenter from the viewpoint of the radiation beam. Optimization of MLC leaf positions, which are far from the dose points in the patient, has a weaker influence on dose than FMO.

However, DAO is mathematically more difficult and creates a non-convex problem, hence simulated annealing is frequently employed to solve this optimization problem[17,149]. The simulated annealing implementation for DAO optimization is an iterative procedure often using many thousands of iterations. At every iteration step, a treatment variable (MLC leaf position, arc weight or beam weight if gantry speed can change) is randomly selected for change. The size of the change is sampled from a probability distribution (e.g. Gaussian) whose width gradually decreases over the course of the optimization based on a schedule. Any MLC or beam weight constraint is easily incorporated at this point by verifying that the selected change does not violate any of the prescribed limits. If the selected change is within allowed tolerances, the objective function is calculated. All changes that improve the objective function are immediately accepted, whereas changes that increase the objective function are accepted with a probability $P(i)$ (Equation (3-13)).

Although DAO requires more time to create a treatment plan than FMO, there is no degradation in the delivered plan quality because the MLC leaf sequencing step is avoided (unlike in FMO). In addition, it has been shown that DAO plans can be delivered with a fewer number of total apertures and less total MU than FMO plans[17]. Thus, resulting treatment times are faster and the patient is exposed to less leakage radiation that could induce secondary cancers[156,157].

3.4 Volumetric Modulated Aperture Therapy (VMAT)

The rotational form of IMRT delivered on a conventional linac is referred to as volumetric modulated arc therapy (VMAT)[158]. Rather than using 5–9 intensity modulated beams, each at a

static (i.e. gantry stationary) gantry angle as in conventional IMRT, VMAT delivers modulated radiation in a continuous arc during gantry rotation of the linac around the patient. A VMAT treatment can consist of one or more full or partial gantry arcs, with optional static or dynamic MLC rotation, and/or couch translation/rotation, although MLC rotation and couch translation/rotation are not commonly used. The additional degrees of freedom achieved via many beam directions allows the creation of even more highly conformal treatment plans with reduced mean dose to normal tissues due to the spread of entrance beam radiation over a greater volume. Also, VMAT's ability to deliver the entire treatment fraction in an uninterrupted fashion, as opposed to the static gantry angles used in conventional IMRT, substantially improves the time efficiency. However, the VMAT optimization problem is more complex than that of static-gantry IMRT and some of VMAT's plan flexibility is lost due to extra mechanical constraints required to ensure seamless rotational delivery.

3.4.1 VMAT development and planning

Rotational fluence-modulated arc therapy delivered on a linac was first proposed by Yu in 1995[12] under the name intensity-modulated arc therapy (IMAT). In the initial study, a dynamic arc was approximated by 55 static beams (control points) spaced 5^{o} apart and the respective intensity maps were determined via FMO. Post-optimization, a conventional IMRT MLC leaf sequencer translated intensity maps into sets of beam apertures. The more modulated an intensity map, the greater the number of apertures in a set.

Figure 3-10(a)-(c) shows a simplified example of the fluence map at gantry angle θ^{o} segmented into a set of 3 apertures. Each aperture in a set was delivered in a separate arc. The work by Yu[12] was a feasibility study and never was adopted clinically due to inefficiencies in

treatment time and plan quality degradation[159]. The reason for the plan degradation was due to the underlying approach to optimizing the individual apertures over the continuous arc. The arcs were approximated by a series of equi-angularly spaced static beams at a high spatial resolution of gantry angles, whereby the solution apertures created at each gantry angle had to be linked such that the MLC positions could be practically achieved between consecutive gantry angles (i.e. aperture connectivity). This approach typically forces the overall solution into a local minimum very quickly in the aperture sampling and does not allow a thorough search of the solution space. In general, 8–10 arcs could only achieve three levels of intensity[160], and up to 13 full and partial arcs were required to deliver a treatment of 250 MU in 14.5 min. Additionally, the deliverable fluence maps were degraded from the optimized ideal fluence maps as they were processed through two separate MLC leaf sequencers.

The goal of VMAT planning is to find the optimal trajectories of the MLC leaves, which yield the best plan quality for a given treatment time. In order to perform optimization for rotational arc therapy plans such as IMRT and VMAT, inverse planning principles are required. However, VMAT planning introduces many degrees of freedom and it cannot be formulated as a convex optimization problem which makes the optimization computationally more difficult. The differences between IMRT and VMAT planning are in the number of beams used to discretize the arc definition, and the consideration for aperture connectivity[158]. The transition between the shapes of the apertures from one beam angle to the next is achieved via dynamic motion of the MLC leaves. During the gantry rotation around the patient while radiation beam is on, it is imperative that the subfields of adjacent beam angles do not require the MLC leaves to travel at speeds that exceed their maximum achievable speed. Ensuring the connectivity between adjacent subfields for smooth and physically allowable leaf motion is a critical requirement[158].

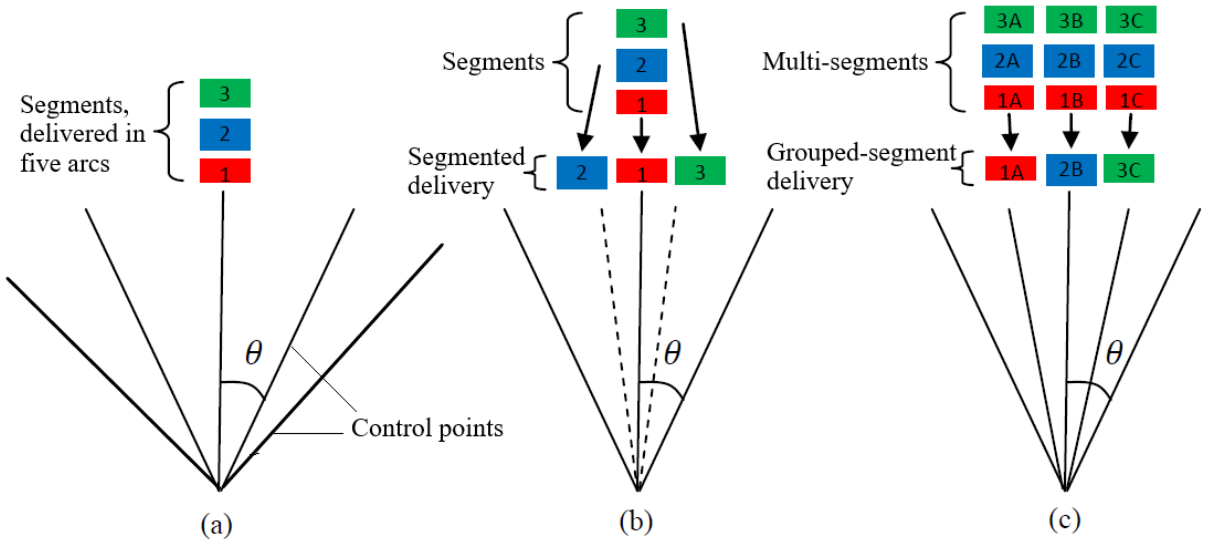

Figure 3-10: Illustration of different VMAT strategies (only three apertures are shown per control point, for simplicity). (a) Method where each sequenced beam aperture for a control point is delivered in a separate arc. (b) Method where all beam apertures of a control point are delivered in a single arc by spreading them out to other angles. (c) Method where several control points are grouped together and only one aperture from each control point is delivered. None of the delivered apertures in a group can have the same beam intensity. Figure reprinted from Chin[75] used with permission.

3.4.2 VMAT optimization methodology

VMAT adopts some of the terminologies utilized for IMRT. Let us represent the patient's target structure as voxels discretized into index *i*; the incident fluence discretized into a 2D beamlet grid by the MLC leaf pair index *n*; and the beamlet position in the leaf travel direction by the index *j*. Thus, assuming a coplanar VMAT delivery whereby the patient couch is fixed while the continuous gantry angle rotation is indexed by θ, the effective beam fluence at any gantry angle is x_{jn}^{θ}. The dose contributed by the fluence at the beam direction θ, MLC row *n*, to the voxel *i*, can then calculated by the dose-influence matrix D_{ijn}^{θ}. Finally, the total dose can thus be calculated by[155]:

$$d = \sum_{\theta} \sum_{j} \sum_{n} D_{ijn}^{\theta} x_{jn}^{\theta} \tag{3-17}$$

In VMAT, the treatment plan created by the optimization platform is usually specified in DICOM format to be translated by the linac control system as a sequence of arc control points (CP). Each CP is defined via a gantry angle, MLC leaf positions, and the cumulative number of beam monitor units (MU) that is delivered[155]. Using the DAO formulation of VMAT planning and assuming one aperture per gantry angle θ, the goal is to determine the left and right MLC leaf positions $\left(n_L^{\theta}, n_R^{\theta}\right)$; the aperture weight y^{θ}; and the effective beam fluence at each CP x_{jn}^{θ}.

Thus, the VMAT optimization problem in DAO formalism can be defined as

$$\min_{y, n_L, n_R} f(d) \tag{3-18}$$

$$\text{subject to } d = \textstyle\sum_{\theta} \sum_{j} \sum_{n} D_{ijn}^{\theta} x_{jn}^{\theta} \tag{3-19}$$

$$x_{jn}^{\theta} = y^{\theta}\left[z_j\left(n_R^{\theta}\right) - z_j\left(n_L^{\theta}\right)\right] \tag{3-20}$$

$$y^{\theta} \geq 0 \tag{3-21}$$

$$n_L^{\theta} \leq n_R^{\theta} \tag{3-22}$$

Here, the intensity of the beamlet *j* is defined by the effective fluence created by the MLC aperture as represented in Equation (3-25) whereby z_j can either be a piecewise linear function or level set function[155,161] to define the aperture weight. This optimization problem is non-convex due to the shape of the function z_j (as x_{jn}^{θ} can be determined only by the time that beamlet *j* is exposed by the MLC leaves) and thus is challenging to solve in a true optimal sense. In practice, VMAT planning also has to consider the rate of the gantry rotation, the dose rate, as well as the delivery time, *T*. Other goals such as the total beam output in monitor units (MU) also need to be considered and included as either optimization parameters or as constraints (described further in Section 3.4.2.1).

The VMAT algorithm developed by Otto[10] is a DAO based method. MLC leaf positions and beam weights are used as optimization parameters. The dynamic 360° arc of the linac is approximated by 177 static beams. To reach an acceptable plan solution, the optimization is guided by a cost function based on dose-volume constraints as described by Bortfeld *et al*[145] (Section 3.3.1). Multiple maximum dose-volume constraints may be pre-set for each target or surrounding OARs and healthy tissue structures. Targets may also be subject to minimum dose-volume constraints (no minimum dose-volume constraint for OARs). The cost of each constraint is calculated using a squared dose-difference function multiplied by a priority value[162]. The total plan cost equals the sum of the individual constraint costs[162] (Section 3.3.1).

3.4.2.1 Gantry angle-dependent constraints

DAO algorithms normally incorporate constraints for MLC leaf widths, maximum leaf speed and maximum dose rate. To ensure smooth rotational delivery, VMAT has additional gantry angle-dependent constraints for the beam weights and MLC leaves, represented by:

$$\frac{\Delta MU}{\Delta \theta} \leq \left(\frac{dMU}{d\theta}\right)_{max} \tag{3-23}$$

and

$$\frac{\Delta n}{\Delta \theta} \leq \left(\frac{dn}{d\theta}\right)_{max} \tag{3-24}$$

whereby MU, θ and n represents the MU beam weight, gantry angle and the MLC leaf positions, respectively. $(dMU/d\theta)_{max}$ and $(dn/d\theta)_{max}$ can be both calculated as

$$\left(\frac{dMU}{d\theta}\right)_{max} = \left(\frac{dMU}{dt}\right)_{max} \Big/ \left(\frac{d\theta}{dt}\right) \tag{3-25}$$

and

$$\left(\frac{dn}{d\theta}\right)_{max} = \left(\frac{dn}{dt}\right)_{max} \Big/ \left(\frac{d\theta}{dt}\right)_{max}. \quad (3\text{-}26)$$

whereby $(d\theta/dt)$ represents the linac gantry rotation speed. For Varian linacs, the gantry requires at least 60 seconds to complete a 360° arc (i.e.$(d\theta/dt)_{max} = 6$ deg/s). Thus, $(d\theta/dt) = (d\theta/dt)_{max}$, if treatment is to be completed as quickly as possible. In a Varian Millennium120-leaf MLC, the maximum leaf speed $(dn/dt)_{max} = 3.0$ cm/s. Thus, $(d\theta/dt)_{max}$ is used to guarantee that excessive leaf motions do not compromise treatment delivery efficiency. Moreover, $(dn/d\theta)_{max}$ cannot be too large or else the assumption that dose calculations for static beams are an accurate approximation of dynamic radiation delivery will fail[10].

Conversely, by allowing gantry speed to decrease within an arc, there is a greater range in the value of $(dMU/d\theta)_{max}$ and dose can be more closely sculpted around the tumour. Note that $(dMU/dt)_{max}$ represents the maximum MU beam weight change with respect to time, and should not be confused with $\dot{M}U_{max}$ which is the notation for the maximum dose rate in a linac (e.g. 2400 MU/min). To illustrate the difference, a continuous radiation beam moving at a constant rotational speed around a target, can be approximated by 60 evenly distributed beams. Each beam can have a weight of 40 MU resulting in the target receiving a total of 2400 MU (Figure 3-11(a)). In contrast, a dose of 2400 MU can be delivered if a single beam irradiates the target at 2400 MU/min for 1 min (Figure 3-11(b)). Thus, the single beam has a MU weight of 2400 MU.

Our VMAT algorithm allows linac gantry speed $(d\theta/dt)$ to fluctuate during delivery and uses a flexible constraint of

$$(dMU/d\theta)_{max} = 0.3 \times \overline{MU_t} \quad (3\text{-}27)$$

whereby $\overline{MU_t}$ is the average MU of all the beam weights present in the optimization at a given point in time, *t*. This approach helps to balance the trade-off between shorter treatment times versus

better plan quality. In order to prevent over modulation of the radiation beam, total MU weight that any given beam aperture can have is set to

$$MU_{beam-max} = 5 \times \overline{MU_t} \tag{3-28}$$

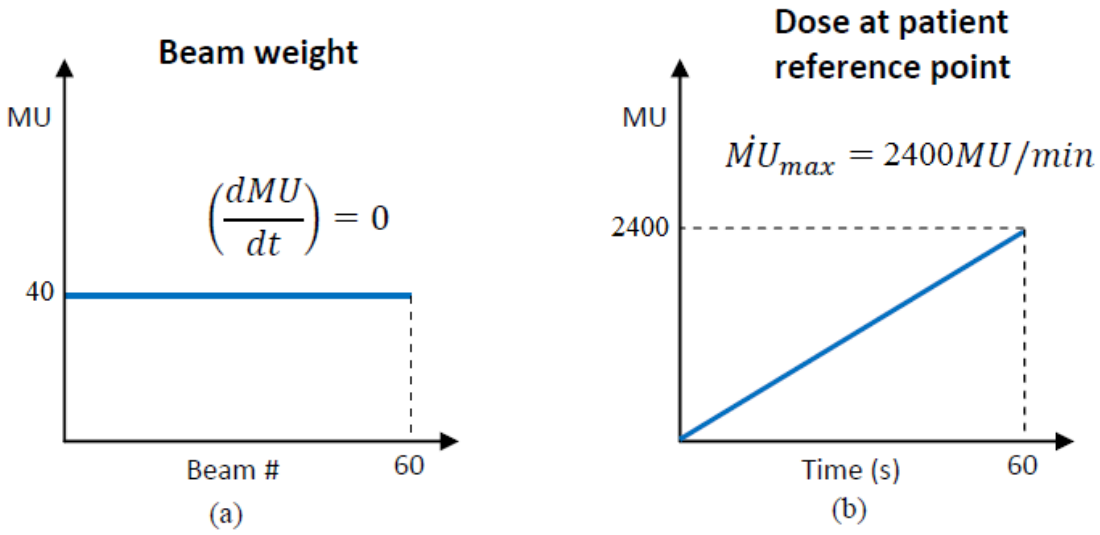

Figure 3-11: Illustrative explanation for (a) beam MU weight change and (b) the linac dose rate. Adapted from Chin[75].

3.4.3 VMAT optimization strategy overview

Generally, methods for IMAT/VMAT optimization can be grouped into two categories: (a) two-step process (arc-based) and (b) one-step process (control point-based). The two-step process consists of intensity distribution or FMO for beam profiles at different gantry angles, discretizing the arc into *beamlets*; and a leaf-sequencing process to convert optimized fluence maps and intensities to deliverable MLC segments or *apertures*[155,158,159,163,164]. However, due to the two-step process there is a dose discrepancy between the FMO and leaf-sequencing stages since fluence maps are only 'approximately' sequenced during the sequencing stage at large/coarse gantry spacing in order to speed up calculations, particularly when delivery efficiency is taken into

consideration. Because the beam aperture shapes are not available in the FMO step, beamlet-based dose calculations are used to determine dose delivered by the treatment plan, thereby contributing to the discrepancy since this approach does not allow for detailed linac-head fluence modeling.

A one-step DAO implementation was proposed by Otto[10], where a coarse-to-fine angular sampling process was implemented using small beams with large angular spacing and shape interpolation for new apertures. Otto developed a single-arc IMAT algorithm which was termed volumetric-modulated arc therapy (VMAT)[165] in a 2008[10] seminal paper. The VMAT algorithm uses progressive resolution sampling of beam angles to optimize many apertures using DAO, via a stochastic search, while also allowing variations in the dose-rate and gantry speed. The aperture shapes and weights are initially optimized for a few coarsely spaced gantry angles with little need for consideration of connectedness in the apertures. Additional gantry angles are added once the solution converges. As the gantry resolution increases, the optimizer searches and considers aperture connectivity during the initialization of aperture shapes as well as during the optimization[158]. Using linear interpolation from neighboring angles, the initial shapes of the newly inserted apertures are determined. Such coarse-to-fine sampling is termed 'progressive sampling', and allows the optimization to converge faster[10,158]. Since the aperture shape connectivity is initially disregarded, the optimizer gains freedom to attain an optimal dose distribution. Hence, the two main advantages to progressive sampling are: (i) it reduces the optimization time and (ii) it circumvents the restrictive leaf motion constraints early in the optimization by exploring an arc that is coarsely sampled, and thus allows for large leaf movements between successive coarse samples[166]. Otto's procedure was adopted commercially in the initial version of RapidArc™ by Varian Medical Systems, termed *progressive resolution optimizer* or PRO (see Figure 3-12 and Section 3.4.3 for a more detailed description). Most of the commercial VMAT implementations

heavily rely on DAO methods. RapidArc™ (Varian) uses a global stochastic optimization to DAO in a one-step approach, without utilizing FMO and arc sequencing methods. SmartArc™ (Philips) as well as MONACO™ (Elekta) use a two-step approach, adopting FMO and arc sequencing methods to obtain a starting point for DAO, via a local gradient-based optimization as a third step.

In a treatment planning system, the dynamic delivery sequence of the VMAT treatment beam is represented as a series of discrete beam segments, each defined as the delivery of a set number of MUs with a defined aperture shape, at a defined gantry angle. Communicating with the linac, such segments are translated into a set of 'control points'[158]. Each control point (CP) represents and defines the MUs, gantry angle, collimator angle, couch angle, and position of secondary collimators and MLC leaves for that point in the arc beam delivery. For dynamic delivery, the first planned static segment is converted to transition dynamically from the first to the second control points. The transition from the second to the third control point then delivers the MUs of the second planned segment[158]. For VMAT, the gantry angle changes from one control point to the next, as does the aperture shape created by the MLC during the simultaneous gantry rotation and irradiation. Thus, the delivered MU or total treatment time serve as independent variables. In static gantry delivery methods, such as in 'sliding window' IMRT, the only dependent variable is the aperture shape which varies with the delivery of MUs at a specific gantry angle. All the other variables such as the dose rate, gantry angle, and collimator angle are set as constants for each radiation beam[158].

It should be noted that existing linacs have different capabilities in controlling the mechanisms for coordinating the dynamic delivery of VMAT as MLC designs are different between vendors. For example, Varian's 120-leaf MLC is mounted on a carriage that acts as a tertiary collimator below the conventional secondary collimator jaws. During VMAT delivery, the

secondary jaws as well as the carriage do not move, limiting the range of motion of the MLC leaves by the carriage design and the large distance from the source[158]. In contrast, Elekta's linac incorporates the MLC as a secondary collimator with thinner back-up jaws placed underneath. Each leaf can travel 12.5 cm across the center and 20 cm from the center. The back-up collimators follow the MLC-shaped fields thus lowering the radiation leakage through the parked, closed leaves[158] (this is because the tips of closed leaves do not perfectly mesh together, so the leakage radiation at those points is higher than through the body of the leaves).

In terms of dose calculation, this is carried out beam by beam (i.e. at each control point) in VMAT as is done in IMRT. However, because VMAT uses many more beams (compared to conventional IMRT) to approximate an arc, the accurate calculation of patient dose in a short time frame is challenging. To accurately calculate dose calculations in treatment plans, high resolution beam angles are needed to represent the treatment delivery[158]. Therefore, treatment planning parameters strongly influence deliverability and the delivery accuracy. In conclusion, accounting for the physical limitations of linacs, MLCs and the intrinsic disconnect between planned and delivered doses (due to the beam aperture using interpolated shapes during dynamic delivery, while the treatment plan is approximated as several static beams placed at low angular resolution) is essential to creating optimal plans for VMAT[158].

For a VMAT algorithm to be successfully implemented in the clinic, it would require the following characteristics[75]:

1) High-resolution sampling of the gantry arc during optimization for accurate dose calculation

2) Flexible optimization allowing creation of highly conformal and time efficient treatment plans despite tight restrictions placed on beam modulation or gantry arc resolution due to #1

3) Quick convergence of the optimization to a solution despite tight restrictions placed on beam modulation due to requirement #1

The VMAT algorithm developed by Otto[10] satisfied these requirements and was quickly commercialized as RapidArc™ by Varian Medical Systems in 2008. All subsequent optimization work presented in this Thesis is based on the early research version of the VMAT algorithm by Otto (otherwise called *MonArc*), upon obtaining express permission to use for research purposes.

3.4.4 Progressive Beam Sampling or Progressive Resolution Optimization (PRO)

A major feature of Otto's VMAT algorithm that differentiates it from previously proposed methods is the progressive sampling of the static beam angles through the progression of the optimization in order to approximate a continuous arc of radiation. As shown in Figure 3-12(a), optimization starts with a coarse sample of distributed beams (e.g. only six beams) whose apertures conform to the target's BEV. Changes to MU beam weights (ΔMU) and MLC leaf positions (Δn) are randomly sampled from uniform distributions. Here, ΔMU and Δn are functions of gantry angle spacing $\Delta\theta$, between the beam aperture being optimized and its nearest neighbours.

A new beam sample is added to the aperture set being optimized, after a period involving many MLC leaf and beam weight changes (Figure 3-12(b)). The new beam sample is inserted mid-way between two existing beams and its MLC leaf positions are linearly interpolated from the MLC positions of adjacent beams. The MU weight of the new sample is based on a redistribution of weights from its immediate neighbours according to the following equations:

$$MU_{new}(S-1) = \frac{2 \times MU_{old}(S-1)}{3}, \tag{3-29}$$

$$MU_{new}(S) = \frac{MU_{old}(S-1)}{3} + \frac{MU_{old}(S+1)}{4}, \tag{3-30}$$

$$MU_{new}(S+1) = \frac{3 \times MU_{old}(S+1)}{4}. \tag{3-31}$$

where S is the sample index of the new beam sample, MU_{new} is the new MU weight, and MU_{old} is the MU weight prior to the addition of the new sample. Optimization continues and further beam samples are added successively (Figure 3-12(c)-(e)) until a desired sampling frequency is satisfied.

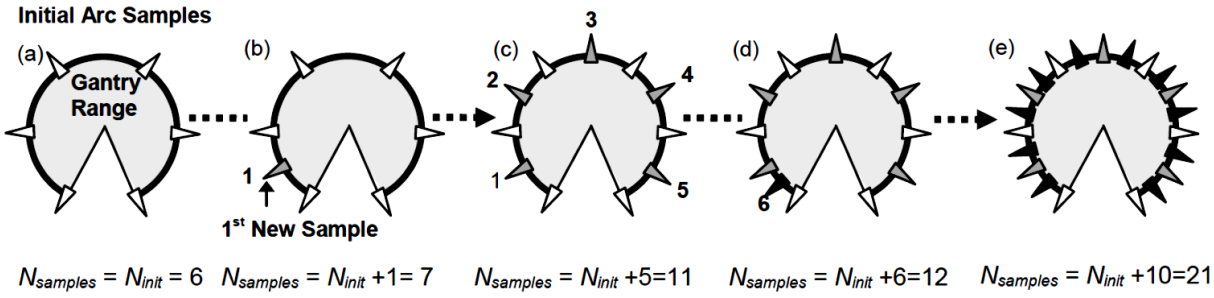

Figure 3-12: Illustration of beam sampling for continuous gantry arc using static beam angles. (a) At the beginning of optimization, the gantry range is coarsely sampled (b) After a given amount of time, a new sample is added between two pre-existing samples (c) - (e) Further beam apertures are added in similar pattern to the set, until the desired sampling frequency is reached. Figure reprinted from Chin[162] used with permission from Wiley.

The use of progressive beam sampling is advantageous to successful implementation of VMAT. It allows VMAT to smoothly balance the competing demands of high-resolution beam sampling for accuracy in dose calculation against flexible optimization parameters needed to easily reach an optimal solution. At the start of optimization, when sample resolution is large and treatment parameters are far from optimal, optimization flexibility is high because the iteration step sizes can be large (Equations (3-23) and (3-24)). Dose calculation accuracy is sacrificed in the beginning in order to quickly reach the optimal plan. As more beam samples are added to the arc and optimal solution is achievable, optimization flexibility diminishes because the value of $\Delta\theta$ decreases, leading to proportionally smaller iteration step sizes. However, the accuracy of dose

calculation increases due to finer arc sampling. The result is a high-quality plan with a high dose accuracy[75].

Progressive beam sampling also allows rapid convergence of the optimization to an optimal solution by avoiding the simulated annealing method. During VMAT optimization, MLC leaf position and beam weight changes are only accepted if the objective or cost function decreases. However, DAO is a non-convex optimization problem. Rather than relying on a time-consuming simulated annealing algorithm, escape from local minima is accomplished by the addition of each new beam sample, which generally perturbs the value of the objective function. The perturbation size will be greater at the start of optimization when few beams represent the treatment arc. This is beneficial because the objective function will also be far from the global minimum. As the gantry range between beams decreases and the objective function approaches the global minimum, adding new beam samples will lead to a smaller disturbance. To compensate for the changing magnitude of the perturbation, the interval between each new beam sample addition (e.g. number of successful iterations) follows the form of a decreasing exponential[75]. Thus, at the beginning when there are fewer beam samples and greater perturbations, it is balanced out by exponentially more iterations. Conversely, when the arc resolution improves and the optimal solution is near, iterations are exponentially reduced.

The effectiveness of progressive beam sampling was demonstrated by Otto's VMAT implementation via creation of a treatment plan superior to static-gantry IMRT for a difficult head and neck cancer example[10]. The treatment plan had multiple (three) targets, all prescribed to different dose levels. Optimization time was 1 h and gantry sample spacing of no more than 2° was necessary to maintain accuracy in dose modeling. In comparison, it was estimated that a VMAT algorithm incorporating all the finely sampled beams right from the start of a simulated

annealing-based optimization would require nearly a month to converge to a solution[10,75]. If given only 1h, the objective function value was at least a magnitude greater than VMAT. Treatment time of VMAT's head and neck plan was 1.8 min for delivery of a 2 Gy fraction using a maximum dose rate of 600 MU/min. This is approximately only a quarter of the static-gantry IMRT time.

3.4.5 Constrained fiducial marker optimization process

Using the PRO method from Otto's DAO implementation as described in Section 3.4.4, we modified the research-based treatment optimization software (termed *MonArc*) to incorporate the fiducial markers as structures in the BEV of each MLC segment associated with individual control points in the plan, by adding visibility constraints to the objective function. The optimization algorithm in *MonArc* utilizes an objective function that finds the optimal shapes and weights of all the MLC segments/apertures in a VMAT delivery, based on the prescribed dose and specified dose constraints to targets and OARs provided by the user.

Thus, for every iteration of the MLC segment introduction during the optimization when the MLC BEV has been initialized, the algorithm searches that the fiducial markers are constrained to be fully visible (100%) based on the voxel points used to characterize each structure set. If a specific constrained marker is not fully visible in the BEV, the dose calculation is not completed, and the next MLC segment is introduced. This process is repeated, until the constrained marker is visible in BEV before the dose computation is completed. Note that we do not specifically account for any dose threshold limitation at the edges of the MLC leaves when the markers are slightly occluded, as the approach ensures the fiducial markers will be fully within the MLC aperture. The flowchart for the procedure can be seen in Figure 3-13.

Finally, dose distributions from plans with added fiducial marker-based visibility constraints were then compared to VMAT plans with no such constraints (i.e. only dosimetric constraints), to analyze the discrepancies. All *MonArc* optimized plans were imported into Eclipse and doses were recalculated with either the Acuros XB (Acuros External Beam) or AAA (Anisotropic Analytical Algorithm) algorithms, to take advantage of the dose visibility and comparison tools available in the commercial Eclipse TPS.

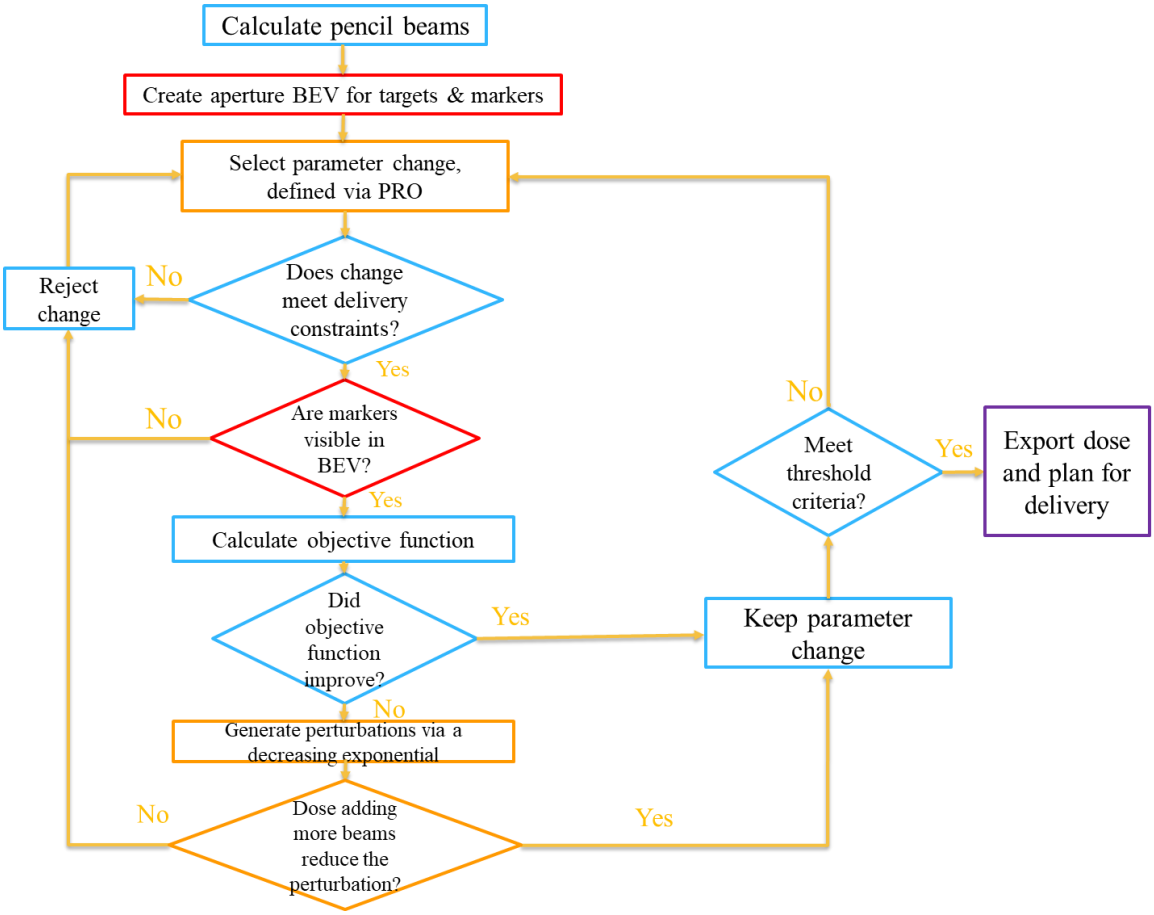

Figure 3-13: Flowchart for the constrained marker-based PRO optimization as implemented in *MonArc*. Modifications from the original algorithm are highlighted in red outline.

Chapter 4 Feasibility study for marker based VMAT optimization towards tumour tracking

In this chapter, we conducted a feasibility study on incorporating fiducial marker visibility constraints into VMAT optimization. Specifically, we have included fiducial markers as structures, as is done with targets and OARs, in the PRO optimization process as detailed in Figure 3-13. Instead of dose to the fiducials, we determine their visibility within the MLC defined aperture, and incorporate that term into the plan optimization. Using the markers as structures simplifies their incorporation into the optimization process. We propose that via this incorporation, one may produce treatment plans that aid real-time tumour tracking approaches employing exit imaging of the therapeutic beam (e.g. via EPID), in addition to satisfying purely dosimetric requirements. We investigated the feasibility of this approach for a thorax and prostate site using optimization software (*MonArc*). This study was submitted and recently accepted for publication in the Journal of Applied Clinical Medical Physics (JACMP)[§].

4.1 Introduction

Globally, lung cancer is the leading cause of cancer death. In Canada, the mortality rate for lung cancer is 71%[167]. Lung cancer can be divided into two types: (a) non-small cell and (b) small cell. Approximately 85% are categorized as non-small cell lung cancer (NSCLC) while 15% are small-cell lung cancer (SCLC). In general, lung tumour motion is non-isotropic and more dominant in the Superior-Inferior (SI) direction. Mageras *et al*[49] evaluated lung tumour motion

[§] Omotayo, A.A., Venkataraman, S., Venugopal, N. and McCurdy, B. (2020), Feasibility study for marker-based VMAT plan optimization toward tumor tracking. J Appl Clin Med Phys, 21: 84-99. https://doi.org/10.1002/acm2.12892

characteristics using four-dimensional CT (4D-CT). They found that the tumour displacement was greater than 10 mm for 7 out of 12 patients, primarily in the SI direction. Yu *et al*[60] compared lung tumour motion characteristics in NSCLC patients between early and locally advanced stage using 4D-CT. They observed that the tumour motion (95^{th} percentile) was greater by more than 50% in the early-stage group than the locally advanced lung cancer group. Early stage tumours located in the lower lobe showed the largest motion (median: 9.2 mm) compared to upper and middle lobe tumours, which showed less motion[60] (median: 3.3 mm). Their results suggest that the range of lung tumour motion differs depending on tumour location and staging of NSCLC. Early stage tumours are more mobile than locally advanced stage NSCLC.

For irradiation of lung tumours, the surrounding lung and OAR tissues and the toxicity that follows will often be a limiting factor. The major dose-limiting toxicities are pneumonitis, myelitis and esophagitis. Conventional fractionated RT (e.g. 6000 cGy/30 fx), however typically targets tumours with large treatment field margins to account for both setup and motion uncertainties. Alternatively for some patients, SBRT with smaller field sizes and hypo-fractionated doses (e.g. 4800 cGy/4 fx) can give local tumour control rates of up to 80–90% with limited toxicity[168]. The use of fewer fractions leads to relative lower radiobiological effectiveness of dose in the target relative to surrounding OARs, therefore the biologically effective dose is somewhat increased for hypofractionated SBRT regimens to achieve a good tumour response. Thus for SBRT, it is highly desirable to reduce OAR exposure by reducing treatment field margins and positional uncertainties related to setup errors and/or respiration[66].

4.2 Motivation

In clinical practice, radio-opaque fiducial markers implanted in or near the tumour have been used for image-guided radiation therapy (IGRT) and for real-time tumour target localization for several tumour sites, via projection imaging. Approaches typically use non-modulated, open fields due to the risk of blocking or shielding the fiducial markers when using full VMAT delivery methods. Li *et al*[169] utilized a Bayesian approach for real-time 3D tumour localization combining the 2D projections from kV x-ray imager available on linear accelerators during treatment, with the aid of gold cylindrical markers, using motion trajectories of a lung and pancreas patient reproduced in a phantom. They reported 3D localization errors of 1.5 and 0.8 mm for the lung and pancreas[169], respectively. However, the maximum *a priori* method employed in their Bayesian approach depends on appropriate hyper-parameter selection for optimal results, which needs to be chosen before treatment (e.g. via x-ray images acquired during patient setup). Also, irregularities in tumour motion patterns may require incorporation of a dynamic motion model.

Azcona *et al*[39] implemented an automated fiducial marker detection algorithm for prostate VMAT using 2D MV cine EPID images. Their approach was based on a combined criterion using template matching and image intensity information, using a dynamic search area that predicts the fiducial position and updates in real-time to track the marker and to account for marker occlusion by MLC leaves. However, the 3D fiducial position is predicted if its expected position lies in open beam which is derived from planning CT. While promising, the approach suffers from sparse image data from few projections due to small arc of gantry rotation[39], especially where all fiducial markers are blocked. Another limitation of this approach is effect of false positives, as a threshold correlation metric value between the EPID and planning CT positions were used. The work acknowledges that it is challenging to apply this approach for tracking where there is fast fiducial

marker motion or occlusion of all the fiducials by MLC leaves. In summary, the prior literature indicates that the more reliably fiducials are visible, the more robust and effective the real-time tracking algorithm will be. This observation motivates the current work.

Another motivation is that marker-based constrained plans can be incorporated into MLC-based tracking along with projection images on electronic portal imaging detectors (EPID) that are readily available with megavoltage (MV) therapy photon beams during treatment. This offers advantages over other image-guided MLC tracking techniques that uses kilovoltage (kV) x-ray imaging[54,170], as no extra patient dose or processing utility is required. We expect this optimization approach will aid tumour tracking, and also reduce the extra need for imaging dose and latency delays that is found in kV-based tracking approach, which needs to be corrected with prediction algorithms. The expected visibility of the fiducial markers in the beam's eye view (BEV) overlaid by the MLC apertures at each gantry angle (i.e. control point) is available in the planning process; we can use this information in the plan optimization strategy. We propose that by incorporating marker visibility in the plan optimization step, one may produce a treatment plan that ensures a higher chance of successful application of real-time tracking techniques, in addition to satisfying dosimetric requirements.

Very few studies have investigated the incorporation of markers into the plan optimization[37]. Ma *et al*[37] investigated the feasibility of 4D IMRT planning with the inclusion of a fiducial marker constraint into the optimization, for one pancreas and lung cancer patient. They introduced a time-resolved, synchronized MLC segments to the ten breathing phases of the 4DCT and added a fiducial visibility constraint to the simulated annealing probability, whereby a fixed penalty term is used such that segmented fields are rejected or accepted if some or all of the markers are blocked during the simulated annealing process. They reported only a slight

degradation in the target dose distribution occurred when all markers were forced to be seen (i.e. a ‘hard’ constraint) in the segmented fields. Similar results were deduced for the organs at risk (OARs). However, they did not report results for VMAT and explored only one penalty term in the optimization.

To our knowledge, our study is the first to incorporate marker-based visibility constraints into VMAT plan optimization. In this work, we use radiotherapy-based optimization development software (*MonArc*) to optimize VMAT-based plans, using a combination of dosimetric and fiducial marker visibility constraints. We demonstrate the feasibility of this approach by introducing visibility constraints into the optimization in addition to the standard dosimetric objectives and produce treatment plans that are clinically acceptable in terms of the pre-defined dosimetric tolerances. We propose that by incorporating marker visibility into the optimization, one may produce treatment plans that ensure a higher chance of successfully applying real-time tumour tracking techniques, in addition to satisfying purely dosimetric requirements. We investigated the feasibility of this approach on a dynamic thorax phantom, a lung SBRT patient and a prostate patient, using *MonArc* (the research-based radiotherapy optimization software introduced in Section 4.3).

4.3 Methods and Materials

4.3.1 Data acquisition on thorax phantom

In order to evaluate the feasibility of our approach, a thorax phantom was used for validation. Lung tumour three-dimensional motion was simulated using a dynamic thorax phantom (CIRS Inc., Norfolk, USA) as shown in Figure 4-1. The phantom consists of a motorized rod with tumour inserts of different sizes made of tissue equivalent materials. Different, pre-set motion

waveforms are available and also patient-specific breathing waveforms that have been previously recorded can be used to reproduce the motion. We used a 1 cm diameter tumour insert for this study, with three artificial fiducial markers implanted around the tumour (within the PTV) in order to emulate BEV visibility and tumour motion during real-time tracking. The phantom also had embedded OAR structures including vertebrae and spinal cord.

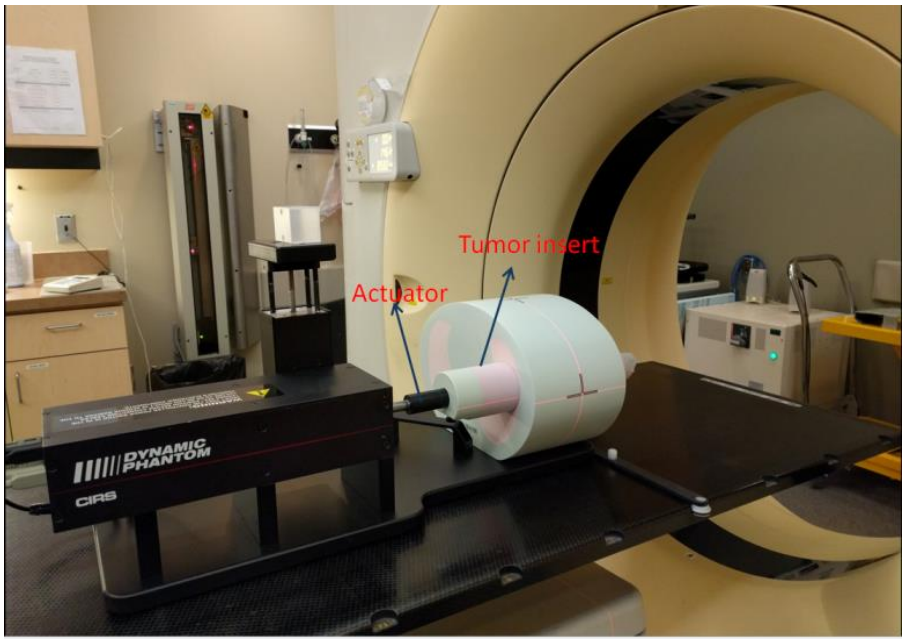

Figure 4-1: Dynamic Thorax phantom (CIRS Inc. Norfolk, USA) used for simulating 3D lung tumour motion.

A 4D-CT data set, representing 3D motion [2 mm SI, 2 mm LR, 0.5 mm AP] of ten phases of the breathing cycle, was used to create a VMAT-based lung SBRT plan with two partial arcs (Arc 1: 179°–315° clockwise; Arc 2: 315°–179° counter-clockwise) in a Varian Eclipse Treatment Planning System (TPS) (version 11.0.31). The prescription dose for the target was 48Gy over four fractions using a 6MV Flattening Filter Free (6X-FFF) X-ray beam from a TrueBeam^{TM} linac. The target structures (i.e. PTV: planning target volume and ITV: internal target volume) and OAR structures were contoured in the Eclipse TPS. The ITV approach of encompassing the entire motion of the tumour in all phases of the breathing cycle was employed for target definition, where

the CT average of the motion is utilized for dose computation. The VMAT plans were then exported to *MonArc* for optimization.

4.3.2 Data acquisition and patient data selection

In addition to the thorax phantom, the feasibility of the technique was also demonstrated on an example clinical lung and prostate VMAT patient dataset which also each had three implanted fiducial markers. We chose a prostate patient because it possesses less homogeneity in its' structures, much less motion relative to lung, and also because fiducial markers are readily used in our clinic at this tumour site. However, any patient dataset with markers in or around the PTV can be used.

The lung SBRT VMAT patient had PTV and GTV target structures (27 cc and 8 cc, respectively) and standard OAR structures including esophagus (24 cc), heart (615 cc), left lung (2110 cc), spinal cord (46 cc) and ribs (27 cc). The prescription dose to the PTV was 48Gy over four fractions with two partial arcs (Arc 1: 330°–179° clockwise; Arc 2: 179°–330° counter-clockwise) and collimator rotation (Arc 1: 30°; Arc 2: 330°), using a 6 MV Flattening Filter-Free X-ray beam (6X-FFF) from a Varian TrueBeam™ linear accelerator.

The prostate VMAT patient had PTV and CTV target structures (107 cc and 39 cc, respectively) and standard OAR structures including rectum (100 cc), bladder (125 cc), head-of-femur (175 cc), and penile bulb (1.1 cc). The prescription dose to the PTV was 72.8Gy over twenty-eight fractions with two arcs (Arc 1: 181°–179° clockwise; Arc 2: 179°–181° counter-clockwise) and collimator rotation (Arc 1: 30°; Arc 2: 330°), using a 6 MV X-ray beam (6X) from a Varian Clinac™ linear accelerator.

4.3.3 Constrained marker-based optimization process

The individual dose objectives for any plan drive the optimization toward solutions that approach the intended dose distribution for the target and critical organs at risk (OARs). To explore the effect of the inclusion of different visibility objectives, fiducial marker visibility requirements were programmed as optimization parameters and were implemented as either 'hard' or 'soft' constraints. During the optimization, as the aperture shapes and dose weights are progressively added, the inclusion of new MLC apertures are either accepted or rejected based on the desired marker visibility constraint ('hard' or 'soft'). That is, a particular marker constraint requires 100% visibility of that marker structure in the BEV. Only after this realization is the dose computed and new apertures added to continue the iterative process.

A hard constraint imposes complete and full visibility of all implanted markers in the BEV (thereby avoiding any shielding or blockage of the markers by the MLC segmented fields/apertures), while a soft constraint restricts visibility for a specific set of markers in the BEV (thereby penalizing MLC blockage for a specified marker). Thus, for the scenarios considered here with three markers implanted, there are six possible combinations of soft constraints: where only a set of two markers are constrained (i.e. SC_{II} = SC12, SC13 or SC23) and where only a single marker is constrained (i.e. SC_{I} = SC1, SC2, or SC3; where 1, 2 and 3 represents the marker index such that SC1 = soft constrained plan for marker 1; SC23 = soft constrained plan for markers 2 and 3 etc.); and just one hard constrained plan whereby all three markers must be visible (i.e. HC ≡ SC123) in the BEV by the MLC aperture. Hence, there are seven possible constrained plan combinations and eight plans in total including the non-constrained (NC) plan, and all were investigated. Note that the dose constraints are fixed per plan, whereas the marker constraints are changed for each constrained optimization per patient thus removing the planner bias. The NC

plans are whereby no marker visibility parameter is included during the optimization, thus is otherwise referred to as the reference plan.

For ease of comparison and presentation over the large number of datasets and plans, we average the quantitative dose metric results for the single- and two-markers SC plan combinations, such that instead of eight plans, we present for each patient dataset four plans in total: NC, SC_I, SC_{II} and HC. Although, we expected the spatial location of the markers as well as the level of inter-marker separation to create different dosimetric results in the SC plans, we noticed only small differences in the quantitative dosimetric values, thus justifying the use of the average for the plan comparison. We highlight situations whereby the differences are noticeable.

Figure 4-2 shows the graphical user interface (GUI) for *MonArc*, with a sample plan imported from Eclipse TPS showing the target, OARs as well as fiducial markers, with the defined plan and optimization constraints which was fixed for all constrained plans by the planner. Table 4-1 details the plan constraints used on the thorax phantom. Table 4-2 and Table 4-3 detail the constraints used on the lung SBRT and prostate patient VMAT dataset, respectively. The values used are based on clinical dose thresholds established at our clinic. As listed, the phantom only contains three OAR structures (spinal cord, vertebrae and lungs) which are much larger than the 1 cm diameter of the ITV.

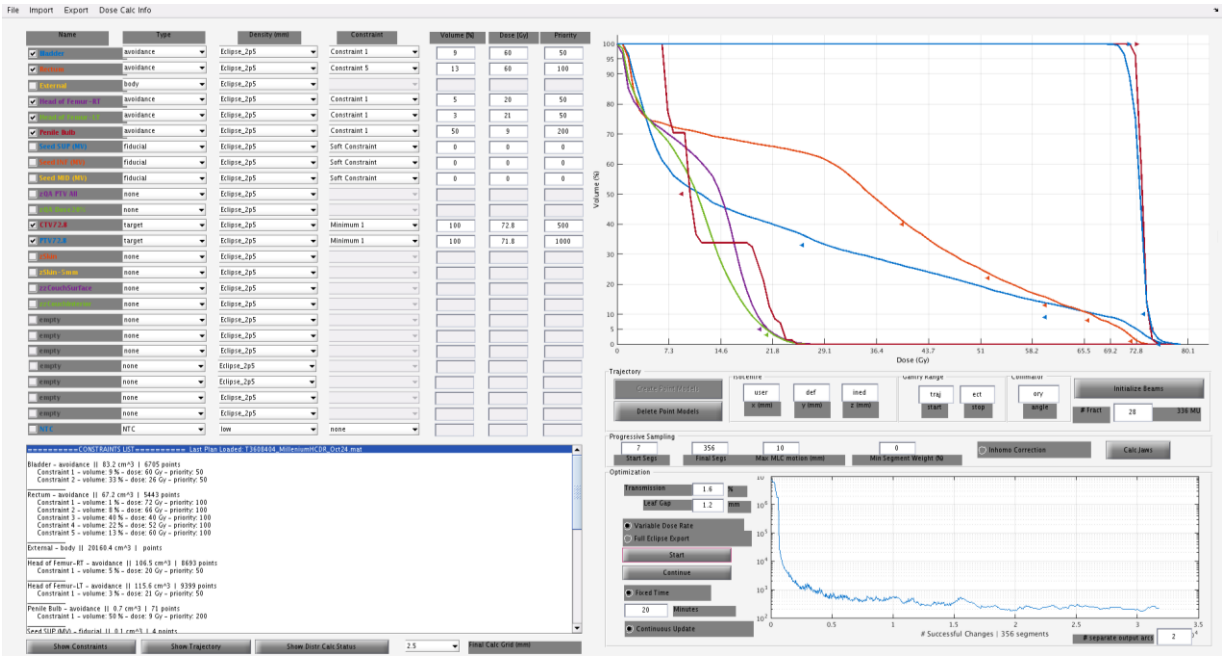

Figure 4-2: Graphical User Interface for optimization tool *MonArc*, showing targets and organs at risk (OAR) structures and plan constraints, along with dose-volume histograms (DVH) and objective function plots.

Table 4-1: Plan constraints for VMAT optimization in the dynamic thorax phantom.

Dose constraints			
Targets: Planning Target Volume (PTV); Internal Target Volume (ITV)			
Structures	**Min dose volume/Dose**	**Max dose volume/Dose**	**Prescribed Dose**
PTV	100%/48Gy	10%/52Gy	48Gy
ITV	100%/44Gy	10%/48Gy	44Gy
Relevant organs-at-risk (OARs): Spinal Cord, Vertebral Body and Lungs			
OAR (Spinal Cord)	50% volume receiving ≤ 10Gy		
OAR (Vertebral body)			
OAR (Lungs)			

Table 4-2: Plan constraints for VMAT optimization in the lung SBRT patient.

Dose constraints			
Targets: Planning Target Volume (PTV); Gross Target Volume (GTV)			
Structures	**Min Dose volume/ Dose**	**Max Dose volume/Dose**	**Prescribed Dose**
PTV	100%/48Gy	0%/52Gy	48Gy
ITV/GTV	100%/48Gy	0%/52Gy	48Gy
Relevant organs-at-risk (OARs): Lung (Left/Right), Esophagus, Heart and Ribs • Specific plan constraints			
OAR (Lung)	• 30% volume receiving < 13Gy (Left Lung) • 30% volume receiving < 10Gy (Right Lung)		
OAR (Esophagus)	• 20% volume receiving < 20Gy • 0.2% volume receiving ≤ 30Gy		
OAR (Heart)	• 3% volume receiving < 25Gy		
OAR (Ribs)	• 4% volume receiving < 32Gy		

Table 4-3: Plan constraints for VMAT optimization in the prostate patient.

Dose constraints			
Targets: Planning Target Volume (PTV); Clinical Target Volume (CTV)			
Structures	**Min Dose volume/ Dose**	**Max Dose volume/Dose**	**Prescribed Dose**
PTV	100%/72.8Gy	0%/75Gy	72.8Gy
CTV	100%/72.8Gy	0%/75Gy	72.8Gy
Relevant organs-at-risk (OARs): Bladder, Rectum and Penile Bulb • Specific plan constraints			
OAR (Bladder)	• 25% volume receiving ≤ 65Gy • 50% volume receiving ≤ 47Gy		
OAR (Rectum)	• 10% volume receiving ≤ 68Gy • 25% volume receiving ≤ 55Gy • 40% volume receiving ≤ 42Gy		
OAR (Penile Bulb)	Mean dose: < 50Gy		

4.3.4 Marker visibility and trackability metric

We assume that including the marker visibility constraints into the optimization would aid real-time tumour tracking, especially for dynamic MLC (DMLC) tracking. Most fiducial marker-based tracking algorithms in the literature require the marker to be seen in a chosen imaging template of a region of interest, and the work of Azcona *et al*[39] showed improved tracking results with increased marker visibility. However, we emphasize that we did not implement real-time tracking methods in this work. Instead, a quantitative metric for marker visibility was defined and evaluated.

Trackability is the measure of visibility for specific markers – which are either inside or near the PTV – in the BEV of the structures, as generated in *MonArc*. For our purposes, we will use the percentage of control points (i.e. percentage of gantry angles) of an arc where the markers are fully visible (i.e. all voxel point values representing the marker structure projections in the

BEV, as generated in *MonArc*), as a metric to define 'trackability'. Ideally the fiducial markers will be visible in 100% of the BEV of control points (gantry angles) of the VMAT arcs. As expected, a hard constrained (HC) plan will elicit 100% trackability as all markers should be visible in the BEV shaped by the MLC apertures.

4.3.5 Plan comparison metrics

We evaluate plans and compare the dosimetry qualitatively using cumulative dose-volume histogram (DVH) plots as well as quantitatively using dose metrics including mean dose, maximum dose, conformity index (CI), homogeneity index (HI) and gradient measure (GM). The target dose conformity index (CI) represents how closely the prescription dose conforms to the target volume and is calculated as the ratio of volume enclosed by the prescribed isodose surface divided by the target volume, i.e.

$$\text{Conformity Index (CI)} = \frac{\text{reference isodose volume}}{\text{target volume}} \tag{4-1}$$

Thus, the CI describes the conformity and the overlap of the prescription isodose with respect to the PTV. Hence, an ideal CI would be a value of 1, although typically the CI is greater than 1. Note that the 'reference isodose volume' is the volume that receives the prescribed (Rx) dose, which is dependent on the plan normalization method selected in this study (i.e. 100% of Rx dose delivered to 95% target volume).

The dose gradient measure (GM)[171] represents the dose slope measured between the equivalent sphere radius of the prescription (Rx) isodose and half-prescription isodose.

$$\text{Gradient measure (GM)} = \frac{\text{(Rx – 50\% Rx dose)}}{\text{average distance between Rx isodose and 50\% Rx isodose}} \tag{4-2}$$

Thus, a smaller GM indicates a higher dose gradient around the target structure volume. A large GM translates into a large dose spillage outside the target. Note that both CI and GM are reported in the Eclipse TPS, but only for the selected target volume (i.e. PTV).

The target dose homogeneity index (HI) is defined by the Radiation Therapy Oncology Group[172] (RTOG 1993) as:

$$\text{Homogeneity Index (HI)} = \frac{\text{maximium dose in target volume}}{\text{reference isodose volume}} \qquad (4\text{-}3)$$

Thus, the ideal HI value is 1, and HI values greater than 2 signify a less homogeneous plan. Note that the 'maximum target isodose volume' is the maximum dose to the PTV, which is always more than 100% of the Rx dose as well as the 'reference isodose volume' as defined above. Hence, as expected HI will always be greater than 1 in our study.

To analyze and compare plans for the patient datasets, we also reported an average index of the above quantitative metrics and used it along with our local physician-created clinical dose metrics for hypo-fractionated prostate and SBRT lung VMAT. Metrics used for the phantom and lung VMAT plans include:

i. PTV: dose to 95% volume greater than 95% Rx (D95% > 95%);
ii. OAR Lung: dose delivered to 30% volume less than 13Gy (D30% < 13Gy);
iii. OAR Esophagus: volume receiving 18.8Gy less than 5 cm^3 (V18.8Gy < 5cc);
iv. OAR Heart: volume receiving 28Gy less than 15 cm^3 (V28Gy < 15cc);

For the prostate VMAT patient plans, metrics used include:

i. PTV: dose delivered to 99% of the target volume (D99% or D99);
ii. OAR Rectum: volume receiving 74Gy is less than 3cm^3 (V74 < 3cc);
iii. OAR Bladder: volume receiving 65Gy is less than 25% of Rx dose (V65 < 25%);
iv. OAR Penile Bulb: mean dose not to exceed 50Gy.

Finally, we reported the percentage differences in the target metrics for the constrained plans with respect to the non-constrained plan. For statistical significance testing between plans, we used the parametric Student's T-test (with a two-tailed hypothesis) or a non-parametric Mann-Whitney U-test (when the assumption of a normally distributed data fails due to limited sample size), both at 5% significance level (whereby $p < .05$ indicates significance).

4.4 Results

4.4.1 Marker-based constrained optimization on thorax phantom

Figure 4-3(a)–(b) shows the DVH and dose distribution comparison between the clinical VMAT plan in Eclipse® TPS and the non-constrained (NC) *MonArc*-based plans for the thorax phantom. As can be observed, the *MonArc*-based plan is slightly inferior in terms of dose conformity to the targets [Figure 4-3a]. However, both plans were able to deliver 100% of prescription dose to 95% of the PTV. Similar results were obtained for the spinal cord and vertebrae OARs [Figure 4-3b]. However, the OAR dose coverage differences were within 2%, and all satisfied the OAR dose tolerance. These results show that the *MonArc*-based optimization produced acceptable results relative to Eclipse®. The disparity is because *MonArc* uses the research version with a simpler version of the multi-resolution PRO, which has since been updated and refined in its RapidArc™ implementation for the Eclipse® TPS.

The investigated plans all show very similar target dose distribution and coverage, with slightly differing OAR dose [Figure 4-4]. As observed, there are no discernable differences in the absolute dose wash plots for all investigated plans, showing that all constrained plans produce similar dosimetry results. As for marker trackability, Figure 4-10 shows the constrained markers

are visible as required in the MLC aperture field openings at each sample gantry control point. For brevity, only one control point is displayed for all investigated plans.

Figure 4-5(a) and Figure 4-5(b) shows the targets' and OAR's zoomed-in DVH plots for the non-, soft- and hard-constrained plans, respectively. For brevity, only two out of the six SC plans was displayed in the plots. The HC plan offered the best optimal dose coverage for the PTV target, as opposed to the NC plan which provided the worst target dose-volume coverage. SC13 plan (i.e. soft-constrained plan for two specific markers, 1 and 3) provided the next best optimal target dose-volume coverage, while the SC1 plan (i.e. soft-constrained plan for one specific marker, 1) provided the least optimal coverage. Similar results were obtained for the lung, and vertebrae OARs with no notable significant differences in the mean doses amongst all the constrained plans. However, for the spinal cord it can be observed that the SC1 and SC2 plan had the lowest dose, while the NC plan had the highest cord dose. This implies that there might be a benefit to using the single marker-based constrained plans to reduce OAR doses.

(a)

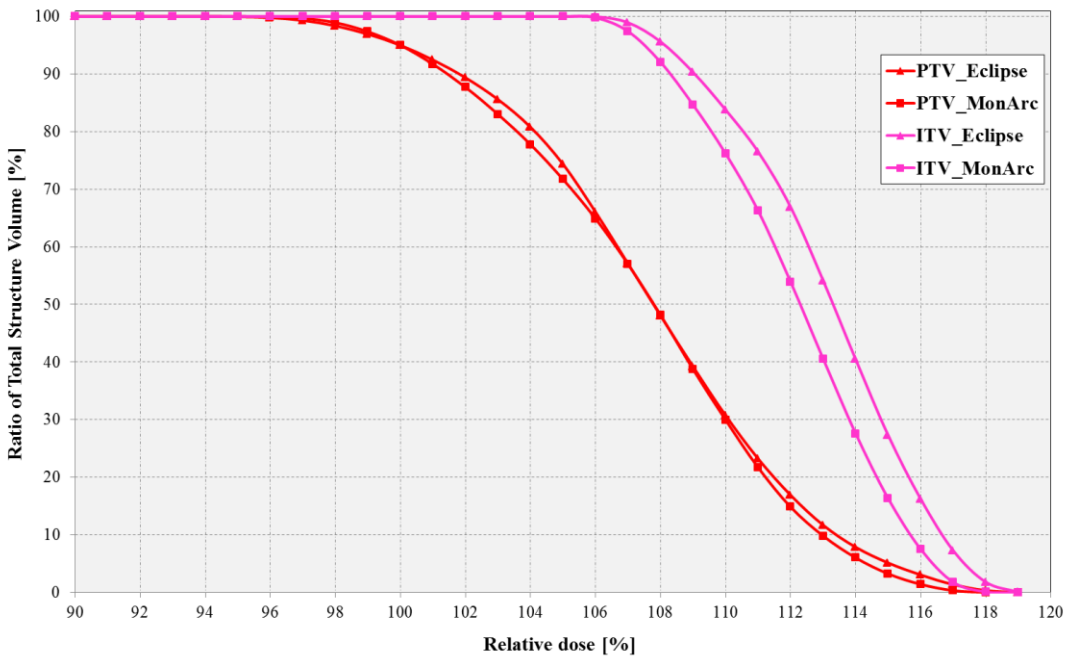

(b)

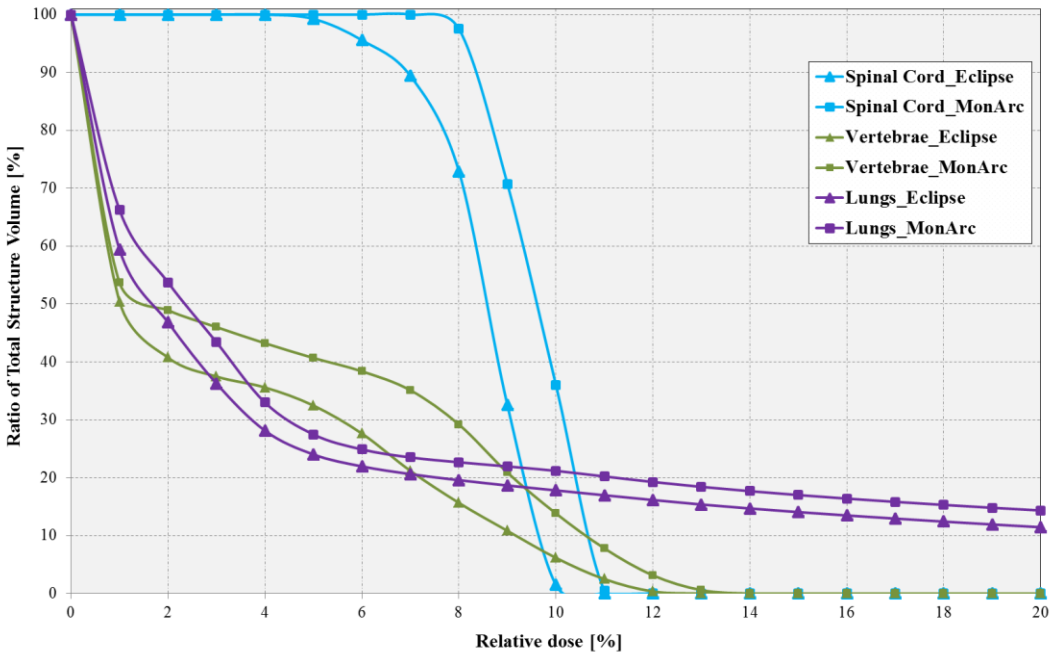

Figure 4-3: Dose-volume histogram (DVH) comparison between non-constrained clinical Eclipse-based (triangle ∇) and *MonArc*-based (square □) VMAT plans for (a) target structures (ITV [pink]; PTV [red]) and (b) OARs (Spinal cord; Vertebrae; Lungs) on the dynamic thorax phantom.

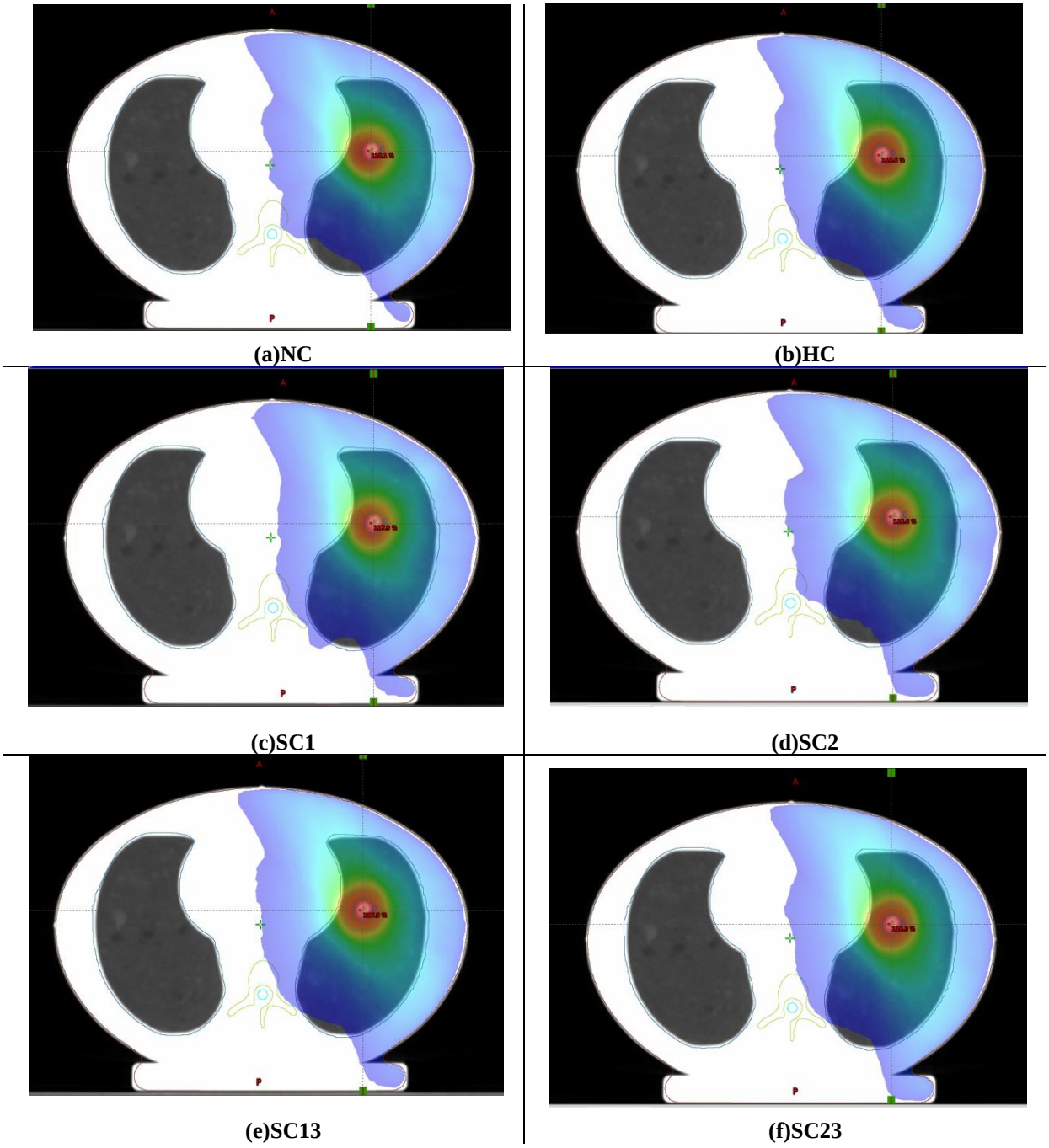

(a)NC **(b)HC**

(c)SC1 **(d)SC2**

(e)SC13 **(f)SC23**

Figure 4-4: Absolute dose distributions for *MonArc*-based optimized VMAT plans on the dynamic thorax phantom, showing (a) non-constrained (NC), (b) hard-constrained (HC), and (c)-(f) soft-constrained (SC) dose wash [where SC1 = soft-constrained plan for marker 1; SC13 = soft-constrained plan for marker 1 and 3 etc.].

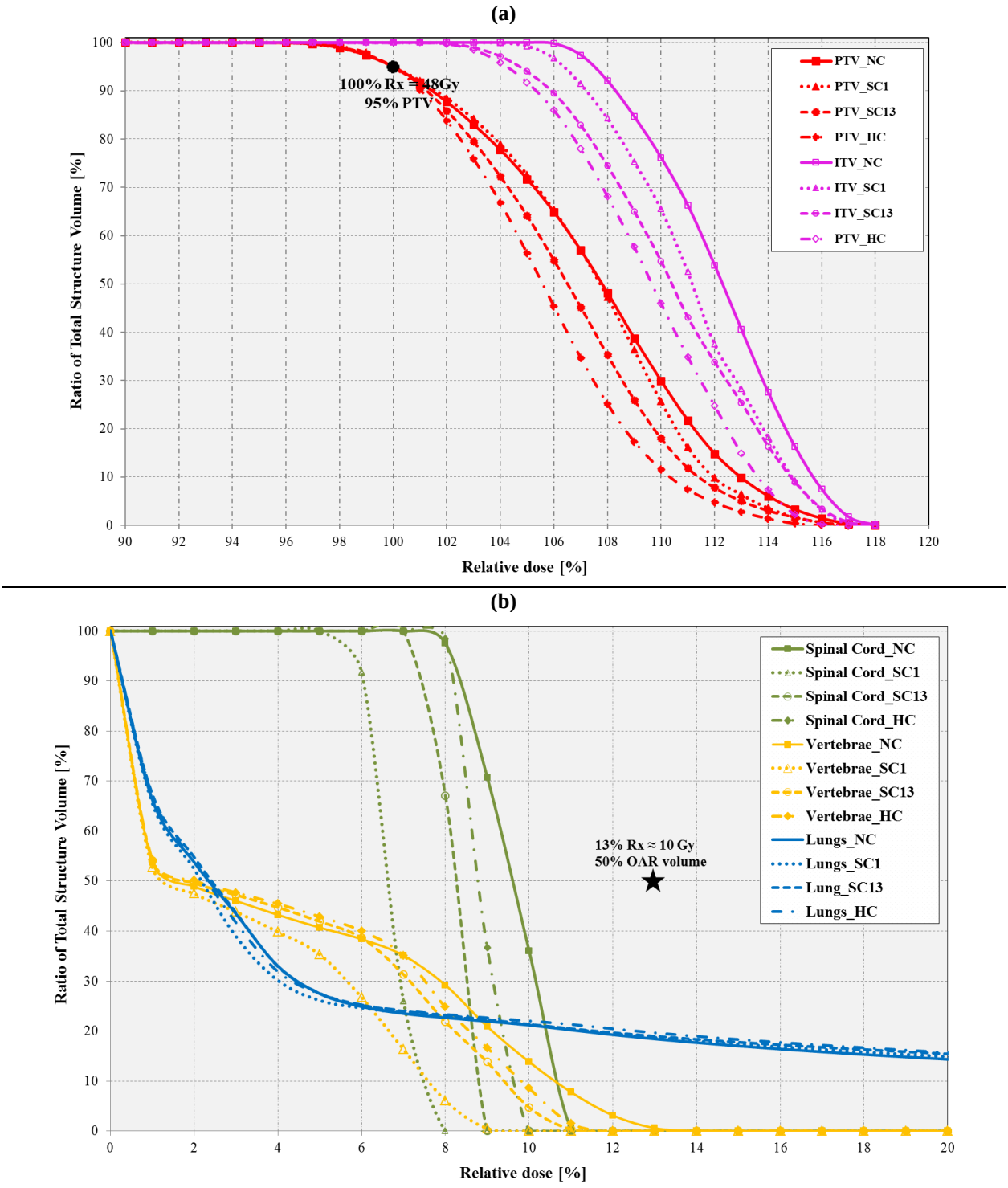

Figure 4-5: Zoomed in DVH for (a) target structures (PTV [red] and ITV [magenta]) (b) OARs (Spinal Cord [green]; Vertebrae [yellow]; Lungs [blue]) using *MonArc*-based non-, soft- and hard-constrained optimized plans in the dynamic thorax phantom. Highlights (black) represent labeled specific dose-quality threshold for PTV and all OARs.

4.4.2 Marker-based constrained optimization on lung SBRT patient

Figure 4-6 shows the DVH plot comparison between the non-constrained clinical Eclipse-based and *MonArc*-based VMAT plans for the lung SBRT patient. As can be observed, the *MonArc*-based plans are inferior in terms of dose conformity to the target for both patients, as there is a steeper dose fall-off obtained with the Eclipse-based clinical plan, which is similar to the phantom data. For the OARs, similar results were obtained between both plans for the heart and lung OARs in both patients, while small differences exist with the esophagus and ribs. However, both plans passed the established site-specific clinical dose tolerances for both the PTV and OARs.

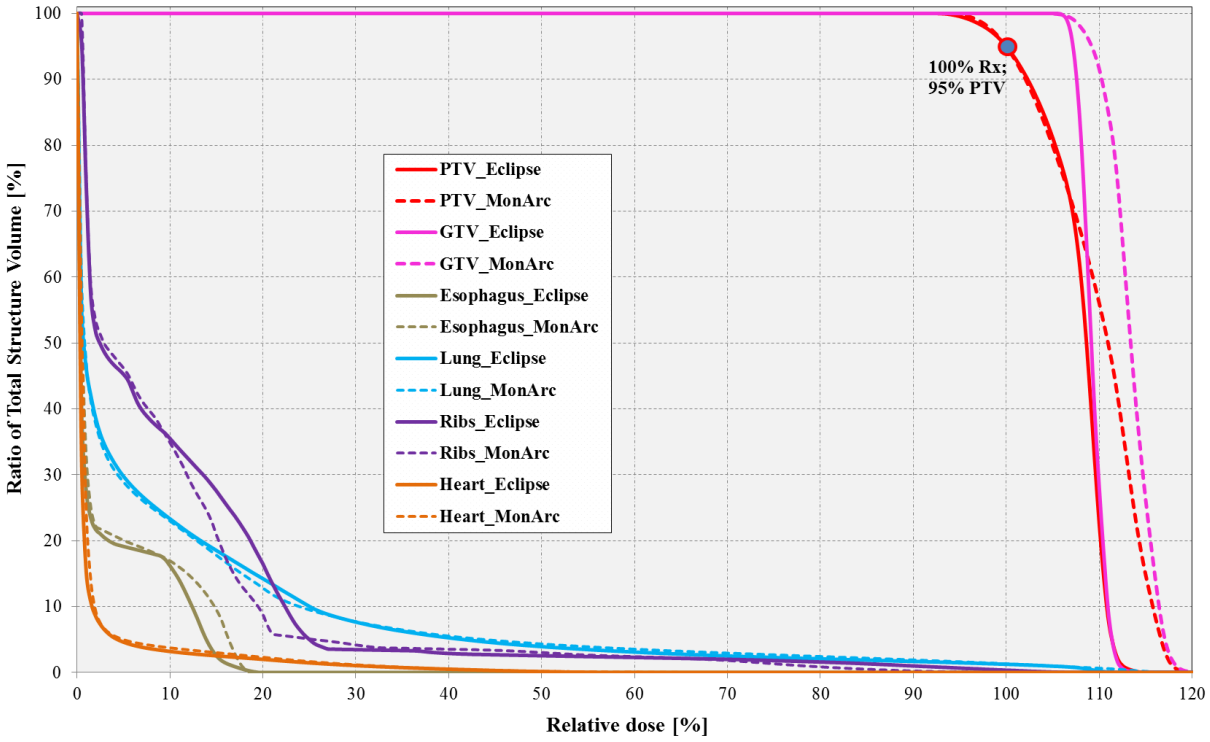

Figure 4-6: DVH comparison between Eclipse-based and *MonArc*-based VMAT plans for the target structures (GTV [pink]; PTV [red]) and OARs (Esophagus [green]; Lung [blue]; Ribs [purple] and Heart [orange]) on the lung SBRT patient. Both plans are non-constrained on the markers.

Figure 4-7(a)-(b) shows the zoomed-in target and OAR DVH plots for the NC, HC and SC VMAT plans for the lung SBRT patient. As observed, the NC plan did not produce the steepest dose fall-off to the PTV target. For the SC plans, SC13 (i.e. inferior + superior marker constrained plan) provided the steepest dose fall-off while SC1 (i.e. inferior marker constrained plan) produced the least steep dose fall-off. However, it should be emphasized that all the plans produced dosimetrically acceptable coverage and conformity for the PTV target as defined by local clinical standards.

For the surrounding lungs OAR [see Figure 4-7(b)], all constrained plans met the clinical dose threshold of D30% < 13Gy (i.e. dose to 30% lung volume is less than 13Gy), including the NC plan. Also, for the esophagus OAR, all constrained plans met the clinical dose threshold of V18.8Gy < 5cc (i.e. volume receiving 18.8Gy dose is less than $5cm^3$). Similarly, for the ribs (V32Gy < 1cc) and heart OAR (V28Gy < 15cc), the clinical thresholds as shown were satisfied by all investigated plans. However, similar to the results for the dynamic phantom, some constrained plans produce reduced OAR doses compared non-constrained plans, albeit not significant.

(a)

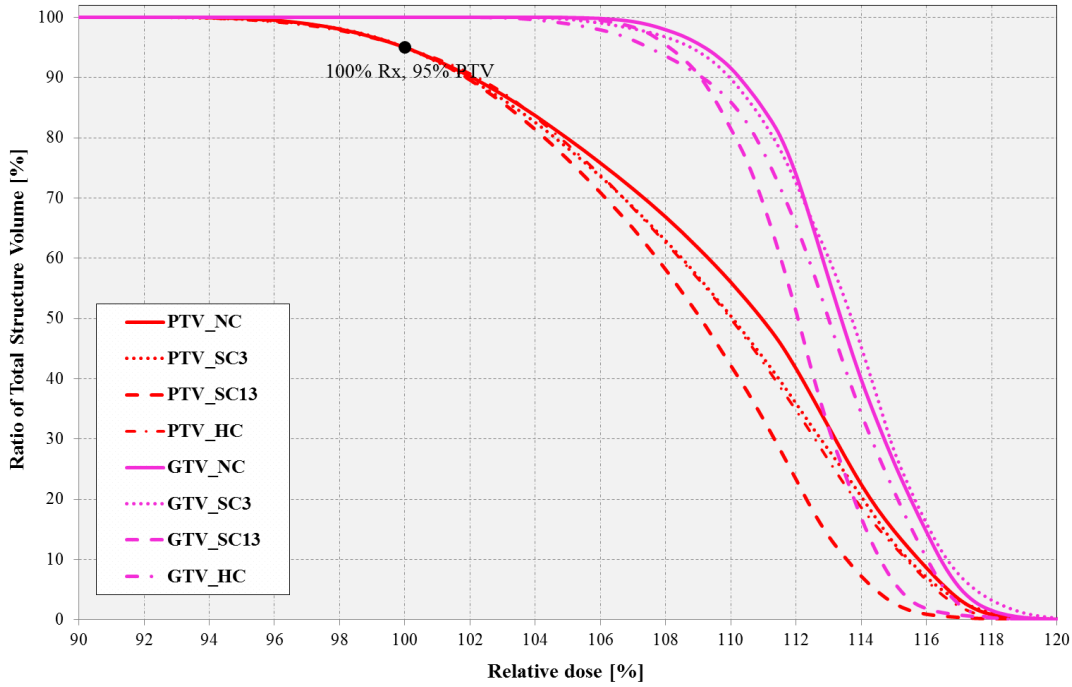

(b)

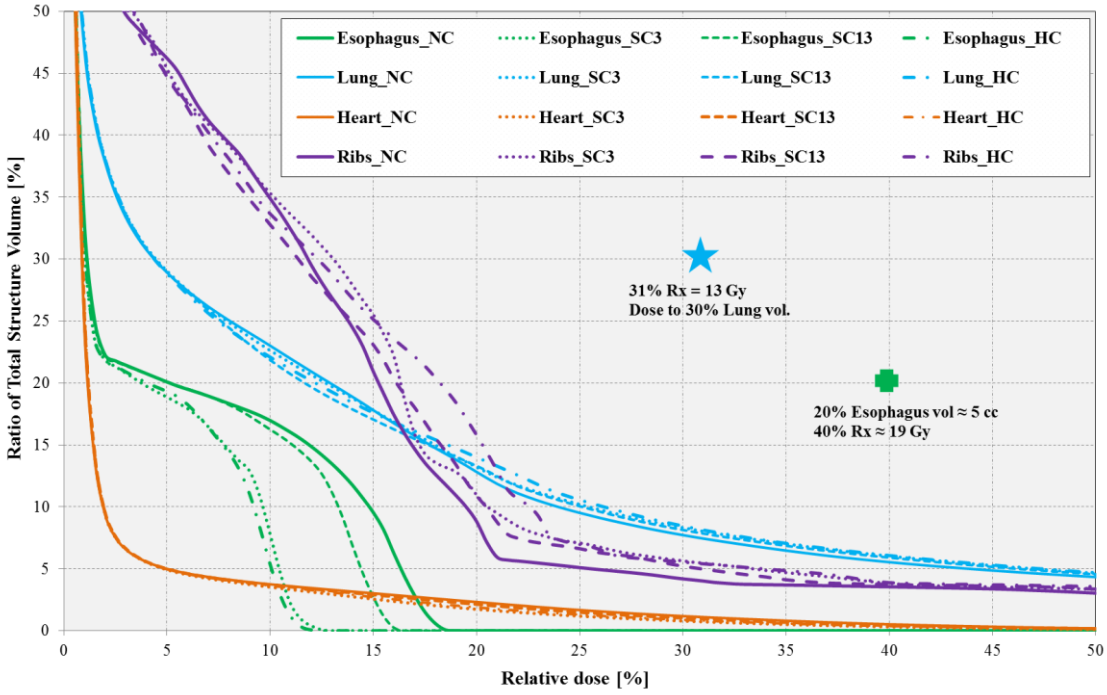

Figure 4-7: DVH comparison for (a) targets (ITV [pink]; PTV [red]) and (b) OARs (Esophagus [green]; Lung [blue]; Heart [orange]; Ribs [purple]) between *MonArc*-based non-constrained (NC), soft-constrained (SC) and hard-constrained (HC) VMAT plans on lung SBRT patient. Highlights (circle, diamond, triangle, star, heart) represent labeled target and OAR-specific dose-quality thresholds.

4.4.3 Marker-based constrained optimization on prostate patient

Figure 4-8 shows the DVH comparison between the non-constrained clinical and *MonArc*-based patient prostate VMAT plans. As can be observed in this case, the *MonArc*-based plan is nearly the same in terms of dose conformity to the target. Similarly, both plans passed the established site-specific clinical dose tolerances for the target and OARs.

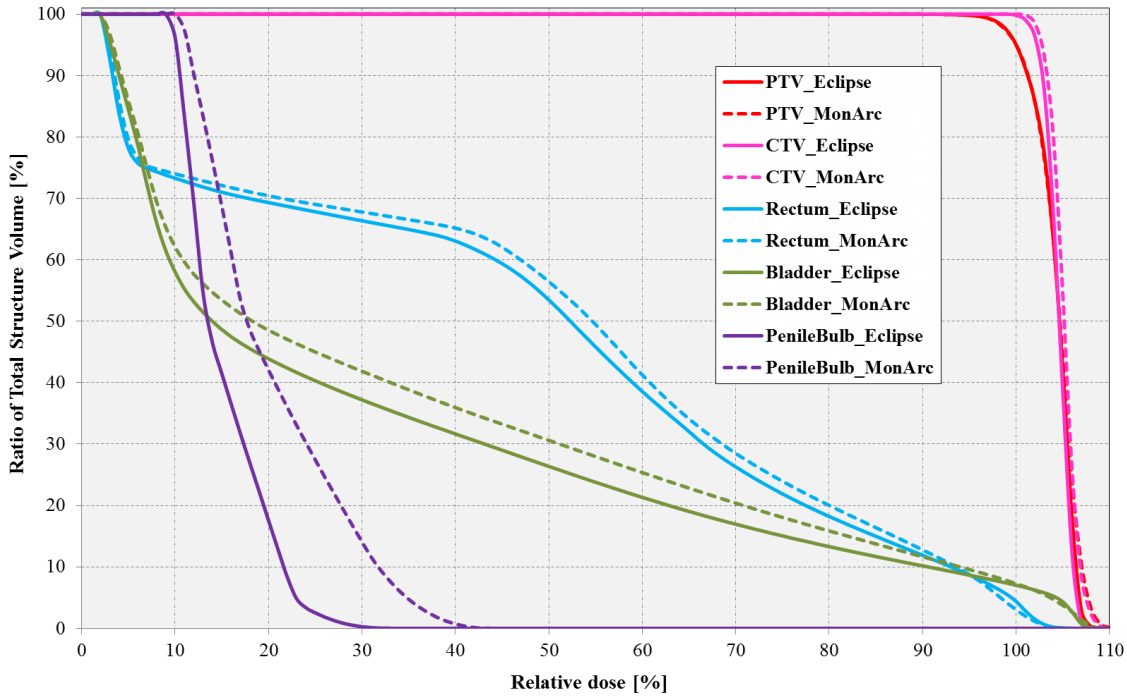

Figure 4-8: DVH comparison between Eclipse-based and *MonArc*-based VMAT plans for the target structures (CTV [pink]; PTV [red]) and OARs (Bladder [green]; Rectum [blue]; Penile Bulb [purple]) on the prostate patient. Both plans are non-constrained on the markers.

Figure 4-9(a) shows the target's zoomed-in DVH plots for the *MonArc*-based NC, HC and SC VMAT plans, respectively. As can be seen, the NC plan offered the best optimal dose coverage for the PTV target. For the SC plans, SC1 (i.e. inferior marker) plan provided the most optimal dose-volume coverage while SC13 (i.e. inferior + superior marker) plan produced the least optimal

dose coverage along with the HC plan. However, all the plans produced dosimetrically acceptable coverage and conformity for the PTV target as defined by local clinical standards.

For the rectum OAR [see Figure 4-9(b) and Table 4-9], all constrained plans met the clinical dose threshold V74Gy < 3cc (i.e. rectal volume receiving 74Gy dose is less than $3cm^3$), including the NC plan safe for the SC13 plan which exceeded the value by 3%. For the bladder OAR, all plans were under the required value of 25% for bladder volume receiving 65Gy (i.e. V65Gy < 25% Rx). For the other OARs (bladder, head-of-femur and penile bulb), all plans also met the clinical dose threshold requirements, except for SC13 plan's rectal coverage [see Figure 4-9(b)].

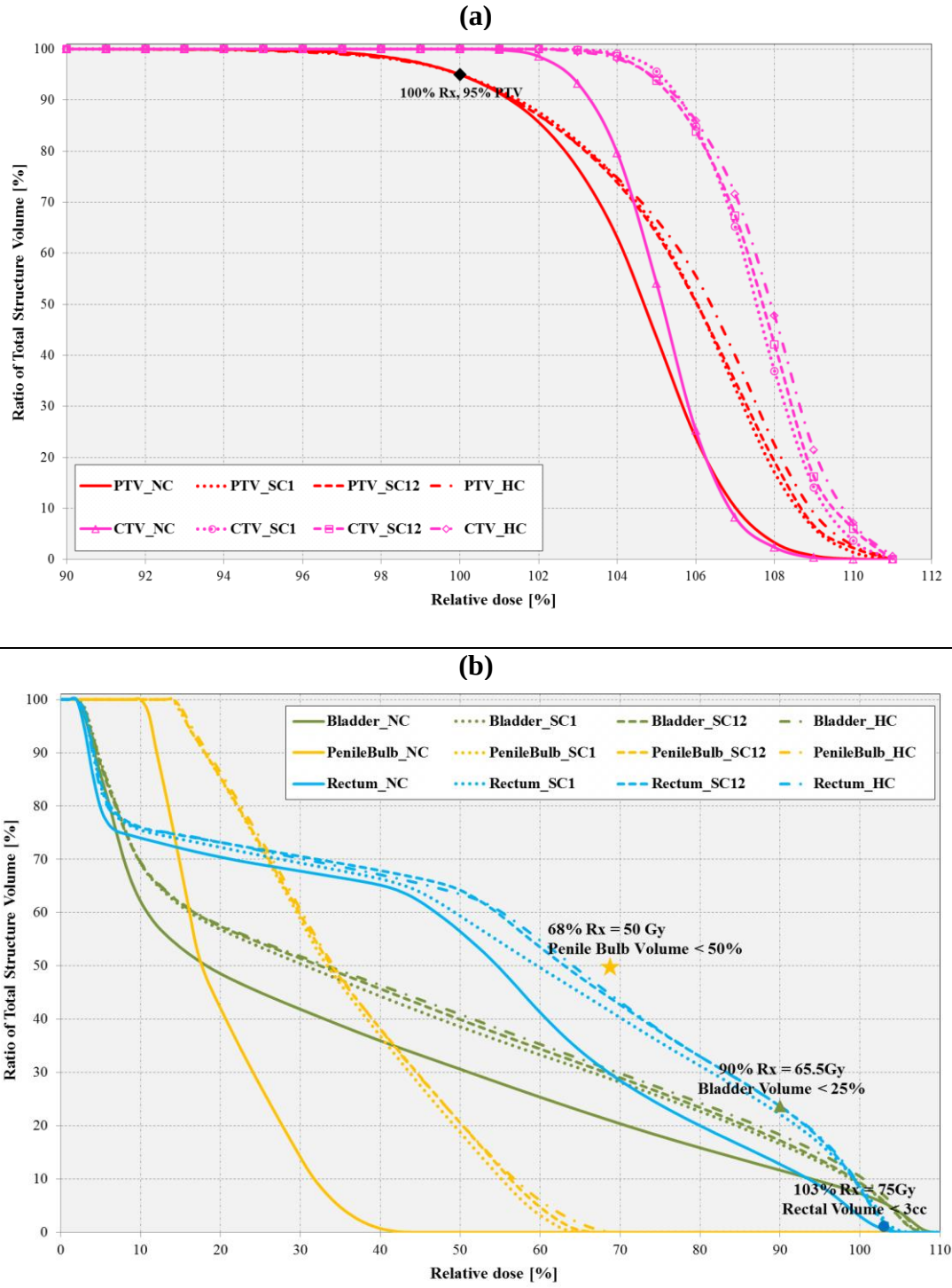

Figure 4-9: DVH comparison for (a) targets (CTV [pink] and PTV [red]) and (b) OARs (Bladder [green], Penile Bulb [yellow] and Rectum [blue]) between *MonArc*-based non-constrained (NC), Soft-constrained (SC) and Hard-constrained (HC) VMAT plans on sample prostate patient. Markers (circle, triangle, star) represent labeled OAR-specific dose-quality thresholds.

4.4.4 Marker visibility and trackability metric on thorax phantom

Figure 4-10 presents the MLC BEV apertures at a selected control point for the NC, HC and SC VMAT plans for the dynamic thorax phantom, respectively. As observed, the fiducial markers can be fully visible at all available control points (CP) based on the specific constrained plan. Also, Table 4-4 shows the trackability metric for the markers visible at all VMAT gantry arc control points in the dynamic thorax phantom. For the non-constrained (NC) plan, all three markers were visible in the BEV in only 20% of the total control points available in the gantry rotation; while only two markers were visible in 48.6%, only one visible in 26.1% and no markers visible in 5.3% of the available gantry control points, respectively. It can be observed that for the single marker-based constrained plans – whereby only one specified marker is required to be fully visible (i.e. SC_I) – all three markers can be visible in 48%–93% of the MLC apertures. For the double marker-based constrained plan, whereby two specified markers are required to be visible (i.e. SC_{II}), all three markers are visible in 61%–97% of the apertures. This implies that as the number of trackable markers increases, more BEV MLC apertures for the soft-constrained (SC) plans approach the hard-constrained (HC) plan optimization requirements, depending on the location of the marker.

Table 4-4: Marker visibility and trackability metric for dynamic thorax phantom on all VMAT optimized plans (i.e. NC, SC and HC) showing the percentage gantry control points whereby the fiducial markers were: all fully trackable, at least two trackable, and at least one trackable in BEV.

Constrained plans	% CP with all three markers in BEV	% CP with only two markers in BEV	% CP with only one marker in BEV	% CP with no marker in BEV	% CP with marker 1 in BEV	% CP with marker 2 in BEV	% CP with marker 3 in BEV
SC1 (Inf)	48.2	37.8	14.0	NA	100	31.7	6.1
SC2 (Mid)	50.4	43.0	6.6	NA	34.3	100	8.7
SC3 (Sup)	92.9	7.1	-	NA	7.0	0.1	100
SC12 (Inf+Mid)	61.3	38.7	NA	NA	100	100	61.3
SC13 (Inf+Sup)	90.9	9.1	NA	NA	100	90.9	100
SC23 (Mid+Sup)	97.0	3.0	NA	NA	97.0	100	100
HC	100.0	NA	NA	NA	100	100	100
Reference/non-constrained plan	% CP with all three markers in BEV	% CP with only two markers in BEV	% CP with only one marker in BEV	% CP with no marker in BEV	% CP with marker 1 in BEV	% CP with marker 2 in BEV	% CP with marker 3 in BEV
NC	20.0	48.6	26.1	5.3	51.6	48.6	23.1

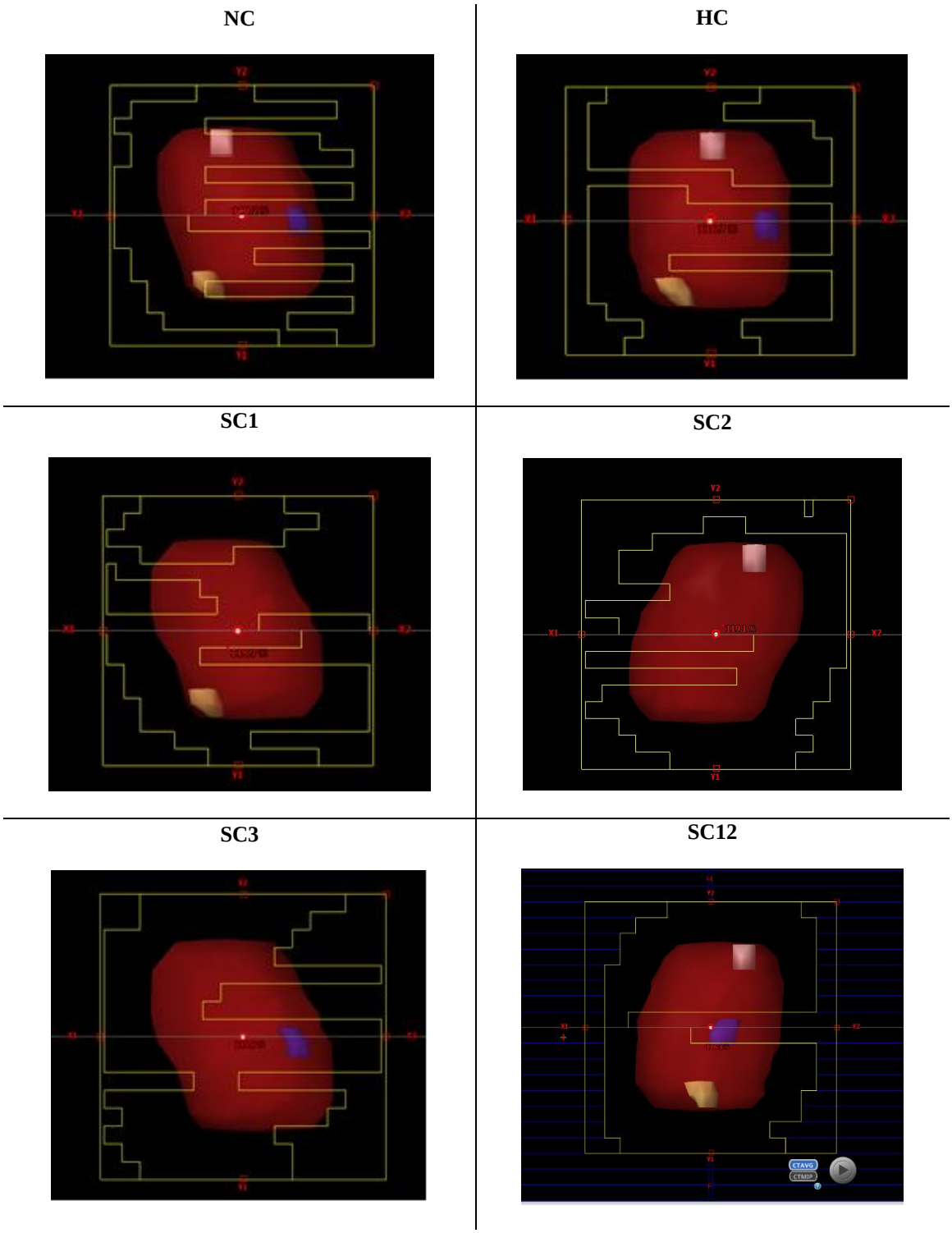

Figure 4-10: Example BEV MLC apertures for different gantry control points in VMAT plans for the dynamic thorax phantom, with the constrained fiducial markers (blue, pink and yellow) visible in the PTV volume (red). [SC1 = soft-constrained plan for marker 1; SC12 = soft-constrained plan for marker 1 and 2].

4.4.5 Marker visibility and trackability metric on lung SBRT patient

Figure 4-11 presents the MLC BEV apertures for the NC, HC and SC VMAT plans for the lung SBRT patient. Similarly, Table 4-5 shows values for the percentage number of markers visible at all VMAT gantry arc control points in the lung patient. For the non-constrained (NC) plan, all three markers were visible and trackable in 15.2% of the total gantry control points; only two markers are trackable in 30.4%; only one trackable in 33.5% and no markers trackable in 20.9% of the control points. For the single marker-based constrained plans – whereby only one specified marker is required to be seen during the optimization (i.e. SC_I) – all three markers are trackable in 39.1% – 45.7% of the MLC apertures. For SC_{II} plans, all three markers are trackable in 57.4% – 88.3% of the MLC apertures. Thus, as the number of constrained marker visibility requirement increases, more BEV MLC apertures for SC plans approach the HC plan optimization requirements, depending on marker location.

Table 4-5: Marker trackability metric for the lung SBRT patient on all VMAT optimized plans (i.e. NC, SC and HC) showing the percentage gantry control points whereby the fiducial markers were: all fully trackable, at least two trackable, and at least one trackable in BEV.

Constrained plans	% CP with all three markers in BEV	% CP with only two markers in BEV	% CP with only one marker in BEV	% CP with no marker in BEV	% CP with marker 1 in BEV	% CP with marker 2 in BEV	% CP with marker 3 in BEV
SC1 (Inf)	39.1	43.5	17.4	NA	100	60.9	60.9
SC2 (Mid)	45.7	48.2	6.1	NA	85.2	100	54.4
SC3 (Sup)	45.2	36.5	18.3	NA	73.5	53.5	100
SC12 (Inf+Mid)	57.4	42.6	NA	NA	100	100	57.4
SC13 (Inf+Sup)	67.8	32.2	NA	NA	100	67.8	100
SC23 (Mid+Sup)	88.3	11.7	NA	NA	88.3	100	100
HC (Inf+Mid+Sup)	100	NA	NA	NA	100	100	100
Reference/non-constrained plan	% CP with all three markers in BEV	% CP with only two markers in BEV	% CP with only one marker in BEV	% CP with no marker in BEV	% CP with marker 1 in BEV	% CP with marker 2 in BEV	% CP with marker 3 in BEV
NC	15.2	30.4	33.5	20.9	41.3	42.6	51.7

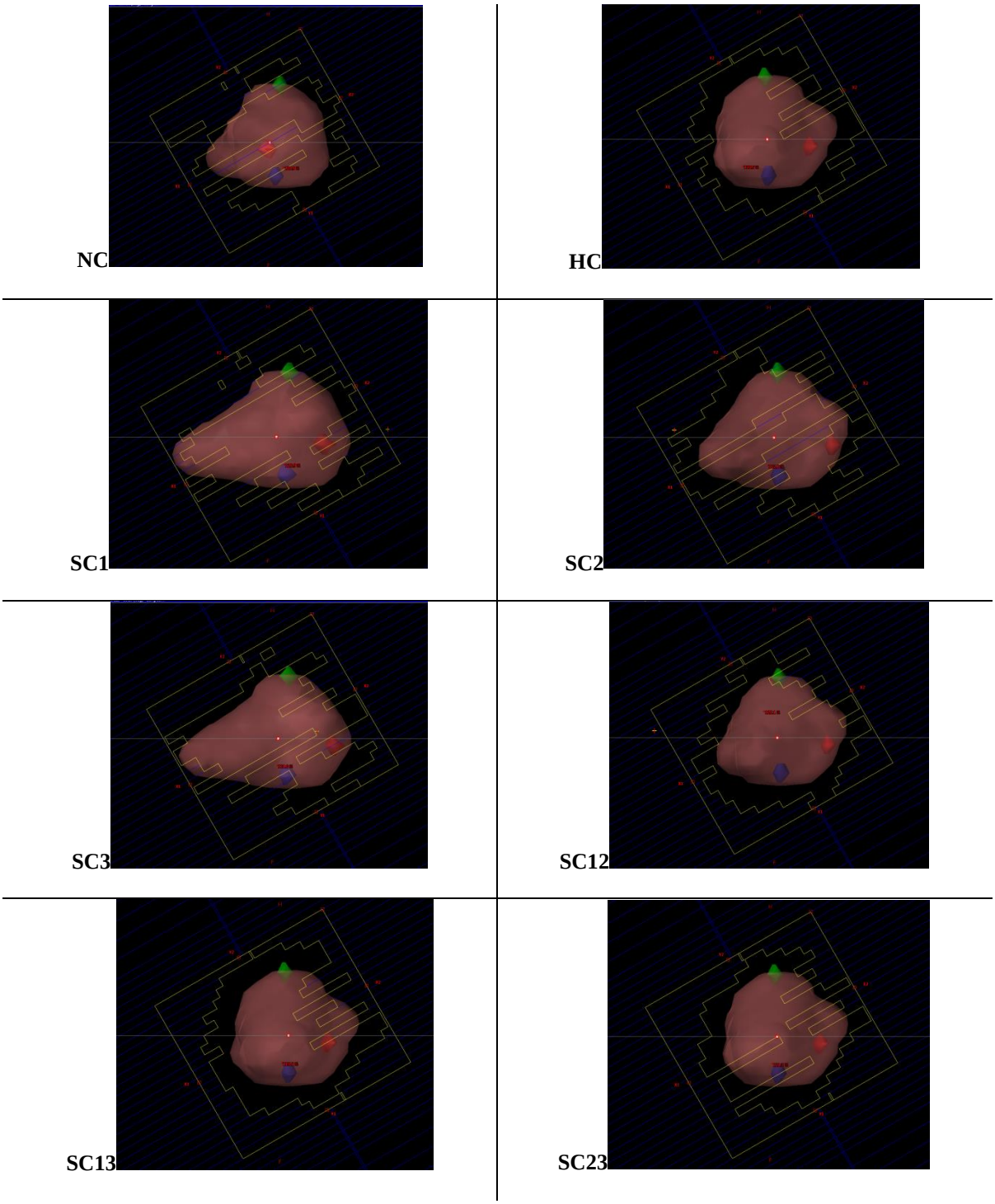

Figure 4-11: Example beams-eye-view (BEV) MLC aperture at different gantry control points in non-constrained (NC) and constrained (HC and SC) VMAT plans for the lung SBRT patient, with the PTV and fiducial markers (Inferior-blue [1]; Middle-red [2]; Superior-green [3]) either blocked and/or fully-visible by the MLCs.

4.4.6 Marker visibility and trackability metric on prostate patient

Figure 4-12 presents an example MLC BEV aperture at different gantry arc control points for the *MonArc*-based NC, HC and SC VMAT plans in the prostate patient, respectively. For the trackability metric, Table 4-6 shows values for the percentage of the markers trackable at all VMAT gantry arc control points in the sample prostate patient. For the NC plan, all three markers are trackable in 27.3% of the gantry control points; while only two markers are trackable in 30.2%, only one trackable in 20.4% and no markers trackable in 22.1% of the BEV gantry control points.

Table 4-6: Marker visibility and trackability metric for the prostate patient for all VMAT optimized plans (i.e. NC, SC and HC) showing the percentage gantry control points (CP) in which fiducial markers were: all fully trackable, at least two trackable, and at least one trackable in BEV

Constrained plans	% CP with all three markers in BEV	% CP with only two markers in BEV	% CP with only one marker in BEV	% CP with no marker in BEV	% CP with marker 1 in BEV	% CP with marker 2 in BEV	% CP with marker 3 in BEV
SC1	81.0	15.6	3.4	NA	100	7.0	8.6
SC2	75.7	17.9	6.4	NA	3.4	100	14.5
SC3	79.9	18.4	1.7	NA	6.7	11.7	100
SC12	96.3	3.7	NA	NA	100	100	96.3
SC13	94.4	5.6	NA	NA	100	94.4	100
SC23	90.8	9.2	NA	NA	90.8	100	100
HC	100.0	NA	NA	NA	100	100	100
Reference/non-constrained plan	% CP with all three markers in BEV	% CP with only two markers in BEV	% CP with only one marker in BEV	% CP with no marker in BEV	% CP with marker 1 in BEV	% CP with marker 2 in BEV	% CP with marker 3 in BEV
NC	27.3	30.2	20.4	22.1	49.7	55.3	57.8

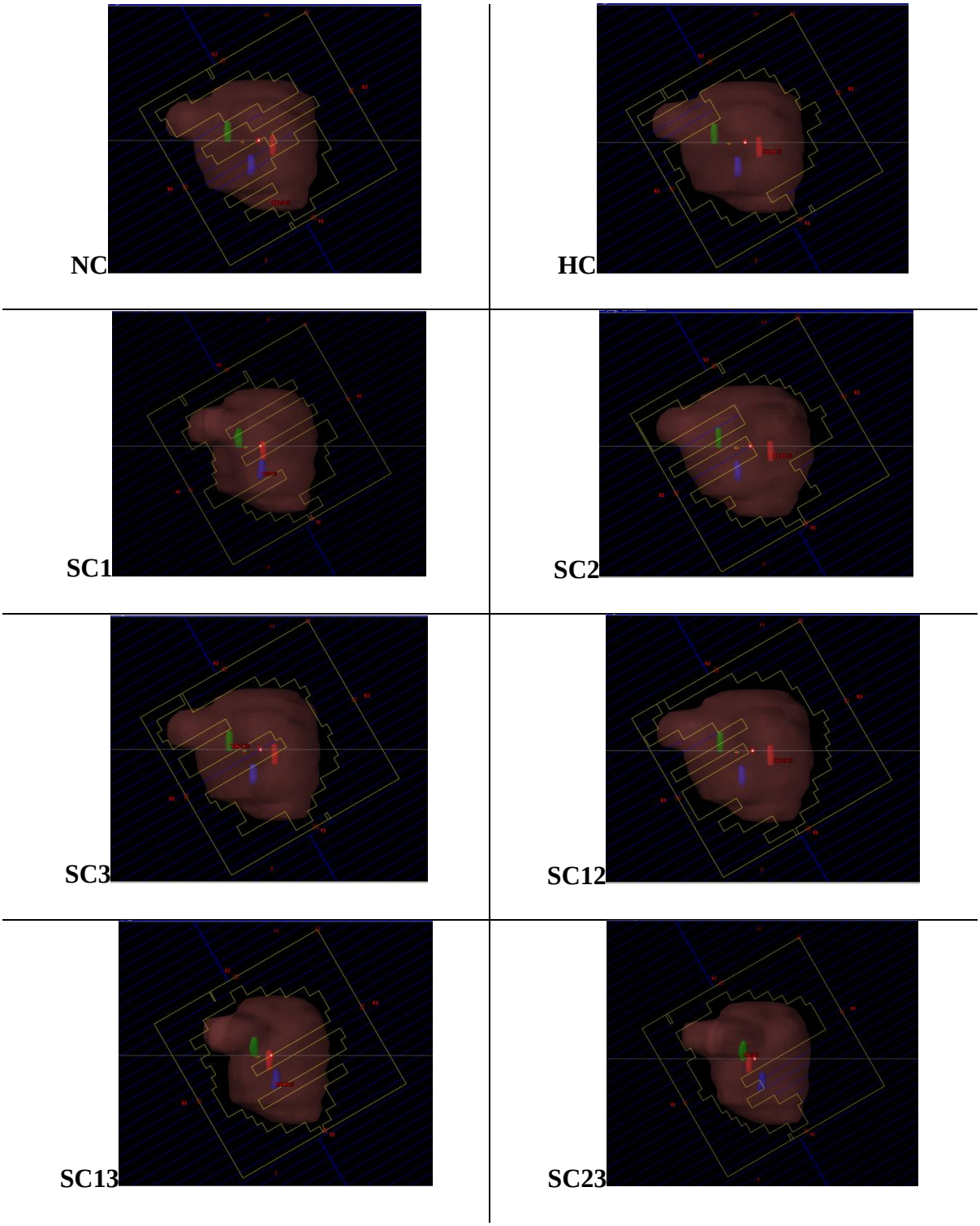

Figure 4-12: Example MLC beams-eye-view (BEV) aperture at different gantry control points in non-constrained (NC) and constrained (HC and SC) VMAT plans for the prostate patient, with PTV and fiducial markers (1-blue, 2-red and 3-green) either blocked and/or fully-visualized by the MLCs.

4.4.7 Plan comparison and dose-quality metrics

Table 4-7 shows the quantitative dose quality metrics (i.e. CI, HI, GM etc.) for all the lung VMAT plans on the dynamic thorax phantom for the NC, HC and SC plans. The lowest CI value of 1.52 belongs to the NC plan, followed by the HC plan with 1.55 CI value. This implies that the NC plan produced the best conformal plan. Using the Gradient Measure (GM), the NC plan produced the best dose falloff slope with a 1.20 GM value, followed by SC3 (1.25 GM) and SC23 (1.25 GM) plans while the HC plan (1.28 GM) produced the worst gradient value. Similar results were obtained using the HI values. Using the average index, the NC plan produced the lowest value and thus best plan, followed closely by the HC plan.

For the OAR spinal cord, the largest mean dose value was produced by the SC_I=SC2 plan, while the lowest mean dose to the spinal cord was produced by the NC plan. The difference between the mean dose values in the spinal cord was up to 35%. For the OAR vertebral body, similar results were obtained as the largest result was produced by the SC_I = SC2 plan, while the lowest mean dose value was produced by the NC plan, a 28% difference. Finally, the mean dose to the lung OAR was lowest with the NC plan, highest with the SC3 plan but only a 5% difference. The beam output monitor units were highest with the NC plan, whereby the NC plan produced the highest output (1098 MU), while the HC plan produced the lowest output (947 MU).

Table 4-7: Quality metrics for *MonArc*-based optimized VMAT plans on the dynamic thorax phantom using: no constraints (NC), hard constraints (HC) and soft constraints (SC). Thus, SC3 = soft-constrained plan for marker 3; SC12 = soft-constrained plan for markers 1 and 2, etc.

Metrics	SC1	SC2	SC3	SC12	SC13	SC23	HC	NC
PTV Conformity Index	1.72	1.71	1.69	1.64	1.62	1.66	1.55	1.52
PTV Homogeneity Index	1.18	1.18	1.19	1.16	1.18	1.18	1.17	1.19
PTV Gradient Measure [cm]	1.27	1.26	1.25	1.26	1.27	1.25	1.28	1.20
PTV average index = (CI+HI)/2	1.45	1.44	1.44	1.40	1.40	1.42	1.36	1.35
$D_{99\%}$ > 95% of Rx dose [%]	97.83	97.40	97.70	97.83	98.13	97.30	97.83	97.87
PTV, D_{mean} [%]	107.63	108.40	106.77	106.78	105.65	106.60	105.50	107.50
OAR Spinal cord, D_{mean} [%]	7.70	7.17	8.63	8.33	8.30	9.20	8.33	9.67
OAR Vertebral body, D_{mean} [%]	3.83	3.47	4.13	3.87	3.93	4.40	4.03	4.47
OAR Lungs, D_{mean} [%]	9.17	9.23	9.47	9.20	9.37	9.37	9.33	9.03
Beam Output [MU]	1075	1075	972	1019	961	958	947	1098

In similar manner, Table 4-8 shows the quantitative dose quality metrics (i.e. CI, HI and GM) for all the investigated plans on the lung SBRT patient. The lowest CI value belongs to the NC plan (CI = 1.24), followed by the SC3 plan (CI = 1.25) and SC13 plan (CI = 1.28). This implies that the NC plan produced the best conformal plan. Using the Gradient Measure (GM), however the SC1 plan produced the best dose falloff slope with a 1.35 GM value, followed by NC (GM = 1.38) and SC12 (GM = 1.38) plans while the HC plan (GM = 1.44) produced the worst gradient value. Similar results were obtained using the HI values. Using the average of the index values, the NC plan produced the best conformal and homogenous plan. The beam output monitor units (MU) were highest with the NC plan, whereby the NC plan produced the highest output of 1181 MU, while the SC13 plan produced the lowest output of 1121 MU.

Similarly, Table 4-9 details the quantitative dose quality metrics for the prostate VMAT plan on the prostate patient with the visibility constraints: NC, HC and SC. The lowest CI value of 1.04 belongs to the NC plan, followed by SC2 and SC3 plans (CI = 1.13) while HC plan had the worst CI value of 1.20. Similarly, the GM values were also lowest with the NC plan, while the HI values were lowest with the SC12 plan. However, using the average index, the NC plan still showed the lowest value, followed by the SC2 plan and the lowest with the HC plan. This shows that the NC plan produced the most optimal conformity, dose fall-off slope and homogeneity. In terms of the treatment beam output in MU, the HC plan produced the lowest beam output value of 470 MU, while the NC plan produced the highest beam output at 613 MU.

Table 4-8: Quality metrics for *MonArc*-based optimized VMAT plans on the lung SBRT patient using: no constraints (NC), hard constraints (HC) and soft constraints (SC). Thus, SC1 = soft-constrained plan for marker 1; SC23 = soft-constrained plan for markers 2 and 3, etc.

Metrics	**SC1**	**SC2**	**SC3**	**SC12**	**SC13**	**SC23**	**HC**	**NC**
PTV Conformity Index	1.36	1.29	1.25	1.33	1.28	1.30	1.30	1.25
PTV Homogeneity Index	1.09	1.11	1.11	1.09	1.10	1.11	1.10	1.10
PTV average index = (CI+HI)/2	1.23	1.20	1.18	1.21	1.19	1.21	1.20	1.17
PTV Gradient Measure [cm]	1.35	1.38	1.43	1.38	1.39	1.43	1.44	1.41
$D_{99\%}$ > 95% of Rx dose [%]	97.0	97.0	96.8	96.5	96.8	97.2	96.4	96.9
PTV D_{mean} [%]	110.1	109.8	109.3	109.5	108.3	109.3	109.3	109.8
OAR Lungs, D30% < 13Gy [Gy]	2.19	2.20	2.14	2.21	2.12	2.06	2.10	2.10
OAR Esophagus, V18 < 5 cc [cm^3]	0	0	0	0	0	0	0	0
OAR Ribs, V32 < 1 cc [cm^3]	0.58	0.57	0.54	0.58	0.59	0.58	0.56	0.56
OAR Heart, V28 < 15 cc [cm^3]	0.34	0.32	0.21	0.31	0.37	0.42	0.31	0.42
Beam Output [MU]	1181	1138	1148	1151	1121	1142	1160	1181

Table 4-9: Quality metrics for *MonArc*-based optimized VMAT plans on the prostate patient using: no constraints (NC), hard constraints (HC) and soft constraints (SC). Thus, SC2 =soft-constrained plan for marker 2, SC13 = soft-constrained plan for markers 1 and 3, etc.

Metrics	**SC1**	**SC2**	**SC3**	**SC12**	**SC13**	**SC23**	**HC**	**NC**
PTV Conformity Index	1.13	1.13	1.16	1.16	1.18	1.18	1.20	1.04
PTV Homogeneity Index	1.08	1.09	1.11	1.07	1.06	1.07	1.06	1.08
PTV average index = (CI+HI)/2	1.11	1.11	1.13	1.12	1.12	1.13	1.13	1.06
PTV Gradient Measure [cm]	1.89	1.92	1.97	1.94	1.94	1.91	2.03	1.79
$D_{99\%}$ > 95% of Rx dose [%]	98.0	97.5	97.8	97.9	97.5	97.5	97.7	97.5
PTV D_{mean} [%]	104.7	104.7	104.9	104.8	105.3	105.0	105.4	104.0
OAR Bladder, V65 < 25% Rx [%]	14.26	14.80	15.13	15.27	14.99	15.66	15.75	11.99
OAR Rectum, V74 < 3cc [cm^3]	1.88	2.06	2.45	2.42	2.91	3.10	2.31	1.35
OAR Penile Bulb, D_{mean} < 50Gy [Gy]	16.09	15.91	15.83	16.19	15.78	16.36	16.33	13.67
Beam Output [MU]	499.6	491.3	502.9	477.7	478.5	480.9	470.2	613.4

4.5 Summary and Discussion

The best dosimetric target coverage for the PTV in the dynamic thorax phantom − as indicated by the DVH plots [see Figure 4-5(a)] and dose-quality metrics such as $D_{99\%}$, conformity index (CI), homogeneity index (HI) and gradient measure (GM) − was produced by the non-constrained (NC) plan, followed by the hard-constrained (HC) and soft-constrained (SC) plans [Table 4-7]. Since no singular quantitative metric is adequate to describe the best plan, an average of HI and CI was deemed appropriate. Using this average, the NC plan still provided the best quantitative metric score. Hence, it can be deduced that the NC plan produced the most dosimetrically optimal plan for the thorax phantom. This is expected as the NC plan has no marker visibility constraints in its implementation.

The difference in the metrics between HC and SC plans were not significant. However, we did not anticipate the HC plan to produce better or similar results compared to SC plan as the HC plans are constrained such that the markers are fully visible at all gantry angles in the beam's eye view, thereby forcing larger MLC fields. Furthermore, the beam output monitor units (MU) were highest with the NC plan. This is expected as there are no fiducial marker visibility constraints in the optimization process for NC plans, so the MLC aperture is more highly modulated to achieve the dose objectives. Alternatively, both the SC13 and HC plans are constrained to see at least two markers, making the beam less modulated as the MLCs are required to be open to visualize two markers.

OAR dosimetry results for the thorax phantom [see Figure 4-5(b)] do not clearly follow the pattern observed for targets, with the SC_I plan outperforming the HC and NC plans. For the spinal cord, the mean dose was between 8.3% − 9.7% across all plans, while for the vertebrae the mean dose was between 3.5% − 4.5%. For the lung critical structure, the mean dose across all

investigated plans was between 9.0% − 9.5%, with no noticeable over or under-dosage for all investigated plans. The discrepancy in target and OAR results for the phantom may be due to the very simple geometry of the phantom, and position of the simulated fiducial markers. However, these preliminary results demonstrate that visibility constraints may be included in plan optimization.

In terms of the trackability metric for the phantom, tracking of the markers is potentially feasible in at least 20% of the gantry angles in the reference clinical lung VMAT plan. For the soft-constrained (SC) plans in the thorax phantom, all three markers are trackable between 48% − 97% of the available gantry arc rotation depending on marker location, and 100% for hard-constrained plans. The SC plans show increased coverage as the constrained markers increased from one specific marker (SC_I = SC1, SC2 or SC3) to two specific markers (SC_{II} = SC12, SC13 or SC23). This shows that as the plans are constrained to visualize more than one marker, the MLCs open to accommodate the specified markers such that more or all inserted/implanted markers are in the BEV. Thus, the wider aperture fields due to the required MLC openings and the accompanying plans are inversely proportional to the beam modulation, resulting in less beam output (MU).

For the VMAT lung SBRT patient dataset, the best dosimetric target coverage [Figure 4-7(a)] for the PTV as indicated by the quality metrics was produced by the SC13 and NC plans. The worst coverage was provided by the SC23 and HC plans. However, there was no significant disparity in target coverage amongst all plans. OAR dosimetry results for the lung patient [Figure 4-7(b)] shows that all plans consistently met the clinical dose objectives. However, some SC_I plans (e.g. SC3 plan for the Superior marker) outperformed the NC plan, exposing the heart OAR to up

to 50% less dose relative to the reference NC plan. In terms of the beam output, the NC plan also produced the highest output as measured in MU, as was observed in the phantom.

In terms of the trackability metric for the lung SBRT patient, trackability of all the markers is feasible in at least 15.2% of the gantry rotation in the reference non-constrained lung VMAT plan, while none of the fiducial would be available for tracking in at least 20.9% of the treatment delivery time. However, for the soft-constrained plans in the lung patient, all three markers were trackable between 39% − 88% of the available gantry arc rotation. The SC plans also exhibited increased coverage as the constrained markers visualized improved from one (SC_I = SC1, SC2 or SC3) to two specific markers (SC_{II} = SC12, SC13 or SC23). This also shows soft-constrained plans approach the hard-constrained plan as more markers are included in the optimization and the MLCs open to accommodate the specified markers.

For the VMAT prostate patient dataset, the best dosimetric target coverage [Figure 4-9(a)] for the PTV as indicated by the dose-quality metrics [Table 4-9] was produced by the non-constrained (NC) plan. All other constrained plans (SC and HC) had similar metrics with no significant disparity in target coverage. OAR dosimetry results for the prostate patient [Figure 4-9(b)] shows that all plans consistently met the clinical dose objectives, except for the rectal threshold for SC23 plan. In general, the bladder, rectal and penile bulb dose objectives were met by all the plans. Nevertheless, some SC plans slightly outperform the HC plans, but they all expose the OARs to up to 4% more dose relative to the reference NC plan.

Similarly, trackability of all the markers is feasible in at least 27% of the gantry rotation for the non-constrained plan, while none of the fiducial would be available for tracking in at least 22% of the treatment delivery time. However, in the soft-constrained prostate plans, all three markers were trackable between 75% − 96% of the available gantry arc rotation. The SC plans

also exhibited increased coverage as the constrained markers visualized improved from one (SC_I) to two specific markers (SC_{II}). This also shows soft-constrained plans approach the hard-constrained plan as more markers are included in the optimization and the MLCs open to accommodate the specified markers.

The approach presented by Azcona *et al*[39] to predict the marker positions for prostate patients, where markers are unavailable or blocked by the MLCs, can be useful in addressing some of the shortcomings for clinical VMAT. However, it requires image filtering and template selection that needs to be small enough to allow real-time processing. The authors point out that the technique will also suffer from sparse data and long successive control points where markers are unavailable. As detailed in the literature, the motion of the tumour needs to be accounted for during the imaging, planning, and treatment delivery stage such that a temporal component can be included in four-dimensional 4D radiotherapy[93]. Methods to obtain 4D radiotherapy can be either via moving a robotic gantry to adjust the radiation beam position with the tumour position, or alternatively by dynamic MLC motion adjustments, or by moving the patient via couch motion[38,93]. However, to perform real-time tumour tracking robustly, the visibility of fiducial markers in the small and irregularly shaped fields found in arc radiotherapy (such as 4D-VMAT) needs to be assured.

A limitation of our work is that we have not studied the effects of the residual motion between the tumour and the healthy tissues when respiration is accounted for (i.e. this feasibility study is not performed in 4D). However, our work could be modified to account for the marker motion relative to the motion of the OARs whereby the control points in the gantry is synchronized to the target motion phases as available in the 4D-CT. A 4D-VMAT implementation introduced by Chin *et al*[162,173], could be modified to account for the marker motion relative to the motion of

the OARs. A future goal of our research includes such an implementation. Another limitation is in the rigid manner of constrained optimization implemented. We could potentially account for additional variations of the soft-constrained implementation for non-specific markers whereby any one or two markers can be constrained into the BEV, as opposed to the same one or two markers throughout the entire VMAT arc. However, for the purposes of tracking, typically a specific marker needs to be visible throughout the VMAT delivery for robustness.

We have shown the feasibility of adding marker visibility parameters into the optimization objective function, successfully combining them together with standard dose objectives. The current work can be extended to a more diverse clinical patient datasets as investigated in 0. It can also be extended to investigate the marker-based constrained optimization for 4D-VMAT (see Section 6.3.2). There is also interest in real-time tumour tracking without markers (i.e. markerless tracking methods), and those strategies also have visibility requirements of the target. Our proposed approach could also be similarly applicable to markerless tracking methods when incorporated into the optimization.

Chapter 5 Constrained optimization for marker-based tumour tracking in VMAT

In this chapter, we completed a retrospective study of the marker-based optimization approach that was introduced in Chapter 4 on clinical VMAT plans at disease sites with differing motion characteristics. Specifically, we studied using lung, liver and prostate sites treated with SBRT or hypo-fractionated treatment delivery. These disease sites were chosen for validation of the modified planning process since they are the most frequently studied in combination with real-time tracking algorithms. Therefore, this allows us to evaluate how the constrained marker-based optimization will affect the dosimetric objectives on well-established tumour sites and help quantify any tradeoffs between marker visibility and plan quality. The results of this study were submitted and published in the Biomedical Physics and Engineering Express journal[**].

5.1 Introduction

Prostate and lung tumours are two of the most common cancers amongst men in Canada. In a study of prostate motion in supine and prone positions[174], it was reported that clear patterns of respiratory motion were seen in the prone patients due to the influence of increased abdominal motion. Averaged over all prone patients, the prostate was displaced > 3mm and > 5mm for 37.8% and 10.1% of the total beam delivery time, respectively. In the supine position, the prostate was displaced > 3mm and > 5mm for 12.6% and 2.9% of the total beam delivery time, respectively. In general, prostate displacement and motion patterns are different from other disease sites.

[**] Constrained optimization towards marker-based tumor tracking in VMAT. Azeez Omotayo *et al* 2021 *Biomed. Phys. Eng. Express* **7** 015011

Stereotactic body radiation therapy (SBRT) has become increasingly used for palliative treatment of patients with metastatic disease and a curative modality for primary sites such as early stage lung cancer, hepatocellular carcinoma, and early stage prostate cancer[175]. However, to reduce the risk of treatment-related toxicity, it is important to reduce excess dose that may affect adjacent normal tissues in SBRT. Timmerman *et al*[176] reported in a Phase I trial for medically-inoperable NSCLC that no treatment failures were observed in patients treated at 18Gy per fractions. They conducted a follow-up Phase II trial[176] evaluating doses of 20–22 Gy per fraction, with local control rates at 2 years up to 95%. However, they reported that treatment of centrally located tumors was associated with severe rates of toxicity (Grade 3-5).

Similarly, for treatment of targets in the liver, motion will often be large because it is coupled to diaphragm motion, and therefore motion management is important. For treatment of moving lung targets, the low-density lung tissue surrounding the target results in a larger dosimetric margin which itself helps account for the respiratory motion; however, this is not the case for liver treatment where the liver is roughly water equivalent. Respiratory management is therefore even more important for liver than for lung radiotherapy[66].

SBRT application for liver cancer is technically challenging[177] as liver tissue has poor soft-tissue contrast and visibility, and thus hard to distinguish from normal liver using x-ray imaging. Also, the radiation tolerance of surrounding normal liver tissue is very low. Thus, the accurate and precise target localization methods which minimize margin sizes are essential in liver SBRT. Nankali *et al*[178] compared the geometric and dosimetric accuracy of SBRT treatments for 15 patients with liver tumors using four motion management strategies: respiratory gating, MLC-based tracking, inter-field couch correction and no motion compensation. The patients received marker-guided respiratory gated IMRT or conformal treatments in three fractions with a 3–4 mm

gating window around the full exhale position, while the other three strategies were simulated. The time-resolved target position error during treatments with the four investigated strategies was used to calculate motion margins and the motion-induced reduction in CTV (D_{95}) relative to the planned dose. With 7 mm margins in the cranio-caudal direction, the mean (range) of ΔD_{95} for the CTV was 8.1 (0.6 – 29.4)%-points (no motion compensation), 4.0 (0.4 – 13.3)%-points (couch shift), 1.0 (0.3 – 2.2)%-points (MLC tracking) and 0.8 (0.1 – 1.8)%-points (respiratory gating)[178]. Their work demonstrates that liver SBRT via MLC tracking and respiratory gating can be effective and clinically valuable.

For tumour tracking capabilities, a recent study of six liver SBRT patients showed that MLC tracking via kV x-ray monitoring of implanted gold markers, achieved higher delivered dose coverage (minimum dose to 95% CTV) relative to the planned dose of 0.2% CTV under covered, compared to 6.3% CTV under covered for the case of no tracking[179]. In 0, we demonstrated the feasibility of a modified treatment plan optimization technique that included the visibility of implanted fiducial markers, showing that this information could be included with the conventional dosimetric objectives, to produce plans that satisfied both dosimetric and visibility needs, but had limited clinical examples[180]. For a more robust and clinical-based analysis, in this chapter we extend the application to a group of prostate, liver and lung patients treated with SBRT VMAT and with differing target sizes and variations in OAR geometry to validate our approach.

5.2 Methods and Materials

5.2.1 Patient data selection

For a more detailed clinical analysis, we retrospectively examined five liver, ten prostate and five lung patient datasets respectively, with different tumour sizes and geometric

characteristics. Due to the limited availability of fiducial marker-based treatments at our clinic, we were restricted to validating on a smaller sample size of lung and liver patients. For the five liver patients previously treated with SBRT VMAT, the three fiducial markers were implanted inside or near the PTV. The prescription dose (dose to 100% isodose) for the PTV target was 45–50Gy over three to five fractions using a 6MV stereotactic or flattening filter free (6X-SRS/6X-FFF) beam with two partial arcs and collimators (Arc 1: 45°, Arc 2: 315°), on a TrueBeam linac with HD120 MLCs. For some datasets, not all markers are implanted inside the PTV target, and hence may not be available in the MLC aperture field. For example, one marker was 10 mm away from the PTV. The largest 3D inter-marker distance was 86 mm (patient 3). The five liver datasets had PTV target volumes ranging between 194–380 cc, and OAR structures including kidney (145–228 cc), esophagus (8–40 cc), stomach (58–162 cc), and heart (425–1037 cc). Table 5-1 details the optimization and dose constraints for the liver datasets.

For the ten prostate patients treated with hypofractionated VMAT, the fiducial markers were all implanted inside the PTV. The prescription dose (100 % isodose) to the PTV was 72.8Gy over twenty-eight fractions using a 6MV x-ray beam (6X) with two full arcs on a Trilogy linac with Millennium-120 MLCs. The largest 3D inter-marker distance was 30.4 mm (patient #8). The ten prostate datasets had PTV target volumes ranging between 42–169 cc. Standard OAR structures included the rectum (35–395 cc), bladder (69–540 cc), femoral head (162–236 cc), and penile bulb (0.6–4.9 cc). Table 5-2 details the optimization and dose constraints for the prostate datasets.

For the five lung patients treated with SBRT VMAT, the three fiducial markers were implanted inside or near the PTV. Note that an internal target volume (ITV) approach was used here to contour the targets. The prescription dose (100% isodose) to the PTV was 48Gy over four

fractions with two partial arcs using a 6 MV flattening filter-free x-ray beam (6X-FFF) on a TrueBeam linac with HD-120 MLCs. Similarly, not all markers are implanted inside the PTV target in the lung dataset. The largest 3D inter-marker distance was 61.9 mm (patient p5). The lung datasets had both PTV (27–174 cc) and ITV (9–99 cc) target structures. Standard OAR structure volumes included lung (2110–8138 cc), ribs (27–66 cc), heart (532–919 cc), and chest-wall (277–858 cc). Table 5-3 details the optimization and dose constraints for the lung datasets.

In all patient cases, recall that the contours for the targets, OARs and fiducial markers were available in the Eclipse plan, and exported to *MonArc* for optimization and study of the marker visibility constrained plans.

Table 5-1: Dose-volume plan constraints for VMAT optimization in liver SBRT patients A – E.

Dose constraints			
Targets: Planning Target Volume (PTV); Internal Target Volume (ITV)			
Structures	**Min. Dose vol./ Dose**	**Max. Dose vol./Dose**	**Fractions/Prescribed Dose**
PTV	100%/50Gy	0%/52Gy	5/50Gy
ITV	100%/50Gy	0%/52Gy	5/50Gy
Relevant organs at risk (OARs): Kidney, Esophagus, Large Bowel and Heart • Specific plan/optimization constraints			
OAR (Kidneys)	• 40% volume to receive maximum 9.0Gy • 50% volume to receive maximum 6.5Gy		
OAR (Esophagus)	• 11% volume to receive maximum 61Gy • 0.2% volume to receive maximum 70Gy		
OAR (Large Bowel)	• 50% volume to receive maximum 32Gy		
OAR (Heart)	• 50% volume to receive maximum 30Gy		

Table 5-2: Dose-volume plan constraints for VMAT optimization in prostate patients #1 − #10.

Dose constraints			
Targets: Planning Target Volume (PTV); Clinical Target Volume (CTV)			
Structures	**Min. Dose vol./ Dose**	**Max. Dose vol./Dose**	**Fractions/Prescribed Dose**
PTV	100%/72.8Gy	0%/75Gy	28/72.8Gy
CTV	100%/72.8Gy	0%/75Gy	28/72.8Gy
Relevant organs at risk (OARs): Bladder, Rectum and Penile Bulb • Specific plan/optimization constraints			
OAR (Bladder)	• 50% volume to receive maximum 47Gy • 25% volume to receive maximum 65Gy		
OAR (Rectum)	• 15% volume to receive maximum 68Gy • 50% volume to receive maximum 42Gy		
OAR (Penile Bulb)	• Mean dose: 50Gy		

Table 5-3: Dose-volume plan constraints for VMAT optimization in lung SBRT patients I – V.

Dose constraints			
Targets: Planning Target Volume (PTV); Gross Target Volume (GTV)			
Structures	**Min. Dose vol./ Dose**	**Max. Dose vol./Dose**	**Fractions/Prescribed Dose**
PTV	100%/48Gy	0%/52Gy	4/48Gy
ITV/GTV	100%/48Gy	0%/52Gy	4/48Gy
Relevant organs at risk (OARs): Lung, Esophagus, Heart and Ribs • Specific plan constraints			
OAR (Lung)	• 30% volume receiving < 13Gy (Left Lung) • 30% volume receiving < 10Gy (Right Lung)		
OAR (Esophagus)	• volume receiving 18.8Gy < 5 cm^3		
OAR (Heart)	• volume receiving 28Gy < 15 cm^3		
OAR (Ribs)	• volume receiving 32Gy < 1 cm^3		

5.2.2 Marker-based constrained optimization

As described in Section 4.3.3, a hard constraint imposes complete and full visibility of all implanted markers in the BEV (thereby avoiding any shielding or blockage of the markers by the MLC segmented fields/apertures), while a soft constraint restricts visibility for a specific set of markers in the BEV (thereby penalizing MLC blockage for a specified marker). Thus, for the scenarios considered here with three markers implanted, there are also six possible combinations of soft constraints: where only a set of two markers are constrained (i.e. SC_{II} = SC12, SC13 or SC23) and where only a single marker is constrained (i.e. SC_{I} = SC1, SC2, or SC3; whereby 1, 2 and 3 represents the marker index such that SC2 = soft constrained plan for marker 2; SC13 = soft constrained plan for markers 1 and 3 etc.); and just one hard constrained plan whereby all three markers must be visualized (i.e. HC ≡ SC123) in the BEV by the MLC aperture. Hence, there are seven constrained plan combinations and eight plans in total including the non-constrained (NC) plan, and all were investigated. Recall, the NC plans are whereby no marker visibility parameter is included during the optimization.

For ease of comparison and presentation over the large number of datasets and plans, we average the quantitative dose-quality metric results for the single- and two-marker SC plan combinations, such that instead of eight plans, we present for each patient dataset four plans in total: NC, SC_{I}, SC_{II} and HC. This approach was taken as observed trends in the averaged metric results were similar to the individual marker-based constrained plans (data not shown).

5.2.3 Marker visibility and trackability metric

We assume that including the marker visibility constraints into the optimization will aid real-time tumour tracking. Most fiducial marker-based tracking algorithms in the literature do

require the marker to be seen in a region of interest of a chosen template, and the work of Azcona *et al*[39] also showed improved tracking results with increased marker visibility. However, we did not implement real-time tracking methods in this work. Instead, a quantitative metric for marker visibility was defined and evaluated.

For this purpose, we use the number of markers fully visualized at each gantry angle or control point in the optimized VMAT plans as a metric, to define visibility and 'trackability'; trackability is the measure of visualizing specific markers in the BEV, which are either inside or in close proximity to the PTV. Hence, our chosen quantitative metric is assumed to depict trackability as defined in Section 4.3.4. For an example patient, the markers were fully visible in the BEV MLC aperture field openings at all gantry control points in each plan [Figure 5-9 for an example BEV for liver SBRT patient B, Figure 5-10 for example lung SBRT patient p1 and Figure 5-11 for an example prostate patient #10 respectively, at a specific control point].

5.2.4 Plan evaluation: comparison metrics

We compare plan dosimetry from the different plans with dose-quality metrics as described in Section 4.3.5. To analyze and compare plans for the patient datasets, we also reported an average index of the quantitative metrics (CI, HI) and used it along with our institution's clinical dose metrics for hypofractionated prostate VMAT, as well as lung and liver SBRT VMAT. For the liver SBRT VMAT plans, metrics used include:

i. PTV: dose delivered to 95% of the volume is at least 100% Rx (D95 or $D_{95\%} \geq 100\%$);
ii. PTV: mean dose delivered to target ($D_{mean} \leq 110\%$ Rx);
iii. OAR Kidney: dose delivered to 10% volume less than 10Gy (D10 < 10Gy);
iv. OAR Esophagus: dose delivered to 0.5cm^3 volume less than 32Gy ($D_{0.5cc} < 32$Gy);

v. OAR Large Bowel: volume receiving 32Gy is less than 0.5cm^3 ($D_{0.5cc}$ < 32Gy)

vi. OAR Heart: volume receiving 30Gy is less than 30cm^3 (D_{30cc} < 30Gy)

For the prostate hypofractionated VMAT plans, metrics used include:

i. PTV: dose delivered to 99% of the volume is at least 95% Rx (D99 or $D_{99\%} \geq 95\%$);

ii. OAR Rectum: volume receiving 74Gy is less than 3cm^3 (V74 < 3cc);

iii. OAR Bladder: volume receiving 65Gy is less than 25% of Rx dose (V65 < 25%);

iv. OAR Penile Bulb: mean dose not to exceed 50Gy.

Metrics used for the lung SBRT VMAT plans include:

i. PTV: dose delivered to 99% volume greater than 90% Rx (D99 > 90%);

ii. OAR Lung: dose delivered to 30% volume less than 13Gy (D30 < 13Gy);

iii. OAR Esophagus: volume receiving 18.8Gy less than 5cm^3 (V18.8Gy < 5cc);

iv. OAR Heart: volume receiving 28Gy less than 15cm^3 (V28Gy < 15cc).

For simplicity in presentation, we focus on the PTV target's $D_{99\%}$ and the average index of its' CI and HI when comparing plans. We will focus on a selected target metric (i.e. the average index) as the dose gradient and dose falloff requirements for the different disease sites are not consistent due to the different dose prescriptions employed. Note that each patient also had different OAR constraints due to varying OAR structure sizes amongst patients, but the clinical thresholds employed per patient for the targets and OARs were consistent across plans. Finally, we reported the percentage differences in the target metrics for the constrained plans with respect to the non-constrained plan. For statistical testing, we used the parametric T-test (with a two-tailed hypothesis) or a non-parametric Mann-Whitney U-test (when the assumption of a normally distributed data fails), both at 5% significance level (whereby $p < .05$ indicates significance), as detailed in Section 4.3.5.

5.3 Results

5.3.1 Marker-based constrained optimization on liver SBRT dataset

Figure 5-1 shows the comparison between the non-constrained clinical-based Eclipse and *MonArc*-based VMAT plans for liver SBRT patient A. The *MonArc*-based plan is slightly inferior in terms of dose conformity to the targets and OARs. However, both plans delivered at least 95% of prescription (Rx) dose to 99% of the PTV as required. The OAR dose results for *MonArc* were also higher than for Eclipse except for the esophagus, but all within dose objectives. This shows that the *MonArc*-based optimization produces acceptable dosimetric results relative to the clinical Eclipse TPS (using the dose delivered to 95% PTV volume metric D_{95} and OAR dose thresholds). The results were similar to the sample and lung prostate patient in Section 4.4. All the other investigated patient plans show similar target dose distribution and coverage [not shown here], with slightly differing OAR dose coverage.

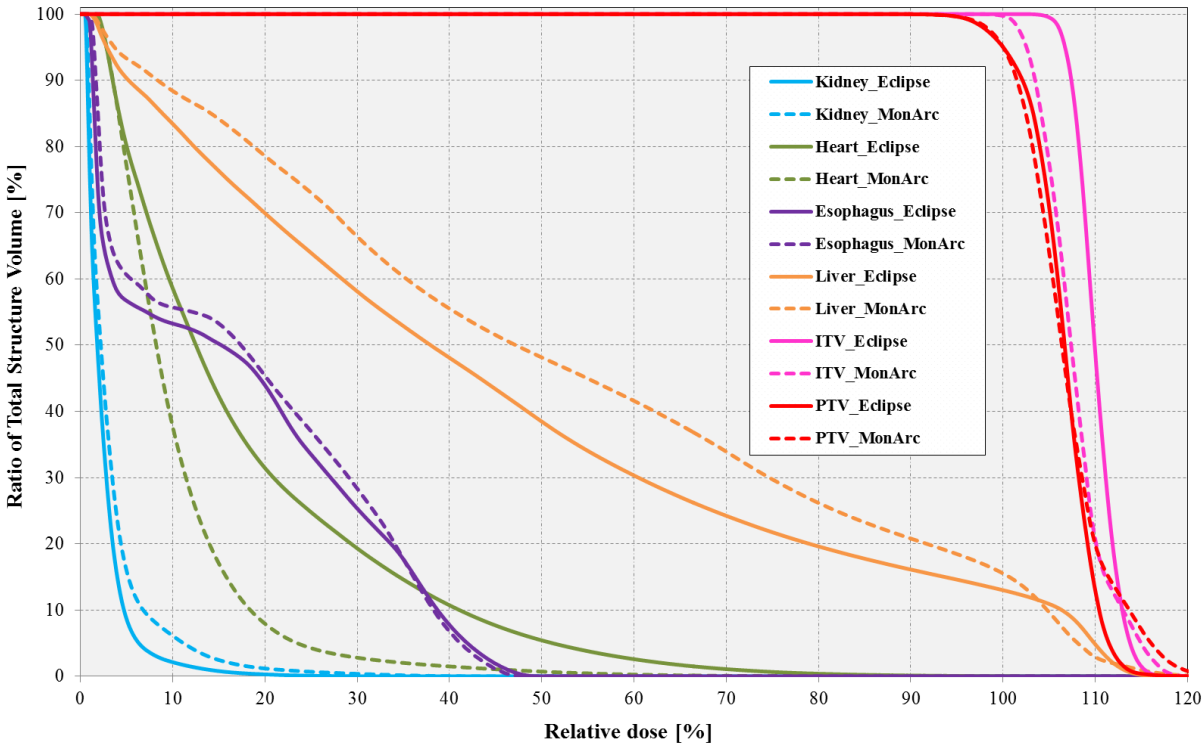

Figure 5-1: Dose-volume histogram (DVH) comparison between optimized non-constrained Eclipse-based (solid line) and *MonArc*-based (dashed line) VMAT plans for target structures (ITV [pink]; PTV [red]) and OARs (Kidney; Heart; Esophagus; Liver) on liver SBRT patient A.

5.3.2 Plan comparison and dose-quality metrics for liver SBRT patients

Figure 5-2(a) and Figure 5-2(b) shows the target PTV's and OAR's DVH plots (zoomed-in) respectively, for optimized VMAT plans for two liver SBRT patients (B and E). The NC plan offered the steepest dose fall-off slope and thus the best dose coverage for the PTV, followed by the SC_I plans. However, for both patients the SC_{II} plan and the HC plan provided the worst dose fall-off slope for patient B and E, respectively. Similar trends were obtained for the other liver patients (A, C and D). The OAR doses were variable between different patients; however, they follow similar trends (as PTV target results) with the lowest OAR doses produced by NC plans and the highest OAR doses produced by HC plans, respectively.

Table 5-4 shows the dose-quality metrics for the plans for all five liver patients A–E. As can be observed, the NC plans offer the best dose metric for the PTV and the lowest doses to the OARs (esophagus, heart and large bowel). Using the average index, the NC plan still produced the lowest value (i.e. 'best') across all datasets, as expected. This is followed by the SC_I plans (average of soft-constrained plans for one specified marker only) and SC_{II} plans (average of soft-constrained plans for two specified markers), respectively. The worst average index values were produced by the HC (or SC_{III}) plans, which is in agreement with the DVH plots for the example liver patient B in Figure 5-2. However, it should be emphasized that all the plans produced dosimetrically acceptable dose coverage and conformity for the PTV target as defined by our locally defined metrics including $D_{95\%}$ ($\geq$ 100% Rx), D_{mean} (103.5% $\leq$ Rx $\leq$ 114.8%) and D_{max} (110.2% $\leq$ Rx $\leq$ 133.9%).

In terms of the percentage differences between the PTV's mean conformity index (CI) of the constrained plans compared to NC plans for all five liver datasets, there was a 10.2% difference for SC_I, 17.7% for SC_{II} and 25% for HC plans respectively. However, using the PTV's mean

homogeneity index values (HI), there was only 3.8% difference for SC_I, 3.3% difference for SC_{II} and 4.1% difference for HC plans respectively, compared to the NC plan across all five liver datasets. Using the average index, there was a 7.1% difference for SC_I, 10.6% for SC_{II} and 14.6% difference for HC plans respectively, compared to NC plans. Using the Mann-Whitney U-Test for significance for all liver SBRT datasets, there is no significant difference in the average index values (at 95% confidence level whereby $p < 0.05$) between the non-constrained (NC) and soft-constrained plans on one marker (i.e. SC_I). However, there is a significant difference between the NC plan and soft-constrained plans on two markers (i.e. SC_{II}), as well as hard-constrained (HC) plans.

For the OARs (esophagus, heart, kidneys and large bowel), all five liver patient plans met the clinically defined thresholds as shown in Table 5-4, except for the large bowel doses in patient C (discussed in further detail in Section 5.4) where the dose was between 37–50Gy for all the investigated plans. For the kidney OAR [not shown], all the constrained plans (i.e. SC_I, SC_{II} and HC) satisfied the clinical dose threshold of $D_{10\%} < 10$Gy, similar to the NC plan. For the esophagus OAR, all investigated plans including the NC plan satisfied the clinical dose threshold of $D_{0.5cc} <$ 32Gy (i.e. esophagus volume receiving 32Gy is less than $0.5cm^3$). Similarly, for the heart OAR, all investigated plans also satisfied the $D_{30cc} < 30$Gy metric (i.e. heart volume receiving 30Gy is less than $30cm^3$) [see Table 5-4].

(a)

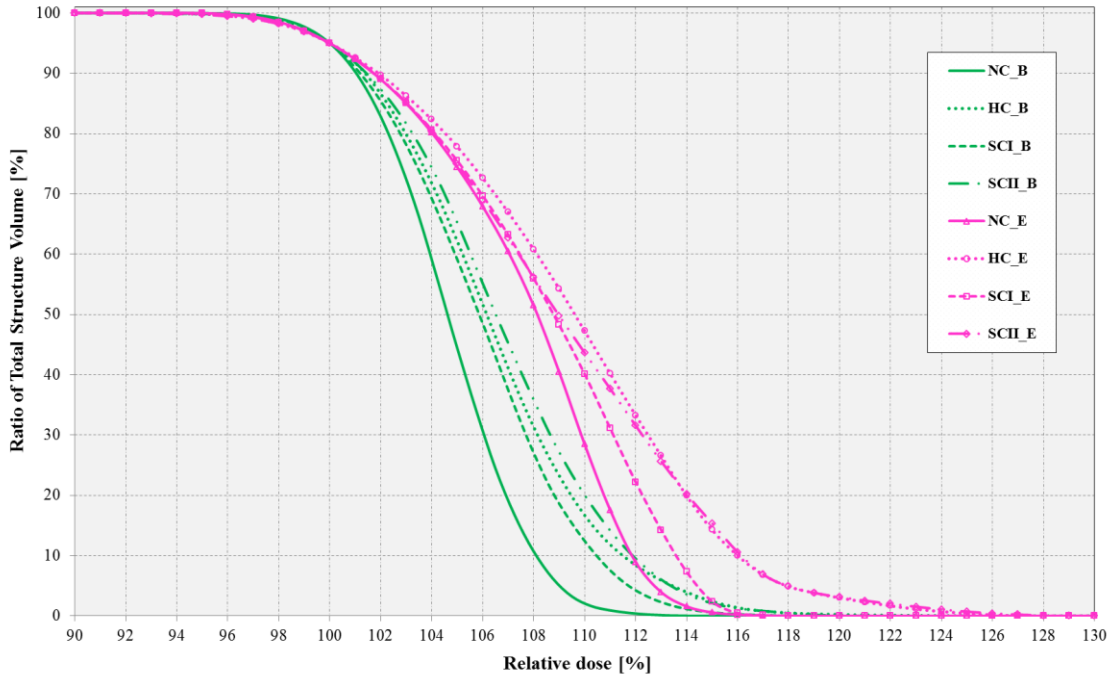

(b)

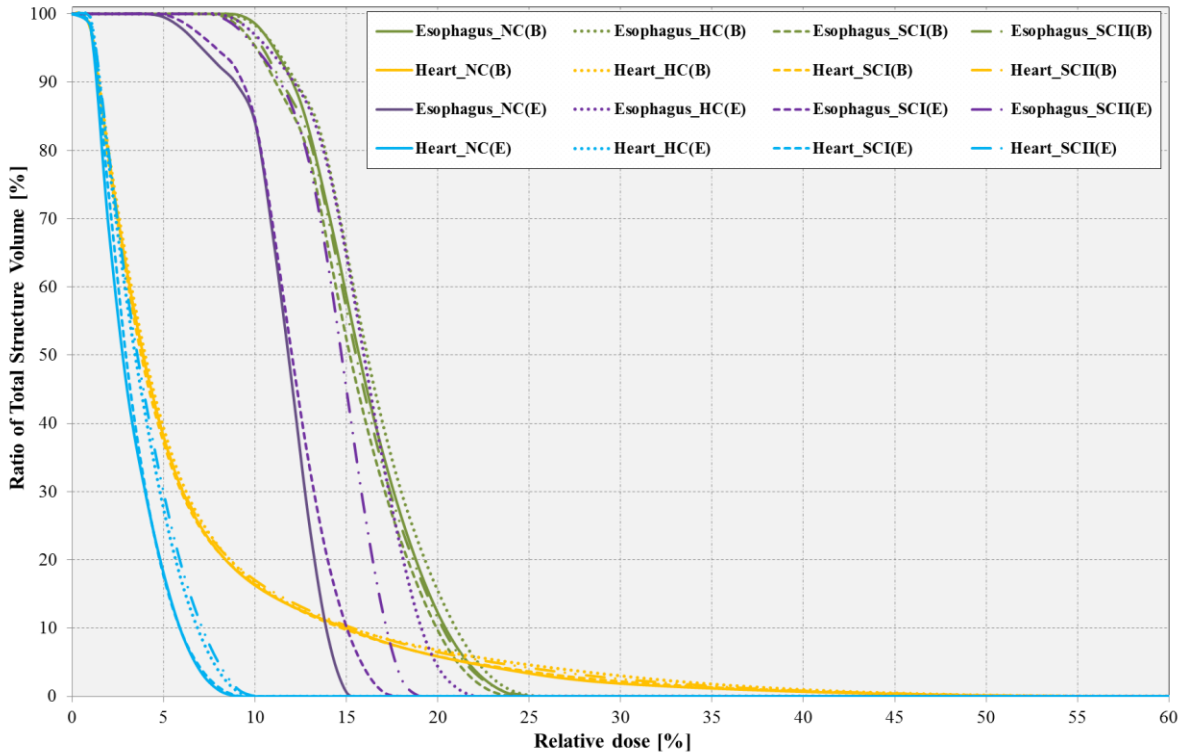

Figure 5-2: DVH comparison (zoomed-in) for (a) PTV and (b) OARs (Esophagus and Heart) between *MonArc*-based non-constrained (NC), soft-constrained (SC_I and SC_{II}) and hard-constrained (HC) SBRT VMAT plans on example liver patients B and E.

Table 5-4: Quality metrics for *MonArc* optimized VMAT plans on liver SBRT patients A − E, where soft constrained metrics for one- and two-markers were averaged, and compared to hard- and non-constrained plans. [CI = conformity index; GM = gradient measure; MU = monitor units]

Metrics/patient	**A**	**B**	**C**	**D**	**E**
Non-constrained plan i.e. NC					
CI	1.180	1.070	1.130	1.220	1.030
HI	1.156	1.106	1.065	1.140	1.099
GM	2.780	2.200	2.050	1.630	1.630
Average Index, (CI+HI)/2	1.168	1.088	1.097	1.180	1.064
PTV mean dose, D_{mean}	106.9%	104.6%	103.5%	106.9%	107.4%
$D_{0.5cc}$ < 32Gy (Esophagus)	17.09	9.99	3.34	4.21	7.21
D_{30cc} < 30Gy (Heart)	11.55	8.30	1.18	1.21	2.75
$D_{0.5cc}$ < 32Gy (Large Bowel)	21.78	3.30	37.10	13.19	2.73
MU	1122.4	1451.7	938.9	1036.6	1124.9
Soft-constrained plan on one marker i.e. SC_I = (SC1 + SC2 + SC3)/3					
CI	1.457	1.113	1.313	1.173	1.150
HI	1.183	1.186	1.165	1.103	1.143
GM	2.843	2.240	2.117	1.710	1.740
Average Index, (CI+HI)/2	1.320	1.150	1.239	1.138	1.146
PTV mean dose, D_{mean}	111.9%	105.9%	107.7%	105.9%	108.5%
$D_{0.5cc}$ < 32Gy (Esophagus)	17.20	10.14	4.13	4.49	8.11
D_{30cc} < 30Gy (Heart)	13.42	8.15	1.25	1.37	2.98
$D_{0.5cc}$ < 32Gy (Large Bowel)	20.89	3.59	44.25	16.41	3.04
MU	772.2	1421.8	808.9	797.6	1010.4
Soft-constrained plan on two markers i.e. SC_{II} = (SC12 + SC13 + SC23)/3					
CI	1.650	1.150	1.383	1.190	1.257
HI	1.160	1.191	1.129	1.108	1.161
GM	2.923	2.233	2.117	1.727	1.743
Average Index, (CI+HI)/2	1.405	1.171	1.256	1.149	1.209
PTV mean dose, D_{mean}	112.2%	106.3%	110.1%	105.7%	108.6%
$D_{0.5cc}$ < 32Gy (Esophagus)	17.68	10.29	4.37	4.51	9.10
D_{30cc} < 30Gy (Heart)	17.01	8.42	1.29	1.43	3.12
$D_{0.5cc}$ < 32Gy (Large Bowel)	21.17	3.76	47.50	17.32	3.19
MU	783.1	1397.4	780.7	771.5	966.4
Hard-constrained plan on all three markers i.e. HC ≡ SC_{III} = SC123					
CI	1.730	1.160	1.460	1.260	1.430
HI	1.170	1.197	1.120	1.138	1.174
GM	2.930	2.220	2.120	1.630	1.750
Average Index, (CI+HI)/2	1.448	1.178	1.290	1.199	1.302
PTV mean dose, D_{mean}	114.8%	106.3%	111.8%	107.4%	109.4%
$D_{0.5cc}$ < 32Gy (Esophagus)	17.21	10.62	4.49	4.87	10.02
D_{30cc} < 30Gy (Heart)	17.73	8.97	1.34	1.62	3.21
$D_{0.5cc}$ < 32Gy (Large Bowel)	20.49	3.82	50.71	18.07	3.27
MU	767.6	1357.9	769.7	745.1	954.3

5.3.3 Marker-based constrained optimization on lung SBRT patients

Figure 5-3 and Figure 5-4 shows the DVH plot comparison between the non-constrained clinical Eclipse-based and *MonArc*-based VMAT plans for lung SBRT patient I and III, respectively. As can be observed, the *MonArc*-based plans are inferior in terms of dose conformity to the target for both patients, as there is a steeper dose fall-off obtained with the Eclipse-based clinical plan. The results are more pronounced for the lung datasets, relative to the liver dataset. For the OARs, similar results were obtained between both plans for the heart and lung OARs in both patients, while small differences exist with the esophagus and ribs. However, both plans passed the established site-specific clinical dose tolerances for both the PTV and OARs. Similar results were obtained for the other three lung SBRT patients [not displayed].

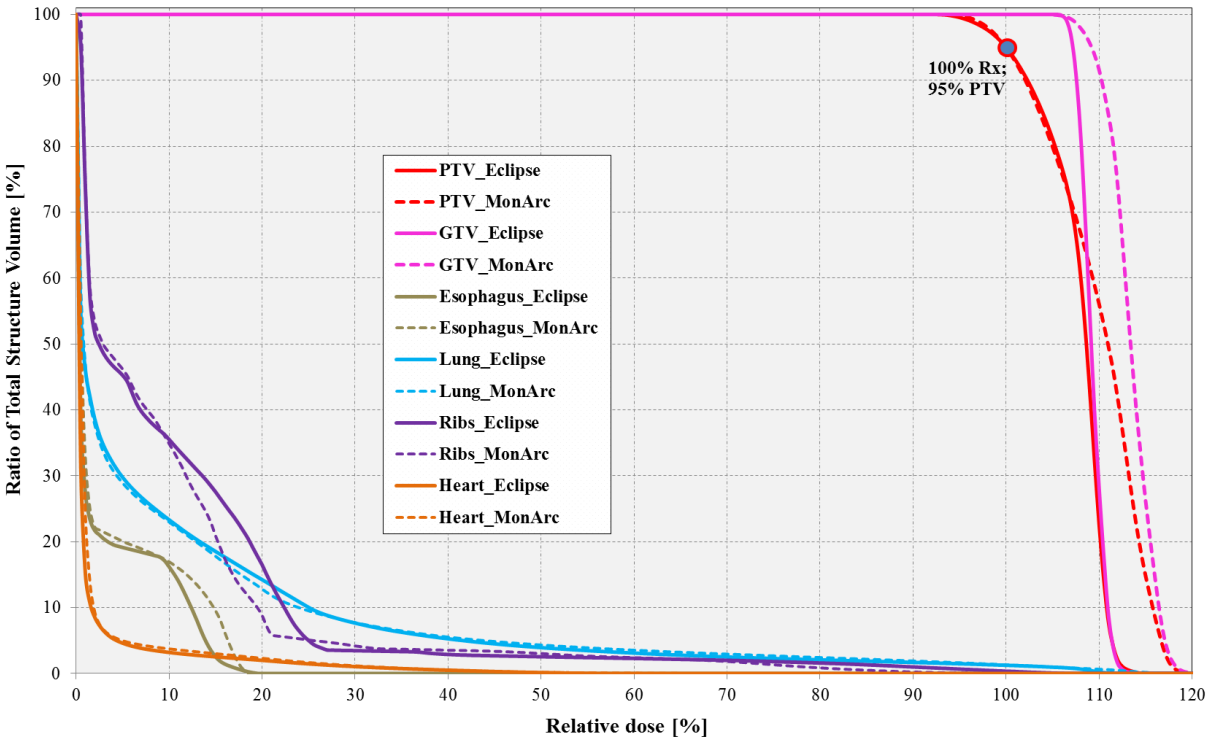

Figure 5-3: DVH comparison between Eclipse-based and *MonArc*-based VMAT plans for the target structures (GTV [pink]; PTV [red]) and OARs (Esophagus [green]; Lung [blue]; Ribs [purple] and Heart [orange]) on lung SBRT patient I. Both plans are non-constrained on the markers.

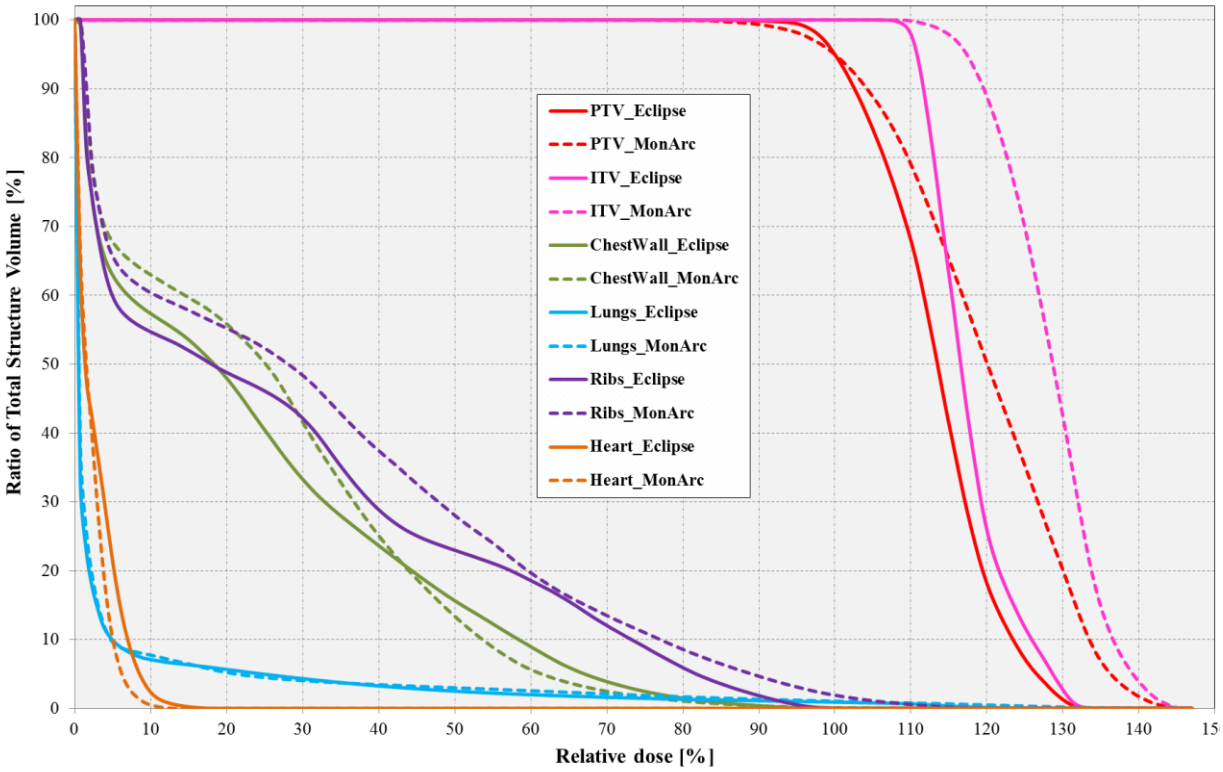

Figure 5-4: DVH comparison between Eclipse-based and *MonArc*-based VMAT plans for the target structures (GTV [pink]; PTV [red]) and OARs (Chest wall [green]; Lung [blue]; Ribs [purple] and Heart [orange]) on lung SBRT patient III. Both plans are non-constrained on the markers.

5.3.4 Plan comparison and dose-quality metrics for lung SBRT patients

Figure 5-5(a)-(b) shows the zoomed-in target and OAR DVH plots for the NC, HC and SC VMAT plans for lung SBRT patient I, respectively. As observed, the NC plan did not produce the steepest dose fall-off to the PTV target. For the SC plans, SC_I = SC13 (i.e. inferior + superior marker constrained plan) provided the steepest dose fall-off while SC_I = SC1 (i.e. inferior marker constrained plan) produced the least steep dose fall-off. However, it should be emphasized that all the plans produced dosimetrically acceptable coverage and conformity for the PTV target as defined by local clinical standards.

For the surrounding lungs OAR [see Figure 5-5(b)], all constrained plans met the clinical dose threshold of D30 < 13Gy (i.e. dose to 30% lung volume is less than 13Gy), including the NC plan. Also, for the esophagus OAR, all constrained plans met the clinical dose threshold of V18.8Gy < 5cc (i.e. volume receiving 18.8Gy dose is less than $5cm^3$). Similarly, for the ribs (V32Gy < 1cc) and heart OAR (V28Gy < 15cc), the clinical thresholds as shown were satisfied by all investigated plans. However, like the results for the dynamic phantom, some constrained plans produce reduced OAR doses compared non-constrained plans, albeit not significant.

Similarly, Figure 5-6(a)-(b) shows the zoomed-in target and OAR DVH plots for the NC, HC and SC VMAT plans for lung SBRT patients II and III, respectively. As observed, the NC plan did not produce the steepest dose falloff for the PTV target. For patient III, SC_{II} = SC23 (i.e. middle + superior marker constrained plan) provided the steepest dose fall-off while the NC plan produced the least steep dose fall-off. Nonetheless, all the plans produced dosimetrically acceptable coverage and conformity to the PTV target as defined by local clinical standards.

For the lungs OAR [see Figure 5-6(b)], all constrained plans met the clinical dose threshold of D30% < 13Gy (i.e. dose to 30% lung volume is less than 13Gy), including the NC plan. For the

chest wall OAR, all constrained plans met the clinical dose threshold of V30Gy < 30cc (i.e. volume receiving 30Gy dose is less than $30cm^3$), including the NC plan. However, for the ribs OAR [Figure 5-6(b)], all plans failed to meet the clinical threshold (i.e. V32Gy < 1cc) including the NC plan. The reason for this might be due to the location of the ribs relative to the lung tumour.

(a)

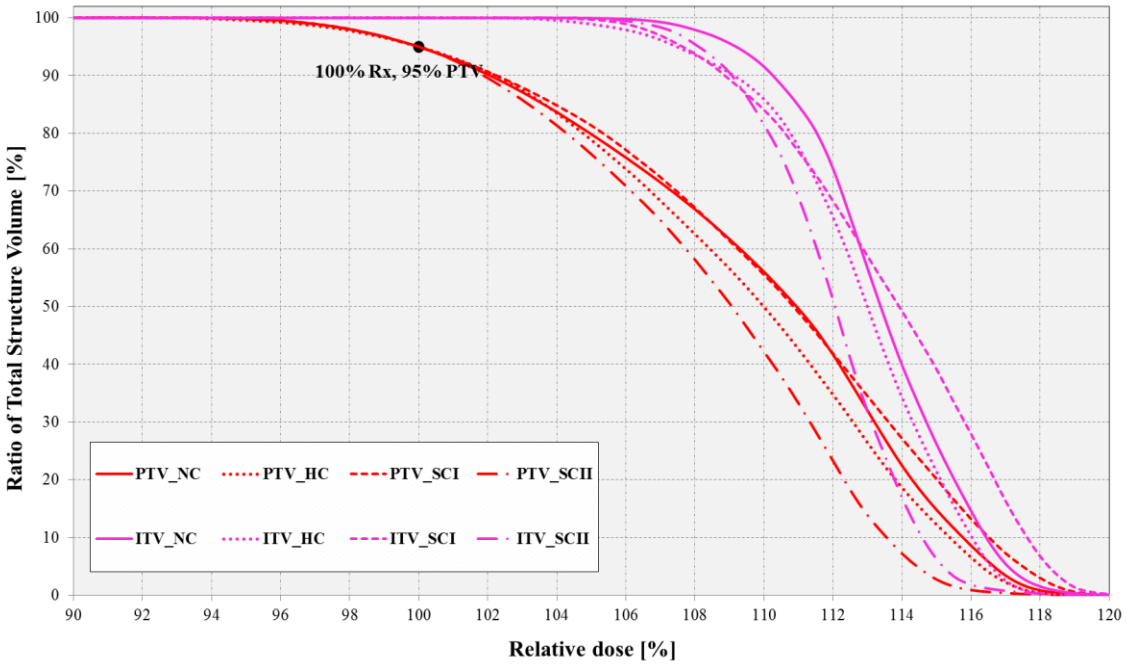

(b)

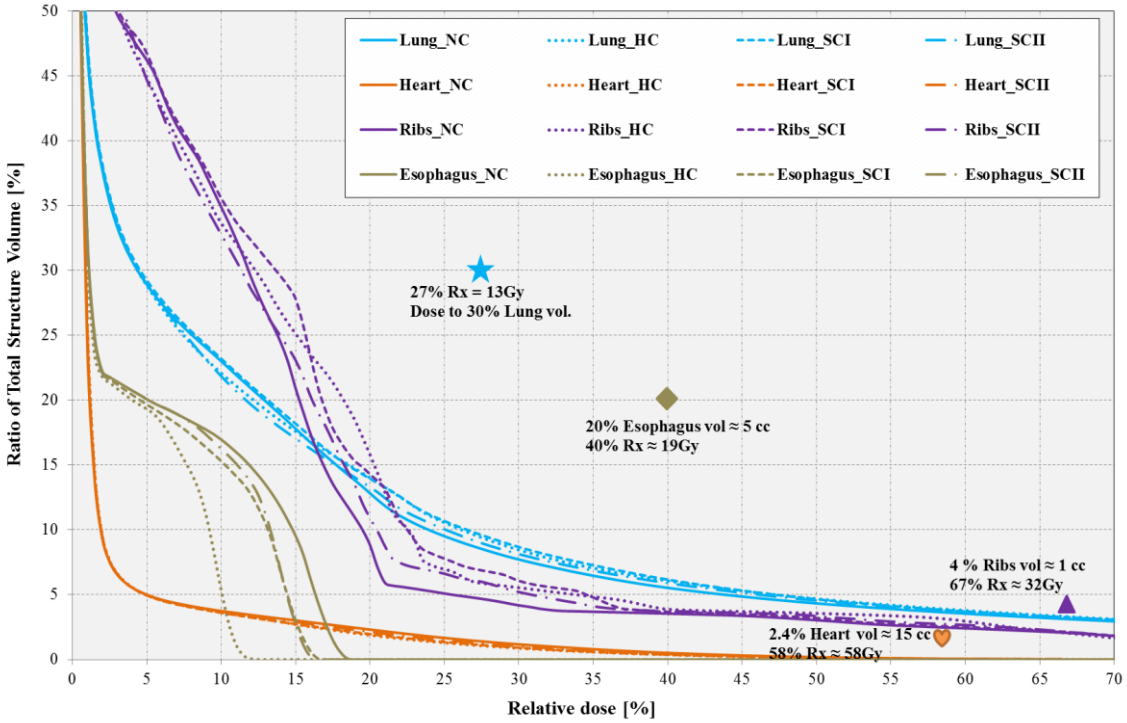

Figure 5-5: DVH comparison for (a) targets (ITV [pink]; PTV [red]) and (b) OARs (Esophagus [green]; Lung [blue]; Heart [orange]; Ribs [purple]) between *MonArc*-based non-constrained (NC), soft-constrained (SC) and hard-constrained (HC) VMAT plans on lung SBRT patient p1. Highlights (circle, diamond, triangle, star, heart) represent labeled target and OAR-specific dose-quality thresholds.

(a)

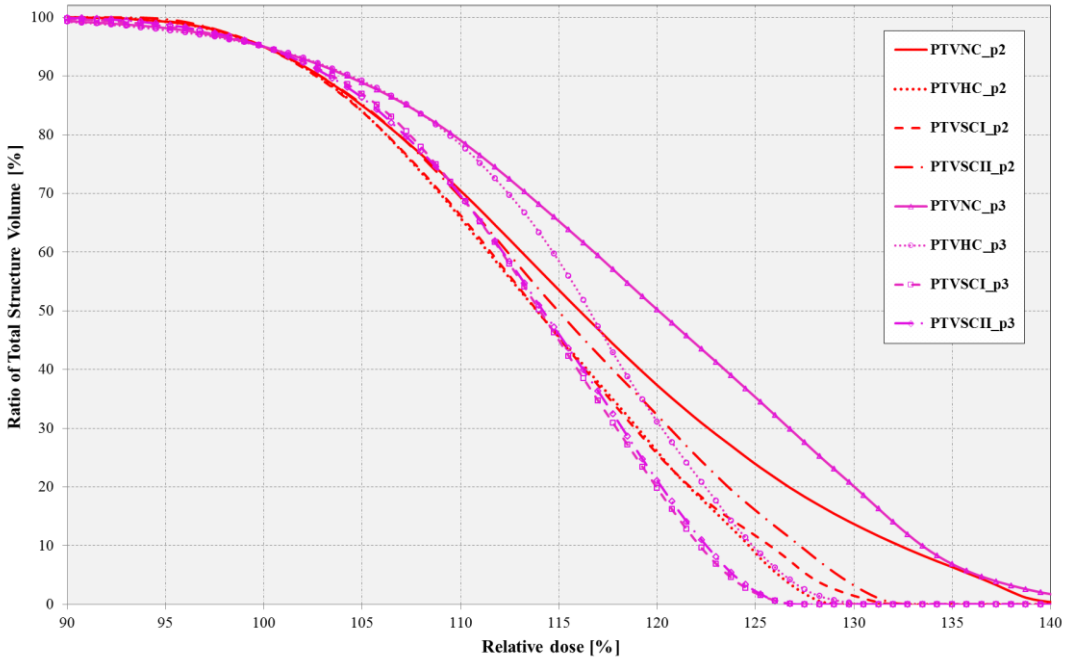

(b)

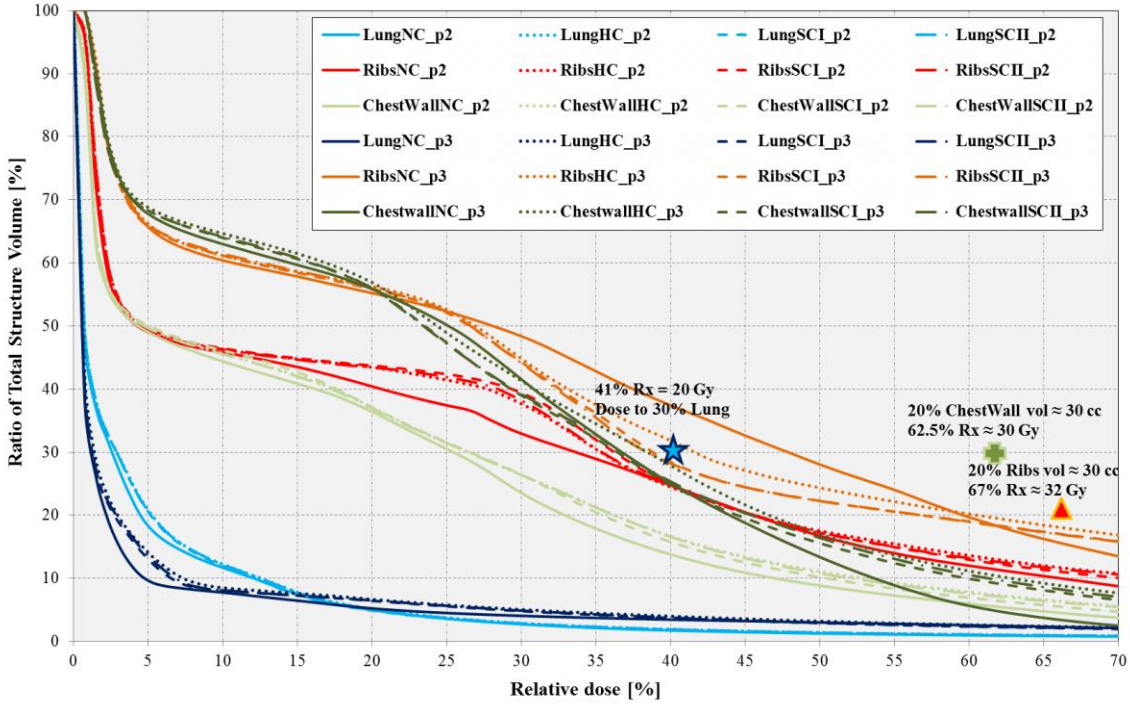

Figure 5-6: DVH [zoomed-in] comparison for (a) PTV targets and (b) OARs (Lung [blue]; Ribs [red/orange]; and Chest]) between *MonArc*-based non-constrained (NC), soft-constrained (SC_I and SC_{II}) and hard-constrained (HC) VMAT plans on two lung SBRT patients, p2 and p3. Highlights (circle, diamond, triangle, star, heart) represent labeled target and OAR-specific dose-quality thresholds.

In similar fashion, Table 5-5 shows the quantitative dose quality metrics (i.e. CI, HI and GM) for all the investigated plans on the lung SBRT patient I–V, respectively. The lowest CI values consistently belong to the NC plan across all five patients, followed by the SC_I and SC_{II} plans, respectively. This implies that the NC plan produced the best conformal plan. Using the Gradient Measure however, the HC (GM = 1.32) and SC_I plan (GM = 1.34) produced the best dose gradient value for patient III, followed by SC_{II} (GM ≈ 1.35) while the NC plan (GM = 1.48) produced the worst gradient value. Using the average index values, the NC plan produced the best conformal and homogenous target dose across all patient datasets, except for patient III whereby the SC_I plan produced the best mean index value. Again, it should be emphasized that all the plans produced dosimetrically acceptable PTV target coverage and conformity, as defined by our local clinical tolerances using $D_{99\%}$ ($91.2\% \leq Rx \leq 96.9\%$), D_{mean} ($109.1\% \leq Rx \leq 121.3\%$), and D_{max} ($120.3\% \leq Rx \leq 153.7\%$).

For the OARs, the NC plans either produced similar or better values compared to the SC and HC plans across all five lung patients. For the lungs OARs, all the investigated plans met the clinical dose threshold (i.e. V20Gy < 30%). Similar results were obtained for the esophagus and spinal cord, as all plans delivered very low dose and thus met the clinical thresholds. For the chest-wall OAR, all plans also passed the clinical threshold (i.e. V30Gy < 30cc), except for lung patient V whereby the chest-wall volume receiving 30Gy ranged from 90 cm^3 for the NC plan, to 130 cm^3 for the HC plan. For the ribs OAR, only lung patient I satisfied the clinical dose threshold (i.e. V32Gy < 1cc). In terms of the beam output, the NC plan produced the largest beam output across all five patients, followed by SC_I plans, while the lowest output is by either the SC_{II} or HC plans across all five lung patients.

In terms of the differences between the PTV's mean CI with respect to NC plans amongst all five lung SBRT patients, there was on average a 10.1% difference for SC_I, 14.1% for SC_{II} and 19.7% for HC plans compared to NC plans for all five patients. Using the PTV's mean HI values, there was a 4.5% difference for SC_I, 5.6% difference for SC_{II} and 5.8% difference for HC plans respectively, compared to the NC plan amongst all five patients. Using the average of the three indices, there was only a 2.7% difference for SC_I, 4.1% difference for SC_{II} and 6.7% difference for HC plans respectively, compared to NC plans. Using the Mann-Whitney paired-means test for significance for all five patients, there is no significant difference in the average index values (at 95% confidence level whereby $p < 0.05$) between the NC and either of the SC_I or SC_{II} plans. In contrast, there is a significant difference ($p > 0.05$) between the NC and HC plans.

For the esophagus OAR, all the constrained plans (i.e. SC_I, SC_{II} and HC) satisfied the clinical dose metric of V18.8Gy < 5cc (i.e. volume of esophagus receiving 18.8Gy is less than $5cm^3$), just like the NC plans for all five patients [not shown here]. Using the V28Gy < 15cc metric for the heart OAR, all investigated plans passed the threshold for all five lung patients [see Table 5-5]. However, for the ribs OAR all investigated plans including the NC plans failed to satisfy the clinical dose threshold of V32Gy < 1cc (i.e. ribs volume receiving 32Gy is less than $1cm^3$), for all patients except patient #1. For the other OARs (e.g. chest-wall), all investigated plans satisfied local clinical dose thresholds, apart from patient #5.

Table 5-5: Quality metrics for *MonArc* optimized VMAT plans on lung SBRT patient I – V, where soft constrained plans for one and two markers were averaged, and compared to hard- and non-constrained plans. [CI = conformity index; HI = homogeneity index; MU = monitor units per arc]

Metrics per patient	**I**	**II**	**III**	**IV**	**V**
Non-constrained plan i.e. NC					
CI	1.240	1.210	1.130	1.180	1.070
HI	1.104	1.219	1.232	1.267	1.216
GM	1.380	1.350	1.480	1.390	2.050
Average Index, (CI+HI)/2	1.172	1.215	1.181	1.224	1.143
$D_{99\%}$ >= 90% of Rx	96.9%	95.7%	92.0%	92.4%	93.8%
V20Gy < 30% (Lungs)	2.10%	1.64%	3.37%	5.02%	12.13%
V28Gy < 15cc (Heart)	0.42	0.00	0.00	0.00	14.12
V32Gy < 1cc (Ribs)	0.56	5.28	10.15	1.62	13.08
MU	1180.8	1384.9	1786.4	1473.2	1507.5
Soft-constrained plan on one marker i.e. SC_I = (SC1 + SC2 + SC3)/3					
CI	1.300	1.433	1.183	1.360	1.143
HI	1.107	1.167	1.149	1.174	1.168
GM	1.387	1.357	1.340	1.520	2.380
Average Index, (CI+HI)/2	1.204	1.300	1.166	1.267	1.156
$D_{99\%}$ >= 90% of Rx	96.9%	96.2%	94.2%	94.3%	93.9%
V20Gy < 30% (Lungs)	2.18%	1.78%	3.53%	5.96%	12.89%
V28Gy < 15cc (Heart)	0.29	0.00	0.00	0.00	13.06
V32Gy < 1cc (Ribs)	0.56	5.94	10.74	3.69	12.09
MU	1155.8	1106.8	1081.6	1043.6	1183.5
Soft-constrained plan on two markers i.e. SC_{II} = (SC12 + SC13 + SC23)/3					
CI	1.303	1.503	1.213	1.443	1.190
HI	1.104	1.156	1.120	1.164	1.154
GM	1.400	1.347	1.347	1.487	2.447
Average Index, (CI+HI)/2	1.203	1.330	1.167	1.304	1.172
$D_{99\%}$ >= 90% of Rx	96.8%	96.0%	94.4%	94.3%	92.8%
V20Gy < 30% (Lungs)	1.99	1.80	3.62	5.18	12.93
V28Gy < 15cc (Heart)	0.37	0.00	0.00	0.00	14.01
V32Gy < 1cc (Ribs)	0.58	6.02	11.20	6.78	12.51
MU	1138.0	1065.3	1008.1	1002.1	1151.0
Hard-constrained plan on all three markers i.e. HC ≡ SC_{III} = SC123					
CI	1.300	1.570	1.420	1.450	1.240
HI	1.102	1.138	1.136	1.160	1.150
GM	1.440	1.330	1.320	1.490	2.540
Average Index, (CI+HI)/2	1.201	1.354	1.278	1.305	1.195
$D_{99\%}$ >= 90% of Rx	96.4%	95.7%	91.2%	94.9%	92.1%
V20Gy < 30% (Lungs)	2.10%	1.81%	3.84%	5.94%	13.16%
V28Gy < 15cc (Heart)	0.31	0.00	0.00	0.00	13.39
V32Gy < 1cc (Ribs)	0.56	6.19	11.87	5.36	13.98
MU	1159.7	1036.5	1041.3	965.4	1107.8

5.3.5 Marker-based constrained optimization on prostate dataset

Figure 5-7 shows the DVH comparison between the non-constrained clinical and *MonArc*-based VMAT plan on prostate patient #8. As observed, the *MonArc*-based plan is nearly the same with the clinical plan in terms of dose conformity to the target. For the OARs, similar trends are observed with MonArc delivering more OAR dose. Nonetheless, both plans passed the established site-specific clinical dose tolerances for the target and OARs, on prostate patient #8.

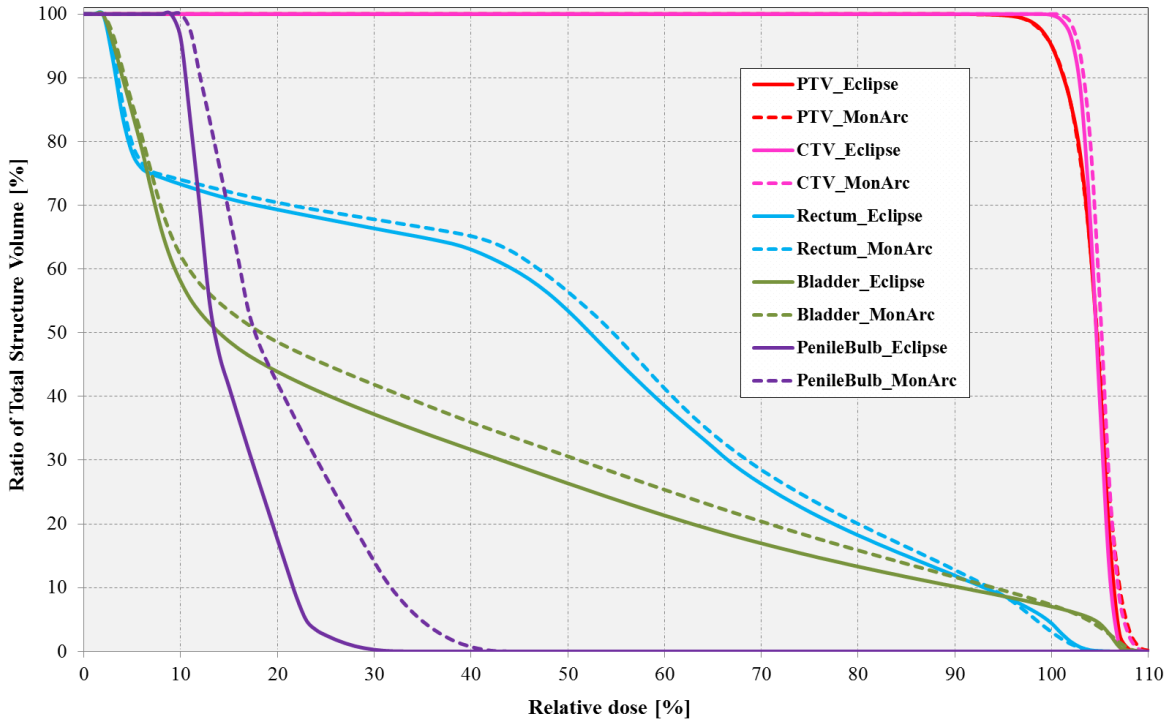

Figure 5-7: DVH comparison between Eclipse-based and *MonArc*-based VMAT plans for the target structures (CTV [pink]; PTV [red]) and OARs (Bladder [green]; Rectum [blue]; Penile Bulb [purple]) on prostate patient #8. Both plans are non-constrained on the markers.

5.3.6 Plan comparison and dose-quality metrics for prostate patients

Figure 5-8(a) and Figure 5-8(b) shows the PTV's and OAR's DVH plots (zoomed-in) for all investigated VMAT plans for three prostate patients (#1, #4 and #8), respectively. In contrast to the lung patients in Section 5.3.4, the NC plans offered the steepest dose fall-off and best optimal dose coverage for the PTV, followed by the SC_I plans across all three patients. The HC plans produced least steep dose fall-off implying the worst coverage across all patients. However, all investigated plans satisfied the target dose metric, as displayed.

For the OARs (bladder and rectum), it can be observed that the doses for all investigated plans to each patient are very similar. For the remaining seven patients, similar trends were obtained. In summary, all OAR dose thresholds were met by the investigated plans. However, the rectum OAR dose threshold was not met for patient #4 while the penile bulb OAR dose constraint was not met for patient #1 [not displayed]. The size and location of these OARs relative to the tumour may have played a factor in this discrepancy.

(a)

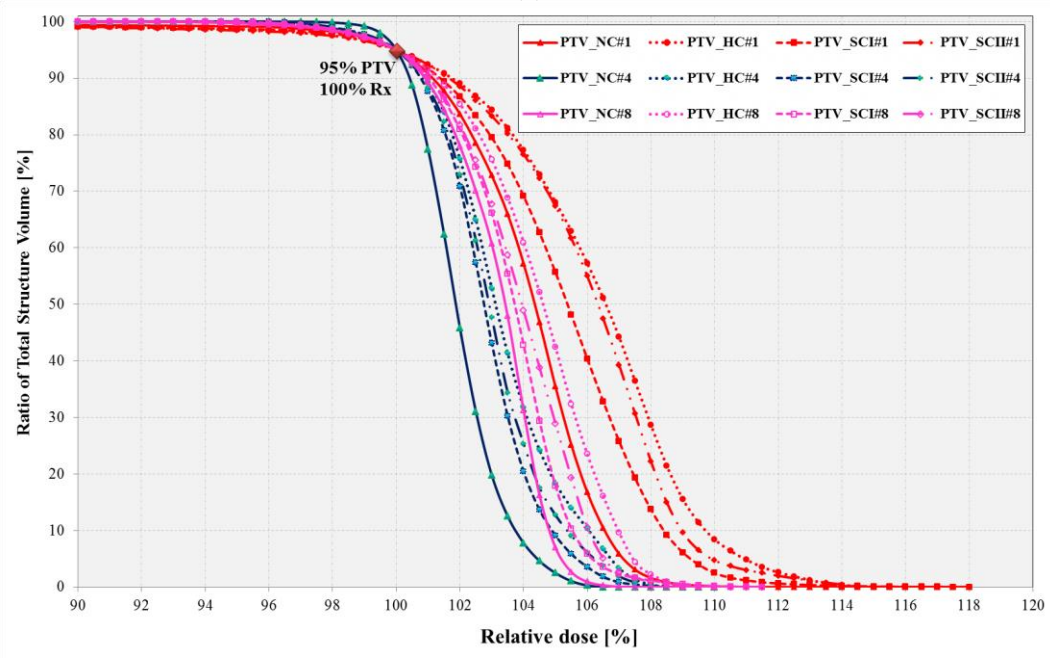

(b)

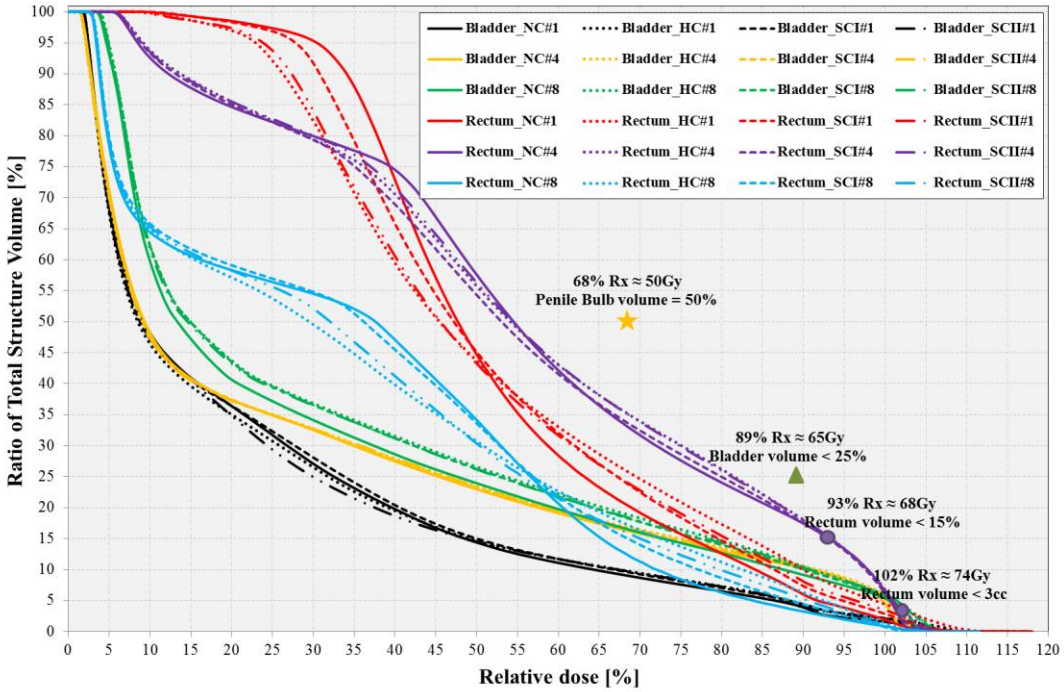

Figure 5-8: DVH comparison for (a) PTV (zoomed in) and (b) OARs (Bladder and Rectum) between *MonArc*-based non-constrained (NC), soft-constrained (SC_I and SC_{II}) and hard-constrained (HC) VMAT plans on prostate patients #1, #4 and #8, respectively. Highlights (●, ▲, ☼) represent labeled OAR-specific dose-quality thresholds.

Similarly, Table 5-6 shows the dose-quality comparison metrics for all ten patient prostate plans #1 − #10. As observed, the NC plans offered the best dose metric for the PTV and the least doses to the main OARs (bladder and rectum). This is followed by the SC_I plan (average of soft-constrained plans for one specified marker only) and SC_{II} plans (average of soft-constrained plans for two specified markers only), respectively. The worst average conformity index was produced by the HC plan. However, it should be emphasized that all the plans (except for patient #1) produced dosimetrically acceptable PTV target coverage and conformity, as defined by our local clinical tolerances using $D_{99\%}$ ($96\% \leq Rx \leq 99\%$), D_{mean} ($101.9\% \leq Rx \leq 105.7\%$), and D_{max} ($104.9\% \leq Rx \leq 117.1\%$). The plan for patient #1 was further re-optimized but still failed to meet the target clinical threshold.

In terms of the differences between the PTV's mean CI with respect to NC plans amongst all ten prostate datasets, there was on average a 7.1% difference for SC_I, 9.4% for SC_{II} and 10.5% for HC plans compared to NC plans. Using the PTV's mean HI values, there was also 3.7% difference for SC_I, 1.8% difference for SC_{II} and 1.5% difference for HC plans respectively, compared to the NC plan amongst all ten prostate datasets. Instead using the average index, there was a 5.4% difference for SC_I, 5.6% difference for SC_{II} and 6.0% difference for HC plans respectively, compared to NC plans. Using the Student's T-test for significance amongst all ten prostate datasets, there is a significant difference (at 95% confidence level whereby $p < 0.05$) in the average index values between the NC and both SC_I ($p = 0.0002$) and SC_{II} plans ($p = 0.0006$). Similarly, there is a significant difference between the NC and HC plans ($p = 0.0006$).

For the bladder OAR, all the constrained plans (i.e. SC_I, SC_{II} and HC) satisfied the clinical dose metrics of V47 < 50% (i.e. bladder volume receiving 47Gy is less than 50% of prescription dose) and V65 < 25% (i.e. bladder volume receiving 65Gy is less than 25% of prescription dose),

as similar to the NC plans for all ten patients albeit at a slightly increased dose [see Table 5-6]. For the rectum OAR, all investigated plans including the NC plans satisfied the clinical dose threshold of V74 < 3cc (i.e. rectal volume receiving 74Gy is less than $3cm^3$), except for patient #4. Using the V68 < 15% metric for the rectum OAR, all investigated plans passed the threshold except for patient #9 (not shown), which was slightly above the threshold by only 2.3–2.6% for all investigated plans [see Table 5-6]. For all the other OARs (head-of-femur and penile bulb), all investigated plans met the clinical dose threshold requirements [not listed].

Table 5-6: Quality metrics for *MonArc* optimized VMAT plans on prostate patient #1 − #10, where soft constrained plans based one-marker and two-markers were averaged, and compared to hard- and non-constrained plans.

Metrics/patient	**#1**	**#2**	**#3**	**#4**	**#5**	**#6**	**#7**	**#8**	**#9**	**#10**
Non-constrained plan per patient i.e. NC										
CI	1.050	1.030	1.080	1.077	1.050	1.030	1.050	1.020	1.090	1.040
HI	1.085	1.067	1.029	1.049	1.050	1.062	1.054	1.042	1.052	1.080
Average Index	1.067	1.049	1.055	1.064	1.063	1.046	1.052	1.031	1.071	1.060
$D_{99\%}$ > 95% Rx	96.2%	96.5%	99.0%	99.1%	98.8%	98.7%	96.9%	97.2%	98.7%	97.5%
V65<25% (Bladder)	4.22%	3.14%	13.14%	10.15%	11.51%	12.90%	5.00%	9.42%	5.57%	11.99%
V68<15% (Rectum)	4.44%	9.64%	8.76%	14.49%	12.97%	5.55%	9.22%	2.39%	17.33%	10.71%
V74<3cc (Rectum)	1.14	2.09	0.76	6.49	1.80	2.23	1.80	0.17	3.68	1.35
MU	464.9	396.1	257.5	596.0	310.6	356.7	352.3	344.9	349.0	306.7
Soft-constrained plan on one marker i.e. SC_I = (SC1 + SC2 + SC3)/3										
CI	1.260	1.120	1.123	1.123	1.120	1.127	1.100	1.070	1.113	1.140
HI	1.128	1.081	1.046	1.077	1.085	1.116	1.104	1.089	1.118	1.094
Average Index	1.194	1.101	1.084	1.103	1.102	1.122	1.102	1.082	1.116	1.121
$D_{99\%}$ > 95% Rx	92.7%	96.8%	98.4%	98.2%	98.2%	97.5%	96.9%	97.6%	98.2%	97.8%
V65<25% (Bladder)	4.82%	3.51%	13.87%	10.55%	13.19%	14.58%	5.89%	10.32%	6.03%	14.73%
V68<15% (Rectum)	5.71%	11.05%	9.91%	14.69%	14.43%	6.59%	10.45%	3.0%	17.54%	13.28%
V74<3cc (Rectum)	1.97	1.99	0.98	3.92	2.06	2.07	2.07	0.15	2.72	2.13
MU	323.1	292.5	245.9	510.0	283.9	285.4	298.2	302.6	286.3	248.9
Soft-constrained plan on two markers i.e. SC_{II} = (SC12 + SC13 + SC23)/3										
CI	1.327	1.153	1.113	1.150	1.143	1.130	1.123	1.093	1.127	1.173

HI	1.099	1.070	1.039	1.061	1.069	1.092	1.086	1.068	1.108	1.068
Average Index	1.213	1.112	1.076	1.106	1.106	1.111	1.105	1.081	1.117	1.121
$D_{99\%}$ > 95% Rx	91.2%	96.5%	98.2%	98.0%	97.7%	97.4%	96.4%	97.6%	97.9%	97.6%
V65<25% (Bladder)	4.81%	3.59%	13.91%	10.79%	13.26%	14.97%	6.15%	10.70%	6.13%	15.31%
V68<15% (Rectum)	6.42%	11.57%	10.11%	14.98%	14.87%	7.20%	10.76%	3.73%	17.42%	14.44%
V74<3cc (Rectum)	2.69	2.44	1.67	5.12	2.05	2.71	2.40	0.22	2.50	2.81
MU	308.1	285.5	242.5	499.3	277.3	274.8	286.1	293.0	276.9	239.5
Hard-constrained plan on all three markers i.e. HC ≡ SC_{III} = SC123										
CI	1.360	1.150	1.110	1.170	1.150	1.130	1.150	1.130	1.120	1.200
HI	1.105	1.065	1.038	1.061	1.071	1.083	1.080	1.058	1.104	1.061
Average Index	1.222	1.107	1.074	1.116	1.110	1.107	1.115	1.094	1.112	1.130
$D_{99\%}$ > 95% Rx	91.4%	96.5%	98.1%	97.8%	97.6%	96.8%	96.0%	97.4%	97.5%	97.7%
V65<25% (Bladder)	4.21%	3.61%	13.60%	18.15%	13.63%	15.34%	6.44%	10.82%	6.09%	15.75%
V68<15% (Rectum)	7.63%	11.84%	10.56%	15.01%	15.69%	7.38%	11.12%	4.55%	17.63%	14.86%
V74<3cc (Rectum)	3.62	2.71	1.41	5.28	2.52	3.07	2.77	0.21	2.18	2.31
MU	307.1	283.2	242.1	496.0	277.0	270.9	283.9	288.9	271.4	235.1

5.3.7 Marker trackability metric for liver SBRT patients

For trackability, Table 5-7 shows values for the percentage of VMAT arc control points where various numbers of markers are visible for liver patient B. For the NC plan, all three markers were visible in the BEV in 14.3% of the control points; only two markers were visible in 36.1%; only one visible in 32.6%; and no markers were visible in 17% of the available gantry control points. For the single marker-based constrained plan – whereby only one specified marker is required to be seen during the optimization (i.e. SC_I) – all three markers are trackable in 32%–52% of the control points. For the double marker-based constrained plan (i.e. SC_{II}), all three markers are visible in 53%–76% of the control points. This also implies that as the constrained marker visibility requirement is increased (i.e. requiring more markers to be visible), more BEV MLC apertures for the soft-constrained (SC) plans approach the hard-constrained (HC) plan optimization requirements, depending on marker location.

Table 5-7: Marker visibility and trackability metric for liver patient B on all SBRT VMAT optimized plans (i.e. NC, SC and HC) showing the percentage gantry control points (CP) in which fiducial markers either were: all fully visible, at least two visible, and at least one visible in BEV.

Constrained plans	%CP with all three markers in BEV	%CP with only two markers in BEV	%CP with only one marker in BEV	%CP with no marker in BEV	%CP with marker 1 in BEV	%CP with marker 2 in BEV	%CP with marker 3 in BEV
SC1 (Inf)	32.2	40.0	27.8	NA	100.0	52.2	52.2
SC2 (Mid)	33.5	46.5	20.0	NA	61.3	100.0	52.2
SC3 (Sup)	52.0	34.0	14.0	NA	62.0	76.0	100.0
SC12 (Inf+Mid)	52.6	47.4	NA	NA	100.0	100.0	52.6
SC13 (Inf+Sup)	76.5	23.5	NA	NA	100.0	76.5	100.0
SC23 (Mid+Sup)	66.0	34.0	NA	NA	66.0	100.0	100.0
HC (Inf+Mid+Sup)	100.0	NA	NA	NA	100.0	100.0	100.0
Reference/non-constrained plan	%CP with all three markers in BEV	%CP with only two markers in BEV	%CP with only one marker in BEV	%CP with no marker in BEV	%CP with marker 1 in BEV	%CP with marker 2 in BEV	%CP with marker 3 in BEV
NC	14.3	36.1	32.6	17.0	49.9	53.5	44.3

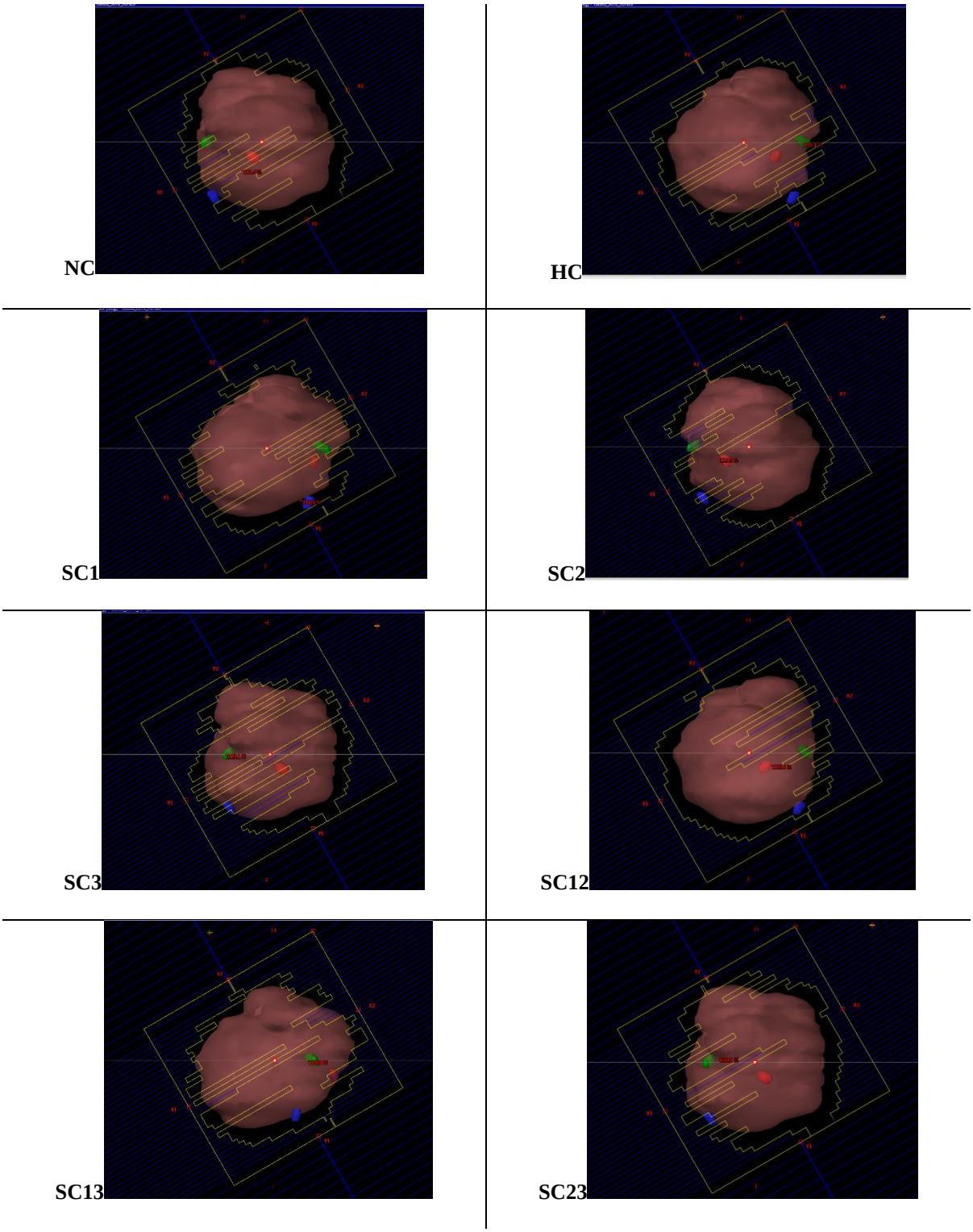

Figure 5-9: Example MLC beams-eye-view (BEV) aperture at one selected gantry control point in each of the non-constrained (NC) and constrained (SC_I, SC_{II}, HC) VMAT plans for liver patient B, with fiducial markers (Inferior-blue; Middle-red; Superior-green) fully-visible or blocked by the MLCs.

5.3.8 Marker trackability metric for lung SBRT patients

Table 5-8 shows values for the percentage number of markers visible at all VMAT gantry arc control points in an example lung patient 1 (p1). For the non-constrained (NC) plan, all three markers were visible and trackable in 15.2% of the total gantry control points; only two markers are trackable in 30.4%; only one trackable in 33.5% and no markers trackable in 20.9% of the BEV and gantry control points. For the single marker-based constrained plans – whereby only one specified marker is required to be seen during the optimization (i.e. SC_I) – all three markers are trackable in 39.1%–45.7% of the MLC apertures. For the double marker-based constrained plans, whereby two specified markers are required to be seen during each optimization (i.e. SC_{II}), all three markers are trackable in 57.4%–88.3% of the MLC apertures. Thus, as the number of constrained marker visibility requirement increases, more BEV MLC apertures for SC plans approach the HC plan optimization requirements, depending on marker location**.**

Table 5-8: Marker trackability metric for lung SBRT patient p1 on all VMAT optimized plans (i.e. NC, SC and HC) showing the percentage gantry control points whereby the fiducial markers were: all fully trackable, at least two trackable, and at least one trackable in BEV.

Constrained plans	% CP with all three markers in BEV	% CP with only two markers in BEV	% CP with only one marker in BEV	% CP with no marker in BEV	% CP with marker 1 in BEV	% CP with marker 2 in BEV	% CP with marker 3 in BEV
SC1 (Inf)	39.1	43.5	17.4	NA	100	60.9	60.9
SC2 (Mid)	45.7	48.2	6.1	NA	85.2	100	54.4
SC3 (Sup)	45.2	36.5	18.3	NA	73.5	53.5	100
SC12 (Inf+Mid)	57.4	42.6	NA	NA	100	100	57.4
SC13 (Inf+Sup)	67.8	32.2	NA	NA	100	67.8	100
SC23 (Mid+Sup)	88.3	11.7	NA	NA	88.3	100	100
HC (Inf+Mid+Sup)	100	NA	NA	NA	100	100	100
Reference/non-constrained plan	% CP with all three markers in BEV	% CP with only two markers in BEV	% CP with only one marker in BEV	% CP with no marker in BEV	% CP with marker 1 in BEV	% CP with marker 2 in BEV	% CP with marker 3 in BEV
NC	15.2	30.4	33.5	20.9	41.3	42.6	51.7

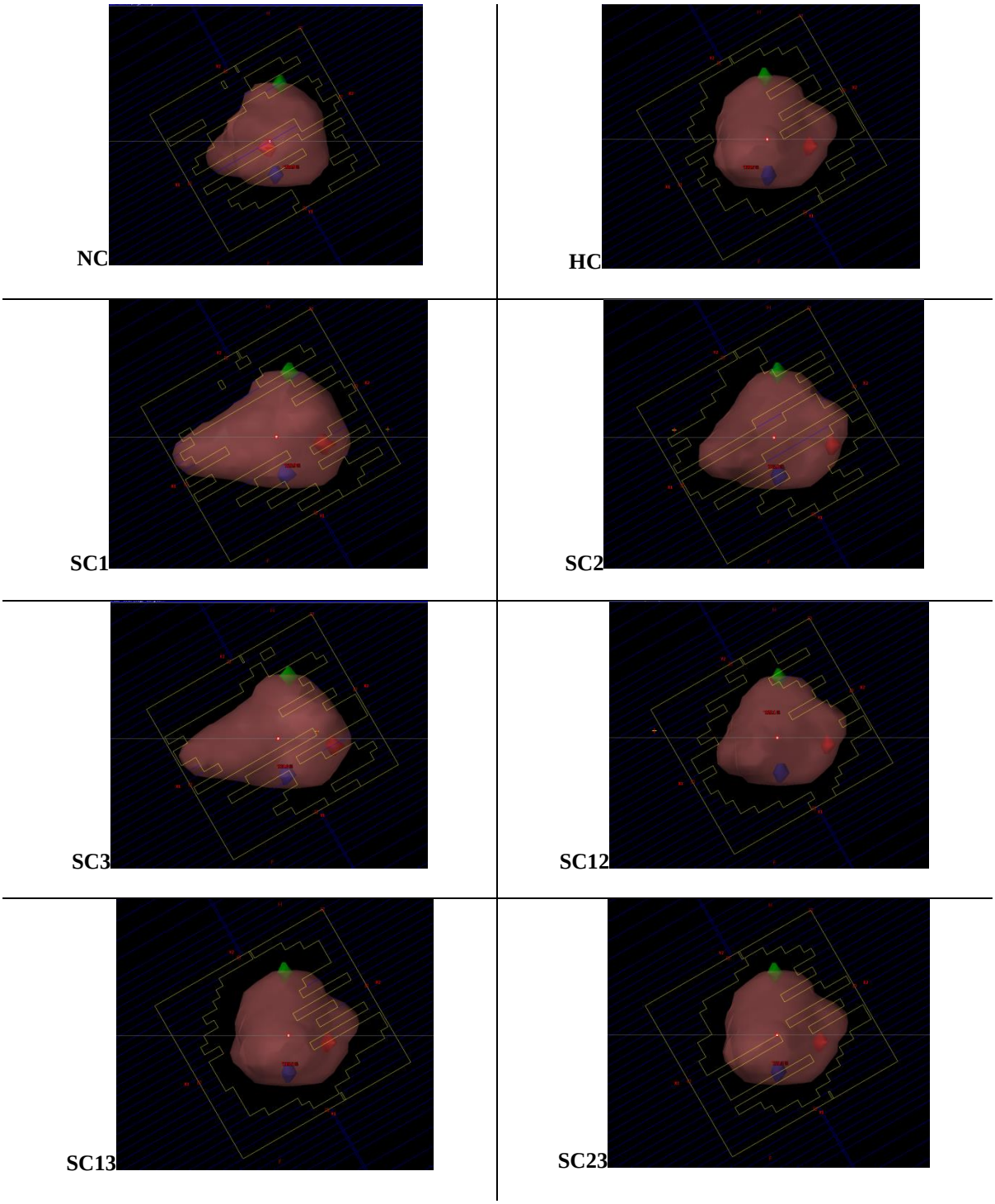

Figure 5-10: Example beams-eye-view (BEV) MLC aperture at different gantry control points in non-constrained (NC) and constrained (HC and SC) VMAT plans for lung SBRT patient p1, with the PTV and fiducial markers (Inferior-blue [1]; Middle-red [2]; Superior-green [3]) either blocked and/or fully-visible by the MLCs.

5.3.9 Marker trackability metric for prostate patients

Figure 5-11 displays the visibility of the markers at a specific gantry control point of all the investigated plans, for prostate patient #8. As observed, the specified constrained markers are fully visible and trackable in the BEV MLC aperture at every control point for tumour tracking application. For example, SC1 represents the soft-constrained plan BEV for marker 1 (green), while SC23 represents the soft-constrained plan BEV for markers 2 and 3 (blue and red).

Table 5-9 shows values for the percentage VMAT gantry arc control points in which the markers are visible, in an example prostate patient #8. For the NC plan, all three markers were visible in the BEV at approximately 32% of the total control points; only two markers were visible in 31%, only one visible in 24.4% and no markers visible in 12.6% of the gantry control points, respectively. It can also be observed that for single marker-based constrained plans – whereby only one specified marker is required to be seen (i.e. SC_I) – all three markers are visible in 60%−63% of the MLC apertures. For double marker-based constrained plans (i.e. SC_{II}), all three markers are visible in 78%−83% of the apertures. This result also shows that as the constrained marker requirements are increased, more MLC apertures incidentally include additional visible markers SC plans, and they approach the visibility for HC plan requirements.

Table 5-9: Marker visibility and trackability metric for prostate patient #8 on all VMAT optimized plans (i.e. NC, SC and HC) showing the percentage gantry control points (CP) in which fiducial markers either were: all three fully visible, at least two visible, and at least one visible in BEV.

Constrained plans	% CP with all three markers in BEV	% CP with only two markers in BEV	% CP with only one marker in BEV	% CP with no marker in BEV	% CP with marker 1 in BEV	% CP with marker 2 in BEV	% CP with marker 3 in BEV
SC1 (Inf)	59.5	28.0	12.5	NA	100.0	72.5	74.5
SC2 (Mid)	63.0	31.0	6.0	NA	79.0	100.0	80.0
SC3 (Sup)	61.0	30.4	8.6	NA	73.8	78.6	100.0
SC12 (Inf+Mid)	83.0	17.0	NA	NA	100.0	100.0	83.0
SC13 (Inf+Sup)	77.9	21.8	NA	NA	100.0	94.4	100.0
SC23 (Mid+Sup)	82.0	18.0	NA	NA	82.0	100.0	100.0
HC (Inf+Mid+Sup)	100.0	NA	NA	NA	100.0	100.0	100.0
Reference/non-constrained plan	% CP with all three markers in BEV	% CP with only two markers in BEV	% CP with only one marker in BEV	% CP with no marker in BEV	% CP with marker 1 in BEV	% CP with marker 2 in BEV	% CP with marker 3 in BEV
NC	32.0	31.0	24.4	12.6	57.7	62.0	62.7

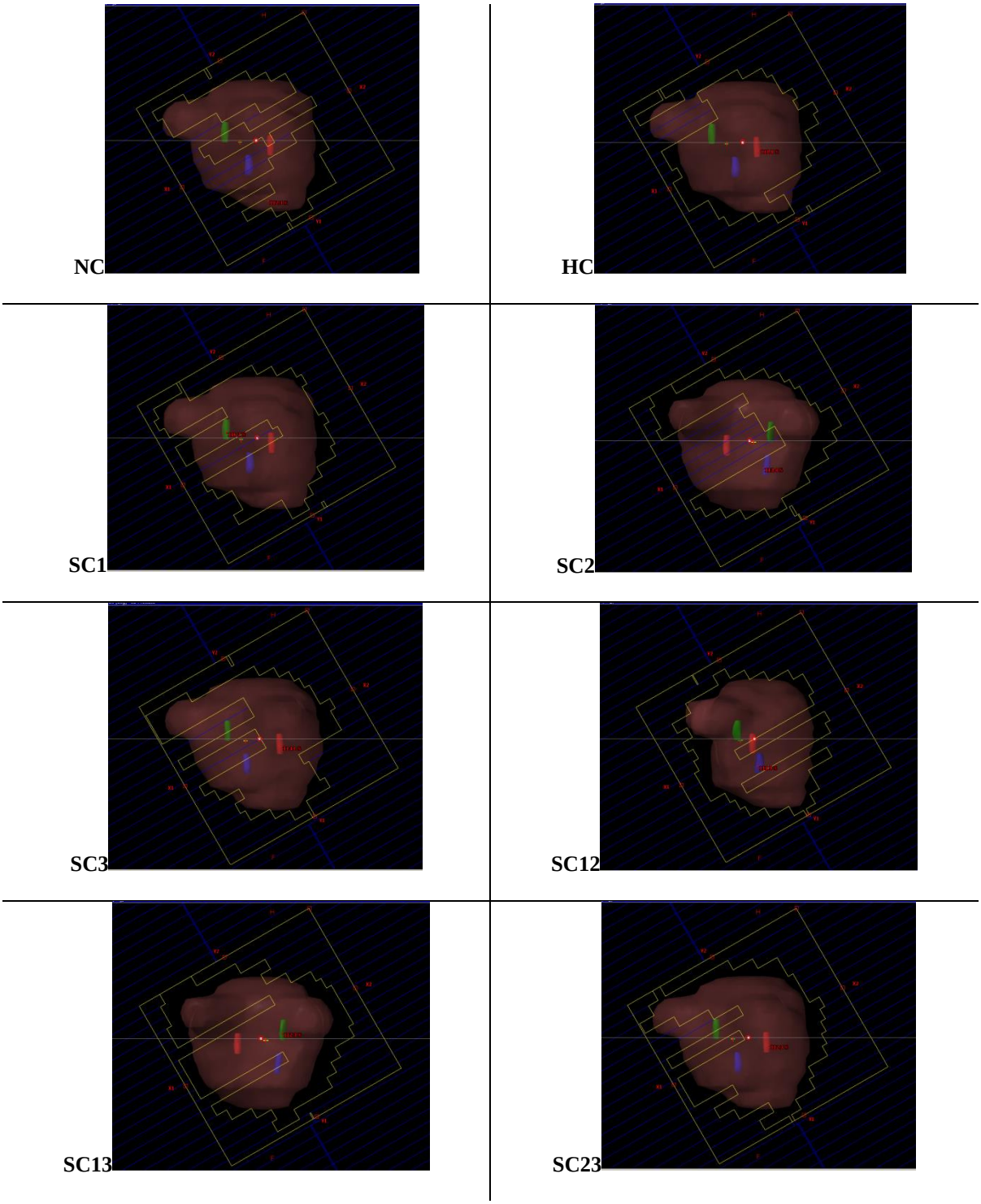

Figure 5-11: Example MLC beams-eye-view (BEV) aperture at one gantry control point in non-constrained (NC) and constrained (HC and SC) VMAT plans for prostate patient #8, with PTV and fiducial markers (1-green; 2-blue; 3-red) either blocked or fully-visible by the MLC apertures.

5.4 Summary and Discussion

For the five liver SBRT VMAT patient datasets, the best dosimetric target coverage for the PTV as indicated by the DVH plots and dose-quality metrics was produced by the non-constrained (NC) plan. The worst target coverage was produced by the HC plan across all five liver datasets [see Figure 5-5 and Table 5-4]. The most optimal dosimetric target PTV coverage for the liver patient dataset – as indicated by the average conformity index – was produced by the non-constrained (NC) plans, followed by the soft-constrained plans. The worst average conformity index was produced by the HC plan. Hence, it can be deduced that the NC plan produced the most optimal plans for the liver datasets. Similarly, the average index value increased as the constrained marker optimization increased from single marker-based (SC_I) plans to double marker-based (SC_{II}) plans and finally triple marker-based (HC ≡ SC_{III}) plans, thus showing the target conformity slightly worsens as more marker constraints are included in the plan optimization.

The dosimetry results of the organs at risk (OARs) for all five liver SBRT patient datasets shows that the constrained plans (SC_I, SC_{II} and HC) all satisfied the clinical dose thresholds for the OAR esophagus and OAR heart [see Table 5-4]. However, for the OAR large bowel in liver patient C, all investigated plans including the NC plan failed the established dose threshold. This may be due to several reasons: the size of the large bowel (approx. 515cm^3) in this patient being the largest in the set, the size of the fiducial markers in the liver patients compared to the prostate patients, and the location of one of the markers in the liver being implanted outside the PTV target, as opposed to the prostate patient datasets where all markers were contained inside the PTV.

In terms of the beam monitor units (MU), the highest values were produced by the NC plans for all the liver patient datasets [Table 5-4], followed by the SC_I and SC_{II} plans respectively. The lowest MU values were obtained with the HC plans. Since there are no fiducial marker

visibility constraints in the optimization process for NC plans, MLC apertures typically possess smaller fields and jaw openings and thus result in higher modulation to achieve the dose objectives. Alternatively, the SC_I and SC_{II} plans are constrained to see at least one- and two-specific markers respectively, making the beam less modulated as the MLCs are required to be open to visualize at least one marker. For the HC plans, the jaw openings and aperture fields are larger, thus resulting in the least modulation. Hence, it can be deduced that the beam modulation is inversely proportional to the number of marker visibility constraints in the optimization.

In terms of the trackability metric for the example liver patient B in Table 5-4, trackability for all three markers is feasible in at least 14% of the gantry rotation in the reference non-constrained VMAT plan, while none of the markers are available for tracking in 17% of the arc delivery. For the constrained plans in liver patient B, all three markers were visible at a range between 32%−100% of the available gantry arc rotation. The SC plans exhibited improved visibility as the marker constraint increased from one to two markers. Thus, the soft-constrained marker implementations approach the hard-constrained requirement for marker visibility. However, trackability comes at the risk of reduced dosimetric coverage, as soft-constrained plans produce slightly worse PTV target dose-volume coverage as marker visibility constraints increases. This also implies that trackability is inversely proportional to the PTV target's dosimetric coverage for the liver patient dataset. Similar conclusions cannot be made for the OARs but notably, all plans in general met the OAR specific clinical dose objectives.

For the VMAT lung SBRT patient datasets, the best dosimetric target coverage for the PTV as indicated by the dose-quality metrics [Table 5-5] was produced by the NC plans. The worst coverage was provided by the HC plans. Using the average conformity index value, the NC plan still provided the best quantitative metric score across all lung patient datasets and therefore the

most dosimetrically optimal plans. However, there were no significant disparities in target coverage amongst all plans. For the lung SBRT datasets, there were statistically significant differences between the NC and HC plans across the group but no statistically significant difference between the NC and SC_I plans. The discrepancy in significance testing result is likely due to the small sample size (n = 5) for the lung SBRT datasets, as the assumption of a normally distributed data points was not met hence the use of a non-parametric test (Mann-Whitney U-test).

OAR dosimetry results for the five lung SBRT patients shows that all plans consistently met the clinical OAR dose objectives [Table 5-5]. However, some SC_I plans (e.g. SC3 plan for the Superior marker) outperformed the NC plan, exposing the heart OAR to up to 50% less dose relative to the reference NC plan. In terms of the beam output, the NC plan produced the highest output as measured in MU. This also shows that beam modulation is inversely proportional to the number of markers visually constrained into the plan optimization, thereby leading to less modulation. This is similar to the trend beam output results for the liver and prostate patients.

For the example VMAT lung SBRT patient I plan, trackability of all three markers is feasible in at least 15.2% of the gantry rotation in the reference non-constrained lung VMAT plan, while none of the fiducials would be available for tracking in at least 20.9% of the treatment delivery [Table 5-8]. However, for the soft-constrained plans in the lung patient, all three markers were trackable between 39%−88% of the available gantry arc rotation, and 100% for hard-constrained plans. The soft-constrained plans also exhibited increased coverage as the constrained marker visibility results improved from one specific marker (SC_I = SC1, SC2 or SC3) to two specific markers (SC_{II} = SC12, SC13 or SC23). This also shows that soft-constrained plans approach the hard-constrained plan as more markers are constrained into the BEV and MLCs open to accommodate the specified markers.

For the ten VMAT prostate patient datasets, the best dosimetric target coverage for the PTV as indicated by the DVH and dose-quality metrics was produced by the non-constrained (NC) plan [see Figure 5-8 and Table 5-6]. All other constrained plans (SC and HC) had similar metrics with no significant disparity in target coverage. The most optimal dosimetric target coverage for the PTV in the prostate patient datasets – as indicated by $D_{99\%}$, conformity index (CI), homogeneity index (HI) and gradient measure (GM) – was produced by the non-constrained (NC) plans, followed by the soft-constrained (SC) and hard-constrained (HC) plans [Table 5-6], respectively.

Using the average conformity index value, the NC plan still provided the best quantitative metric score across all prostate patient datasets and therefore the most dosimetrically optimal plans. This was expected as previously reported and is in agreement with our preliminary feasibility study on prostate data[180]; the NC plan has no marker visibility constraints in its implementation. In terms of the constrained marker-based position, the SC1 (Inferior) or SC3 (Superior) marker-based plans produced the best results for the set of SC_I plans, while the HC plans – using the volume covered by 107% of the prescribed Rx dose $V_{107\%}$ [not shown here] – produced the worst dosimetric coverage across all patients. The difference in the metrics between HC and SC plans were not always significant across the prostate patient dataset. However, we did not anticipate the HC plans to produce comparable results to some SC plans as the HC plans are constrained such that all three fiducial markers are fully visible at all gantry angles in the beam's eye view, thereby forcing larger MLC apertures. Generally, it can be deduced that the target dose conformity worsens as the constrained marker parameters increases from one marker-based SC_I plans to two marker-based SC_{II} plans, and to three marker-based HC plans.

Furthermore, the required total monitor units (MU) were highest with the NC plans for all prostate patient datasets, followed by the SC_I and SC_{II} plans respectively. The lowest MU was

obtained with HC plans [see Table 5-6]. Since there are no fiducial marker visibility constraints in the optimization process for NC plans, MLC apertures possess smaller fields and jaw openings and thus result in high modulation to achieve the dose objectives. Alternatively, the SC_I and SC_{II} plans are constrained to see at least one and two specific markers respectively, making the beam less modulated as the MLCs are required to be open to visualize at least one marker. For the HC plans, the jaw openings and aperture fields are larger, thus resulting in the least modulation. Hence, it can be deduced that the beam modulation is inversely proportional to the number of marker visibility constraints included in the optimization, which was as reported and agrees with the liver dataset and our preliminary study on prostate dataset.

In terms of organs at risk (OARs), dosimetry results for all ten prostate datasets showed that the constrained plans (i.e. SC_I, SC_{II} and HC) mostly satisfied the clinical dose thresholds for the bladder and rectum [see Table 5-6], as well as for the femoral head and penile bulb [not listed]. The locally defined bladder and femoral head dose thresholds were satisfied by all the investigated plans for all ten patients, while the rectal dose objective was met by all the plans, except for one patient (patient #9) where all plans including the NC plan failed. The single-marker based SC_I plans produced slightly better OAR dose-quality results compared to the SC_{II} plans, while the HC plan produced the worst. In general, locally defined OAR dose thresholds were satisfied by all investigated plans including SC and HC plans for the ten prostate datasets.

In terms of trackability, for the example NC prostate plan in patient #8, all three markers [see Table 5-9] were visible in 32% of the gantry angles, while none of the fiducials would be available for tracking in at least 12% of the gantry angles. However, in all the soft-constrained prostate plans, all three markers were visible at a range between 60% − 100% of the gantry angles. The SC plans also exhibited improved visibility as the marker constraint increased from one to

two markers. This shows the SC plans approach the HC plan as more markers are included in the optimization as the MLCs open to accommodate the required markers.

The approach presented by Azcona *et al*[39] attempted to reduce the dependency on marker visibility for VMAT tumour tracking applications by predicting the future fiducial marker positions for prostate patients including those gantry angles where markers may be blocked by the MLCs. However, their technique requires template selection that needs to be small enough to allow processing in real-time; and the authors point out that the technique suffers when data is sparse and for consecutive control points where markers are unavailable. Therefore, some minimum visibility of fiducial markers in the small and irregularly shaped fields found in arc radiotherapy (e.g. 4D-VMAT) needs to be assured to perform real-time tumour tracking robustly.

A few limitations of our work include that we have not studied the effects on more patient datasets due to the limited data availability at our clinic. We also did not study the statistical power of sample size on our results as we did not have anecdotal data related to our study. Hence, we were limited to the availability of data. Also, our work could be modified to account for the marker motion relative to the motion of the OARs whereby the control points in the gantry are synchronized to the target motion phases as available in the 4D-CT. We were also limited somewhat in the manner in which the constrained optimization was implemented, whereby the visibility of specific markers was enforced through the entire planned VMAT arc. We could potentially remove this limitation and provide more flexibility in tracking the markers, for example by ensuring visibility of any one out of the three markers (instead of a single specific marker), or any two out of the three markers during the optimization. However, due to the relationship between marker positions, MLC leaf motion and gantry control points, such an approach might be difficult to implement in real-time tracking methods considering the required connectedness between MLC

leaf positions[158] in respective adjacent control points. Also, when applying a tracking algorithm for the purposes of marker-based tumor tracking, typically a specific marker needs to be visible in a template or region[39] throughout the VMAT delivery for successful tracking. This may conflate the identification of the markers during tracking and reduce robustness.

Another limitation is we have used the classical ICRP definitions of the target dose homogeneity index, which uses point-based dose values as opposed to voxel-based parameters. However, an examination using several other definitions of HI[181] did not produce values that were significantly different than our results (not shown). Finally, in terms of statistical significance, the PTV conformity and homogeneity results show that the constrained plans were significantly different from the NC plans for the prostate datasets. However, all the constrained plans met the local dose objectives. For the liver and lung SBRT datasets, there were statistically significant differences between the NC and HC plans across the group but no statistically significant difference between the NC and SC_I plans. The discrepancy and limitation in significance testing result is likely due to the small sample sizes ($n = 5$) for the lung and liver SBRT datasets, as an assumption of normally distributed data points may not be met in order to satisfy the test. Thus, we believe that the statistical test is not a decision parameter as it does not translate to clinical significance.

Chapter 6 Summary, Conclusions and Future Work

6.1 Summary

Radiation therapy treatments have become increasingly more complex with recent advancements including adoption of volumetric modulated arc therapy (VMAT) and stereotactic body radiation therapy (SBRT). VMAT is adopted due to its improved tumour dose conformality, improved sparing of normal tissue structures, and increased delivery efficiency compared to classic treatment techniques. This results in acceptable tumour control with reduced normal tissue complications as described in Section 3.1. However, SBRT poses additional challenges due to the higher treatment doses per fraction (hypofractionation) delivered.

Respiratory motion in certain tumours (thoracic and abdominal) creates further complications during radiation treatment delivery, as the tumour position or location needs to be known or estimated in real-time. A common strategy to locate the tumour is by using radio-opaque fiducial 'markers' inserted at or near the tumour tissue before treatment delivery. Due to the contrast differences, the markers can be easily visualized as a surrogate for the tumour position in x-ray projection images. Such projection images can be obtained from the megavoltage (MV) treatment beam on amorphous silicon (a-Si) electronic portal imaging devices (EPIDs), or kilovoltage (kV) images from on-board x-ray imagers.

Multiple methods to account for tumour motion have been described in Section 2.5. Of all the methods, dynamic tumour tracking offers the most promising approach as it allows the most aggressive shrinking of the target margins and can be delivered much more efficiently while maintaining patient comfort. Many approaches to dynamic tumour tracking have been discussed in Section 2.5.5, but the most practicable approach of all is dynamic multi-leaf collimator (DMLC) tracking as it utilizes the MLC to define, shape and modulate the treatment beam intensity during

delivery without the need for extra imaging from stereoscopic KV x-ray devices which increases patient dose, as required for the Vero® gimbal and CyberKnife® dynamic tumour tracking systems.

The objective of this thesis was to develop and test a new optimization approach for volumetric modulated arc therapy (VMAT) that could incorporate visibility constraints of fiducial markers of moving tumours, while still satisfying the required dosimetric quality. This thesis is based on MLC-based tracking approaches for VMAT plans. Specifically, we focus on the optimization of hypofractionated VMAT plans using fiducial marker visibility constraints in order to aid MLC tumour tracking. With the visibility of the markers in the beam's-eye-view (BEV) during treatment, the tumour can be 'seen' and tracked in real-time such that the most optimal delivery of the prescribed dose could be achieved in order to improve clinical performance. As discussed in Section 3.4.4, progressive resolution optimization (PRO) was the primary optimization method employed for all investigated treatment plans, using the *MonArc* optimization development software. PRO was chosen because it provides better efficiency in the optimization due to its distribution of the radiation beam treatment delivery and MLC restrictions in VMAT, compared to the static-gantry delivery in IMRT.

In Chapter 4, the 3D-VMAT algorithm developed by Otto[10] was modified in MATLAB® to include marker visibility constraints in the MLC BEV into the optimization process (Section 3.4.5). This was developed and tested using a dynamic thorax phantom, and initially applied to two example clinical datasets to evaluate feasibility. Each phantom/patient case examined included three fiducial markers, the most commonly used number of fiducials clinically. Optimization constraints applied to all visibility combinations of one, two, or three markers were studied, resulting in seven different constrained plans for each phantom/patient case (Section 4.3.3).

After the technique was validated, it was retrospectively applied in 0 on a larger number of patient datasets from three different disease sites including five lung, five liver and ten prostate patients, in order to quantitatively assess the impact of varying patient geometry and fiducial marker placement on the visibility and dosimetry of produced plans. To compare treatment plan qualities relative to non-constrained plans, we used standard DVH and quantitative dose-quality metrics, along with the trackability metric (Sections 5.3.1 – 5.3.9).

6.2 Conclusions

6.2.1 Constrained optimization for liver SBRT patients

For the five liver SBRT patients, the most optimal target coverage for the PTV as indicated by a combination of the qualitative evaluation of the DVH plots and the quantitative dose-quality metrics was produced by the non-constrained (NC) plan. The worst target coverage was produced by the hard-constrained (HC) plan across the liver datasets. Similarly, the average index value increased as the constrained marker optimization increased from single marker-based (SC_I) plans to double marker-based (SC_{II}) plans and finally triple marker-based ($HC \equiv SC_{III}$) plans, thus showing the target conformity slightly worsens as more marker constraints are included in the plan optimization.

The dosimetry results of the organs at risk (OARs) for all five liver SBRT patient datasets shows that the constrained plans (SC_I, SC_{II} and HC) all satisfied the clinical dose thresholds for the OAR esophagus and OAR heart. However, situations where the markers in the liver were implanted outside the target volume may lead to overexposure of OARs.

6.2.2 Constrained optimization for lung SBRT patients

Similarly, for the five lung SBRT patients, the most optimal target coverage for the PTV as indicated by a combination of the qualitative evaluation of the DVH plots and the quantitative dose-quality metrics was produced by the non-constrained (NC) plan. The worst target coverage was produced by the hard-constrained (HC) plan across the lung datasets. Similarly, the average index value increased as the constrained marker optimization increased from one marker-based (SC_I) plans to two marker-based (SC_{II}) plans and finally three marker-based ($HC \equiv SC_{III}$) plans. The rates of increase between the plans were more noticeable for the lung datasets, compared to the liver datasets.

OAR dosimetry results for the five lung SBRT patients shows that all plans consistently met the clinical OAR dose objectives. However, some soft-constrained SC_I plans (e.g. SC3 plan for the superior marker) outperformed the non-constrained NC plan, exposing the heart OAR to up to 50% less dose relative to the NC plan. The reason for this discrepancy is attributed to the relative location of the fiducial markers in proximity to the target volume and sensitive tissues.

6.2.3 Constrained optimization for hypofractionated prostate patients

Similarly, for the ten prostate patients, the most optimal target coverage for the PTV using the DVH plots and quantitative dose-quality metrics was produced by the non-constrained (NC) plan, followed by the soft-constrained (SC_I, SC_{II}) plans; the worst target coverage was produced by the hard-constrained (HC) plan. However, the difference in the metrics between HC and SC plans were not always significant across the prostate patient datasets. The reason for this is again due to the apparent location of the fiducials being entirely inside the target volume, allowing for less MLC modulation differences.

In terms of OARs, dosimetry results for all ten prostate datasets showed that the constrained plans (i.e. SC_I, SC_{II} and HC) mostly satisfied the clinical dose thresholds for the OAR bladder and OAR rectum, as well as for the femoral head and penile bulb, except for one patient (patient #9) where all plans including the NC plan failed to satisfy the rectal dose threshold.

6.2.4 General conclusion

The results presented in this study show the evaluation of incorporating tumour visibility objectives together with dose objectives in the optimization of VMAT treatment plans, and their relative success achieving both types of objectives. Testing on three different tumour sites show that plans can be developed that satisfy visibility requirements to ensure visibility of fiducial markers at all MLC apertures, while still achieving the dosimetric objectives of the target and OARs. In terms of trackability, across all the disease sites, one marker is always fully visible at all BEV apertures (i.e. 100% of the gantry arc control points) for the constrained plans. All three markers were fully visible in at least 33% of BEV apertures for the constrained plans, while also satisfying the required dosimetric objectives. Although dose metrics showed some deterioration for constrained plans (-6% for SC_I up to -15% for HC, when compared to NC using the PTV average index), the required dosimetric objectives were still satisfied in at least 90% of patients.

Using soft constraints (SC_I, SC_{II}) achieved acceptable dosimetry metrics for both the target and OARs across all tumour sites. Especially for lung and liver tumours where soft constrained plans on one marker (SC_I) produced plans that satisfied the dosimetric objectives across all patient datasets. However, OAR doses may be increased depending on the number of constrained markers and their location in the BEV. This is related to the realization that fiducial markers for those lung and liver patients are not necessarily located within the PTV, causing the MLCs to extend to their

limits. In some patients, the soft-constrained plans on two markers (SC_{II}) performed worse than the hard-constrained (HC) plans. This discrepancy is again primarily due to the relative fiducial marker location in those patients. Hence, the use of hard-constrained (HC) plans is not recommended for tracking when optimal dose delivery is paramount to the target and surrounding OARs.

In terms of estimating fractional treatment times, all constrained plans exhibited reduced beam outputs (i.e. lower MUs) compared to the reference clinical non-constrained plans, as expected (i.e. varying with allowed beam modulation). Hence, it can be deduced that the beam modulation is inversely proportional to the number of constrained marker visibility in the optimization. However, there is a trade-off between the enforced marker-visibility constraints versus the dosimetric objectives in the plan optimization. In conclusion, our results show that the fiducial marker visibility/trackability can be improved by adding appropriately designed constraints in the optimization step, while still preserving acceptable dosimetric plan quality. This work should help to improve the performance of real-time tumour tracking applications during VMAT delivery.

6.3 Future Work

6.3.1 Real-time DMLC tracking

Based on the literature demonstrating improved real-time tumour tracking with increased marker visibility, we are confident that incorporating marker visibility into treatment plan optimization will lead to improved success of real-time tumour tracking applications. However, we have not explicitly shown this and therefore this should be the subject of future work. Some examples of real-time tracking algorithms implemented for moving tumours are the DMLC

algorithms from Sawant *et al*[21] as introduced in Section 2.5.5.3, which have been used to guide prostate[182] and lung[170] tumours. A DMLC algorithm was recently combined with kV X-ray monitoring to guide and track fiducial markers and liver SBRT tumours with very high accuracy in the CTV delivered dose distribution[179] (ΔD_{95}: 0.2% with tracking and 6.3% without tracking). Although, the authors reported that hotspots were created in tumour motion perpendicular to the MLC leaf travel, this can be compensated for by using a 3D probability-based approach to estimate the motion here[169].

6.3.2 4D-VMAT implementation

Even though this work is intended to support real-time tumour tracking methods, the VMAT optimization approach used here uses an average CT dataset created from the 4D-CT data to create the 3D representation of the phantom/ patient's planning dataset. Therefore, respiratory motion is not accounted for and so the unaccounted relative motion between the targets and the surrounding tissues and OARs may lead to larger or lower dose depositions during actual treatment delivery. One method to account for patient respiratory motion in the planning step is to synchronize all ten respiratory phase information from the CT dataset to the expected gantry arc rotation of VMAT. This respiratory phase-gantry arc rotation synchronization is the basis of 4D-VMAT.

The key characteristic of the 4D-VMAT system is that while other radiation therapy techniques, such as gated-VMAT and 3D-VMAT, rely on a static representation of the patient based on 3D CT data (including an averaged 4D-CT), a true 4D-VMAT optimization integrates the patient's 4D-CT data into the optimization process. This is achieved by correlating consecutive beam apertures to consecutive CT phases [Figure 6-1]. Thus, only one CT phase is assigned per

beam, generating treatment plans with respiratory phase-optimized apertures whose deliveries are synchronized to the patient's breathing motion. The 4D-VMAT system may improve radiation sparing of the OAR by integrating temporal information on patient anatomy and tumour motion into treatment planning.

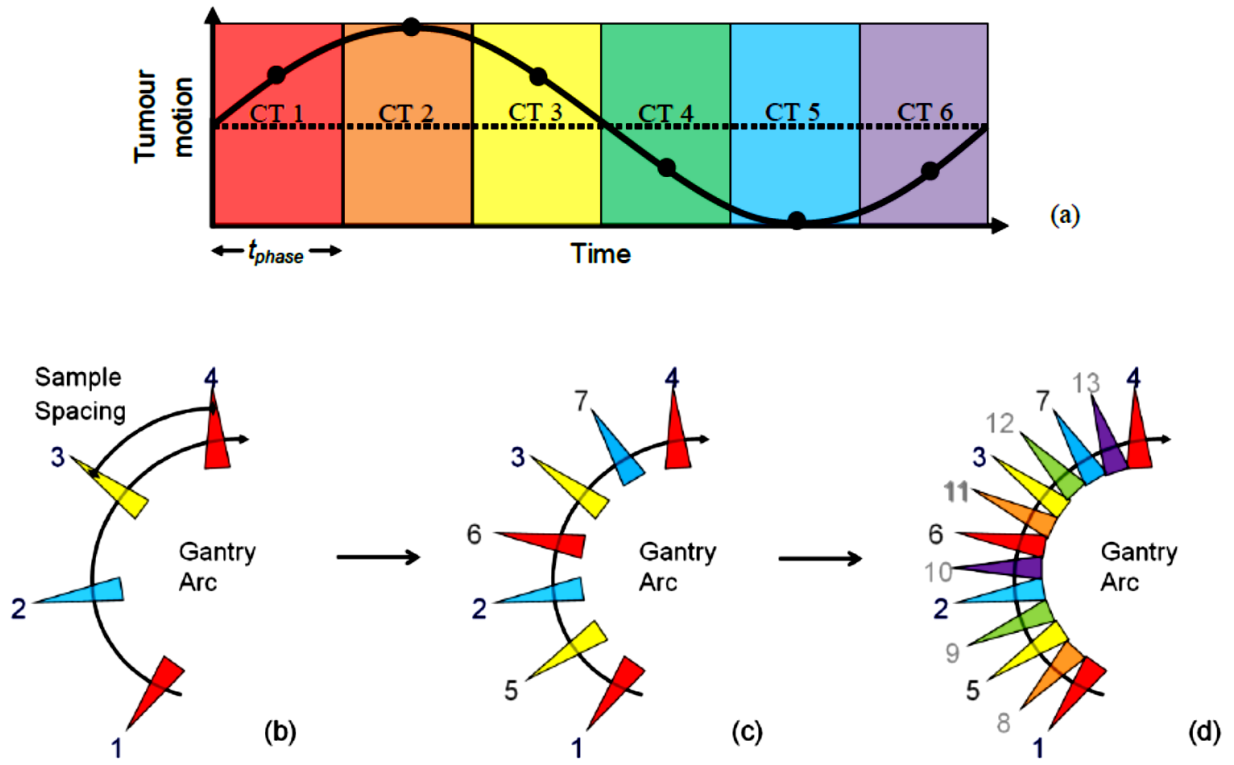

Figure 6-1: (a) Schematic representation of the respiratory cycle into multiple phases. Colours represent specific CT phases 1–6. (b) At the start of plan optimization, the arc is largely sampled with few beam apertures. (c) As optimization progresses, beam resolution increases. Numbers represent the order in which beam apertures are introduced into the optimization. (d) By the end of optimization, the arc is fully sampled and sequentially delivered beams correlate to sequential CT phases. The 4D-CT data is sampled multiple times over the arc. Reprinted from Chin *et al*[173] used with permission from IOP Publishing.

Previous work on 4D-VMAT was carried out by Ma *et al*[38] using a digital phantom to simulate a lung and pancreas case. The work of Chin *et al*[173] as well as Niu *et al*[183] investigated 4D-VMAT on patients and the ability to spare normal health tissues based on the relative motion

between OARs and targets, as well as the shape of the tumour and OAR. 4D-VMAT enhanced OAR sparing by exploiting large tumour motions. Therefore, for smaller tumour motions (e.g. less than 1cm), 4D-VMAT may be unnecessary as VMAT provides similar level of OAR sparing if margins smaller than the motion encompassing margins are used to generate the PTV, as suggested by van Herk *et al*[5]. However, even with this limitation, a potentially impactful area of future research would be investigating the adaptation of the proposed optimization method to 4D-VMAT.

A significant downside to using 4D-VMAT is the reduced efficiency due to longer treatment times as a result of the speed of gantry rotation being affected by the patient's respiratory period. A way to address this limitation is to align the collimator such that leaf motion is parallel to tumour motion. Nonetheless, studies[21] have reported that this approach may detrimentally affect the algorithm's intensity modulation flexibility in the axis perpendicular to tumour motion. A more viable approach may be to restrict beam weight constraints in the 4D-VMAT optimization algorithm to limit excessive beam modulation. A more efficient approach is to use a 'segment aperture morphing' method as presented by Klawikowski *et al*[184]. This method adjusts the MLC positions due to the change of target contour projection in the BEV, upon creating a treatment plan on a reference phase (e.g. end of exhale – EoE phase) and then deforming to the remaining phases.

Another concern is that 4D-VMAT is a respiratory correlated technique. As a result, treatment plans are tailored to specific patient respiratory motions given by 4D-CT data. Thus, to be an accurate representation of motion, the patient must breathe in a similar fashion during treatment delivery as during planning 4D-CT. Another common error limiting the practicality of 4D-VMAT is desynchronization errors (random and systematic). Especially for highly mobile tumours (e.g. lung), there is increased possibility that the treatment delivery may lag the patient

breathing by a couple of respiratory phases. This may lead to reduced dose coverage of the desired target volume and OARs, as was reported by Chin *et al*[173].

When tumour motion is involved in radiation therapy, there are three primary strategies available to reduce dose to healthy tissues: (a) eliminate or minimize the motion encompassing margin used to ensure target coverage (b) temporally spread the instantaneous dose delivered to the tumour over its motion trajectory (c) optimize radiation dose delivery to respiratory phases that maximize the relative distance between the target and OARs. Chin *et al*[173] reported that 4D-VMAT is able to match and spare OARs as much as obtained by gated-VMAT in many scenarios, and at reduced treatment times compared to gated-VMAT.

In conclusion, if sparing the OAR is of the utmost priority, then the preferred treatment options would be gated-VMAT or 4D-VMAT. Notably, the benefits of gated-VMAT or 4D-VMAT are less likely to be observed for tumour motions below 1 cm as expansion of treatment margins may only be in the range of a few millimeters[185]. Further areas of future research would be investigating the adaptation 4D-VMAT to irregular patient breathing.

6.4 Bibliography/References

1. Brenner DR, Weir HK, Demers AA, et al. Projected estimates of cancer in Canada in 2020. *Can Med Assoc J*. 2020;192(9):E199-E205. doi:10.1503/cmaj.191292
2. Keall PJ, Mageras GS, Balter JM, et al. *The Management of Respiratory Motion in Radiation Oncology - Report of AAPM Task Group 76*. Vol 33.; 2006. doi:10.1118/1.2349696
3. Verma PS, Wu H, Langer MP, Das IJ, Sandison G. Survey: Real-Time tumor motion prediction for image-guided radiation treatment. *Comput Sci Eng*. 2011;13(5):24-35. doi:10.1109/MCSE.2010.99
4. McKenzie AL, van Herk M, Mijnheer B. The width of margins in radiotherapy treatment plans. *Phys Med Biol*. 2000;45:3331-3342.
5. van Herk M. Errors and Margins in Radiotherapy. *Semin Radiat Oncol*. 2004;14(1):52-64. doi:10.1053/j.semradonc.2003.10.003
6. Seppenwoolde Y, Lebesque J V., De Jaeger K, et al. Comparing different NTCP models that predict the incidence of radiation pneumonitis. *Int J Radiat Oncol Biol Phys*. 2003;55(3):724-735. doi:10.1016/S0360-3016(02)03986-X
7. Kwa SLS, Lebesque J V., Theuws JCM, et al. Radiation pneumonitis as a function of mean lung dose: An analysis of pooled data of 540 patients. *Int J Radiat Oncol Biol Phys*. 1998;42(1):1-9.
8. Mehta V. Radiation pneumonitis and pulmonary fibrosis in non-small-cell lung cancer: Pulmonary function, prediction, and prevention. *Int J Radiat Oncol Biol Phys*. 2005;63(1):5-24. doi:10.1016/j.ijrobp.2005.03.047
9. Palma DA, Senan S, Haasbeek CJA, Verbakel WFAR, Vincent A, Lagerwaard F. Radiological and clinical pneumonitis after stereotactic lung radiotherapy: A matched analysis of three-dimensional conformal and volumetric-modulated arc therapy techniques. *Int J Radiat Oncol Biol Phys*. 2011;80(2):506-513. doi:10.1016/j.ijrobp.2010.02.032
10. Otto K. Volumetric modulated arc therapy: IMRT in a single gantry arc. *Med Phys*. 2008;35(1):310-317. doi:10.1118/1.2818738
11. Bzdusek K, Friberger H, Eriksson K, Hårdemark B, Robinson D, Kaus M. Development and evaluation of an efficient approach to volumetric arc therapy planning. *Med Phys*.

2009;36(2009):2328-2339. doi:10.1118/1.3132234

12. Yu CX. Intensity-modulated arc therapy with dynamic multileaf collimation: an alternative to tomotherapy. *Phys Med Biol*. 1995;40(9):1435-1449. doi:10.1088/0031-9155/40/9/004
13. Cao D, Afghan MKNN, Ye J, Chen F, Shepard DM. A generalized inverse planning tool for volumetric-modulated arc therapy. *Phys Med Biol*. 2009;54(21):6725-6738. doi:10.1088/0031-9155/54/21/018
14. Ulrich S, Nill S, Oelfke U. Development of an optimization concept for arc-modulated cone beam therapy. *Phys Med Biol*. 2007;52(14):4099-4119. doi:10.1088/0031-9155/52/14/006
15. Cao D, Holmes TW, Afghan MKN, Shepard DM. Comparison of Plan Quality Provided by Intensity-Modulated Arc Therapy and Helical Tomotherapy. *Int J Radiat Oncol Biol Phys*. 2007;69(1):240-250. doi:10.1016/j.ijrobp.2007.04.073
16. Milette MP, Otto K. Maximizing the potential of direct aperture optimization through collimator rotation. *Med Phys*. 2007;34(4):1431-1438. doi:10.1118/1.2712574
17. Shepard DM, Earl MA, Li XA, Naqvi S, Yu C. Direct aperture optimization: A turnkey solution for step-and-shoot IMRT. *Med Phys*. 2002;29(6):1007-1018. doi:10.1118/1.1477415
18. Seppenwoolde Y, Berbeco RI, Nishioka S, Shirato H, Heijmen B. Accuracy of tumor motion compensation algorithm from a robotic respiratory tracking system: a simulation study. *Med Phys*. 2007;34(7):2774-2784. doi:10.1118/1.2739811
19. Depuydt T, Poels K, Verellen D, et al. Treating patients with real-time tracking using the Vero gimbaled linac system: Implementation and first review. *Radiother Oncol*. 2014;112(3):343-351. doi:10.1016/j.radonc.2014.05.017
20. Dean MK, Ahmed AA, Johnson P, Elsayyad N. Distribution of dedicated stereotactic radiosurgery systems in the United States. *Appl Radiat Oncol*. 2019;8(1):26-30.
21. Sawant A, Venkat R, Srivastava V, et al. Management of three-dimensional intrafraction motion through real-time DMLC tracking. *Med Phys*. 2008;35(5):2050-2061. doi:10.1118/1.2905355
22. Sawant A, Smith RL, Venkat RB, et al. Toward Submillimeter Accuracy in the Management of Intrafraction Motion: The Integration of Real-Time Internal Position Monitoring and Multileaf Collimator Target Tracking. *Int J Radiat Oncol Biol Phys*. 2009;74(2):575-582. doi:10.1016/j.ijrobp.2008.12.057

23. Keall PJ, Sawant A, Cho B, et al. Electromagnetic-guided dynamic multileaf collimator tracking enables motion management for intensity-modulated arc therapy. *Int J Radiat Oncol Biol Phys*. 2011;79(1):312-320. doi:10.1016/j.ijrobp.2010.03.011
24. Buzurovic I, Huang K, Yu Y, Podder TK. A robotic approach to 4D real-time tumor tracking for radiotherapy. *Phys Med Biol*. 2011;56(5):1299-1318. doi:10.1088/0031-9155/56/5/005
25. Krauss A, Nill S, Tacke M, Oelfke U. Electromagnetic real-time tumor position monitoring and dynamic multileaf collimator tracking using a Siemens 160 MLC: Geometric and dosimetric accuracy of an integrated system. *Int J Radiat Oncol Biol Phys*. 2011;79(2):579-587. doi:10.1016/j.ijrobp.2010.03.043
26. Keall PJ, Colvill E, O'Brien R, et al. The first clinical implementation of electromagnetic transponder-guided MLC tracking. *Med Phys*. 2014;41(2):020702. doi:10.1118/1.4862509
27. Wilbert JJ, Meyer JJ, Baier K, et al. Tumor tracking and motion compensation with an adaptive tumor tracking system (ATTS): System description and prototype testing. *Med Phys*. 2008;35(9):3911-3921. doi:10.1118/1.2964090
28. Cho B, Poulsen PR, Sawant A, Ruan D, Keall PJ. Real-time target position estimation using stereoscopic kilovoltage/megavoltage imaging and external respiratory monitoring for dynamic multileaf collimator tracking. *Int J Radiat Oncol Biol Phys*. 2011;79(1):269-278. doi:10.1016/j.ijrobp.2010.02.052
29. Colvill E, Booth J, Nill S, et al. A dosimetric comparison of real-time adaptive and non-adaptive radiotherapy: A multi-institutional study encompassing robotic, gimbaled, multileaf collimator and couch tracking. *Radiother Oncol*. 2016;119(1):159-165. doi:10.1016/j.radonc.2016.03.006
30. Palma D, Vollans E, James K, et al. Volumetric Modulated Arc Therapy for Delivery of Prostate Radiotherapy: Comparison With Intensity-Modulated Radiotherapy and Three-Dimensional Conformal Radiotherapy. *Int J Radiat Oncol Biol Phys*. 2008;72(4):996-1001. doi:10.1016/j.ijrobp.2008.02.047
31. Holt A, Van Vliet-Vroegindeweij C, Mans A, Belderbos JS, Damen EMFF. Volumetric-modulated arc therapy for stereotactic body radiotherapy of lung tumors: A comparison with intensity-modulated radiotherapy techniques. *Int J Radiat Oncol Biol Phys*. 2011;81(5):1560-1567. doi:10.1016/j.ijrobp.2010.09.014
32. Ong CL, Verbakel WFAR, Cuijpers JP, Slotman BJ, Lagerwaard FJ, Senan S. Stereotactic

radiotherapy for peripheral lung tumors: A comparison of volumetric modulated arc therapy with 3 other delivery techniques. *Radiother Oncol*. 2010;97(3):437-442. doi:10.1016/j.radonc.2010.09.027

33. Bertholet J, Knopf A, Eiben B, et al. Real-time intrafraction motion monitoring in external beam radiotherapy. *Phys Med Biol*. 2019;64(15). doi:10.1088/1361-6560/ab2ba8
34. Skouboe S, Ravkilde T, Bertholet J, et al. First clinical real-time motion-including tumor dose reconstruction during radiotherapy delivery. *Radiother Oncol*. 2019;139:66-71. doi:10.1016/j.radonc.2019.07.007
35. Poulsen PR, Fledelius W, Cho B, Keall P. Image-based dynamic multileaf collimator tracking of moving targets during intensity-modulated arc therapy. *Int J Radiat Oncol Biol Phys*. 2012;83(2):e265-e271. doi:10.1016/j.ijrobp.2011.12.053
36. Mao W, Hsu A, Riaz N, et al. Image-Guided Radiotherapy in Near Real Time With Intensity-Modulated Radiotherapy Megavoltage Treatment Beam Imaging. *Int J Radiat Oncol Biol Phys*. 2009;75(2):603-610. doi:10.1016/j.ijrobp.2009.04.068
37. Ma Y, Lee L, Keshet O, Keall P, Xing L. Four-dimensional inverse treatment planning with inclusion of implanted fiducials in IMRT segmented fields. *Med Phys*. 2009;36(6):2215-2221. doi:10.1118/1.3121425
38. Ma Y, Chang D, Keall P, et al. Inverse planning for four-dimensional (4D) volumetric modulated arc therapy. *Med Phys*. 2010;37(11):5627-5633. doi:10.1118/1.3497271
39. Azcona JD, Li R, Mok E, Hancock S, Xing L. Development and clinical evaluation of automatic fiducial detection for tumor tracking in cine megavoltage images during volumetric modulated arc therapy. *Med Phys*. 2013;40(3):1-11. doi:10.1118/1.4791646
40. Shirato H, Seppenwoolde Y, Kitamura K, Onimura R, Shimizu S. Intrafractional Tumor Motion: Lung and Liver. *Semin Radiat Oncol*. 2004;14(1):10-18. doi:10.1053/j.semradonc.2003.10.008
41. Dürichen R. From Univariate to Multivariate Respiratory Motion Compensation. Published online 2014.
42. Wade OL. Movements of the Thoracic Cage and Diaphragm in Respiration. *J Physiol*. 1954;124:193-212.
43. Giraud P, De Rycke Y, Dubray B, et al. Conformal radiotherapy (CRT) planning for lung cancer: Analysis of intrathoracic organ motion during extreme phases of breathing. *Int J*

Radiat Oncol Biol Phys. 2001;51(4):1081-1092. doi:10.1016/S0360-3016(01)01766-7

44. Shirato H, Shimizu S, Kunieda T, et al. Physical aspects of a real-time tumor-tracking system for gated radiotherapy. *Int J Radiat Oncol Biol Phys*. 2000;48(4):1187-1195. doi:10.1016/S0360-3016(00)00748-3
45. Shirato H, Suzuki K, Sharp GC, et al. Speed and amplitude of lung tumor motion precisely detected in four-dimensional setup and in real-time tumor-tracking radiotherapy. *Int J Radiat Oncol Biol Phys*. 2006;64(4):1229-1236. doi:10.1016/j.ijrobp.2005.11.016
46. Seppenwoolde Y, Shirato H, Itamura K, et al. Precise and Real-Time measurement of 3D Tumor motion in Lung due to breathing and heartbeat, measured during radiotherapy. *Int J Radiat Oncol Biol Phys*. 2002;53(4):822-834.
47. Suh Y, Dieterich S, Cho B, Keall PJ. An analysis of thoracic and abdominal tumour motion for stereotactic body radiotherapy patients. *Phys Med Biol*. 2008;53(13):3623-3640. doi:10.1088/0031-9155/53/13/016
48. Harold C. Urschel J, Kresl JJ, Luketich JD, Papiez L, Timmerman RD, Schulz RA. *Treating Tumors That Move with Respiration*. (Harold C. Urschel J, ed.). Springer; 2007.
49. Mageras GS, Pevsner A, Yorke ED, et al. Measurement of lung tumor motion using respiration-correlated CT. *Int J Radiat Oncol Biol Phys*. 2004;60(3):933-941. doi:10.1016/j.ijrobp.2004.06.021
50. Kitamura K, Shirato H, Seppenwoolde Y, et al. Tumor location, cirrhosis, and surgical history contribute to tumor movement in the liver, as measured during stereotactic irradiation using a real-time tumor-tracking radiotherapy system. *Int J Radiat Oncol Biol Phys*. 2003;56(1):221-228. doi:10.1016/S0360-3016(03)00082-8
51. Park JC, Park SH, Kim JH, et al. Liver motion during cone beam computed tomography guided stereotactic body radiation therapy. *Med Phys*. 2012;39(10):6431-6442. doi:10.1118/1.4754658
52. Brix L, Ringgaard S, Sørensen TS, Poulsen PR. Three-dimensional liver motion tracking using real-time two-dimensional MRI. *Med Phys*. 2014;41(4). doi:10.1118/1.4867859
53. Padhani AR, Khoo VS, Suckling J, Husband JE, Leach MO, Dearnaley DP. Evaluating the effect of rectal distension and rectal movement on prostate gland position using cine MRI. *Int J Radiat Oncol Biol Phys*. 1999;44(3):525-533. doi:10.1016/S0360-3016(99)00040-1
54. Hewson EA, Nguyen DT, O'Brien R, et al. The accuracy and precision of the KIM motion

monitoring system used in the multi-institutional TROG 15.01 Stereotactic Prostate Ablative Radiotherapy with KIM (SPARK) trial. *Med Phys*. 2019;46(11):4725-4737. doi:10.1002/mp.13784

55. Gierga DP, Chen GTY, Kung JH, Betke M, Lombardi J, Willett CG. Quantification of respiration-induced abdominal tumor motion and its impact on IMRT dose distributions. *Int J Radiat Oncol Biol Phys*. 2004;58(5):1584-1595. doi:10.1016/j.ijrobp.2003.09.077
56. Goldstein SD, Ford EC, Duhon M, McNutt T, Wong J, Herman JM. Use of Respiratory-Correlated Four-Dimensional Computed Tomography to Determine Acceptable Treatment Margins for Locally Advanced Pancreatic Adenocarcinoma. *Int J Radiat Oncol Biol Phys*. 2010;76(2):597-602. doi:10.1016/j.ijrobp.2009.06.009
57. Pham D, Kron T, Foroudi F, Schneider M, Siva S. A review of kidney motion under free, deep and forced-shallow breathing conditions: Implications for stereotactic ablative body radiotherapy treatment. *Technol Cancer Res Treat*. 2014;13(4):315-323. doi:10.7785/tcrt.2012.500387
58. Abhilash RH, Chauhan S, Che MV, Ooi CC, Bakar RA, Lo RHG. Quantitative study on the effect of abnormalities on respiration-induced kidney movement. *Ultrasound Med Biol*. 2016;42(7):1681-1688. doi:10.1016/j.ultrasmedbio.2016.01.015
59. Huang C-Y, Tehrani JN, Ng JA, et al. Six Degrees-of-Freedom Prostate and Lung Tumor Motion Measurements Using Kilovoltage Intrafraction Monitoring. *Int J Radiat Oncol Biol Phys*. 2015;91(2):368-375. doi:10.1016/j.ijrobp.2014.09.040
60. Yu ZH, Lin SH, Balter P, Zhang L, Dong L. A comparison of tumor motion characteristics between early stage and locally advanced stage lung cancers. *Radiother Oncol*. 2012;104(1):33-38. doi:10.1016/j.radonc.2012.04.010
61. Plathow C, Ley S, Fink C, et al. Analysis of intrathoracic tumor mobility during whole breathing cycle by dynamic MRI. *Int J Radiat Oncol Biol Phys*. 2004;59(4):952-959. doi:10.1016/j.ijrobp.2003.12.035
62. Preiswerk F, Arnold P, Fasel B, Cattin PC. A Bayesian framework for estimating respiratory liver motion from sparse measurements. In: *Lecture Notes in Computer Science (Including Subseries Lecture Notes in Artificial Intelligence and Lecture Notes in Bioinformatics)*. ; 2012. doi:10.1007/978-3-642-28557-8_26
63. Sawant A, Keall P, Pauly KB, et al. Investigating the feasibility of rapid MRI for image-

guided motion management in lung cancer radiotherapy. *Biomed Res Int*. Published online 2014. doi:10.1155/2014/485067

64. Kipritidis J, Hugo G, Weiss E, Williamson J, Keall PJ. Measuring interfraction and intrafraction lung function changes during radiation therapy using four-dimensional cone beam CT ventilation imaging. *Med Phys*. 2015;42(3):1255-1267. doi:10.1118/1.4907991
65. Nehmeh SA, Erdi YE, Ling CC, et al. Effect of respiratory gating on reducing lung motion artifacts in PET imaging of lung cancer. *Med Phys*. 2002;29(3):366-371. doi:10.1118/1.1448824
66. Korreman SS. Motion in radiotherapy: photon therapy. *Phys Med Biol*. 2012;57(23):R161-R191. doi:10.1088/0031-9155/57/23/R161
67. Bögel M, Hofmann HG, Hornegger J, Fahrig R, Britzen S, Maier A. Respiratory motion compensation using diaphragm tracking for cone-beam C-arm CT: a simulation and a phantom study. *Int J Biomed Imaging*. Published online 2013. doi:10.1155/2013/520540
68. Filipovic M, Vuissoz PA, Codreanu A, Claudon M, Felblinger J. Motion compensated generalized reconstruction for free-breathing dynamic contrast-enhanced MRI. *Magn Reson Med*. 2011;65(3):812-822. doi:10.1002/mrm.22644
69. Wong JW, Sharpe MB, Jaffray DA, et al. The use of active breathing control (ABC) to reduce margin for breathing motion. *Int J Radiat Oncol Biol Phys*. 1999;44(4):911-919. doi:10.1016/S0360-3016(99)00056-5
70. Yamamoto T, Langner U, Loo BW, Shen J, Keall PJ. Retrospective Analysis of Artifacts in Four-Dimensional CT Images of 50 Abdominal and Thoracic Radiotherapy Patients. *Int J Radiat Oncol Biol Phys*. 2008;72(4):1250-1258. doi:10.1016/j.ijrobp.2008.06.1937
71. Macgowan CK, Wood ML. Phase-encode reordering to minimize errors caused by motion. *Magn Reson Med*. 1996;35(3):391-398. doi:10.1002/mrm.1910350318
72. Kragl G, af Wetterstedt S, Knäusl B, et al. Dosimetric characteristics of 6 and 10 MV unflattened photon beams. *Radiother Oncol*. 2009;93(1):141-146. doi:10.1016/j.radonc.2009.06.008
73. Vassiliev ON, Titt U, Pönisch F, Kry SF, Mohan R, Gillin MT. Dosimetric properties of photon beams from a flattening filter free clinical accelerator. *Phys Med Biol*. 2006;51(7):1907-1917. doi:10.1088/0031-9155/51/7/019
74. Asuni G. Investigation of Advanced Dose Verification Techniques for External Beam

Radiation Treatment. Published online 2013.

75. Chin EMY, Submitted AT, Partial IN, et al. A Four Dimensional Volumetric Modulated Arc Therapy Planning System for Stereotactic Body Radiation Therapy in Lung Cancers. 2013;(March).
76. Lee B, Lee S, Sung J, Yoon M. Radiotherapy-induced secondary cancer risk for breast cancer: 3D conformal therapy versus IMRT versus VMAT. *J Radiol Prot*. 2014;34(2):325-331. doi:10.1088/0952-4746/34/2/325
77. Timlin C, Warren DR, Rowland B, et al. 3D calculation of radiation-induced second cancer risk including dose and tissue response heterogeneities. *Med Phys*. 2015;42(2):866-876. doi:10.1118/1.4905158
78. Grantzau T, Thomsen MS, Væth M, Overgaard J. Risk of second primary lung cancer in women after radiotherapy for breast cancer. *Radiother Oncol*. 2014;111(3):366-373. doi:10.1016/j.radonc.2014.05.004
79. Negoro Y, Nagata Y, Aoki T, et al. The effectiveness of an immobilization device in conformal radiotherapy for lung tumor: reduction of respiratory tumor movement and evaluation of the daily setup accuracy. *Int J Radiat Oncol Biol Phys*. 2001;50(4):889-898. doi:10.1016/S0360-3016(01)01516-4
80. Kubo HD, Hill BC. Respiration gated radiotherapy treatment: A technical study. *Phys Med Biol*. 1996;41(1):83-91. doi:10.1088/0031-9155/41/1/007
81. Ierga DAPG, Rewer JOB, Harp GRCS, et al. The correlation between internal and external markers for abdominal tumors: Implications for respiratory gating. *Int J Radiat Oncol Biol Phys*. 2005;61(5):1551-1558. doi:10.1016/j.ijrobp.2004.12.013
82. Wu H, Zhao Q, Berbeco RI, Nishioka S, Shirato H, Jiang SB. Gating based on internal/external signals with dynamic correlation updates. *Phys Med Biol*. 2008;53:7173-7150. doi:10.1088/0031-9155/53/24/009
83. Kimura T, Hirokawa Y, Murakami Y, et al. Reproducibility of organ position using voluntary breath-hold method with spirometer for extracranial stereotactic radiotherapy. *Int J Radiat Oncol Biol Phys*. 2004;60(4):1307-1313. doi:10.1016/j.ijrobp.2004.07.718
84. Rosenzweig KE, Hanley J, Mah D, et al. The deep inspiration breath-hold technique in the treatment of inoperable non-small-cell lung cancer. *Int J Radiat Oncol Biol Phys*. 2000;48(1):81-87. doi:10.1016/S0360-3016(00)00583-6

85. Berson AM, Emery R, Rodriguez L, et al. Clinical experience using respiratory gated radiation therapy: Comparison of free-breathing and breath-hold techniques. *Int J Radiat Oncol Biol Phys*. 2004;60(2):419-426. doi:10.1016/j.ijrobp.2004.03.037
86. Kim T, Kim S, Park Y-K, Youn KK, Keall P, Lee R. Motion management within two respiratory-gating windows: feasibility study of dual quasi-breath-hold technique in gated medical procedures. *Phys Med Biol*. 2014;59(21):6583-6594. doi:10.1088/0031-9155/59/21/6583
87. Qian J, Xing L, Liu W, Luxton G. Dose verification for respiratory-gated volumetric modulated arc therapy. *Phys Med Biol*. 2011;56(15):4827-4838. doi:10.1088/0031-9155/56/15/013
88. Nicolini G, Vanetti E, Clivio A, Fogliata A, Cozzi L. Pre-clinical evaluation of respiratory-gated delivery of volumetric modulated arc therapy with RapidArc. *Phys Med Biol*. 2010;55(12). doi:10.1088/0031-9155/55/12/N01
89. Vedam SS, Keall PJ, Kini VR, Mohan R. Determining parameters for respiration-gated radiotherapy. *Med Phys*. 2001;28(10):2139-2146. doi:10.1118/1.1406524
90. Ionascu D, Jiang SB, Nishioka S, Shirato H, Berbeco RI. Internal-external correlation investigations of respiratory induced motion of lung tumors. *Med Phys*. 2007;34(10):3893-3903. doi:10.1118/1.2779941
91. Hoisak JDP, Sixel KE, Tirona R, Cheung PCF, Pignol JP. Correlation of lung tumor motion with external surrogate indicators of respiration. *Int J Radiat Oncol Biol Phys*. 2004;60(4):1298-1306. doi:10.1016/j.ijrobp.2004.07.681
92. Kothary N, Heit JJ, Louie JD, et al. Safety and Efficacy of Percutaneous Fiducial Marker Implantation for Image-guided Radiation Therapy. *J Vasc Interv Radiol*. 2009;20(2):235-239. doi:10.1016/j.jvir.2008.09.026
93. Keall PJ, Todor AD, Vedam SS, et al. On the use of EPID-based implanted marker tracking for 4D radiotherapy. *Med Phys*. 2004;31(12):3492-3499. doi:10.1118/1.1812608
94. Poulsen PR, Cho B, Ruan D, Sawant A, Keall PJ. Dynamic multileaf collimator tracking of respiratory target motion based on a single kilovoltage imager during arc radiotherapy. *Int J Radiat Oncol Biol Phys*. 2010;77(2):600-607. doi:10.1016/j.ijrobp.2009.08.030
95. Matsuo Y, Ueki N, Takayama K, et al. Evaluation of dynamic tumour tracking radiotherapy with real-time monitoring for lung tumours using a gimbal mounted linac. *Radiother Oncol*.

2014;112(3):360-364. doi:10.1016/j.radonc.2014.08.003

96. Hoogeman M, Prevost J-B, Nuyttens J, Poll J, Levendag P, Heijmen B. Clinical Accuracy of the Respiratory Tumor Tracking System of the CyberKnife: Assessment by Analysis of Log Files. *Int J Radiat Oncol Biol Phys*. 2009;74(1):297-303. doi:10.1016/j.ijrobp.2008.12.041
97. Shah AP, Kupelian PA, Waghorn BJ, et al. Real-Time Tumor Tracking in the Lung Using an Electromagnetic Tracking System. *Int J Radiat Oncol Biol Phys*. 2013;86(3):477-483. doi:10.1016/j.ijrobp.2012.12.030
98. Smith RL, Lechleiter K, Malinowski K, et al. Evaluation of linear accelerator gating with real-time electromagnetic tracking. *Int J Radiat Oncol Biol Phys*. 2009;74(3):920-927. doi:10.1016/j.ijrobp.2009.01.034
99. Mao W, Wiersma RD, Xing L. Fast internal marker tracking algorithm for onboard MV and kV imaging systems. *Med Phys*. 2008;35(5):1942-1949. doi:10.1118/1.2905225
100. Wiersma RD, Mao W, Xing L. Combined KV and MV imaging for real-time tracking of implanted fiducial markers. *Med Phys*. 2008;35(4):1191-1198. doi:10.1118/1.2842072
101. Kim JH, Nguyen DT, Huang CY, et al. Quantifying the accuracy and precision of a novel real-time 6 degree-of-freedom kilovoltage intrafraction monitoring (KIM) target tracking system. *Phys Med Biol*. 2017;62(14):5744-5759. doi:10.1088/1361-6560/aa6ed7
102. Kim JH, Nguyen DT, Booth JT, et al. The accuracy and precision of Kilovoltage Intrafraction Monitoring (KIM) six degree-of-freedom prostate motion measurements during patient treatments. *Radiother Oncol*. 2018;126(2):236-243. doi:10.1016/j.radonc.2017.10.030
103. Ernst F, Schlaefer A, Schweikard A. Predicting the outcome of respiratory motion prediction. *Med Phys Med Phys Phys*. 2011;38(10):417051118-14794497. doi:10.1118/1.3633907
104. Ozhasoglu C, Saw CB, Chen H, et al. Synchrony - Cyberknife Respiratory Compensation Technology. *Med Dosim*. 2008;33(2):117-123. doi:10.1016/j.meddos.2008.02.004
105. Kilby W, Dooley JR, Kuduvalli G, Sayeh S, Maurer CR. The CyberKnife® robotic radiosurgery system in 2010. *Technol Cancer Res Treat*. 2010;9(5):433-452. doi:10.1177/153303461000900502
106. Hansen R, Ravkilde T, Worm ES, et al. Electromagnetic guided couch and multileaf

collimator tracking on a TrueBeam accelerator. *Med Phys*. 2016;43(5):2387-2398. doi:10.1118/1.4946815

107. Depuydt T, Verellen D, Haas O, et al. Geometric accuracy of a novel gimbals based radiation therapy tumor tracking system. *Radiother Oncol*. 2011;98(3):365-372. doi:10.1016/j.radonc.2011.01.015
108. Buzurovic I, Yu Y, Werner-Wasik M, et al. Implementation and experimental results of 4D tumor tracking using robotic couch. *Med Phys*. 2012;39(11):6957-6967. doi:10.1118/1.4758064
109. Poulsen PR, Cho B, Sawant A, Ruan D, Keall PJ. Detailed analysis of latencies in image-based dynamic MLC tracking. *Med Phys*. 2010;37(9):4998-5005. doi:10.1118/1.3480504
110. Isaksson M, Jalden J, Murphy MJ. On using an adaptive neural network to predict lung tumor motion during respiration for radiotherapy applications. *Med Phys*. 2005;32(12):3801-3809. doi:10.1118/1.2134958
111. Murphy MJ, Dieterich S. Comparative performance of linear and nonlinear neural networks to predict irregular breathing. *Phys Med Biol*. 2006;51:5903-5914. doi:10.1088/0031-9155/51/22/012
112. Sahih A, Haas OOCL, Goodband JH, Putra D, Mills JA, Burnham KJ. Respiratory motion prediction for adaptive radiotherapy. In: *IAR Annual Meeting*. ; 2006:1-6.
113. Lee SJ, Motai Y, Murphy M. Respiratory Motion EstimationWith Hybrid Implementation of Extended Kalman Filter. *IEEE Trans Ind Electron*. 2012;59(11):4421-4432. doi:10.1109/TIE.2011.2158046
114. Bukhari W, Hong S-M. Real-time prediction and gating of respiratory motion in 3D space using extended Kalman filters and Gaussian process regression network. *Phys Med Biol*. 2016;61(5):1947-1967. doi:10.1088/0031-9155/61/5/1947
115. Ramrath L, Schlaefer A, Ernst F, Dieterich S, Schweikard A. Prediction of respiratory motion with a multi-frequency based Extended Kalman Filter. In: *Proceedings of the 21st International Conference and Exhibition on Computer Assisted Radiology and Surgery*. ; 2007:1-4.
116. Ernst F, Schweikard A. Forecasting respiratory motion with accurate online support vector regression (SVRpred). *Int J Comput Assist Radiol Surg*. 2009;4(5):439-447. doi:10.1007/s11548-009-0355-5

117. Ernst F, Dürichen R, Schlaefer A, Schweikard A. Evaluating and comparing algorithms for respiratory motion prediction. *Phys Med Biol*. 2013;58(11):3911-3929. doi:10.1088/0031-9155/58/11/3911
118. Ruan D, Keall P. Online prediction of respiratory motion: multidimensional processing with low-dimensional feature learning. *Phys Med Biol*. 2010;55(11):3011-3025. doi:10.1088/0031-9155/55/11/002
119. Dürichen R, Pimentel MAF, Clifton L, et al. Multitask Gaussian processes for multivariate physiological time-series analysis. *IEEE Trans Biomed Eng*. 2015;62(1):314-322. doi:10.1109/TBME.2014.2351376
120. Dürichen R, Wissel T, Schweikard A. Controlling motion prediction errors in radiotherapy with relevance vector machines. *Int J Comput Assist Radiol Surg*. 2015;10(4):363-371. doi:10.1007/s11548-014-1008-x
121. Schweikard A, Glosser G, Bodduluri M, Murphy MJ, Adler JR. Robotic Motion Compensation for Respiratory Movement during Radiosurgery. *Comput Aided Surg*. 2000;5(4):263-277. doi:10.1002/1097-0150(2000)5:4<263::AID-IGS5>3.0.CO;2-2
122. Ahn S, Yi B, Suh Y, et al. A feasibility study on the prediction of tumour location in the lung from skin motion. *Br J Radiol*. 2004;77(919):588-596. doi:10.1259/bjr/64800801
123. Koch N, Liu HH, Starkschall G, et al. Evaluation of internal lung motion for respiratory-gated radiotherapy using MRI: Part I - Correlating internal lung motion with skin fiducial motion. *Int J Radiat Oncol Biol Phys*. 2004;60(5):1459-1472. doi:10.1016/j.ijrobp.2004.05.055
124. Yan H, Yin F-F, Zhu G-P, Ajlouni M, Kim JH. The correlation evaluation of a tumor tracking system using multiple external markers. *Med Phys*. 2006;33(11):4073-4084. doi:10.1118/1.2358830
125. Ernst F, Bruder R, Schlaefer A, Schweikard A. Correlation between external and internal respiratory motion: A validation study. *Int J Comput Assist Radiol Surg*. 2012;7(3):483-492. doi:10.1007/s11548-011-0653-6
126. Ruan D, Fessler JA, Balter JM, Berbeco RI, Nishioka S, Shirato H. Inference of hysteretic respiratory tumor motion from external surrogates: a state augmentation approach. *Phys Med Biol*. 2008;53(11):2923-2936. doi:10.1088/0031-9155/53/11/011
127. Ruan D, Fessler JA, Balter JM. Mean position tracking of respiratory motion. *Med Phys*.

2008;35(2):782-792. doi:10.1118/1.2825616

128. Li R, Lewis JH, Berbeco RI, Xing L. Real-time tumor motion estimation using respiratory surrogate via memory-based learning. *Phys Med Biol*. 2012;57(15):4771-4786. doi:10.1088/0031-9155/57/15/4771

129. Jöhl A, Ehrbar S, Guckenberger M, et al. The ideal couch tracking system—Requirements and evaluation of current systems. *J Appl Clin Med Phys*. 2019;20(10):152-159. doi:10.1002/acm2.12731

130. Brahme A. Dosimetric precision requirements in radiation therapy. *Acta Oncol (Madr)*. 1984;23(5):379-391. doi:10.3109/02841868409136037

131. Kinsella TJ, Sohn J, Wessels B. Principles of radiation oncology. In: Chang AE, Hayes DF, Pass HI, et al., eds. *Oncology: An Evidence-Based Approach*. Springer, New York, NY; 2006:41-57. doi:10.1007/0-387-31056-8

132. Arimura H. *Image-Based Computer-Assisted Radiation Therapy*. (Arimura H, ed.). Springer Nature, Singapore; 2017. doi:10.1007/978-981-10-2945-5

133. Brown JM, Carlson DJ, Brenner DJ. The tumor radiobiology of SRS and SBRT: Are more than the 5 Rs involved? *Int J Radiat Oncol Biol Phys*. 2014;88(2):254-262. doi:10.1016/j.ijrobp.2013.07.022

134. Stephans KL, Woody NM, Reddy CA, et al. Tumor Control and Toxicity for Common Stereotactic Body Radiation Therapy Dose-Fractionation Regimens in Stage I Non-Small Cell Lung Cancer. *Int J Radiat Oncol Biol Phys*. 2018;100(2):462-469. doi:10.1016/j.ijrobp.2017.10.037

135. Davis JN, Medbery C, Sharma S, et al. Stereotactic body radiotherapy for centrally located early-stage non-small cell lung cancer or lung metastases from the RSSearch(®) patient registry. *Radiat Oncol*. 2015;10(113):1-10. doi:10.1186/s13014-015-0417-5

136. Guerrero M, Li XA. Extending the linear-quadratic model for large fraction doses pertinent to stereotactic radiotherapy. *Phys Med Biol*. 2004;49(20):4825-4835. doi:10.1088/0031-9155/49/20/012

137. Park HJ, Griffin RJ, Hui S, Levitt SH, Song CW. Radiation-Induced Vascular Damage in Tumors: Implications of Vascular Damage in Ablative Hypofractionated Radiotherapy (SBRT and SRS). *Radiat Res*. 2012;177(3):311-327. doi:10.1667/rr2773.1

138. Song CW, Chinsoo MKL, Dusenbery K, Sperduto PW. Radiobiological basis of SBRT and

SRS. Published online 2014:570-578. doi:10.1007/s10147-014-0717-z

139. Brown JM, Wilson WR. Exploiting tumour hypoxia in cancer treatment. *Nat Rev Cancer*. 2004;4(6):437-447. doi:10.1038/nrc1367

140. Brizel DM, Dodge RK, Clough RW, Dewhirst MW. Oxygenation of head and neck cancer: Changes during radiotherapy and impact on treatment outcome. *Radiother Oncol*. 1999;53(2):113-117. doi:10.1016/S0167-8140(99)00102-4

141. Storchi P, Woudstra E. Calculation of the absorbed dose distribution due to irregularly shaped photon beams using pencil beam kernels derived from basic beam data. *Phys Med Biol*. 1996;41(4):637-656. doi:10.1088/0031-9155/41/4/005

142. Storchi PRM, van Battum LJ, Woudstra E. Calculation of a pencil beam kernel from measured photon beam data. *Phys Med Biol*. 1999;44:2917-2928.

143. Jin J-Y, Wen N, Ren L, Glide-Hurst C, Chetty IJ. Advances in Treatment Techniques. *Cancer J*. 2011;17(3):166-176. doi:10.1097/ppo.0b013e31821f8318

144. Bortfeld T. The number of beams in IMRT—theoretical investigations and implications for single-arc IMRT. *Phys Med Biol*. 2010;55(1):83-97. doi:10.1088/0031-9155/55/1/006

145. Bortfeld T. Optimized planning using physical objectives and constraints. *Semin Radiat Oncol*. 1999;9(1):20-34. doi:10.1016/S1053-4296(99)80052-6

146. Men C, Romeijn HE, Taşkin ZC, Dempsey JF. An exact approach to direct aperture optimization in IMRT treatment planning. *Phys Med Biol*. 2007;52(24):7333-7352. doi:10.1088/0031-9155/52/24/009

147. Spirou S V., Chui CS. A gradient inverse planning algorithm with dose-volume constraints. *Med Phys*. 1998;25(3):321-333. doi:10.1118/1.598202

148. Zhang X, Liu H, Wang X, Dong L, Wu Q, Mohan R. Speed and convergence properties of gradient algorithms for optimization of IMRT. *Med Phys*. 2004;31(5):1141-1152. doi:10.1118/1.1688214

149. Optimization by Simulated Annealing Author (s): S . Kirkpatrick , C . D . Gelatt and M . P . Vecchi Published by : American Association for the Advancement of Science Stable URL : https://www.jstor.org/stable/1690046. 2019;220(4598):671-680.

150. Deasy JO. Multiple local minima in radiotherapy optimization problems with dose- volume constraints. *Med Phys*. 1997;24(7):1157-1161. doi:10.1118/1.598017

151. Wu Q, Mohan R. Multiple local minima in IMRT optimization based on dose-volume

criteria. *Med Phys*. 2002;29(7):1514-1527. doi:10.1118/1.1485059

152. Llacer J, Deasy JO, Bortfeld TR, Solberg TD, Promberger C. Absence of multiple local minima effects in intensity modulated optimization with dose-volume constraints. *Phys Med Biol*. 2003;48(2):183-210. doi:10.1088/0031-9155/48/2/304
153. Salari E, Unkelbach J. A column-generation-based method for multi-criteria direct aperture optimization. *Phys Med Biol*. 2013;58(3):621-639. doi:10.1088/0031-9155/58/3/621
154. Cassioli A, Unkelbach J. Aperture shape optimization for IMRT treatment planning. *Phys Med Biol*. 2013;58(2):301-318. doi:10.1088/0031-9155/58/2/301
155. Unkelbach J, Bortfeld T, Craft D, et al. Optimization approaches to volumetric modulated arc therapy planning. *Med Phys*. 2015;42(3):1367-1377. doi:10.1118/1.4908224
156. Eric J. Hall. Intensity-Modulated Radiation Therapy, Protons, And The Risk Of Second Cancers. *Int J Radiat Oncol Biol Phys*. 2006;65(1):1-7.
157. Xu XG, Bednarz B, Paganetti H. A review of dosimetry studies on external-beam radiation treatment with respect to second cancer induction. *Phys Med Biol*. 2008;53(13). doi:10.1088/0031-9155/53/13/R01
158. Yu CX, Tang G. Intensity-modulated arc therapy: principles, technologies and clinical implementation. *Phys Med Biol*. 2011;56(5):R31-R54. doi:10.1088/0031-9155/56/5/R01
159. Shepard DM, Cao D, Afghan MKN, Earl MA. An arc-sequencing algorithm for intensity modulated arc therapy. *Med Phys*. 2007;34(2):464-470. doi:10.1118/1.2409239
160. Earl MA, Shepard DM, Naqvi S, Li XA, Yu CX. Inverse planning for intensity-modulated arc therapy using direct aperture optimization. *Phys Med Biol*. 2003;48(8):1075-1089. doi:10.1088/0031-9155/48/8/309
161. Papp D, Unkelbach J. Direct leaf trajectory optimization for volumetric modulated arc therapy planning with sliding window delivery. *Med Phys*. 2013;41(1):011701. doi:10.1118/1.4835435
162. Chin E, Otto K. Investigation of a novel algorithm for true 4D-VMAT planning with comparison to tracked, gated and static delivery. *Med Phys*. 2011;38(5):2698-2707. doi:10.1118/1.3578608
163. Bedford JL. Treatment planning for volumetric modulated arc therapy. *Med Phys*. 2009;36(2009):5128-5138. doi:10.1118/1.3240488
164. Mahnam M, Gendreau M, Lahrichi N, Rousseau L-MM. Simultaneous delivery time and

aperture shape optimization for the volumetric-modulated arc therapy (VMAT) treatment planning problem. *Phys Med Biol*. 2017;62(14):5589-5611. doi:10.1088/1361-6560/aa7447

165. Dieterich S, Cavedon C, Chuang CF, et al. Report of AAPM TG 135: Quality assurance for robotic radiosurgery. *Med Phys*. 2011;38(6):2914. doi:10.1118/1.3579139
166. Oliver M, Gagne I, Popescu C, Ansbacher W, Beckham WA. Analysis of RapidArc optimization strategies using objective function values and dose-volume histograms. *J Appl Clin Med Phys*. 2010;11(1):10-23.
167. Canadian Cancer Statistics 2019: summary of projected number of cancer cases and deaths. Published 2019. cancer.ca/Canadian-Cancer-Statistics-2019-EN
168. Li X, Yang Y, Li T, Fallon K, Heron DE, Huq MS. Dosimetric effect of respiratory motion on volumetric-modulated arc therapy-based lung SBRT treatment delivered by TrueBeam machine with flattening filter-free beam. *J Appl Clin Med Phys*. 2013;14(6):195-204. doi:10.1120/jacmp.v14i6.4370
169. Li R, Fahimian BP, Xing L. A Bayesian approach to real-time 3D tumor localization via monoscopic x-ray imaging during treatment delivery. *Med Phys*. 2011;38(7):4205-4214. doi:10.1118/1.3598435
170. Nguyen DT, O'Brien R, Kim JH, et al. The first clinical implementation of a real-time six degree of freedom target tracking system during radiation therapy based on Kilovoltage Intrafraction Monitoring (KIM). *Radiother Oncol*. 2017;123(1):37-42. doi:10.1016/j.radonc.2017.02.013
171. Sung W, Park JM, Choi CH, Ha SW, Ye S-J. The effect of photon energy on intensity-modulated radiation therapy (IMRT) plans for prostate cancer. *Radiat Oncol J*. 2012;30(1):27-35. doi:10.3857/roj.2012.30.1.27
172. Shaw E, Kline R, Gillin M, et al. Radiation Therapy Oncology Group: Radiosurgery Quality Assurance Guidelines. *Int J Radiat Oncol Biol Phys*. 1993;27(5):1231-1239. doi:10.1016/S0001-2092(07)67640-6
173. Chin E, Loewen SK, Nichol A, Otto K. 4D VMAT, gated VMAT, and 3D VMAT for stereotactic body radiation therapy in lung. *Phys Med Biol*. 2013;58(4):749-770. doi:10.1088/0031-9155/58/4/749
174. Shah AP, Kupelian P a, Willoughby TR, Langen KM, Meeks SL. An evaluation of intrafraction motion of the prostate in the prone and supine positions using electromagnetic

tracking. *Radiother Oncol*. 2011;99(1):37-43. doi:10.1016/j.radonc.2011.02.012

175. Schefter TE, Kavanagh BD, Raben D, et al. A phase I/II trial of stereotactic body radiation therapy (SBRT) for lung metastases: Initial report of dose escalation and early toxicity. *Int J Radiat Oncol Biol Phys*. 2006;66(4 SUPPL.):120-127. doi:10.1016/j.ijrobp.2006.08.018
176. Timmerman R, McGarry R, Yiannoutsos C, et al. Excessive toxicity when treating central tumors in a phase II study of stereotactic body radiation therapy for medically inoperable early-stage lung cancer. *J Clin Oncol*. 2006;24(30):4833-4839. doi:10.1200/JCO.2006.07.5937
177. Benedict SH, Yenice KM, Followill D, et al. Stereotactic body radiation therapy: The report of AAPM Task Group 101. *Med Phys*. 2010;37(8):4078-4101. doi:10.1118/1.3438081
178. Nankali S, Worm ES, Hansen R, et al. Geometric and dosimetric comparison of four intrafraction motion adaptation strategies for stereotactic liver radiotherapy. *Phys Med Biol*. 2018;63(14). doi:10.1088/1361-6560/aacdda
179. Poulsen PR, Murtaza G, Worm ES, et al. Simulated multileaf collimator tracking for stereotactic liver radiotherapy guided by kilovoltage intrafraction monitoring: Dosimetric gain and target overdose trends. *Radiother Oncol*. 2020;144:93-100. doi:10.1016/j.radonc.2019.11.008
180. Omotayo A, Venkataraman S, McCurdy B. *Feasibility Study for Marker-Based VMAT Plan Optimization towards Real-Time Tumour Tracking*.; 2020. doi:10.1002/acm2.12892
181. Kataria T, Sharma K, Subramani V, Karrthick KP, Bisht SS. Homogeneity Index: An objective tool for assessment of conformal radiation treatments. *J Med Phys*. 2012;37(4):207-213. doi:10.4103/0971-6203.103606
182. Colvill E, Booth JT, O'Brien RT, et al. Multileaf Collimator Tracking Improves Dose Delivery for Prostate Cancer Radiation Therapy: Results of the First Clinical Trial. *Int J Radiat Oncol Biol Phys*. 2015;92(5):1141-1147. doi:10.1016/j.ijrobp.2015.04.024
183. Niu Y, Betzel GT, Yang X, et al. Planning 4D intensity-modulated arc therapy for tumor tracking with a multileaf collimator. *Phys Med Biol*. 2017;62(4):1480-1500. doi:10.1088/1361-6560/aa56b7
184. Klawikowski S, Tai A, Ates O, Ahunbay E, Li XA. A fast 4D IMRT/VMAT planning method based on segment aperture morphing. *Med Phys*. 2018;45(4):1594-1602. doi:10.1002/mp.12778

185. Guckenberger M, Krieger T, Richter A, et al. Potential of image-guidance, gating and real-time tracking to improve accuracy in pulmonary stereotactic body radiotherapy. *Radiother Oncol*. 2009;91(3):288-295. doi:10.1016/j.radonc.2008.08.010